STUDIES IN ORBITAL SYMMETRY CONSTRAINTS OF THE REACTIVITY OF GROUP (V) TRI-*TERT*-BUTYL SILOXIDE COMPOUNDS AND IN THE EPHEMERAL EXISTENCE OF DESTABILIZED 2-AZA-ALLYL ANIONIC LIGANDS

A Dissertation

Presented to the Faculty of the Graduate School

of Cornell University

in Partial Fulfillment of the Requirements for the Degree of

Doctor of Philosophy

by

Elliott Baines Hulley

May 2011

STUDIES IN ORBITAL SYMMETRY CONSTRAINTS OF THE REACTIVITY OF GROUP (V) TRI-*TERT*-BUTYL SILOXIDE COMPOUNDS AND IN THE EPHEMERAL EXISTENCE OF DESTABILIZED 2-AZA-ALLYL ANIONIC LIGANDS

Elliott Baines Hulley, Ph.D.

Cornell University 2011

The olefin complex $(silox)_3Nb(\eta^2$-*trans*-1-phenyl-2-vinylcyclopropane) (**2-PhVi^{c}Pr**, silox = $^tBu_3SiO$) was synthesized as a means of testing the existence a hypothesized biradical transition state for olefin dissociation. The binding of the olefin to $(silox)_3NbPMe_3$ (**2-PMe$_3$**) produces two diastereomeric complexes (**2-maj** and **2-min**) that undergo cyclopropane ring-cleavage and α-H atom abstraction to yield isomeric alkylidene-ene products *cis/trans*-$(silox)_3Nb{=}CH\text{-}CH{=}CH\text{-}CH_2CH_2Ph$ (***cis*-2-alk** and ***trans*-2-alk**) upon thermolysis. The two diastereomers rearranged at different rates and kinetic models suggest that ***trans*-2-alk** converts to ***cis*-2-alk** prior to ring cleavage and rearrangement. Phenomenological kinetic isotope effects were consistent with the kinetic models.

Efforts were undertaken to synthesize $[(silox)_3Ta]_2N_2$ in order to circumvent the apparent kinetic barrier to dinitrogen activation by $(silox)_3Ta$ (**1**). N-aminoazidirines reacted with $(silox)_3Ta$ to produce the parent imide $(silox)_3TaNH$ (**1=NH**) and with $(silox)_3Ta{=}CH_2$ to produce alkyl hydrazide complexes. The methyl hydrazide $(silox)_3Ta(CH_3)NHNH_2$ (**3-NHNH$_2$**) thermally degraded to the tetraaza-bimetallacycle $[(CH_3)(silox)_2Ta](\mu\text{-}NH\text{-}N)(\mu\text{-}NHNH)[(CH_3)(silox)_2Ta]\bullet 2\,^tBu_3SiOH$ (**4.2^{t}Bu$_3$SiOH**) with concomitant evolution of CH_4. The dinitrogen complex $[(silox)_2Ta(Cl)]_2N_2$ could be prepared via salt metathesis and methylated to produce

$[(silox)_2Ta(CH_3)]_2N_2$. Attempts to oxidatively couple **1=NH** or $(silox)_3TaNLi$ resulted only in decomposition or production of **1=NH**. White phosphorus (P_4) was found to react with **1** (at –78 °C) and **2-PMe$_3$** (at room temperature) to produce $[(silox)_3M]_2(\eta^1,\eta^1{:}\mu^2)P_2$ (M = Nb, Ta). When **2-PMe$_3$** was treated with P_4 at –78 °C for 16 h the novel complex $[(silox)_3Nb(^cP_3)]_2$ was formed.

Attempts to create new ligands containing the 2-aza-allyl anion resulted in CC-coupling chemistry that produced interesting organic frameworks. Both 3- and 5-membered rings and [4.4.0]-bicyclic systems could be constructed from the same precursor ligand, $(CH_3)_2C(CHNCH_2Py)_2$, upon treatment with different metal complexes. Chromium, cobalt and nickel bis(amide) complexes produced unique metal-metal bonded species as a result of the triple CC-coupling reaction that produces 4,4,8,8-tetramethyl-2,6-di(pyridin-2-yl)-3,7-bis((E)-(pyridin-2-ylmethylene)amino)-octahydro-1,5-naphthyridine (**14**) as an octadentate ligand.

BIOGRAPHICAL SKETCH

Elliott Baines Hulley was born in 1983 to Michael and Kathleen Hulley in Washington, D.C. His interest in science was fostered from a very early age by his mother, who quizzed him with algebra problems on the way to elementary school, and by his father, who answered his seven-year-old son's questions with, "Well, to a first approximation…" His interest in chemistry was first piqued in high school by Mrs. Gayle Meehan, an unusually exuberant and unfailingly encouraging teacher. Having chosen a scientific path, he risked certain doom in the unkempt, wild, and backward lands of the greater Philadelphia area to attend Ursinus College. At Ursinus, he learned the basics of chemical research through studying the oligomerization of aldoketenes. Through the NSF REU program he also had the opportunity to spend a summer studying organic biradicals with Prof. David Shultz at North Carolina State University and another summer attempting to synthesize chiral lactide derivatives with Prof. Mitch Smith at Michigan State University. While at Ursinus he also managed to obtain minor concentrations in Physics and Ancient Greek, although he apparently forgot to turn in the form confirming a minor in the latter. Ursinus played a much more important role in his life than he realized at the time, for it was there he had the fortune to meet his future wife Abigail. He and Abigail both decided to brave the cold and bitter North and make camp in Ithaca for a few years. He had the great honor to join the Wolczanski laboratory and was able to witness the Chadeayne-Marshak dynamic duo. After five-and-a-half years of messing about across the periodic table he completed his degree in December 2010. He and Abigail have now set their sights west, and he will soon join the laboratory of Morris Bullock at Pacific Northwest National Laboratory in Richland, Washington.

For Dad

ACKNOWLEDGEMENTS

First I would like to thank my advisor Pete Wolczanski, whose guidance and patience for my considerable eccentricities is unrivalled. I have no end of respect for him, both as a scientist and a person, and his clarity of thought breaks down the most complex system into its most essential parts.

My sincere gratitude also go to my remaining Committee members, Paul Chirik and Dave Collum. Paul has been exceedingly helpful over the years, both in private conversations and at Tuesday Lit Lunch. On many occasions I was very fortunate to have his input. Dave was also very helpful, particularly on kinetic and mechanistic problems, and the source of some of my most memorable conversations. I would also like to thank Barry K. Carpenter, who helped my understanding of computational chemistry and physical organic chemistry considerably. A great many thanks go to Ivan Keresztes, without whom a great deal of the data in this thesis would not exist. David Zax also deserves tremendous credit for the helping with my understanding of ^{93}Nb NMR, as well as spending two whole days obtaining solid-state NMR spectra. Tom Cundari is also thanked for his calculational contributions, which make their appearance in Chapters 1 and 2. Emil Lobkovsky is thanked for his crystal structure determinations, which, besides the NMR data, make up the bulk of the information in this work.

I would also like to thank Denise Wurtenburg and Josh Wakeman for making trips to the stockroom entertaining and enjoyable over the years. Dave Neish and Larry Stull were always helpful and always game for great conversation (particularly about the legislative process). I would also like to thank Pat Hine, Sharon De Roos, Sharon Calhoun, and Vonnie Ellis for the many great interactions I have had with them over the years.

During my graduate school career I have received considerable help from members of the Chirik group, most notably my fellow Ursinus alumnus Jon Darmon. He was always willing to help out with instrumentation or materials, for myself and others in the Wolczanski group, and his contributions to our work are considerable. I wish him the best of luck with his research and look forward to seeing his considerable scientific skill put to work. I would also like to give my thanks to Carsten Milsmann, who put up with my many questions about computational chemistry, Broken Symmetry, and the meaning of Ψ.

A special thanks goes to the Wolczanski group, past, present and future. Kurt Hirsekorn, Andrew Chadeayne, Mike Marshak, Matt Chambers and Dave Kuiper all ensured that my first few years were unforgettable and chock full of great stories. I would especially give credit to Kurt, who initially trained me and gave me great advice on what to do when I finished at Cornell.

My classmates Emily Volpe and Brenda Frazier have been, of course, an integral part of my graduate school experience. In Brenda both Emily and I found a determination and strength of will that helped us put our chemical lives into perspective. Brenda is a wonderful friend and a fantastic labmate, whose attention to detail often counterbalanced my scattered approach to things. Emily is, of course, the most admirable person I have ever met. In Emily both Brenda and I continually found someone who was always willing to listen and help with any particular problem, and she always gave my philosophical and religious questions far more consideration than they likely deserved. I am, for lack of a better word, blessed, to have known the two of them for my entire graduate career and I hope to keep contact with my chemical siblings for as long as they can stand me. Special thanks go to Erika Bartholomew, whom I have gotten to know very well over the past few years. She has come to be one of my closest friends, and I am far more fortunate for it. I have zero doubt she has

the capability to take all of her predecessors' strengths to heart and go far in the chemical sciences. I look forward to the day we are colleagues as well as close friends. My final year at Cornell would not have been the same were it not for Wesley Morris and Valerie Williams. They are both very capable scientists and, more importantly, great people. They both ensure that the group dynamic remains positive. I would also like to thank Brian Lindley, the newest group member, whose well-timed comments have proven his ability to change the dynamic of tense situations.

Finally, and most importantly, I would like to thank my family for putting up with my flightiness and at-best occasional communication. My mother, without whom none of this would be possible, has allowed her son to put many things on hold in the hope of finishing this program and going on in the sciences, and no amount of gratitude can ever repay her. My sister has put up with my borderline unannounced visits more than a dozen times due to my hectic "schedule", and her hospitality has made my life considerably easier at the expense of her inconvenience. Abigail, my wife and clearly better-half, has put up with a lot over the past six years. We have helped each other through our graduate school programs, although I clearly needed more support than she did. Her ability to console and reassure is beyond any comparison. As we go forward in life with our new jobs and family, know that any success we have is due to her diligence, patience, and affection. My love for the three of them is without measure.

TABLE OF CONTENTS

Biographical Sketch iii

Dedication iv

Acknowledgements v

List of Figures x

List of Schemes xv

List of Tables xvi

1. Experimental Evidence for a Biradical Transition State in Olefin Dissociation from $(silox)_3Nb$ (silox = $^tBu_3SiO$).

    Introduction 1
    Results and Discussion 8
    Conclusions 22
    Experimental 23
    References 28

2. Synthetic Efforts Towards $[(silox)_3Ta]_2N_2$: Variegated NH-Additions to Ta and Other Collateral Discoveries.

    Introduction 30
    Results and Discussion 36
    Conclusions 61
    Experimental 62
    References 68

3. Activation of White Phosphorus (P_4) with $(silox)_3Ta$ and $(silox)_3NbPMe_3$.

    Introduction 72
    Results and Discussion 75
    Conclusions 85
    Experimental 86
    References 89

4. Synthesis and Reactivity of Destabilized 2-Aza-Allyl Anionic Ligands.

    Introduction 91
    Results and Discussion 101
    Conclusions 164
    Experimental 165

References 189

Appendix:

^{93}Nb NMR in Solution 195
Experimental 199
References 200

LIST OF FIGURES

Figure 1.1 Ligand field diagrams of $(HO)_3M$ (M = Nb, Ta) 2

Figure 1.2 Orbital symmetry requirements for olefin dissociation and association to $(silox)_3M$. 4

Figure 1.3 Reaction coordinate illustrating olefin dissociation from $(silox)_3M$. . . 4

Figure 1.4 Transition state for olefin dissociation from $(silox)_3M$. 5

Figure 1.5 Stereochemistry of $PhVi^cPr$ complexes of $(silox)_3Nb$. 9

Figure 1.6 Calculated structures of diastereomeric $PhVi^cPr$ complexes of $(silox)_3Nb$. 10

Figure 1.7 ^1H and ^2H NMR spectra of **2-alk** and **2-alk-d_2**. 14

Figure 1.8 Plot of the decay of **2-maj** and **2-min**. 17

Figure 1.9 Change in the **2-maj**:**2-min** ratio over time. 18

Figure 1.10 Plot of the decay of **2-maj** and **2-min** in the presence of C_2H_4 20

Figure 2.1 Orbital-symmetry considerations in nitrogenation of **1**. 31

Figure 2.2 Calculated density map for one of the SOMOs of **[1-N_2]^3**. 32

Figure 2.3 ^1H NMR Spectrum of thermolyzed **3-$NHNH_2$** (downfield) 39

Figure 2.4 ^1H NMR Spectrum of thermolyzed **3-$NHNH_2$** (upfield) 39

Figure 2.5 ^1H-^{15}N HMBCAD Spectrum of thermolyzed **3-$NHNH_2$** (narrow) . . . 40

Figure 2.6 ^1H-^{15}N HMBCAD Spectrum of thermolyzed **3-$NHNH_2$** (wide) 41

Figure 2.7 Proposed structure of **3-$NHNH_2$** thermolysis product. 42

Figure 2.8 VT ^1H NMR spectra of **4.**2 $^tBu_3SiOH$ (upfield) 43

Figure 2.9 VT ^1H NMR spectra of **4.**2 $^tBu_3SiOH$ (downfield) 44

Figure 2.10 ^1H 1D-EXSY spectra of **4.**2 $^tBu_3SiOH$. 45

Figure 2.11 Proposed TS for interconversion of H_γ and H_δ protons of **4.**2 $^tBu_3SiOH$ 45

Figure 2.12 ^1H NMR spectrum of **3-$NH^{Me}N_{az}$** thermolysis product 47

Figure 2.13 Molecular structure of [(silox)$_3$MeTa](μ-η^2-N,N:η^1-C-NHNHCH$_2$CH$_2$CH$_2$)[Ta(κ-O,C-OSi^{t}Bu$_2$CMe$_2$CH$_2$)(silox)$_2$] 48

Figure 2.14 Proposed structure of **3-NH^{Me}N$_{az}$** thermolysis product. 50

Figure 2.15 Various attempts at coupling at coupling **1=NH** and **1=NLi** 52

Figure 2.16 Side-on and end-on molecular views of **7-Cl$_2$**. 53

Figure 2.17 Proposed reaction leading to formation of **1=CPPh$_3$** 55

Figure 2.18 Molecular structure of **1=CPPh$_3$** 56

Figure 2.19 Synthesis and spectral data for (silox)$_3$Ta(Et)(NHNH$_2$) 57

Figure 2.20 Proposed skeletal structure of **8**. 58

Figure 2.21 Proposed syn/anti isomerism between **9a** and **9b** 60

Figure 3.1 Previously observed M$_n$(P$_m$) complexes. 72

Figure 3.2 Possible mechanism for the synthesis of M$_2$(μ^2:η^2,η^2-P$_2$) 73

Figure 3.3 Molecular structure of **[1]$_2$P$_2$** 75

Figure 3.4 Molecular structure of **[2]$_2$P$_2$** 77

Figure 3.5 Molecular structure of **[2-^{c}P$_3$]$_2$** 80

Figure 3.6 VT ^{31}P-NMR spectra of **[2-^{c}P$_3$]$_2$**. 81

Figure 3.7 Eyring plot for the interconversion of phosphorus environments in **[2-^{c}P$_3$]$_2$**. 82

Figure 3.8 Possible transition states for the interconversion of phosphorus environments in **[2-^{c}P$_3$]$_2$**. 82

Figure 3.9 Spectral characterization of **2-^{c}P$_3$H**. 83

Figure 3.10 VT ^{31}P-NMR spectra of **[(2-^{c}P$_3$)(I)]** 84

Figure 3.11 Eyring plot for the interconversion of phosphorus environments in **[(2-^{c}P$_3$)(I)]** 85

Figure 3.12 Proposed structure and spectral characterization of **[(2-^{c}P$_3$)(I)]** 85

Figure 4.1 Imine/azomethine ylid equilibrium and analogs 91

Figure 4.2 Attack of **(smif)$_2$Fe** on organic isocyanates 92
Figure 4.3 Prepared and proposed 2-aza-allyl-based ligands 94
Figure 4.4 Ligand architectures targeted for study 94
Figure 4.5 Coupling of 2-aza-allyl anions to yield iminopyridine ligands 95
Figure 4.6 Bond lengths in reduced iminopyridine ligand fragments 95
Figure 4.7 Interactions between two p-orbitals and two π^*-orbitals 96
Figure 4.8 Expected spin orientations in weakly-coupled biradicals 97
Figure 4.9 Orbital diagrams and wavefunction diagrams of TCSCF and BS descriptions of two weakly-interacting p-orbitals 98
Figure 4.10 Ligands incorporating the 2,6-dissubstituted pyridine fragment . . . 101
Figure 4.11 Syntheses and spectral properties of **H$_2^R$PBA** (R = H, ^{t}Bu) 103
Figure 4.12 Synthesis and spectral properties of putative **H$_2^H$mcSmif** 104
Figure 4.13 Synthesis and spectral properties of putative **H$_2^{tBu}$mcSmif** 104
Figure 4.14 Molecular structure of **(^{PDI}MC)Fe** 107
Figure 4.15 Structure and bond lengths of **PDI** and **PDI$^-$** 107
Figure 4.16 Molecular structure of **(12-Cr)$_2$**. 109
Figure 4.17 Rotated view of the coordination environment of **(12-Cr)$_2$**. 110
Figure 4.18 Dehydrogenative coupling of **(ImCH$_2$Py$_2$)Ar$_2$CH$_2$** to form **12** 112
Figure 4.19 ^{1}H and ^{13}C NMR spectral data and assignments for **(12-Fe)$_2$**. 113
Figure 4.20 Proposed structure of **(12-Fe)$_2$**. 114
Figure 4.21 Two proposed mechanisms for the production of **(12-M)$_2$** (M = Cr, Fe) 115
Figure 4.22 ^{1}H NMR spectrum of **NpImPy** + Cr(N(TMS)$_2$)$_2$(THF)$_2$ 118
Figure 4.23 Molecular structure of **(NpImPy)Ni** 121
Figure 4.24 Electronic structure calculations of **(NpImPy)Ni** 122
Figure 4.25 Comparison of **(NpImPy)Ni** with (RImPy)$_2$Ni (R = 2,6-

diisopropylphenyl) 123
Figure 4.26 Reductive cyclic voltammogram of **(NpImPy)Ni** 124
Figure 4.27 Oxidative cyclic voltammogram of **(NpImPy)Ni** 125
Figure 4.28 Molecular structure of **14-Cr$_2$** 127
Figure 4.29 Skeletal drawing of **{(tmtaa)Cr}$_2$** 129
Figure 4.30 Definition of the torsion angle ω 130
Figure 4.31 View of **14-Cr$_2$** along the Cr-Cr bond 131
Figure 4.32 Views of **14-Cr$_2$** illustrating the angle ϕ and C7-C7' proximity. . . . 131
Figure 4.33 Skeletal drawings of **14-Cr$_2$** illustrating the offset angle α 132
Figure 4.34 Skeletal structure of the neutral ligand framework **14** 134
Figure 4.35 Skeletal structure of C-profluorocurine 134
Figure 4.36 VT ^{1}H-NMR spectra of **14-Cr$_2$** in toluene-d_8 136
Figure 4.37 Nonlinear least-squares fit of **14-Cr$_2$** ^{1}H NMR data to thermal population of a triplet excited state. 137
Figure 4.38 Molecular orbital diagram illustrating M-M multiple bonding 138
Figure 4.39 Calculated highest-lying α- and β-SOMOs of **14-Cr$_2$** 139
Figure 4.40 Remaining α- and β-SOMOs of **14-Cr$_2$** 140
Figure 4.41 ^{1}H-NMR spectrum of **(HN$_4$)Fe(N(TMS)$_2$)** 141
Figure 4.42 Possible structures of **(HN$_4$)Fe(N(TMS)$_2$)** 142
Figure 4.43 Molecular structure of **14-Ni$_2$** 147
Figure 4.44 Molecular orbital diagrams for the d_8-d_8 M-M interaction between two face-to-face square planes 149
Figure 4.45 Product mixture from quench of **14-Ni$_2$** with dimethylglyoxime . . . 150
Figure 4.46 Molecular structure of **14-Co$_2$** 151
Figure 4.47 Comparison of imino-pyridine distances in **14-Cr$_2$**, **14-Co$_2$**, **14-Ni$_2$**, and **(NpImPy)Ni** 152

Figure 4.48 Structural comparison of **14-Cr_2**, **14-Co_2**, and **14-Ni_2** 154

Figure 4.49 Calculated electronic structure of **14-Ni_2** 157

Figure 4.50 Bonding and antibonding d_{z^2} interactions for **14-Ni_2** 158

Figure 4.51 Molecular orbital diagram for the d_8-d_8 M-M interaction between two offset square planes 158

Figure 4.52 Calculated electronic structure of **14-Co_2** 159

Figure 4.53 Magnetic orbitals of **14-Co_2** 160

Figure 4.54 Molecular structure of **($^{cPr}H_2N_4$)$TiCl_2$• ½ C_6H_6**. 162

Figure A.1 Plot of ^{93}Nb chemical shifts for the complexes in Table A.1 196

Figure A.2 Variable-temperature ^{93}Nb NMR spectra for (silox)3Nb^{13}C^{13}CO . . .197

LIST OF SCHEMES

Scheme 1.1 M(olefin) and M(alkylidene) isomerism via cyclometallation 1

Scheme 1.2 Synthesis of (±)*trans*-1-phenyl-2-vinylcyclopropane 9

Scheme 1.3 Illustration of dissociation and ring-opening transition states 12

Scheme 1.4 M(olefin) and M(alkylidene) isomerism preceding ring cleavage . . . 13

Scheme 1.5 Stepwise and concerted paths towards **2-alk** products 15

Scheme 1.6 Kinetic analysis of the **2-PhVi^{c}Pr** system 19

Scheme 2.1 Proposed utility of N-aminoaziridines towards synthesizing **[1]$_2$N$_2$** . . 35

Scheme 2.2 Reactivity of N-aminoaziridines with **1** 37

Scheme 4.1 Synthesis of (4-(tert-butyl)pyridine-2,6-diyl)dimethanol 102

Scheme 4.2 Synthesis of (4-(tert-butyl)pyridine-2,6-diyl)dimethanaminium dibromide 102

Scheme 4.3 Synthesis of H_2mcPDDM from 6,6'-methylenebis(4-(tert-butyl)-2-methylphenol 105

Scheme 4.4 Synthesis of **((ImCH$_2$Py)Ar)$_2$CH$_2$** 109

Scheme 4.5 Hypothetical dimerization of **(N$_4$)Cr** 133

Scheme 4.6 Proposed catalytic oxidative cyclization of **Me$_2$C(ImCH$_2$Py)$_2$** 143

Scheme 4.7 Reactivity of **^{c}Pr(ImCH$_2$Py)$_2$TiCl$_2$** with LiHMDS 163

LIST OF TABLES

Table 1.1 Rate constants obtained from kinetic simulation for disappearance of **2-maj** and **2-min** 21

Table 2.1 Selected bond angles and interatomic distances for **5** 48

Table 2.2 X-ray crystallographic data for **5**, **7-Cl$_2$**, **1=CPPh$_3$** 49

Table 2.3 Selected bond angles and interatomic distances for **7-Cl$_2$** 53

Table 2.4 Selected bond angles and interatomic distances for **1=CPPh$_3$** 56

Table 2.5 Selected NMR data for **8-11**, **2=O**, **2=CHCH$_3$**, **2-C$_2$H$_4$** 60

Table 3.1 Selected bond angles and interatomic distances for **[1]$_2$P$_2$** 76

Table 3.2 Selected bond angles and interatomic distances for **[2]$_2$P$_2$** 77

Table 3.3 X-ray crystallographic data for **[1]$_2$P$_2$**, **[2]$_2$P$_2$**, **[2-^{c}P$_3$]$_2$** 78

Table 3.4 Selected bond angles and interatomic distances for **[2-^{c}P$_3$]$_2$** 80

Table 4.1 Selected bond angles and interatomic distances for **(^{PDI}MC)Fe** . . . 106

Table 4.2 Selected bond angles and interatomic distances for **(12-Cr)$_2$** 110

Table 4.3 X-ray crystallographic data for **(^{PDI}MC)Fe** and **(12-Cr)$_2$** 111

Table 4.4 Selected bond angles and interatomic distances for **(NpImPy)Ni** from X-ray crystallography and DFT calculations 122

Table 4.5 Selected bond angles and interatomic distances for **14-Cr$_2$** 126

Table 4.6 Fit parameters for fit of **14-Cr$_2$** ^{1}H NMR data to Eq. 4.2 137

Table 4.7 Selected bond angles and interatomic distances for **14-Ni$_2$** 148

Table 4.8 Selected bond angles and interatomic distances for **14-Co$_2$** 152

Table 4.9 X-ray crystallographic data for **(NpImPy)Ni, 14-Cr$_2$•2(C$_6$H$_6$), 14-Co$_2$, 14-Ni$_2$, and ^{c}Pr(ImCH$_2$Py)$_2$TiCl$_2$•½(C$_6$H$_6$)**. 155

Table 4.10 Selected bond angles and interatomic distances for **^{c}Pr(ImCH$_2$Py)$_2$TiCl$_2$•½(C$_6$H$_6$)**. 162

Table A.1. ^{93}Nb Data for a series of available niobium complexes 196

Chapter 1

Experimental Evidence for a Biradical Transition State in Olefin Dissociation from $(silox)_3Nb$ (silox = $^tBu_3SiO$)*

Introduction

The discovery that olefin and alkylidene isomers of complexes of $(silox)_3M$ (M = Nb, Ta) existed in equilibrium[1] for several different starting olefins represented a unique opportunity to probe both the relative binding of the two ligand types and the fundamental differences between 2nd and 3rd row transition metal complexes.[2] It was discovered that the isomerization took place *via* participation of the normally ancillary silox ligand in the manner shown in Scheme 1.1.

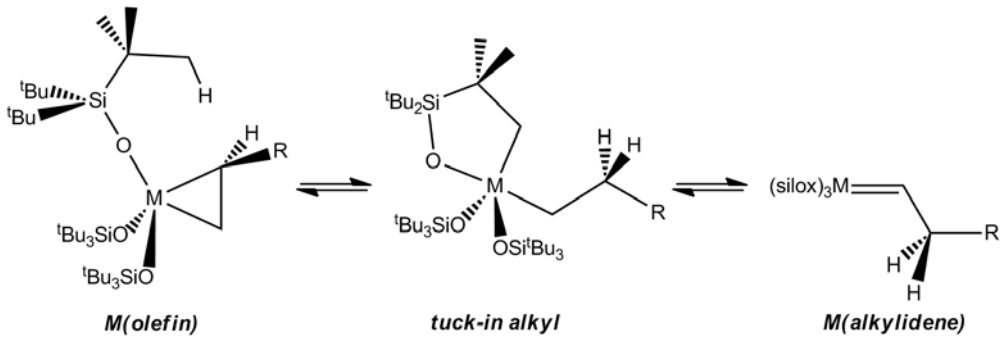

Scheme 1.1. Reversible cyclometallation of the $(silox)_3M$ provides a means for interconverting olefin and alkylidene isomers.

Both terminal and cyclic olefins were competent for this isomerization, and while the intermediate tuck-in alkyl species was observable for Ta it was only observed in a single Nb case (R = ^{t}Bu). The starting olefin complexes themselves could be synthesized directly for Ta, for which $(silox)_3Ta$ (**1**) is isolable, or via substitution for Nb, from either $(silox)_3NbPMe_3$ (**2**-PMe_3) or $(silox)_3Nb(\eta^2$-4-picoline). Indications of the substantial differences in the two systems arose during these syntheses, in which it

* Reproduced with permission from: Hirsekorn, K. F.; Hulley, E. B.; Wolczanski, P. T.; Cundari, T. R. *J. Am. Chem. Soc.* **2008,** *130,* 1183-1196

takes several days at room temperature for olefins to associate to **1** whereas it is an essentially instantaneous reaction for **2**-PMe_3 under the same conditions. It was surmised, and later confirmed,[3] that **2**-PMe_3 dissociates rapidly (~10^3 s^{-1}) and acts as a fast source of unisolable $(silox)_3Nb$ (**2**). Assuming this is the case, Nb associates with olefins faster than Ta by over six orders of magnitude. It was noticed that while Nb olefin complexes substituted olefins with relative ease at temperatures well below their isomerization temperatures, olefin binding to **1** appeared to be irreversible and only isomerization was observed. In an apparent contradiction to this evidence, computationally-obtained ΔG_{bind} values indicated that $(silox)_3Nb(ole)$ complexes were *more* stable than their Ta analogs with respect to dissociation. A full series of kinetic, thermodynamic, and computational studies were conducted to rationalize these inconsistencies. To understand these, first we must consider the nature of $(silox)_3M$.

The electronic structures of **1** and **2**,[4] represented in Figure 1.1 using the hydroxy model complexes, explain the superior stability of the Ta congener and illustrate the origin of electronic differences between 2nd and 3rd row transition metals.

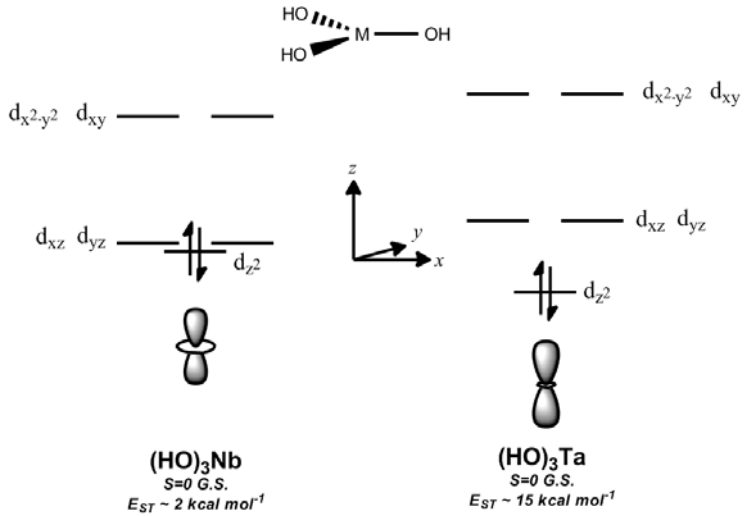

Figure 1.1. Simplified electronic structures and orbital splittings calculated for $(HO)_3Nb$ and $(HO)_3Ta$. Representations of d_{z^2} for each metal are shown below the splitting diagram.

Relativistic contributions to atomic orbital energies lead to a net reduction in the 6s/5d energy gap for Ta relative to the 5s/4d energy gap in Nb. This allows for more s-orbital mixing into the d-manifold, reducing the amount of σ* character of d_{z^2} in Ta by attenuation of its toroidal component.[5] Such attenuation is not nearly as significant for Nb, and as a result the HOMO-LUMO gap is far narrower and its triplet state is more accessible. This picture explains many of the properties of **1**, including its curious inability to accept pure σ-donor ligands despite its electronic unsaturation,[6] since incoming ligands are constrained by the silox groups to approach along the *z*-axis and encounter the repulsive d_{z^2} orbital. This interpretation was successfully used to explain similar inconsistencies in O-atom transfer reactions to $(silox)_3M$ (M=V, Nb, Ta).[4]

The unique stability of $(silox)_3Ta$ and its slow olefin association allowed for direct measurement of association rates and accompanying barrier heights ($\Delta G_a^{\ddagger}$) for olefin substrates, though the inability to observe substitution meant that the dissociation barriers ($\Delta G_d^{\ddagger}$) had to be computed for each olefin complex. The opposite was true of the Nb system; $\Delta G_a^{\ddagger}$ values were computed and $\Delta G_d^{\ddagger}$ were obtained from kinetic analysis of substitution experiments. It was discovered that in the *associative* direction there existed a linear free-energy (LFE) relationship between $\Delta G_a^{\ddagger}$ and ΔG_{bind} for Ta, such that the more strongly bound olefins associated more quickly, but no such relationship for Nb. In the *dissociative* direction the opposite was true; a $\Delta G_d^{\ddagger}$–ΔG_{bind} LFE relationship existed for Nb but not for Ta. This observation is a consequence of fact that the calculated dissociation barriers for $(silox)_3Ta(olefin)$ are similar for the different olefin substrates (40.6–43.5 kcal mol^{-1}) but quite different for $(silox)_3Nb(olefin)$ (25.0–34.5 kcal mol^{-1}), and the fact that the calculated association barriers for Nb are 10-20% the magnitude of those for Ta.

The final piece of the puzzle involves the structure of the transition states for olefin dissociation/association, but we must first consider the electronic nature of the reactant (M(ole)) and products (M + ole) for dissociation, shown in Figure 1.2.

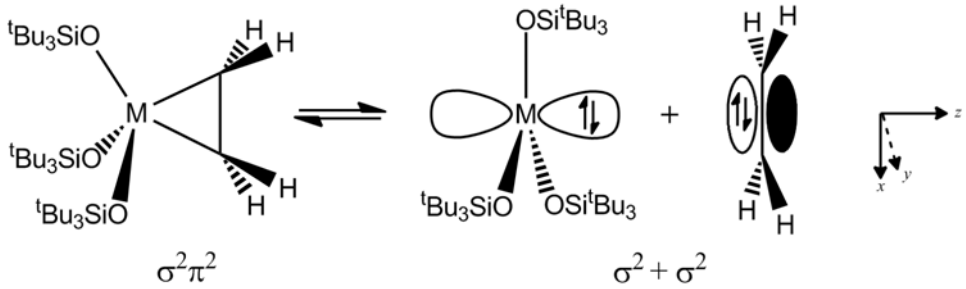

Figure 1.2. Orbital symmetry requirements for olefin dissociation and association to $(silox)_3M$.

Using either the metallacyclopropane or π-backbonding[7] models to represent the bonding in M(ole), one must assign two electrons to a σ-type orbital and two electrons to a π-type orbital. Since the *ground state* electronic structure of **1** and **2** are both *S*=0 with the two electrons in the σ-type d_{z^2} orbital, dissociation requires a state crossing during the procession from reactant to products. A parabolic reaction-coordinate, as represented in Figure 1.3, illustrates how orbital symmetry requirements explain both the barrier for olefin substitution *and* the fundamental difference between Ta and Nb.

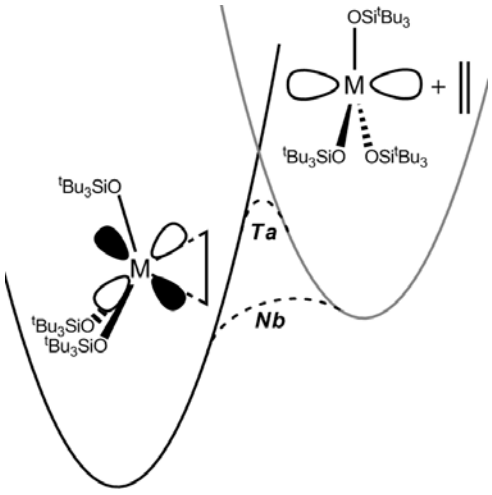

Figure 1.3. Reaction coordinate illustrating olefin dissociation from $(silox)_3M$.

The orbital defining the π-bonding interaction in M(ole), d_{xz} (using the axes in Figure 1.2), is part of the degenerate set that represent the LUMO orbitals in **1** and **2**. As such, the procession *directly* to products in Figure 1.3 would yield a $(d_{xz})^2$ configuration, a state at an energy that was estimated as twice the singlet-triplet gap. The crossing from reactant to product surface requires intervention of states that populate both d_{z^2} and d_{xz}; since the singlet-triplet gap is so much smaller for Nb than Ta, the states used for crossing are energetically closer together and allow for a much lower crossing surface. The steric requirements of the silox ligands ensure that the *geometric* distortions that would normally allow these state crossings are not accessible and the *inherent* differences between the metals involved are experimentally visible.

The structure of the calculated transition state (TS) for dissociation of ethylene from $(silox)_3M(C_2H_4)$ indicates the *geometric* consquences of this state crossing, as shown in Figure 1.4. The electron configuration of the TS is most instructive, showing

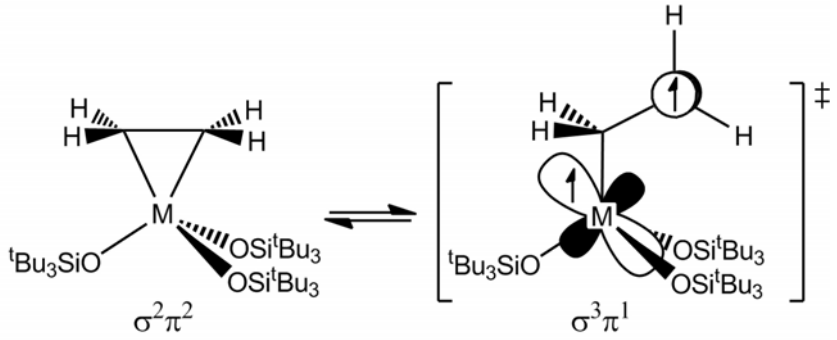

Figure 1.4. Illustration of the calculated transition state (TS) for olefin dissociation from $(silox)_3M(C_2H_4)$. The two unpaired electrons in the TS represent separate orbitals.

an asymmetric dissociation with respect to the outgoing olefin. The π-bond of the olefin has been broken and a lone electron SOMO is localized to a p-orbital orthogonal to the original π-bond plane. Of significant interest is the nature of the metal-localized SOMO, composed of an orbital that is an apparent σ-type d_{z^2}–d_{xz} hybrid that rationalizes the overall orbital symmetry changes.

This unusual result is the origin of the current project; as this TS explains how the complex accomplishes the required interconversion of orbital identity, it seemed logical to devise a test for any biradical character in the olefin substitution transition state. Two possibilities for testing this transition state suggest themselves. First, the TS for ethylene dissociation is calculated to *totally* break the π-bond, thus ethylene that is stereospecifically labeled should show scrambling upon coordination. Second, the presence of a radical on the β-carbon of the olefin should make it susceptible to interception with a radical trap. The interception of a transition state is a complicated enterprise; since a given transition state can *only* have one product,[8] there is no guarantee that the trap will indicate radical character of the TS for *any* substitution, only that *its* association or dissociation was radical in nature. Any trap that perturbs the olefin dramatically will lead to ambiguities about the generality of the conclusions. Of all the common radical clocks,[9] it was decided to use an olefin that would generate the so-called[10] "ultrafast" phenylcyclopropylcarbinyl radical during binding. The ring-opening reaction, shown in Eq. 1.1, has a rate constant of 3×10^{11} s^{-1} at 25 °C.[9b]

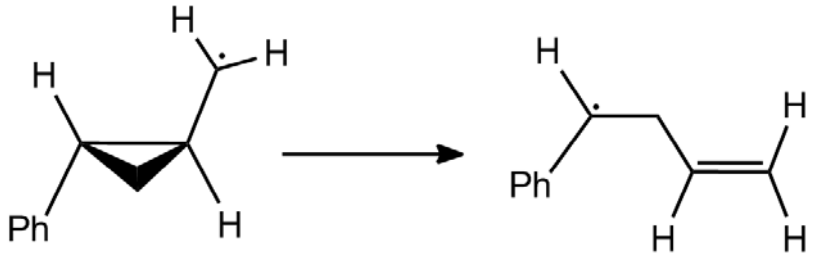

Eq. 1.1

This approach has been used before to probe the possibility of radical character in aziridination[11] and other various oxidations.[12] The Shaik[13] and Ingold[14] groups have, among others,[15] used the phenylcyclopropylcarbinyl radical clock in one form or another to determine important mechanistic insights into Cytochrome P450 oxidations of alkanes and alkenes. In those studies, the possibility of different oxidations that are productive and non-productive towards ring-opened products complicated mechanistic

analysis. The present study should not be affected by such difficulty since we are looking only for what happens upon coordination of 1-phenyl-2-vinylcyclopropane (PhVi^{c}Pr) to **1** and **2**.

Preliminary studies focused on *cis*- and *trans*-1,2-dideutereoethylene complexes of Nb and Ta. While both complexes were synthesized easily, the ^{1}H NMR spectra could not resolve the amount, if any, of epimerization present after binding. As such, displacement reactions to free the labeled ethylene were conducted and gas mixtures analyzed by IR spectroscopy. Unfortunately, as the ethylene is the most strongly bound olefin for both Nb and Ta, the thermal conditions necessary for convenient release of ethylene also resulted in scrambling from competitive cyclometallation. Additionally, it was found that both *cis*- and *trans*- PhVi^{c}Pr failed to bind to (silox)$_3$Ta, and cyclometallation to the tuck-in hydride was observed instead. The study was therefore limited to the association and dissociation reactions of *trans*-PhVi^{c}Pr with (silox)$_3$Nb.

Results and Discussion

1.1. Synthesis of 1-Phenyl-2-Vinylcyclopropane and its Complexes of Nb

Previous work by Hirsekorn revolved around the preparation of 1-phenyl-2-vinylcyclopropane (PhVi^{C}Pr) from the catalyzed reaction of phenyldiazomethane, prepared by deprotonation of the tosylhydrazone of benzaldehyde, with 1,3-butadiene as shown in Eq. 1.2.[16]

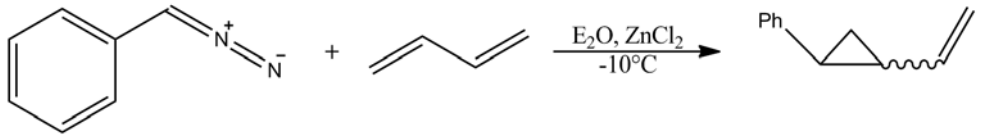

Eq.1.2

The above reaction apparently proceeds by way of $Zn(CHCl(Ph))_2$,[17] producing the cyclopropanated olefin as a mixture of racemic *cis*- and *trans*-isomers. The nascent olefin mixture was treated with $(silox)_3NbPMe_3$ and produced a series of signals consistent with Nb-olefin adducts. Thermolysis of the mixture above 100 °C overnight produced a mixture of *cis*-and *trans*- isomers of a Nb-alkylidene, as shown in Eq. 1.3.

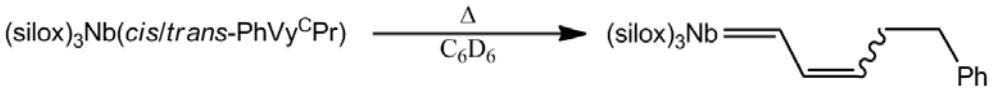

Eq. 1.3

The *cis*- and *trans*-isomers were produced in a 45:55 ratio, respectively, and the cyclopropane ring-scission implied the substrate was intercepting the desired transition state. A more well-defined starting material was desired to properly determine the origin of the two alkylidene products and for kinetic analysis of the reaction. As such, the current work began with the synthesis of exclusively *trans*-PhVi^{C}Pr from the synthesis shown in Scheme 1.2.

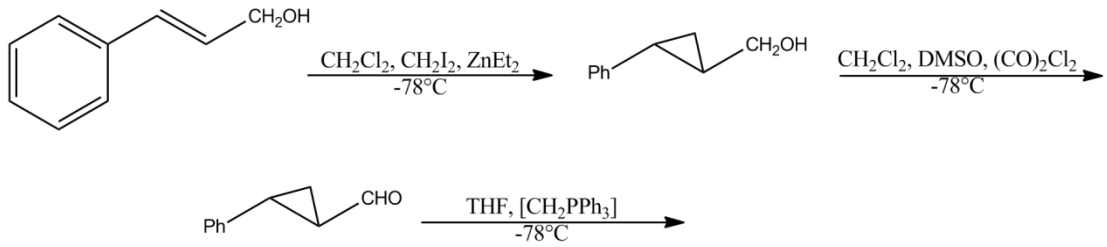

Scheme 1.2. Synthesis of (±)*trans*-1-phenyl-2-vinylcyclopropane from cinnamyl alcohol.

Commercially-available cinnamyl alcohol was cyclopropanated with $Zn(CH_2I)_2$ generated *in situ*, followed by PCC oxidation, and Wittig-olefination with *in situ*-generated methylenetriphenylphosphine.[18] The resultant olefin was purified by vacuum distillation and used for binding experiments.

A pentane solution of PhVi^{c}Pr was slowly added to a pentane solution of $(silox)_3NbPMe_3$ at –78 °C and allowed to warm to room temperature over the course of an hour. The resultant brown solution yielded an olive-brown oil that possessed ^{1}H NMR spectral signatures consistent with two products in a 2.2:1 ratio. Using COSY, HSQC and HMBC spectroscopies the two products were identified as two isomers of the desired olefin adduct. Since the β-carbon of PhVi^{c}Pr is prochiral, we would expect two diastereomers of the *trans*-PhVi^{c}Pr adduct from coordination at the *Re*- and *Si*-face of the olefin, as shown in Figure 1.5.

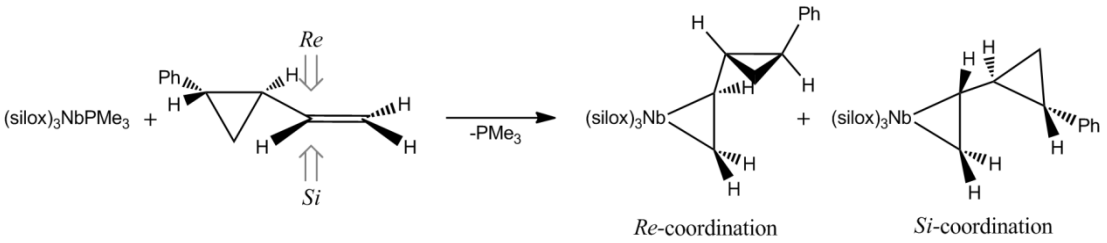

Figure 1.5. Stereochemistry of the diastereomeric PhVi^{c}Pr complexes of $(silox)_3Nb$. Only [R,R,R] and [S,R,R] diastereomers are shown.

Although the above 2D-NMR techniques only established connectivity and deconvoluted the ^{1}H and ^{13}C spectra, NOESY techniques shed light on which set of resonances correlated with which diastereomer by indicating observable through-space interactions. To aid the interpretation of the NOESY results, the structures of the two diastereomers were calculated. The results are presented in Figure 1.6.

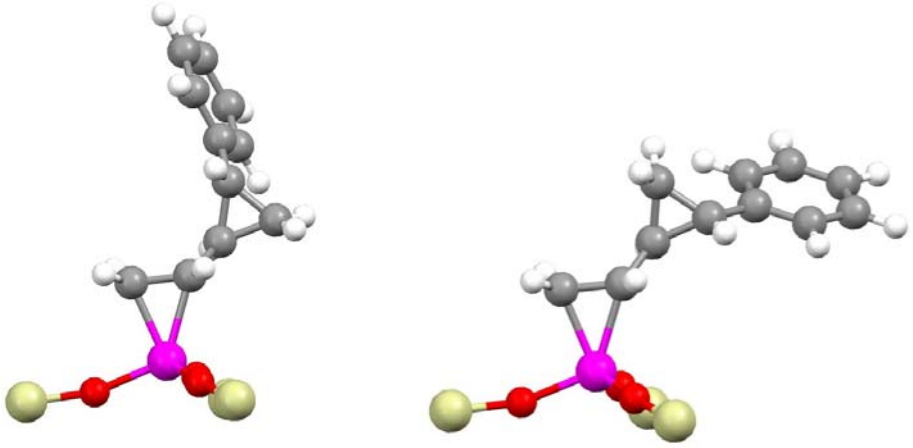

Figure 1.6. Calculated structures of the diastereomeric PhVi^{c}Pr complexes of $(silox)_3Nb$. For clarity, the [R,R,R] (left, *Si*-product) and [R,S,S] (right, *Re*-product) diastereomers are shown and ^{t}Butyl groups have been omitted.

In a series of 1D-NOESY experiments, irradiation of the benzylic-CH of the minor diastereomer gave NOE resonances to all three protons of the bound olefin. Irradiation of the same residue on the major isomer gave a resonance to only the β-proton of the bound olefin. Using the calculated structures and these data we could conclude that the minor diastereomer was the result of *Si*-coordination whereas the major diastereomer was due to *Re*-coordination. The exact origin of the modest selectivity for the *Re*-face is uncertain, as the *minor* isomer (**2-min**) is predicted to be more stable than the *major* isomer (**2-maj**) by ~2 kcal/mol. Of course, as there is essentially no dissociation (and no equilibrium) at low temperature the product ratio is almost totally kinetic in nature. When PhVi^{c}Pr and $(silox)_3NbPMe_3$ are added together at 22 °C the same products are produced in the slightly reduced ratio of 1.7:1. As the temperature-dependence of the

product ratio arises from the magnitude of $\Delta\Delta H^{\ddagger}$,[19] the modest effect of temperature indicates that the association rate differences are largely entropic in nature.

The two diastereomers could not be separated under normal conditions and were used as a mixture in further studies. Thermolysis of the diastereomer mixture at 150 °C for 5h yielded the same emerald-green *cis*- and *trans*-alkylidene-ene products in the same ratio as above in Eq. 2. The fact that such disparate reactants produced the same products in the same amount seemed unlikely and it was surmised that the *cis*- and *trans*-alkylidene-ene products could interconvert under the reaction conditions. ^{1}H NMR Exchange spectroscopy (EXSY) established that the olefinic γ-CH protons of the two isomers exchanged on the NMR timescale at 120 °C, putting an upper limit on the barrier to interconversion of *cis* to *trans* of 24 kcal mol^{-1} at that temperature. Due to this exchange there was no way to determine the exact course of the ring cleavage from the different possible isomers.

It was clear that PhVi^{c}Pr was not intercepting the proposed biradical transition state in the manner we had hoped for since the olefin had successfully associated to Nb without springing the cyclopropane ring. It is possible that the transition state for ring cleavage may be different from that for olefin association due to different structural requirements, such as different optimal C_{cPr}-C_{Vy} rotamers. The principle of microscopic reversibility holds on a *free energy* surface; the entropic and enthalpic requirements in the associative and dissociative directions are likely to be different. Alternatively, it is possible that simply cleaving the ring is reversible and unproductive until coupled to radical quenching via H-atom transfer. Ring cleavage of the cyclopropylcarbinyl radical to an olefin and benzylic radical is thermodynamically downhill (–19.13 kcal mol^{-1} using Benson Group Additivity)[20] but that gain could be offset by concomitant reduction to Nb(IV). Both of these explanations may play a role in the energy landscape of this system. The transition state for ring cleavage may

require a distortion from that for the association to the metal; a plausible reason for this is shown in Scheme 1.3.

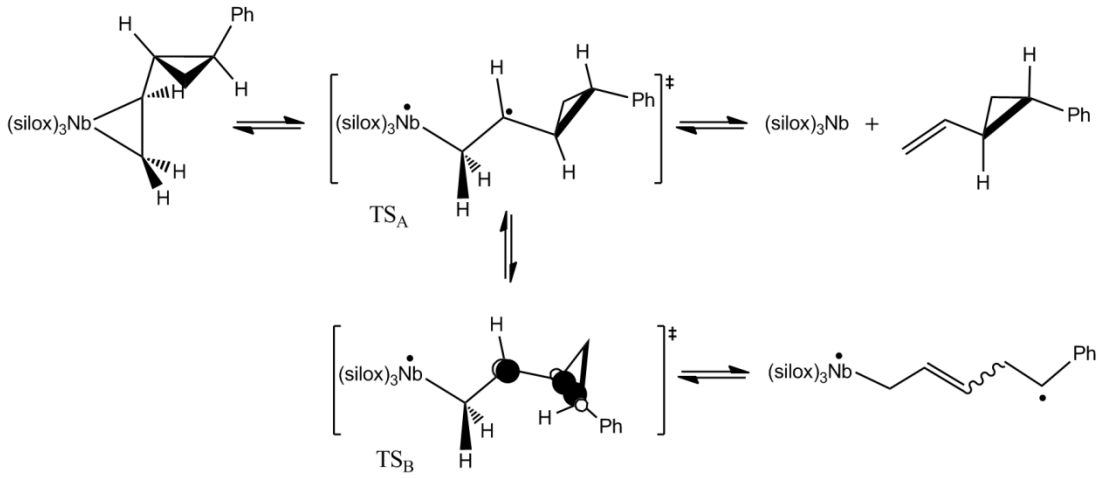

Scheme 1.3. Diagram representing the possible difference between dissociation and ring-opening transition states. Only the *trans*-producing transition state is shown for clarity.

Cycloproprane ring-opening requires a C_{cPr}-C_{Vy} rotamer that places the radical-containing p-orbital coplanar with the C-C bond to be cleaved. There are two ways to rotate the ^{c}Pr ring in TS_A to get to such a rotamer, with negligible structural differences, and these rotations will ultimately produce either the *cis*- or *trans*-alkylidene-ene after CH-activation of the α-carbon.

The fact that ring cleavage occurred at elevated temperatures indicated that the transition states for association and ring cleavage could be energetically adjacent, as suggested above. However, as was carefully established,[1] olefin adducts of $(silox)_3Nb$ are known to rearrange to their alkylidene isomers by means of reversible CH-activation of the silox ligands. It was possible this type of isomerization was occurring and that the cyclopropane ring-cleavage occurred thermally after generation of the alkylidene. This pathway, shown in Scheme 1.4, had to be excluded from being operative under the reaction conditions.

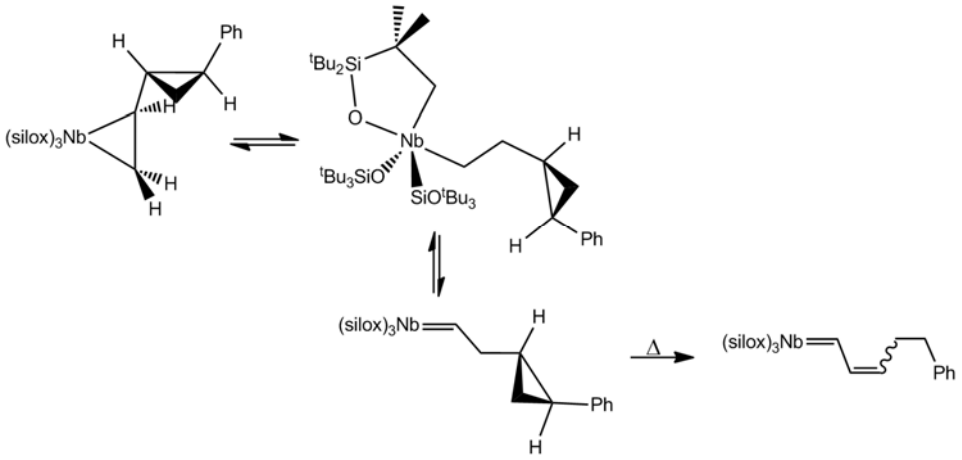

Scheme 1.4. Olefin-to-alkylidene isomerization preceding ring cleavage of the cyclopropane.

Rearrangement of the olefin using the previously-established mechanism could be tested via deuteration of the terminal CH_2 of the vinyl moiety; if it were active, rearrangement via cyclometallation would scramble the deuterium label into the silox framework. Synthesis of the α,α-dideutereo-1-phenyl-2-vinylcyclopropane (d_2-PhVi^{c}Pr) was conveniently accomplished via Wittig olefination of the precursor aldehyde with Ph_3PCD_2 generated *in situ* by deprotonation of $[Ph_3PCD_3]I$. Treatment of $(silox)_3NbPMe_3$ with d_2-PhVi^{c}Pr at 22 °C afforded the dideuterio analog of the adduct quantitatively with a major:minor diastereomer ratio of 1.8:1. Thermolysis at 120 °C for 4 h cleanly produced deuterated versions of the same *cis*- and *trans*-alkylidene-ene products observed in the protio case. In both isomers the alkylidene proton (Nb=C*H*) was absent and there was a change in the CH_2 proton integration for the two isomers. Though the allylic protons of the *trans* isomer and the benzylic protons of both isomers share the same resonance (2.58 ppm), the integration relative to the allylic protons of the *cis* isomer changed from 6:2 to 4:2 upon deuteration. Additionally, the allylic protons of the *cis* isomer changed from a pseudo-quartet to a pseudo-triplet. These results are consistent with deuteration at only the alkylidene

(Nb=CH) and benzylic positions in the ring-opened product. This was confirmed by ^{2}H NMR spectroscopy, which showed two sets of signals for those moieties. There was no observable incorporation of deuterium into the silox ligands, indicating cyclometallation processes were not competitive with isomerization. These data are presented in Figure 1.7.

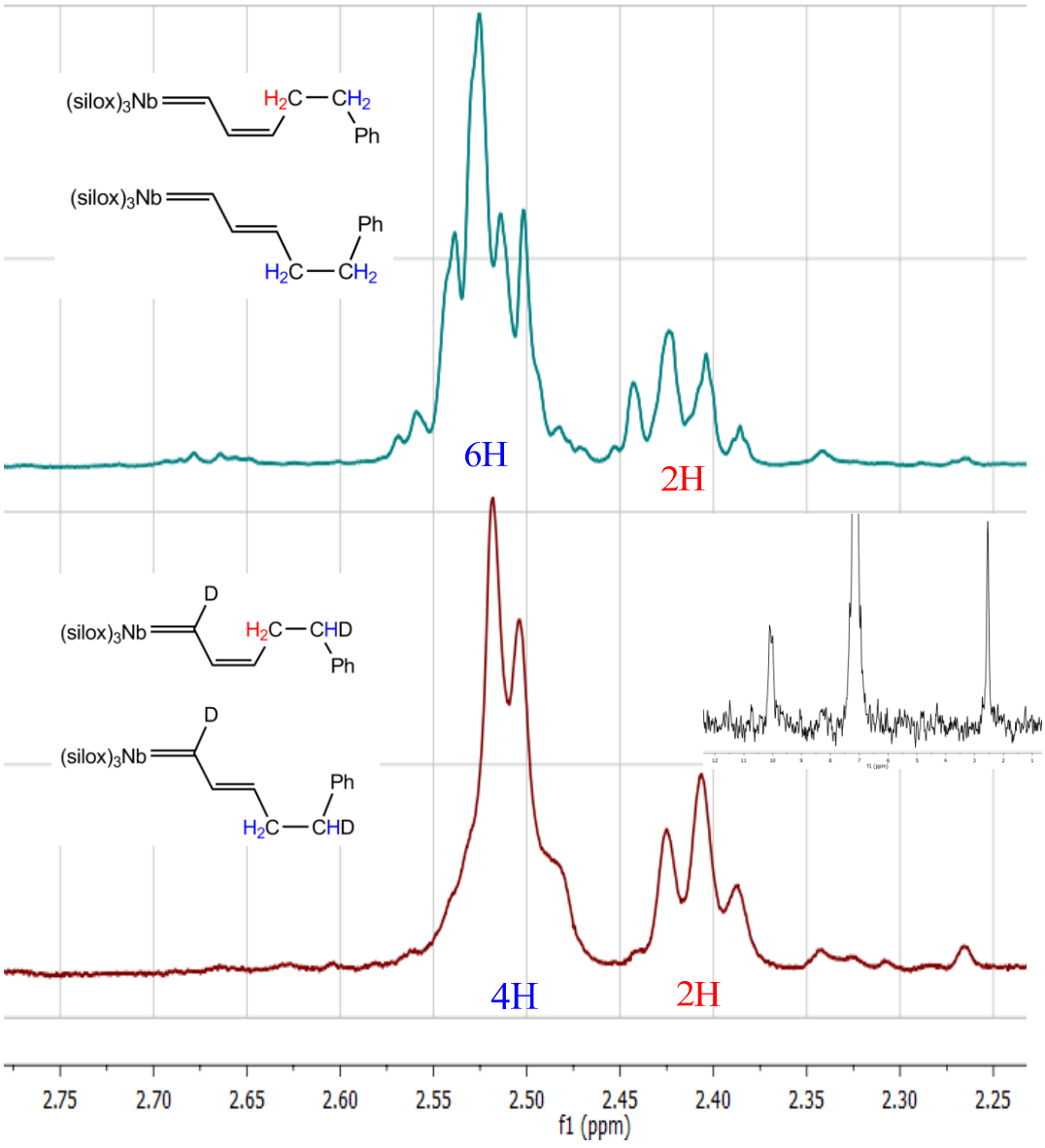

Figure 1.7. ^{1}H and ^{2}H (inset) NMR Spectra of protio (top) and deuterio (bottom) alkylidene-ene CH_2 protons.

The lack of silox involvement suggested the ring opening was proceeding via the radical process we were looking for. Although there are heterolytic mechanisms for arylvinylcyclopropane ring openings,[21] they are usually implicated in systems designed to stabilize cationic or anionic cleavages and the present ring opening is likely to be homolytic in nature.[22] In this system, the reaction could occur by either a stepwise ring-opening followed by α-H-abstraction or a concerted process. The stepwise and concerted paths considered here are shown in Scheme 1.5.

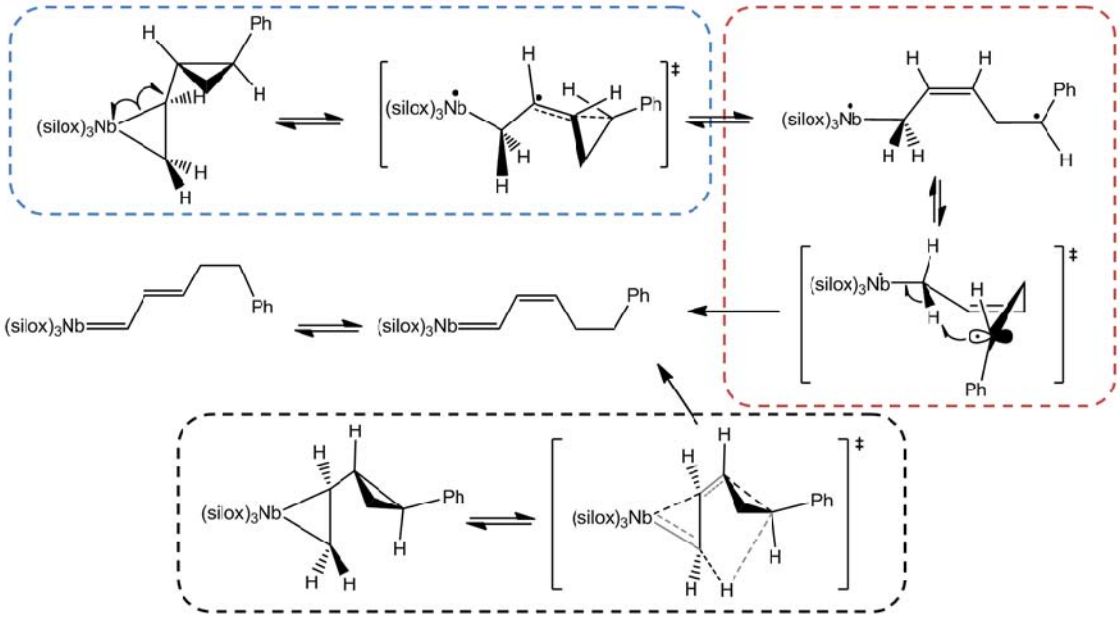

Scheme 1.5. Stepwise (blue, red) and concerted (black) paths towards the observed alkylidene-ene products (middle). The *cis*-productive stepwise path is shown.

The stepwise pathway involves homolytic cleavage of the Nb-C_β bond (using the metallacyclopropane formalism), a process likely coupled to the cyclopropane cleavage as discussed above. The nascent Nb(IV)-benzyl biradical would need to reorganize to a six-membered transition state for H-atom abstraction and generation of the alkylidene.

Due to the relatively fast kinetics of 3-member ring closures,[23] it is plausible these two steps are reversible and occurring during association of PhVi^{c}Pr to $(silox)_3Nb$. This might be expected to scramble the stereochemistry of the cyclopropane ring between *cis* and *trans* geometries of the phenyl and vinyl substituents, with the *trans* isomer being more thermodynamically favorable. To test this, *cis*-1-phenyl-2-vinylcyclopropane was synthesized[24] and treated with $(silox)_3NbPMe_3$. An adduct formed with ^{1}H NMR spectral characteristics consistent with two diastereomers, neither of which corresponded to those observed for the *trans* isomer. Thermolysis of this adduct for 3h at 150 °C gave quantitative conversion to the same alkylidene-ene products observed for the *trans*, consistent with the preliminary results obtained from a *cis*/*trans* mixture.

The transition state for olefin binding, if truly biradical in nature, was again not intercepted by the incoming radical trap and suggested it was energetically isolated from that for any sort of cyclopropane ring-opening reaction. If such a reversible ring-opening were operative at higher temperature prior to alkylidene-ene formation, the two *trans*-PhVi^{c}Pr adduct diastereomers might be expected to interconvert in a non-dissociative manner. The lack of observable EXSY crosspeaks at 75 °C indicative of diastereomer interconversion puts a lower limit on that barrier of 23 kcal mol^{-1}. Moreover, the two possible C_{cPr}-C_{Vy} rotamers implied by Scheme 1.2 would give different stereochemistries about the double bond in the biradical intermediate. Scheme 1.2 and Scheme 1.3 have indicated production of only the *cis*-alkene, since the *trans*-biradical would need to adopt a *trans* six-membered transition state that is highly disfavored.[25]

The *concerted* pathway shown in Scheme 1.3 can be seen as having a similar (or identical) chain of events as the stepwise path, in which case none of the proposed structures would be stable intermediates. The distinction between the stepwise and

concerted pathways is further complicated by the reality that the two different diastereomers, having different ground state structures, are likely to have quite different ring-opening opportunities. The calculated structure for the minor diastereomer, supported by NOESY data, places the benzylic carbon within 4Å of the α-protons of the olefin and may be much more amenable to a concerted rearrangement than the major diastereomer.

1.2. Kinetic Analysis of Rearrangement

It was quickly determined that **2-maj** and **2-min** had different rates of disappearance during the isomerization. The average data of three kinetic runs conducted at 85 °C are presented in Figure 1.8.

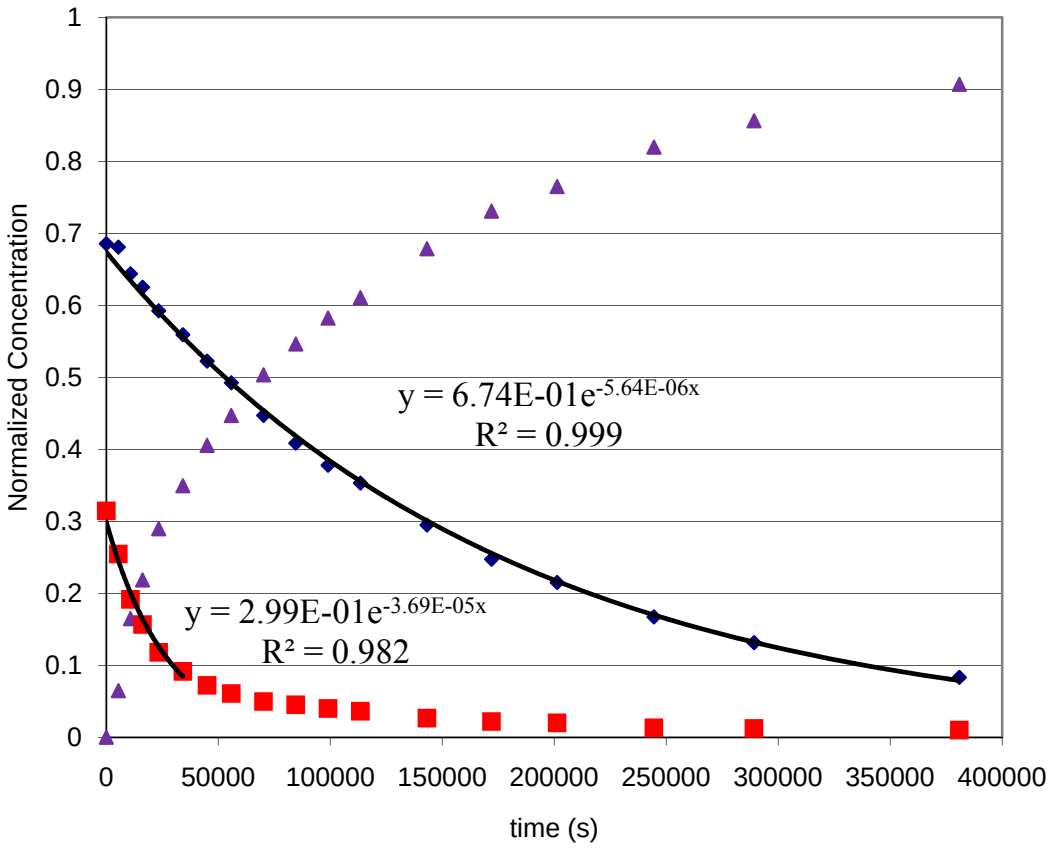

Figure 1.8. Decay of **2-maj** (blue diamonds), **2-min** (red squares) and appearance of cis/trans-**2-alk** (purple triangles).

The decay of **2-maj** nicely fits a first-order model with a rate constant of 5.6×10^{-6} s^{-1}, but neither the disappearance of **2-min** nor the appearance of *cis*/*trans*-**2-alk** follow a straightforward mathematical model. The initial six data points fit a first-order decay with a rate constant of 3.7×10^{-5} s^{-1}, indicating an initial decay that is almost an order of magnitude faster than **2-maj**. The ratio of **2-maj** to **2-min** changes as the isomerization progresses, as might be expected, but it curiously changes in two distinct linear regimes. This is shown graphically in Figure 1.9.

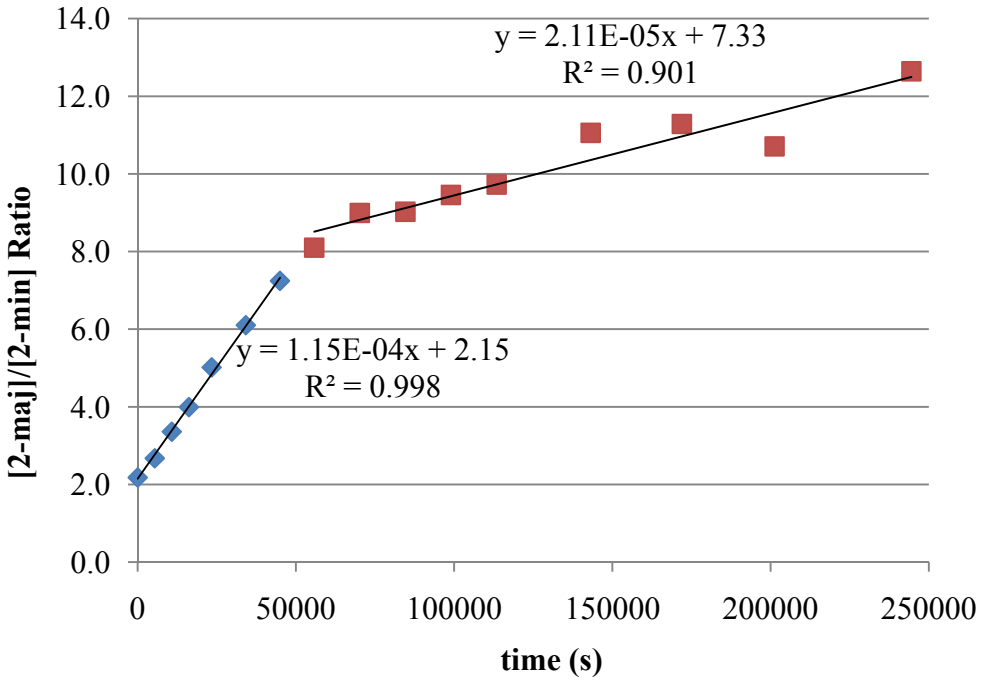

Figure 1.9. Evolution of the ratio of **2-maj** to **2-min** during the course of isomerization. The two regimes are highlighted for clarity.

These two regimes seem to be indicative of two different phases of the reaction. To understand this, we must examine all the mechanistic possibilities as laid out in Scheme 1.6.

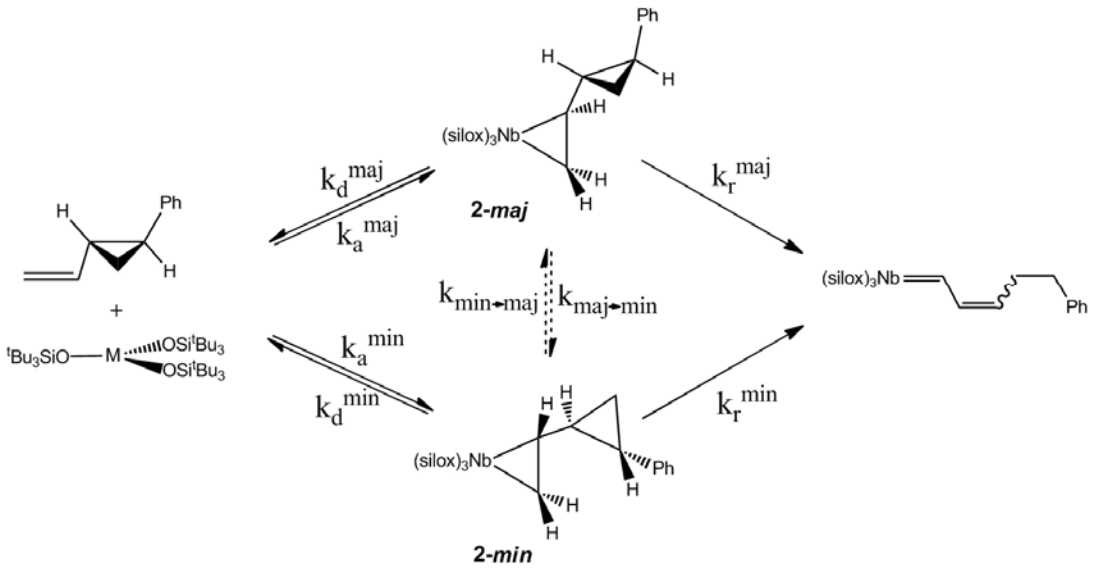

Scheme 1.6. Kinetic analysis of the **2-PhVi^{c}Pr** system with dissociation/association processes on the left and rearrangement processes on the right.

The reaction system outlined in Scheme 1.6 suffers from the presence of only three observables yet eight unknown rate constants. We lacked the ability to observe *direct* interconversion between **2-maj** and **2-min**, a process that should be viable if reversible ring-opening processes are occurring. For brevity we designed kinetic models ignoring this possibility and as such those models may not reflect the true system. We could constrain the *ratio* of association rate constants k_a to 1.4, the value (at 85 °C) extrapolated from the product distributions obtained at –78 °C and 25 °C, but this places some doubt on the accuracy (or relevance) of any information gained from kinetic simulation. To restrict the possible spread of dissociation rate constants a set of tubes was thermolyzed under identical conditions with the addition of 10 eq. of ethylene. The association rate constant of ethylene should be competitive for PhVicPr and its dissociation rate constant at 85 °C is negligible (6.6×10^{-9} s^{-1}), rendering it effectively irreversible. This should have the effect of quenching nascent $(silox)_3Nb$

and interconversion of **2-maj** and **2-min** by the indirect dissociative route. These results are presented in Figure 1.10.

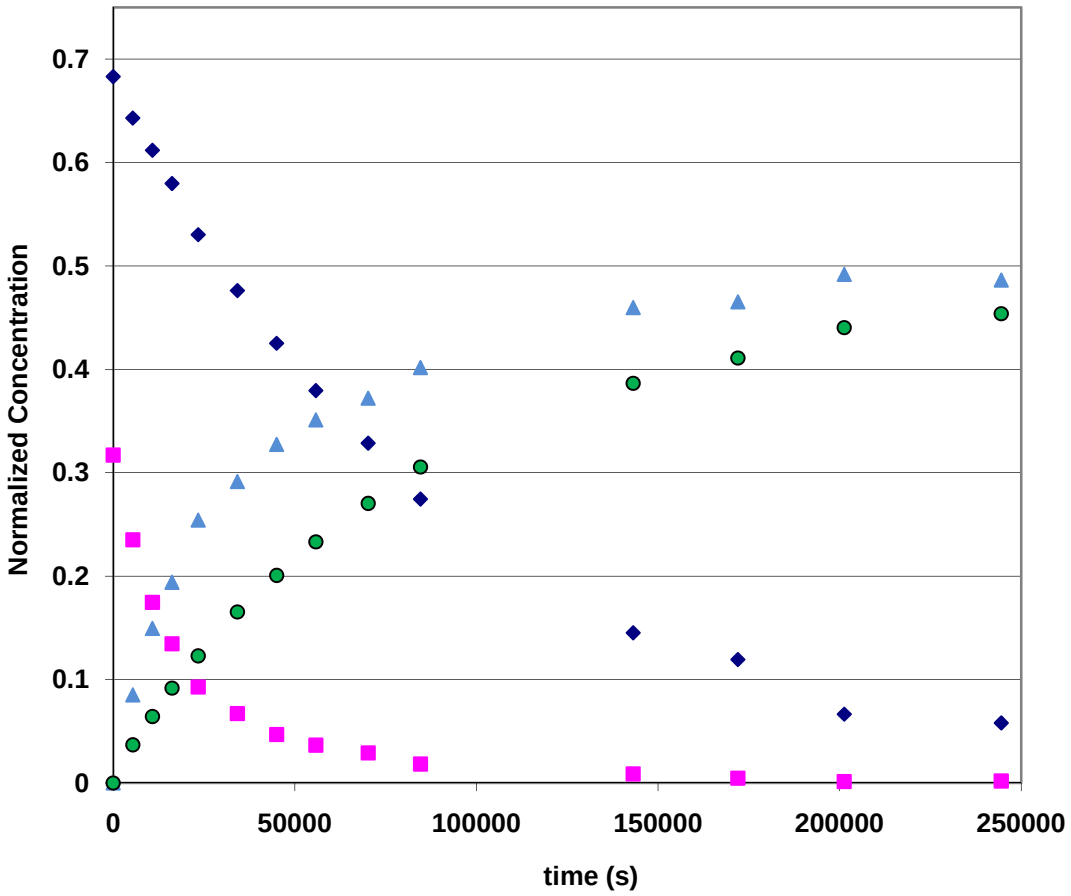

Figure 1.10. Thermolysis of **2-maj** (dk. blue) and **2-min** (squares) in the presence of excess ethylene to produce *cis/trans*-**2-alk** (lt. blue triangles) and **2-C_2H_4** (circles).

The disappearance of **2-maj** again fit a first-order decay model well with an apparent rate constant of 1.1×10^{-5} s^{-1}, almost twice as fast as without ethylene. This suggests that it substitutes at a rate on the same order as it isomerizes to the alkylidene-ene product. The disappearance of **2-min** for the first six data points also fits a first order decay model with an apparent rate constant of 4.6×10^{-5} s^{-1}, only marginally faster than without ethylene, suggesting its isomerization rate is appreciably faster than its substitution rate. These are, however, speculative, and a proper understanding could

only be gained by kinetic simulation. The values obtained assuming no *direct* interconversion of **2-maj** and **2-min** are presented in Table 1.1, where the data in absence of ethylene and in the presence of ethylene were fit simultaneously.

Table 1. 1. Rate constants obtained by kinetic simulation for the parameters in Scheme 1.6.

k_d^{maj}	$7.6(4)\times10^{-6}$ s^{-1}
k_d^{min}	$3(2)\times10^{-6}$ s^{-1}
k_r^{maj}	$3.4(3)\times10^{-6}$ s^{-1}
k_r^{min}	$4.6(2)\times10^{-5}$ s^{-1}

The model predicts that that **2-maj** dissociates about twice as often as it rearranges to the alkylidene-ene whereas **2-min** rearranges about an order of magnitude faster than it dissociates. This seems to reflect the first-order k_{obs} for **2-maj**, whose disappearance is dominated by its conversion to the minor isomer by dissociation and quickly isomerized. This could be the origin of the observed two-phase behavior shown in Figure 1.6.

Further information can be obtained by kinetic analysis of the disappearance of the α,α-dideuterio species, which gave *phenomenological* k_H/k_D values of 1.1(1) for disappearance of **2-maj** and 4.1(1) for the disappearance of **2-min**. Kinetic simulations for the deuterium-labeled species using the mechanism in Scheme 1.6 gave a similar disparity between the two diastereomers; the major diastereomer incurred a negligible isotope effect whereas the minor diastereomer had a significant primary isotope effect. This would be consistent with either mechanism in Scheme 1.5, where there is either a concerted H-atom transfer or stepwise bond-cleavage followed by H-atom abstraction. It is possible **2-min** operates primarily by a concerted pathway given the proximity of the abstracting carbon to the H-atom ultimately transferred (Fig. 1.6), whereas **2-maj** has a viable intermediate stage and operates by a stepwise mechanism.

Conclusion

We determined that while simply binding PhVi^{c}Pr to Nb was insufficient to spring the radical trap and intercept the biradical transition state, we did observe behavior consistent with radical ring-opening and isomerization. The temperatures and rates at which this isomerization occurred were consistent with a transition state for ring-opening that was separated from the transition state for substitution by fractions of a kcal mol^{-1}. As stated in the introduction, the experimentally determined rate for ring-opening of the phenylcyclopropylcarbinyl radical is 3×10^{11} s^{-1}, translating to a barrier of 1.8 kcal mol^{-1}. Given that the calculated barriers for olefin association to Nb range from 1.1-5.1 kcal mol^{-1}, translating to rates between 1.1×10^{9} s^{-1} and 9.7×10^{11} s^{-1}, it's possible that the above results show that the radical clock simply was not fast enough to ring open during association. In this way, the Nb(IV) generated in the transition state can be seen as a faster radical clock than the fastest known radical clock.

Experimental

General Considerations. All manipulations were carried out either using a nitrogen glovebox or high-vacuum and Schlenk techniques. All glassware was oven dried. Benzene-d_6 was refluxed over sodium metal, vacuum distilled and stored under nitrogen over activated 4Å molecular sieves. All solvents were distilled from sodium metal or sodium benzophenone-ketyl solutions. 1-Phenyl-2-vinylcyclopropane was synthesized via literature procedures[15a] and vacuum distilled prior to use. $(silox)_3NbPMe_3$ was synthesized according to literature procedures.[4] 1,2-d_2-Ethylene isomers (*cis* and *trans*) were purchased from Cambridge Isotope Laboratories and used as received.

^1H, ^2H and $^{13}C\{^1H\}$ NMR spectra were obtained on Varian 300 MHz (Mercury), 400 MHz (INOVA), 500 MHz (INOVA), and 600 MHz (INOVA) spectrometers. For historical consistency, NMR shifts for silox-containing compounds are referenced to benzene-d_6 (^1H, δ 7.15 ppm; ^2H, δ 7.15 ppm; ^{13}C, δ 128.39 ppm). ^{93}Nb NMR spectra were obtained in C_6D_6 and referenced to external $NbCl_5$ in acetonitrile (0.00 ppm).

Synthesis. 1. $(silox)_3Nb(\eta^2$-1-phenyl-2-vinylcyclopropane) (1-VyCy). A 100-ml three-necked round-bottom flask was charged with 350 mg (0.479 mmol) $(silox)_3NbPMe_3$, a side arm containing 68 mg (0.472 mmol) *trans*-1-phenyl-2-vinylcyclopropane, and a 180° adapter were attached to one of the flask. The flask was evacuated on the high-vacuum line and pentane (50 ml) was condensed into the flask. The vinylcyclopropane was added at –78° C and the solution was allowed to warm to room temperature with a concomitant color change from blue-purple solution to brown. After stirring for 1h at room temperature the volatiles were stripped *in vacuo* and the remaining brown-olive oil was triturated 3x with pentane (20 ml). ^1H NMR analysis indicated two sets of resonances consistent with a 1:2.2 ratio of diastereomers

of the **1-VyCy** (95%). Samples made at room temperature in C_6D_6 showed identical products but in a diminished 1:1.7 ratio. This material was used directly to make stock solutions in C_6D_6 for use in subsequent experiments. ^{93}Nb NMR (C_6D_6): δ 361.5 ($\nu_{½}$ = 21 kHz, diastereomers overlap)

Major diastereomer: ^{1}H NMR (C_6D_6): δ 1.22 (s, -Si(C(C***H***$_3$)$_3$), 81H), 1.24 (m, -CH***H***- (on ring), 1H), 1.33 (m, -C***H***H- (on ring), 1H), 1.82 (m, C***H***-CH=CH$_2$,1H), 2.01 (ddd, J = 4.2 Hz, 4.4 Hz, 8.8 Hz, PhC***H***, 1H), 2.13 (m, CH=C***H***H,1H), 2.15 (m, C***H***=CH$_2$, 1H), 2.74 (m, CH=CH***H*****,** 1H), 7.01 (t, J = 7.2 Hz, ^{p}C*H*, 1H), 7.10 (d, J = 6 Hz, 2H, ^{o}C*H*), 7.17 (t, J = 7.2 Hz, ^{m}C*H*, 2H). ^{13}C NMR (C_6H_6): δ 21.26 (-***C***H$_2$- (on ring)), 23.81 (Si(C(***C***H$_3$)$_3$)), 29.85 (Ph***C***H), 34.10 (Si(***C***(CH$_3$)$_3$)), 35.50 (***C***H-CH=CH$_2$), 71.33 (CH=***C***H$_2$), 81.03 (***C***H=CH$_2$), 125.64 (^{p}*C*), 126.42 (^{o}*C*), 134.61 (^{m}*C*), 144.91 (^{ipso}*C*).

Minor diastereomer: ^{1}H NMR (C_6D_6): δ 1.16 (m, -CH***H***- (on ring), 1H), 1.23 (s, Si((C(C***H***$_3$)$_3$)$_3$, 81H), 1.27 (m, -C***H***H- (on ring), 1H), 1.73 (dd, J = 8 Hz, 13 Hz, CH=CH***H*****,** 1H), 1.94 (ddd, J = 4.4 Hz, 4.6 Hz, 8.8 Hz, PhC***H*****,** 1H), 2.28 (m, C***H***-CH=CH$_2$,1H), 2.54 (dd, J = 8.4 Hz, 15.2 Hz, CH=C***H***H,1H), 2.88 (ddd, J =8.4 Hz, 13.6 Hz, 15.2 Hz, C***H***=CH$_2$,1H), 7.03 (t, J = 6.7 Hz, ^{p}C*H*,1H), 7.09 (d, J = 7.2 Hz, ^{o}C*H*, 2H), 7.18 (t, J = 7.6 Hz, ^{m}C*H*, 2H). ^{13}C NMR (C_6H_6): δ 18.09 (-***C***H$_2$- (on ring)), 23.84 (-Si(C(***C***H$_3$)$_3$)), 27.95 (Ph***C***H), 31.1 (Si(***C***(CH$_3$)$_3$)), 31.83 (***C***H-CH=CH$_2$), 64.19 (CH=***C***H$_2$), 82.53 (***C***H=CH$_2$), 125.75 (s, ^{p}*C*), 126.24 (s, ^{o}*C*), 134.46 (^{m}*C*), 141.21 (^{ipso}*C*).

2. (silox)$_3$Nb(η^2-1-phenyl-2-(α,α-dideuteriovinyl)cyclopropane) (1-d$_2$VyCy). Synthesized in the same manner as the protio congener. The methylene protons on the cyclopropane ring for both diastereomers were buried underneath the silox groups and attempts were not made to identify them.

Major diastereomer: ^{1}H NMR (C_6D_6): δ 1.22 (s, Si(C(C***H***$_3$)$_3$) , 81H), 1.82 (m, C***H***-CH=CD$_2$,1H), 2.01 (ddd, J = 4.2 Hz, 4.4 Hz, 8.8 Hz, PhC***H***,1H), 2.15 (d, J = 8Hz,

C***H***=CH_2), 1H), 7.01 (t, J = 7.2 Hz, ^{p}C*H*, 1H), 7.10 (d, J = 5.6 Hz, ^{o}C*H*, 2H), 7.17 (t, J = 6.8 Hz, ^{m}C*H*, 2H).

Minor diastereomer: ^{1}H NMR (C_6D_6): δ 1.23 (s, Si(C(C***H***$_3$)$_3$)$_3$, 81H), 7.09 (d, J = 7.2 Hz, ^{o}C*H*, 2H), 7.03 (t, J = 6.4 Hz, ^{p}C*H*, 1H), 2.86 (br s, C***H***=CD_2, 1H), 2.28 (m, C***H***-CH=CH_2, 1H), 1.93 (ddd, J =4.4 Hz, 4.6 Hz, 8.8 Hz, PhC***H***, 1H), 7.18 (t, J = 7.6 Hz, ^{p}C*H*, 2H)

3. (silox)$_3$Nb=CH-CH=CH-CH$_2$-CH$_2$-Ph (2-alk). A C_6D_6 solution of the VyCy-adduct was thermolyzed for 5h at 150° C, during which time the solution turned from an olive-brown to emerald-green. gCOSY and gHSQC NMR experiments allowed identification of two products that were cis-trans isomers in a 1:1.2 ratio. The alkylidene carbon could not be identified by ^{13}C spectroscopy due to broadening by the quadropolar Nb.

trans*-2-alk:** ^{1}H NMR (C_6D_6): δ 1.28 (s, SiC(CH***$_3$)$_3$, 81H), 2.59 (m, -C***H***$_2$C***H***$_2$-, 4H), 4.40 (dt, *J* = 14.8, 6.8 Hz, Nb=CH-CH=C***H***, 1H), 7.05 (m, 3H, ^{o}C*H* & ^{p}C*H*), 7.15 (m, ^{m}C*H*, 2H), 7.75 (dd, *J* = 10.6 Hz, 14.8 Hz, Nb=CH-C***H***=CH, 1H), 9.86 (d, *J* = 10.6 Hz, Nb=C***H***, 1H). ^{13}C (C_6D_6): δ 23.92 (s, Si***C***$(CH_3)_3$), 30.99 (s, SiC(***C***$H_3)_3$), 34.18 (***C***H_2CH_2Ph), 38.24 (CH_2***C***H_2Ph), 113.81 (s, Nb=CH-CH=***C***H), 126.36 (^{p}C), 128.92 (^{o}C), 129.12 (^{m}C) , 134.62 (s, Nb=CH-***C***H=CH) , 143.05 (^{ipso}C). δ 73.9 ($\nu_{½}$ = 2.7 kHz).

cis*-2-alk:** ^{1}H NMR (C_6D_6): δ 1.28 (s, SiC(CH***$_3$)$_3$, 81H), 2.48 (dt, *J* = 7.7, 7.5 Hz, C***H***$_2$$CH_2$Ph, 2H), 2.59 (m, CH_2C***H***$_2$Ph, 2H), 4.11 (dt, *J* = 10.6, 7.5 Hz, Nb=CH-CH=C***H***, 1H), 7.05 (m, ^{o}C*H*/^{p}C*H,* 3H), 7.15 (m, ^{m}C*H*, 2H), 7.81 (dd, *J* = 10.6 Hz, 10.6 Hz, Nb=CH-C***H***=CH, 1H), 9.95 (d, *J* = 10.6 Hz, Nb=C***H***, 1H). ^{13}C (C_6D_6): δ 23.89 (Si***C***$(CH_3)_3$), 29.98 (***C***H_2CH_2Ph), 30.99 (SiC(***C***$H_3)_3$), 37.34 (CH_2***C***H_2Ph), 111.85 (Nb=CH-CH=***C***H), 126.29 (^{p}C), 128.89 (^{o}C), 129.08 (^{m}C), 134.43 (Nb=CH-***C***H=CH), 142.91 (^{ipso}C). ^{93}Nb NMR (C_6D_6): δ 76.5 ($\nu_{½}$ = 5 kHz).

4. (silox)$_3$Nb=CD-CH=CH-CH$_2$-CHD-Ph (2-d$_2$alk). Prepared in the same manner as **2-alk**. The *cis*- and *trans*-isomers were present in a 1:1.2 ratio.

trans*-2-d$_2$alk**. ^{1}H NMR (C_6D_6): δ 1.28 (s, SiC(CH***$_3$)$_3$, 81H), 2.57 (m, C***H***$_2$C***H***D, 3H), 4.38 (dt, *J* = 14.6, 6.4 Hz, Nb=CH-CH=C***H***, 1H), 7.05 (m, ^{o}C*H*/^{p}C*H*, 3H), 7.15 (m, ^{m}C, 2H), 7.78 (d, *J* = 14.7 Hz, Nb=CH-C***H***=CH, 1H). ^{13}C (C_6D_6): δ 23.92 (Si***C***(CH$_3$)$_3$), 31.00 (SiC(***C***H$_3$)$_3$), 34.10 (***C***H$_2$CHDPh), 37.89 (t, J_{CD} = 19.2 Hz, CH$_2$***C***HDPh), 113.71 (Nb=CH-CH=***C***H), 126.35 (^{p}C), 128.92 (^{o}C), 129.11 (^{m}C), 134.62 (Nb=CH-***C***H=CH), 143.01 (^{ipso}C). ^{2}H NMR (C_6H_6): δ 2.55 (bs, CH$_2$CH***D***), 10.00 (s, Nb=C***D***)

cis*-2-d$_2$alk.** ^{1}H NMR (C_6D_6): δ 1.28 (s, SiC(CH***$_3$)$_3$, 81H), 2.47 (dd, *J* = 7.4, 7.5 Hz, C***H$_2$***CHD, 2H), 2.59 (m, CH$_2$C***H***D, 1H), 4.11 (dt, *J* = 10.2, 7.4 Hz, Nb=CD-CH=C***H***, 1H), 7.05 (m, ^{o}C*H*/^{p}C*H*, 3H), 7.15 (m, ^{m}C*H*, 2H), 7.83 (d, *J* = 10.0 Hz, Nb=CD-C***H***=CH, 1H). ^{13}C (C_6D_6): δ 23.90 (Si***C***(CH$_3$)$_3$), 29.88 (***C***H$_2$CHDPh), 31.00 (SiC(***C***H$_3$)$_3$), 36.99 (t, J_{CD} = 19.2 Hz, CH$_2$***C***HDPh), 111.75 (Nb=CD-CH=***C***H), 126.29 (^{p}C)), 128.89 (^{o}C), 129.08 (^{m}C), 134.42 (Nb=CD-***C***H=CH), 142.86 (^{ipso}C). ^{2}H NMR (C_6H_6): δ 2.55 (bs, CH$_2$CH***D***), 10.01 (s, Nb=C***D***).

Kinetic Experiments. NMR tubes used for kinetics were flame dried on the high-vacuum line prior to use. Olefin dissociation experiments were monitored by ^{1}H NMR spectroscopy with C_6D_6 as the solvent and ethylene (20 equiv.) as the trapping olefin. Conversion was determined by the ratio of integrations of the starting olefin complex to the ethylene adduct and the alkylidene-ene. Rearrangement experiments were monitored by ^{1}H NMR spectroscopy with C_6D_6 and conversion was determined by the ratio of integrations of the starting olefin to the alkylidene-ene. The ethylene adduct was identified as δ 2.40 (s, 4H), the two diastereomers of the PhVi^{cy}Pr-adduct were identified as δ 2.88 (ddd, 1H, minor C***H***=CH$_2$) and δ 2.74 (m, 1H, major CH=CH***H***), and the alkylidene-ene isomers were identified together as δ 7.78 (m, 1H,

cis+*trans* Nb=CH-C***H***=CH). The rapid interconversion of the *cis* and *trans* isomers of the alkylidene-ene allowed for the two species to be treated as one product. A stock solution of the adduct in C_6D_6 (0.04 M) was prepared and equal amounts (0.5 mL) of the stock solution were added to three NMR tubes (attached to 14/20 adaptors) for each run (9 total). The tubes were fixed to 180° adapters and freeze-pump-thaw degassed three times on the high-vacuum line. Ethylene was added to the substitution tubes by calibrated gas bulb. One of the substitution tubes malfunctioned during the run and the data from that run is based on two NMR tubes.

REFERENCES

1. Hirsekorn, K. F.; Veige, A. S.; Marshak, M. P.; Koldobskaya, Y.; Wolczanski, P. T.; Cundari, T. R.; Lobkovsky, E. B. *J. Am. Chem. Soc.* **2005,** *127,* 4809-4830.
2. Hirsekorn, K. F.; Hulley, E. B.; Wolczanski, P. T.; Cundari, T. R. *J. Am. Chem. Soc.* **2008,** *130,* 1183-1196.
3. Hirsekorn, K. F. Ph.D. Thesis, Cornell University, Ithaca, NY, **2005**.
4. Veige, A. S.; Slaughter, L. M.; Lobkovsky, E. B.; Wolczanski, P. T.; Matsunaga, N.; Decker, S. A.; Cundari, T. R. *Inorg. Chem.* **2003,** *42,* 6204-6224.
5. (a) 13. Drago, R. S. *J. Phys. Chem.* **1958,** *62,* 353–357. (b) 14. Power, P. P. *Chem. Rev.* **1999,** *99,* 3463–3503.
6. Covert, K. J.; Neithamer, D. R.; Zonnevylle, M. C.; LaPointe, R. E.; Schaller, C. P.; Wolczanski, P. T. *Inorg. Chem.* **1991,** *30,* 2494-2508.
7. (a) Dewar, M. *Bull. Soc. Chim. Fr.* **1951,** *18,* C71-C79. (b) Chatt, J.; Duncanson, L. A. *J. Chem. Soc.,* **1953,** 2939-2947.
8. Peterson, T. H.; Carpenter, B. K. *J. Am. Chem. Soc.* **1992,** *114,* 1496-1498.
9. (a) Griller, D.; Ingold, K. U. *Acc. Chem. Res.* **1980,** *13,* 317-323. (b) Newcomb, M. *Tetrahedron* **1993,** *49,* 1151-1176.
10. Choi, S. Y.; Toy, P. H.; Newcomb, M. *J. Org. Chem.***1998,** *63,* 8609-8613.
11. Catino, A. J.; Nichols, J. M.; Forslund, R. E.; Doyle, M. P. *Org. Lett.* **2005,** *7,* 2787-2790.
12. (a) Fu, H.; Newcomb, M.; Wong, C.H. *J. Am. Chem. Soc.* **1991,** *113,* 5878-5880. (b) Silverman, R. B.; Zelechonok, Y.; *J. Org. Chem.* **1992,** *57,* 6373-6374. (c) Buchanan, R. M.; Chen, S.; Richardson, J. F.; Bressan, M.; Forti, L.; Morvillo, A.; Fish, R. H. *Inorg. Chem.* **1994,** *33,* 3208-3209.
13. Derat, E.; Kumar, D.; Hirao, H.; Shaik, S. *J. Am. Chem. Soc.* **2006,** *1218,* 473-484.

14. (a) Atkinson, J. K.; Ingold, K. U. *Biochem.* **1993,** *32,* 9209-9214. (b) Atkinson, J. K.; Hollenberg, P. F.; Ingold, K. U.; Johnson, C. C.; Le Tadic, M. H.; Newcomb, M.; Putt, D. A. *Biochem.* **1994,** *33,* 10630-10637.
15. (a) Miller, V. P.; Fruetel, J. A.; de Montellano, P. R.O. *Arch. Biochem. Biophys.* **1992,** *298,* 697-702. (b) Sbaragli, L.; Woggon, W. D. *Synthesis* **2005,** *9,* 1538-1542. (c) Rittle, J.; Green, M. T. *Science* **2010,** *330,* 933-937.
16. Goh, S. H.; Closs, L.E.; Closs, G. L. *J. Org. Chem.***1969,** *34,* 25-31.
17. Goudreau, S. R.; Charette, A. B. *J. Am. Chem. Soc.***2009,** *131,* 15633-15635.
18. Wittig, G.; Haag, W. *Chem. Ber.* **1955,** *97,* 1654-1666.
19. Carey, Francis A.; Sundberg, Richard J.; *Advanced Organic Chemistry Part A Structure and Mechanisms*, 2nd ed.; Plenum Press: New York, N.Y., 1984.
20. Cohen, N.; Benson, S. W. *Chem. Rev.* **1993,** *93,* 2419-2438.
21. Sneen, R. A.; Lewandowski, K. M.; Taha, I. A. I.; Smith, B. R. *J. Am. Chem. Soc.* **1961,** *83,* 4843-4848.
22. (a) Creary, X.; Willis, E. D.; Gagnon, M. *J. Am. Chem. Soc.* **2005,** *127,* 18114-18120.
23. (a) Stirling, C. J. M. *J. Chem. Ed.* **1973,** *50,* 844-845. (b) Galli, C.; Illuminati, G.; Mandolini, L.; Tamborra, P. *J. Am .Chem. Soc.* **1977,** *99,* 2591-2597.
24. Theberge, C. R.; Verbicky, C. A.; Zercher, C. K. *J. Org. Chem.* **1996,** *61,* 8792-8798.
25. Johnson, R. P.; DiRico, K. J. *J. Org. Chem.* **1995,** *60,* 1074-1076.

Chapter 2

Synthetic Efforts Towards $[(silox)_3Ta]_2N_2$: Variegated NH-Additions to Ta and Other Collateral Discoveries[†]

Introduction

Homogeneous small-molecule activation is one of the long-standing areas of study within inorganic chemistry, and few molecules have had as much scientific attention as N_2. The difficulties surrounding *catalytic* N_2 activation are plentiful,[1,2] and although adequate catalytic systems remain elusive, stoichiometric systems have been developed and well-studied.[3] Ultimately, a metal compound must be simultaneously electrophilic enough to bind the relatively inert N_2 *and* be reducing enough to weaken the N-N triple bond. There are now a plethora of low oxidation state early-metal complexes that bind and activate N_2 to differing degrees. One glaring exception is $(silox)_3Ta$ (**1**), an isolable Ta(III) compound that is by all measures inert to a nitrogen atmosphere. Ta(III) complexes have been shown to have the reducing power to bind nitrogen; Schrock's $(PMe_3)_4Ta(CH^tBu)Cl$ irreversibly binds N_2 and loses PMe_3 to produce $[(PMe_3)_2TaCl(CH^tBu)]_2(\mu\text{-}N_2)$.[4] Calculations agree with this observation, showing Eq. 2.1 as downhill by 55.6 kcal mol^{-1}.[5]

$$\underset{\boxed{1}}{2\ (silox)_3Ta} + N_2 \longrightarrow \underset{\boxed{[1]_2N_2}}{(silox)_3Ta{=}N{-}N{=}Ta(silox)_3} \qquad \textbf{Eq. 2.1}$$

The thermodynamic favorability of this reaction indicates the failure to generate $\mathbf{[1]_2N_2}$ is kinetic in nature. As discussed in Chapter 1, the bulky silox groups of **1** constrain the approach of incoming ligands such that they encounter 4-electron repulsion with d_{z^2}. Beyond that, however, the reaction is fundamentally limited by

[†] Reproduced with permission from: Hulley, E. B.; Bonanno, J. B.; Wolczanski, P. T.; Cundari, T. R.; Lobkovsky, E. B. *Inorg. Chem.* **2010,** *49,* 8524-8544

orbital symmetry considerations for reasons analogous to those that hindered olefin dissociation from $(silox)_3Ta(olefin)$.[6] Such considerations are illustrated in Figure 2.1.

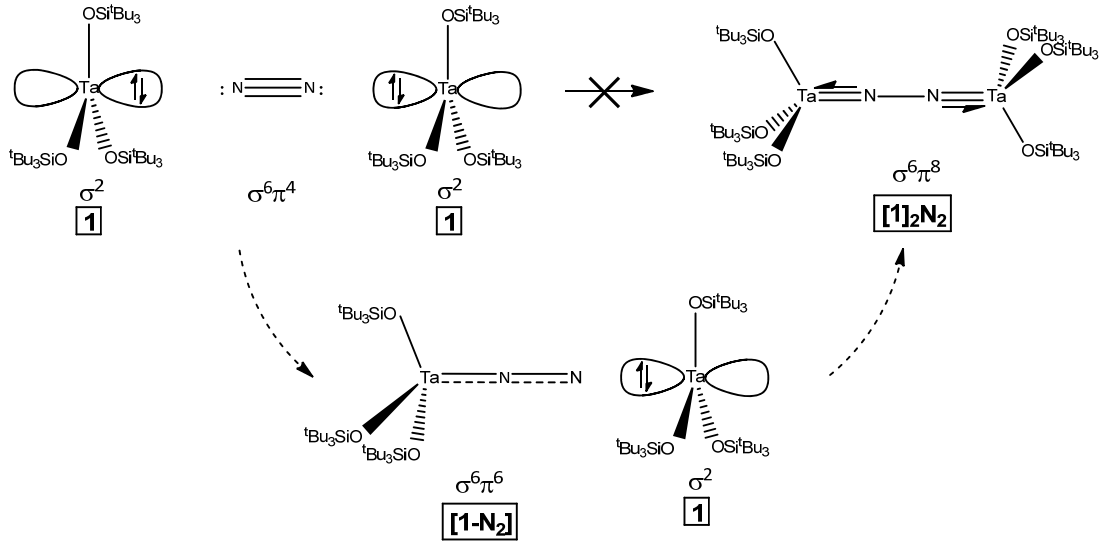

Figure 2.1. Orbital-symmetry considerations in nitrogenation of **1**.

As with olefin dissociation, the central problem with the reaction depicted in Fig. 2.1 is that the ground state of **1** has two electrons in a σ-type orbital that must each be promoted to π-type orbitals to make the necessary bonds. In the case of $\mathbf{[1]_2N_2}$ there must be a total of four electrons promoted to what amounts to the doubly-excited state of **1**. This is borne out in the calculated electronic structure of the first addition product, $\mathbf{1\text{-}N_2}$, which manifests as a ground-state triplet with a $(d_{xz})^1(d_{yz})^1$ configuration. One of the calculated SOMOs of this degenerate set is presented in Figure 2.2. There is modest π-bonding character between Ta and N1, however the coefficient on N1 is small relative to that on Ta and N2. Ultimately, the electron in each orbital is best represented as localized on Ta with some delocalization on N2. The calculated N1-N2 distance of $\mathbf{1\text{-}N_2}$ is 1.18 Å, longer than both free N_2 (1.109)[7]and calculated N_2^- (1.17),[8] and is consistent with significant π-backbonding into N_2.

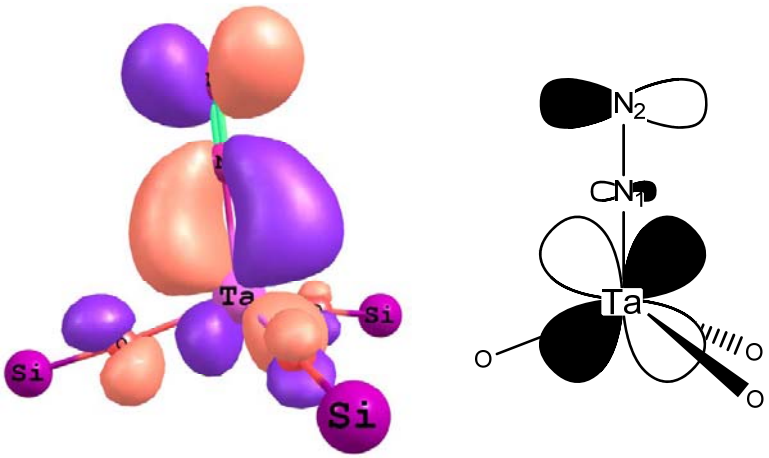

Figure 2.2. Calculated density for one of the SOMOs of triplet **1-N_2** (left) and an illustration of the relative atomic orbital coefficients (right).

1-N_2 is predicted to be only 7.2 kcal mol^{-1} above the reactants, however its electronic structure is derived from an excitation of **1** to a $^3A_2$' state that reflects promotion of *both* d_{z^2} electrons to d_{xz} and d_{yz}. The large gap between d_{z^2} and d_{xz} /d_{yz} (19 kcal mol^{-1}) in **1** ensures this state is almost inaccessibly high in energy (~38 kcal mol^{-1}) and as such cannot effectively assist crossover from reactant to product surfaces. Nearly identical problems exist in the reaction between **1** and **1-N_2** to produce **[1]$_2$$N_2$**, resulting in a similar barrier height for this second step.

The symmetry requirements considered above are, of course, within the context of constraining a linear reaction coordinate. Such requirements are usually circumvented by geometric distortions that allow more state mixings that can facilitate surface crossings.[6,9] Similar considerations are analyzed in the well-known splitting of N_2 by two equivalents of $Mo(N(Ph)R)_3$ to form $NMo(N(Ph)R)_3$ (R = ^{t}Bu-d_6).[3a,b] There are in fact two major steps in the process governed by orbital symmetry; producing the μ-dinitrogen complex analogous to **[1]$_2$$N_2$** ($[(N(Ph)R)_3Mo]_2N_2$) and cleavage of the N-N bond. In this case the ground-state electronic structure of the Mo(III) starting

material is S=3/2 and requires promotion to S=1/2 in order to transition to the intermediate dinitrogen complex. This system differs significantly from that of **1** due to the fact that only two electrons need change identity from σ to π. Moreover, the energy difference between S=3/2 and S=1/2 states is calculated to be 14 kcal mol^{-1} for $Mo(NH_2)_3$,[10] significantly smaller than the required promotion in **1**. This energy is likely to be an upper estimate for the barrier of the first association, as geometric distortions of the anilide framework can help facilitate the orbital identity change. Such a distortion is effectively unavailable to **1** due to the severe steric constraints of the silox ligand. Finally, every step in the association of N_2 to $Mo(N(Ph)R)_3$ is calculated to be exothermic. In the Cummins system the symmetry-forbidden reaction is the *cleavage* of N_2, which requires another two electrons to change identity, and results from the steric demands of the 'zig-zag' transition state required to make two σ-orbitals split into a σ- and π-type orbital.

While $(silox)_3Nb$ (**2**) cannot be made, $(silox)_3NbPMe_3$ (**2-PMe$_3$**) is isolable and acts as a source of **2**. This complex is stable to N_2 under normal and high pressure conditions. The calulated gap between d_{z^2} and (d_{xz} /d_{yz}) is smaller for **2** (2 kcal mol^{-1}), and the density of states available for surface crossing is much higher than for **1**. Using the above arguments, the fact that the corresponding $[(silox)_3Nb]_2N_2$ complex has yet be made is possibly due to the instability of $(silox)_3Nb(N_2)$ (**2-N$_2$**) with respect to products. However, **2-N$_2$** has been implicated as a player in P-C bond-cleavage reactivity discovered with **2-PMe$_3$**.[11] In hydrocarbon solvents under ambient light, **2-PMe$_3$** will cleave all the P-C bonds in PMe_3 over the course of 4 months to generate a mixture of products including $(silox)_3NbPH$, $(silox)_3NbCH_2$, CH_4, and H_2. It was found that, under 350 torr of H_2 in ambient light, a brick-red solid was produced and crystallographically identified as the bimetallic $(silox)_3NbP(H)$-$Nb(silox)_3$. Under 350

torr of H_2 and 350 torr N_2, the same compound was produced in 75% within 12 h. This reproducible result was attributed to the equilibrium in Eq. 2.2.

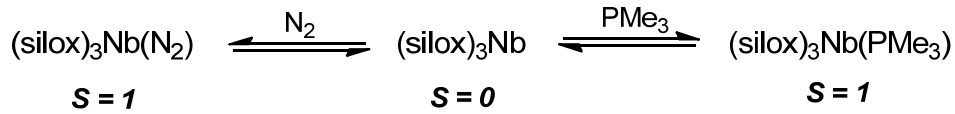

Eq. 2.2

It was proposed that trapping of **2** by **2=PH** was slow due to the repulsion felt by **2=PH** to the two electrons in d_{z^2}, and was instead facilitated by a spin-state change to S=1. Since the spin states of both **2-PMe$_3$** and **2-N$_2$** are S=1, associative attack of **2=PH** on **2-N$_2$** was proposed to be swifter than on **2-PMe$_3$**. Thus, there is evidence for some interaction between **2** and N_2, though it seems that proceeding to **[2]$_2$N$_2$** possesses a significant energetic barrier.

For these reasons it was thought that if **[1]$_2$N$_2$** could be synthesized by other means it would be an interesting test of the consequences of orbital symmetry. Indeed, given that any dissociation process (loss of N_2 or N-N cleavage) for the dinitrogen compound is forbidden by orbital symmetry it could represent one of the most stable dinitrogen complexes known. There are several synthetic routes that suggest themselves based on the known reactivity of **1**. The activation of NH-bonds by **1** is well studied,[12] and in the case of primary amines will produce amide hydrides of **1** that produce imides by 1,2-H_2 elimination as shown in Eq. 2.3.

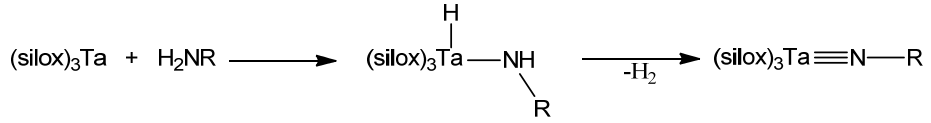

Eq. 2.3

It was initially thought that addition of hydrazine to two equivalents of **1** could generate the desired dinitrogen complex via the intermediate N-aminoamide **1=NNH$_2$**. An alternative method to the production of imido species comes from the oxidative addition of aziridines to **1** followed by retrocycloaddition as shown in Eq. 2.4.

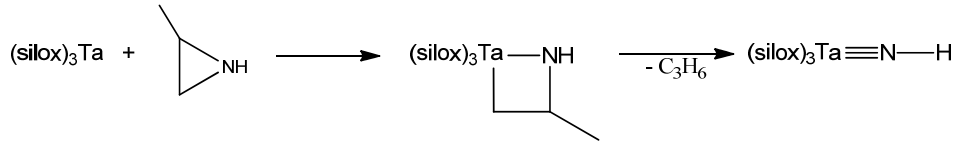

Eq. 2.4

It was thought that we might be able to couple the NH-bond activation with CN-bond activation via N-aminoaziridines as shown in Scheme 2.1. Using excess **1**, the expected products H_2 and C_3H_6 would be removed from the system as $(silox)_3Ta(\eta^2\text{-}C_3H_6)$ and $(silox)_3TaH_2$.

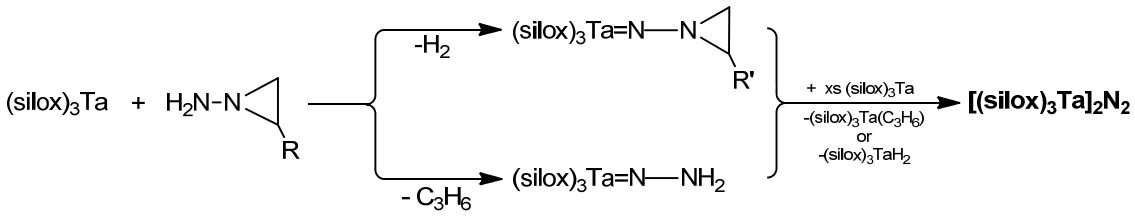

Scheme 2.1. Proposed reactivity of N-aminoaziridines with **1** as a route to $\mathbf{[1]_2N_2}$.

Efforts towards $\mathbf{[1]_2N_2}$ were focused on obtaining either intermediate from Scheme 2.1 as isolated compounds or transient species, as they were based on the most established chemistry. Another possibility is the simple salt metathesis reaction between NaSilox and a complex that already contains the dinitrogen ligand, such as $[(THF)_2TaCl_3]_2N_2$.[13] Aside from being intellectually unsatisfying, salt metathesis has an inherent disadvantage; preparation of $(silox)_3TaCl_2$ via metathesis requires several days of temperatures in excess of 120 °C and it was unknown if intermediate complexes en route to $\mathbf{[1]_2N_2}$ would be thermolytically stable.

Prior to this work, Chadaeyne[14] did a preliminary study of the reaction between **1** and hydrazine. It was found that rather than the expected $\mathbf{1{=}NNH_2}$, the ammonia adduct of parent imide ($\mathbf{1{=}NH(NH_3)}$) was formed. As such, efforts were focused on slightly more (and later less) sophisticated routes.

Results and Discussion

2.1. Direct Nitrogenation

In the drive towards a dinitrogen complex of **1** or **2** we began with the most straightforward – direct association under forcing conditions. Concentrated solutions of **1** treated with pressurized N_2 (3-4 atm) result only in cyclometallation.[15] Concentrated solutions of **2-PMe$_3$** treated with high pressures of N_2 are stable for >2 years when stored in the dark to avoid P-C bond cleavage reactions.[11] Since N_2-dissociation and olefin dissociation appear to be constrained by similar orbital-symmetry considerations, the barriers to dissociation from **1-N$_2$** and **[1]$_2$N$_2$** may be greater than for **2-N$_2$** and **[2]$_2$N$_2$**. Thus **[1]$_2$N$_2$** is more likely to be isolable and it seemed prudent to focus on synthesizing the Ta dinitrogen complex.

2.2. Aminoaziridination

The attempts utilizing aminoaziridine oxidative addition routes seemed the most likely to be successful. Syntheses of N-amino-2-methylaziridine ($^{Me}N_{az}NH_2$) and N-amino-2-phenylaziridine ($^{Ph}N_{az}NH_2$) were accomplished by the synthetic routes set out in Eq. 2.5 and Eq. 2.6.[16]

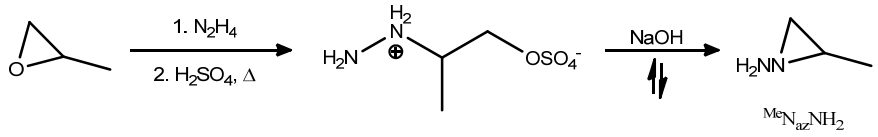

Eq. 2.5

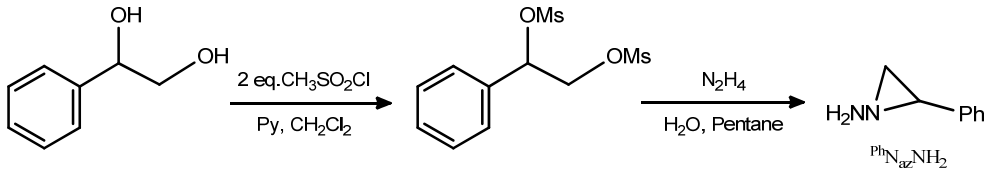

Eq. 2.6

Treatment of **1** with either aminoaziridine at low temperature leads to the parent imide, **1-NH**, as the most significant product. In the case of $^{Me}N_{az}NH_2$ the parent imide can be isolated in decent yields, suggesting minimal contribution of the 1,2-H_2-

elimination pathway we had hoped to see. In the case of $^{Ph}N_{az}NH_2$, although no isolation was attempted, ^{1}H NMR analysis indicated a mixture where the parent imide represented 70% of products. These results and a plausible mechanism are shown in Scheme 2.1.

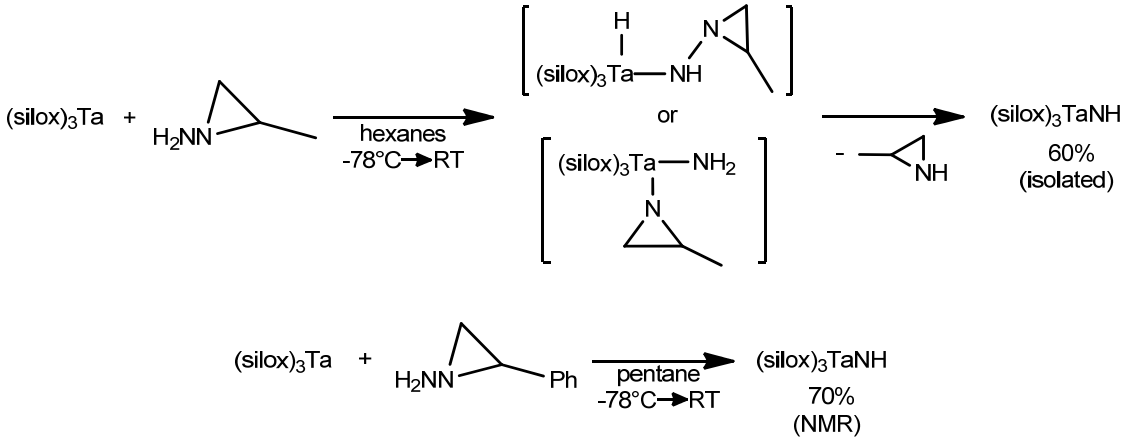

Scheme 2.2. Reactivity of aminoaziridines with $(silox)_3Ta$.

The analogous reactions with **2-PMe$_3$** were far less clean, yet in both cases the parent imide **2-NH** was present. We cannot discriminate between N-N and N-H activation, but the analogous hydrazine reaction (see the Introduction) gives some insight. Hydrazine treated with **1** yields the the parent imide with negligble amounts of its ammonia adduct, **1-NH(NH$_3$)**, and the bis-amido species **1-(NH$_2$)$_2$**.[5,14] Previous studies[17] indicated **1-(NH$_2$)$_2$** should be stable and observable under these conditions if it were the kinetic product, suggesting N-N activation is not competitive with N-H activation for hydrazine. It was surmised that aziridine-based substrates that did not contain NH bonds would be attractive targets, specifically biaziridines. The syntheses for known biaziridines are low-yielding (<10%) and prohibitively explosive.[18] An attempt was made to synthesize 2,2'-diphenyl-1,1'-biaziridine from the precursor dimesylate shown in Eq. 2. As shown in Eq. 2.7, treatment of the dimesylate with sodium N-amino-2-phenylaziridinide, generated by deprotonation of the parent

aziridine with NaH, resulted only in deprotonation and elimination of the styrene derivative shown.

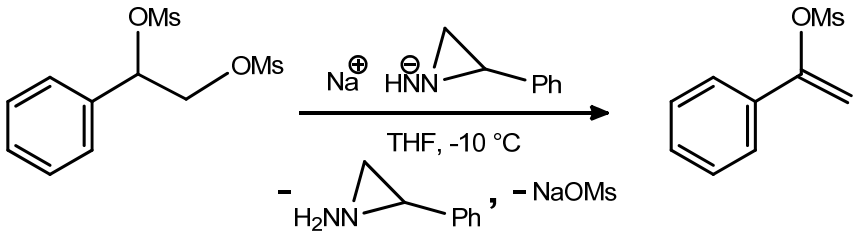

Eq. 2.7

2.3. Hydrazine 1,2-Addition and RH 1,2-Elimination

Believing the 1,2-elimination was still a viable approach, the next series of syntheses focused on 1,2-addition of NH-bonds across the M=C bond in **1-CH$_2$** in anticipation of methane elimination to form the desired imido intermediate. Addition of excess (4.7 eq) hydrazine to a benzene solution of **1-CH$_2$** resulted in swift (< 5 min) decoloration and precipitation of **3-NHNH$_2$**. Washing with pentane and filtration through celite yielded **3-NHNH$_2$** in 47% yield as a white crystalline solid (Eq. 2.8).

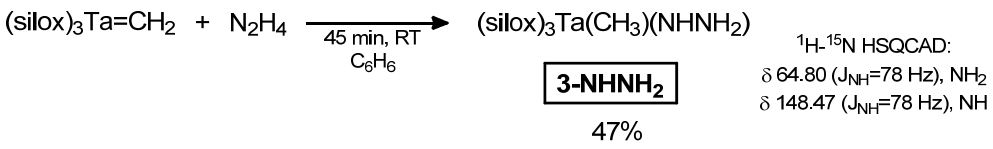

Eq. 2.8

The yields of **3-NHNH$_2$** were variable (40-70%) due to varying amounts of hydrazine, carried over with the crystalline product, that required multiple celite filtrations and recrystallizations to remove. The ^{15}N NMR shifts, obtained from HSQCAD[19] indirect experiments on natural-abundance material, indicated two nitrogen environments correlated with the observed singlets in the ^{1}H NMR spectrum (2.86 ppm, 5.36 ppm).

Thermolysis of methyl hydrazide **3-NHNH$_2$** in C_6D_6 for 12 h at 80 °C resulted in the complete consumption of starting material and evolution of methane (δ 0.15 ppm). The ^{1}H NMR spectrum of the resulting solution is shown in Figures 2.1 and 2.2.

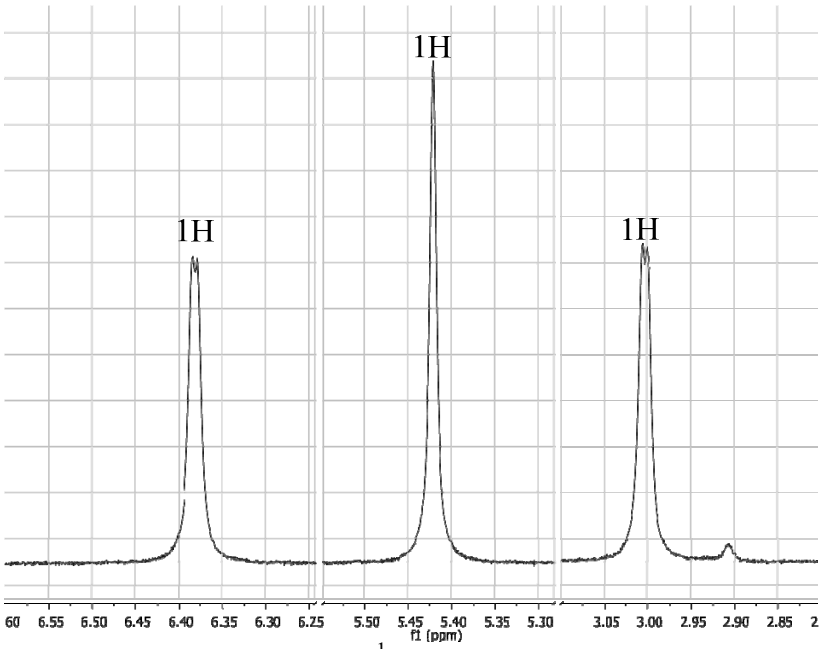

Figure 2.2. Downfield region of the ^{1}H NMR spectrum after thermolysis of **3-NHNH$_2$**. Integrations for the relevant peaks are indicated.

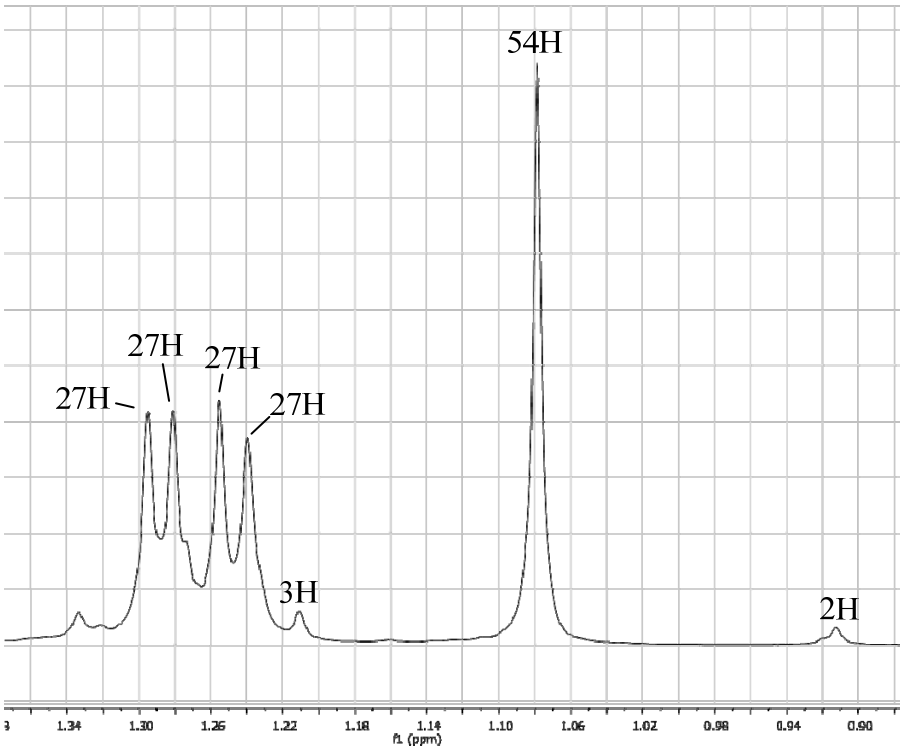

Figure 2.3. Upfield region of the ^{1}H NMR spectrum after thermolysis of **3-NHNH$_2$**. Integrations for the relevant peaks are indicated.

Ordinarily such a large number of distinct silox regions would signify degradation to multiple products, but the integrations were far too regular to ignore. The large singlet at 1.08 ppm and small singlet at 0.91 ppm are consistent with two equivalents of $^{t}Bu_3SiOH$ relative to the downfield singlets. The other shifts in the upfield region are consistent with four distinct silox groups and a methyl group which was later established by ^{1}H-^{13}C HSQC to be Ta-bound (38.31 ppm). The downfield region shows three resonances in the same general region as the NH protons in the starting hydrazide, two of which are coupled to each other (J = 2 Hz). The lack of observable ^{13}C-satellites confirmed their identity as NH-protons, and a full 2D correlation study was performed. The ^{15}N-^{1}H HMBCAD spectra are shown in Figures 2.3 and 2.4.

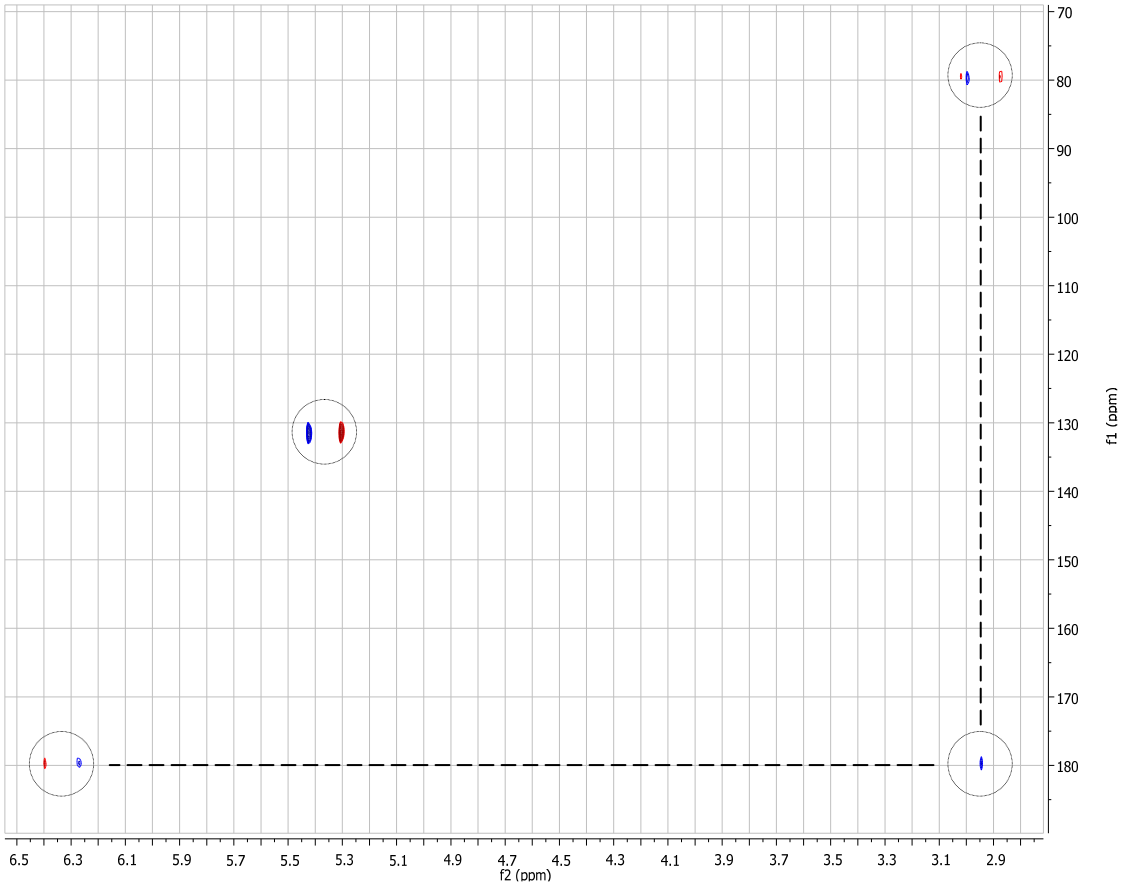

Figure 2.5. ^{15}N-^{1}H HMBCAD spectrum for the product of **3-NHNH$_3$** thermolysis. (narrow ^{15}N window)

Figure 2.6. ^{15}N-^{1}H HMBCAD spectrum for the product of **3-NHNH$_3$** thermolysis. (wide ^{15}N window)

The three protons at 3.01 ppm, 5.33 ppm, and 6.33 ppm showed strong correlations with ^{15}N signals at 79.50 ppm, 131.27 ppm, and 179.70 ppm respectively. The 3.01 ppm and 6.33 ppm resonances showed an HMBC crosspeak indicative of direct connection between the corresponding nitrogen atoms. Even more provocative was the appearance of a *second* ^{15}N correlation for the 5.33 ppm proton shift, with a weaker coupling constant (J_{NH} = 8 Hz) indicative of a multiple bond correlation. The nitrogen-containing moieties implied by this data were an NNH unit and an asymmetrical HNNH (diazenido) unit. While all these pieces from the ^{1}H, ^{13}C, and ^{15}N data could, in principle, be parts of multiple products, it was difficult to conceive of any possible products that had the necessary asymmetry to give four inequivalent silox resonances. It was concluded that all these resonances (except for the aforementioned silanol resonances) belonged to a *single* product that was the result of cyclization of *two*

molecules of the starting methyl hydrazide. The most likely structure for this product and a summary of its spectral characteristics are shown in Figure 2.9 and a plausible mechanism for its production shown in Eq 2.5.

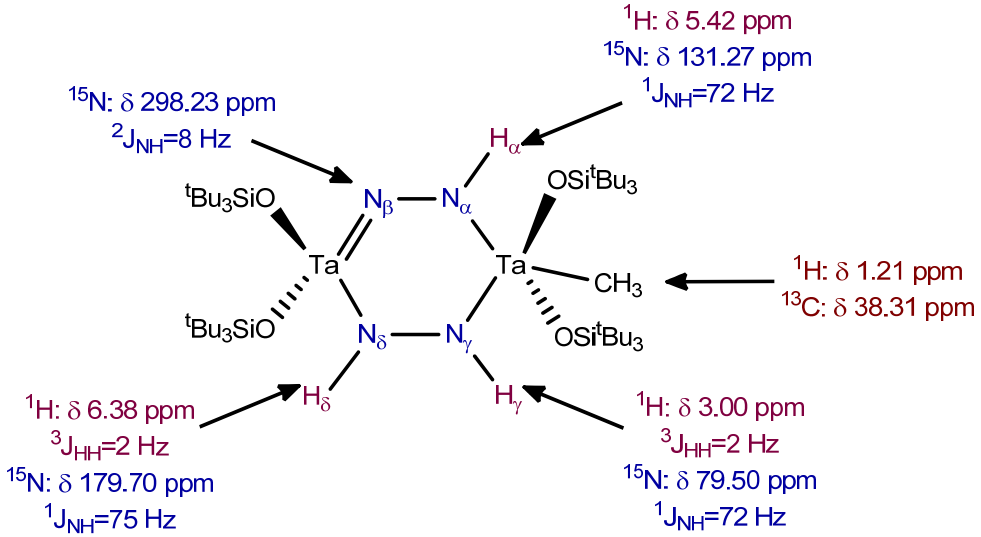

Figure 2.7. Proposed structure for the thermal decomposition product of **3-NHNH$_2$**.

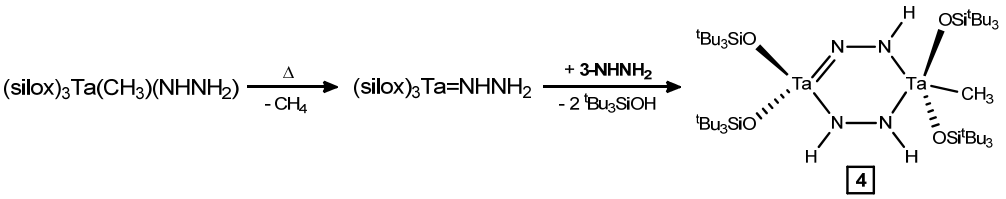

Eq. 2.9

The disappearance of **3-NHNH$_2$** appears first order and has a rate constant k_{obs} on the order of 1×10^{-4} s^{-1} at 80 °C, though the measured value varied between different experiments. The apparent first-order behavior was reproducible, however, and suggested rate-limiting loss of methane followed by fast trapping by **3-NHNH$_2$**. It was hoped we might favor production of the aminoimide **1-NNH$_2$** by thermolysis at high dilution. Tandem NMR experiments with concentrations of **3-NHNH$_2$** differing by more than an order of magnitude were thermolyzed and not only did the dilute tube form the cyclized product **4**, it formed it *faster* than the concentrated tube. It seemed likely trace hydrazine was affecting the reaction and the kinetics were not studied

further. Attempts at thermolysis in alternative solvents (THF-d_8, pyridine-d_5) and with competitive trapping agents (PMe_3) gave mixtures of unidentifiable products. Bulk samples of **4** could not be purified from the silanol byproduct by crystallization; the mixture is a yellow oil that is highly soluble in all hydrocarbon solvents. Most of the silanol could be removed via deprotonation with benzylpotassium and precipitation as K(silox), but the crystallization of **4** was hampered by decomposition. This suggested that, although spectroscopically identical to pure silanol, the observed silanol was somehow stabilizing the structure of **4** in a way that might be dynamically observable. The variable-temperature ^{1}H NMR spectrum for the silox region is presented in Figure 2.6.

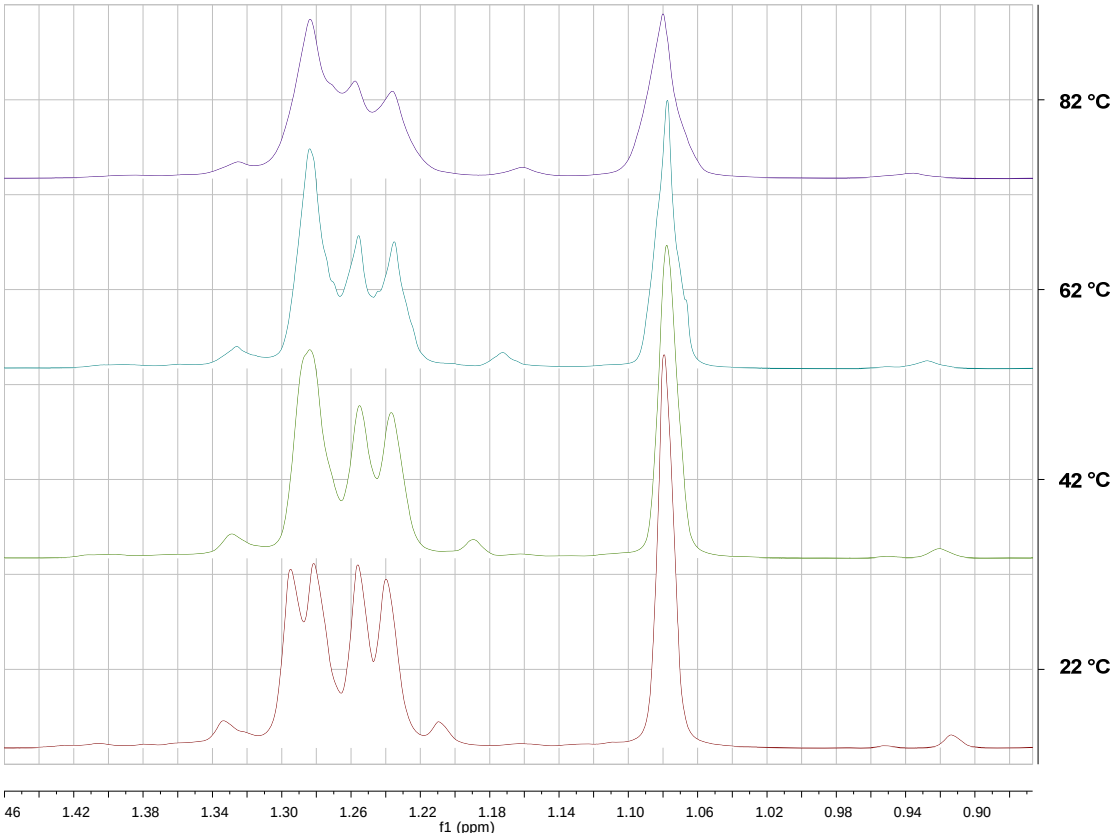

Figure 2.8. Variable-temperature ^{1}H NMR spectra of the upfield region of **4**·2^{t}Bu$_3$SiOH.

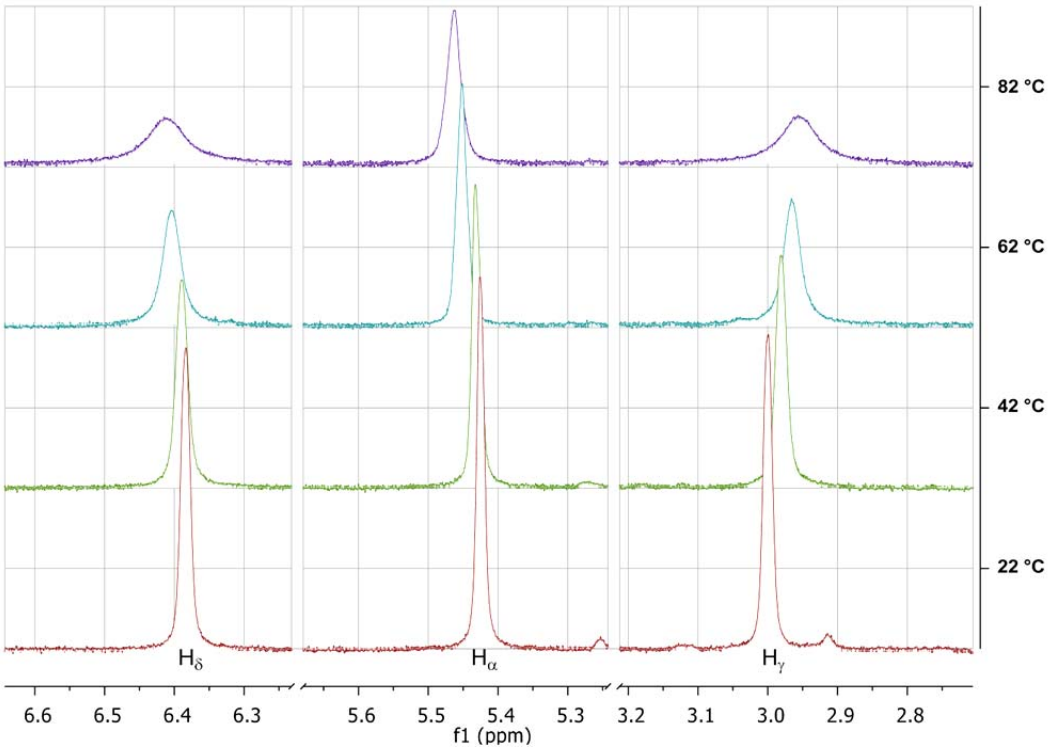

Figure 2.9. Variable-temperature ^{1}H NMR spectra of the downfield region of **4**·2^{t}Bu$_3$SiOH.

The increase in linewidth of the silanol methyl-group protons is consistent with a dynamic interaction between it and **4**, possibly through intermolecular hydrogen-bonding to the amide or imido moieties. The resonances for the silox ligands of **4** show a broadening consistent with coalescence phenomena and suggest interchange of silox groups, however this is speculative as the three-dimensional structure is not known. The downfield NH-region of the spectrum also shows interesting VT behavior. While all three resonances broaden with increasing temperature, H_γ and H_δ broaden more significantly than H_α and both broaden to the same degree. An EXSY experiment was conducted to determine what the exchange behavior was in this system. The spectra for irradiation of these three protons are shown in Figure 2.7.

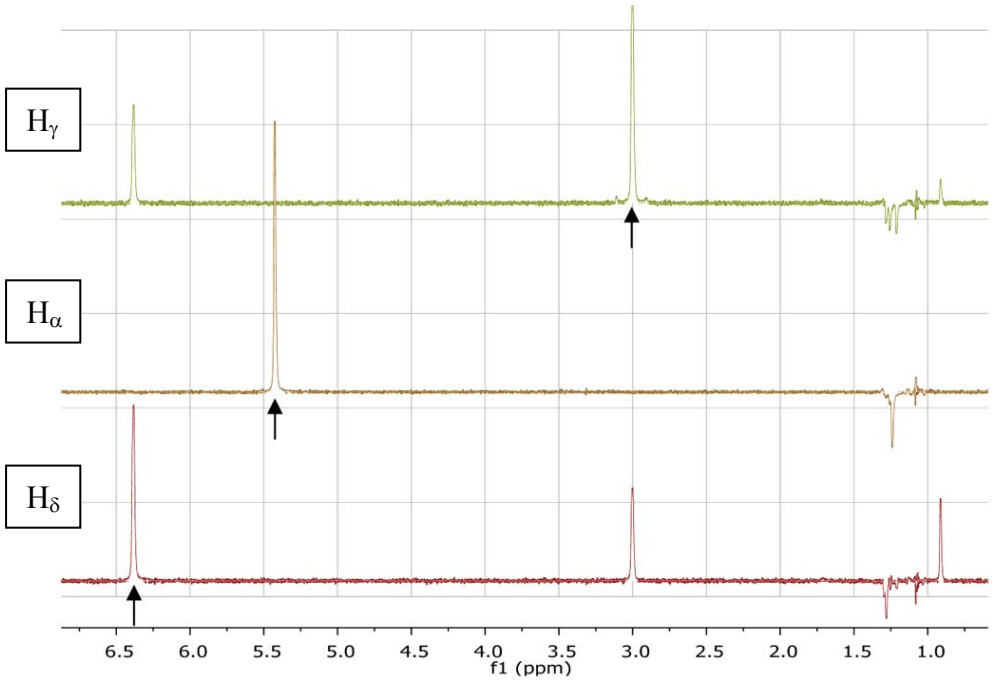

Figure 2.10. ^{1}H 1D-EXSY spectra for irradiation of H_γ, H_α and H_δ, respectively. The irradiated resonance is indicated. Opposite-phase peaks represent NOE interactions.

The EXSY experiment revealed that H_γ and H_δ are in dynamic exchange with each other whereas H_α appear dynamically inert. It was also evident from these experiments that the silanol OH proton (0.91 ppm) is involved in exchange with H_γ and H_δ, supporting the contention that silanol is weakly bound to **4**. The EXSY data was fitted to a three-site exchange model and rate constant for H_γ/H_δ exchange was determined to be $9.9(1)\times10^{-1}$ s^{-1}. A plausible structure through which *only* these protons exchange with one another is shown in Figure 2.8.

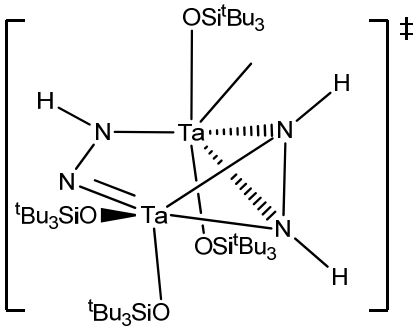

Figure 2.11. Possible transition state for interconversion of H_γ and H_δ protons.

Dimeric complexes containing the μ-diazenido moiety are well-known,[20] and Peters *et al.* have reported an iron dimer that contained both side-on and end-on coordination modes of diazene.[20e]

The presence of a Ta-Me in **4** suggested that further thermolysis might drive the reaction forward towards the desired product, **1=NNH$_2$**, with evolution of a second equivalent of methane. Thermolysis of a pure sample of **4·2^{t}Bu$_3$SiOH** at 135 °C for 15 h followed by half an hour at 210 °C showed *reuptake* of one equivalent of silanol, evolution of additional methane, and the appearance of two new silox resonances integrating 2:3. Unfortunately there were no other resonances attributable to NH or TaH protons and the nature of this material could not be determined.

2.4. N-Amino-2-methylaziridination of 1=CH$_2$

The successful 1,2-addition of hydrazine across the methylidene Ta=C bond suggested that the same may be accomplished with the aminoaziridine $^{Me}N_{az}NH_2$. The aziridine has the effect of acting as a protected hydrazine, ensuring that the nascent Ta-aziridinoimide following CH_4 elimination would be far less likely to be attacked by starting material as in the case of **4**. To this end 3-NH^{Me}N$_{az}$ was synthesized from **1=CH$_2$** and $^{Me}N_{az}NH_2$ in ether as shown in Eq. 2.10.

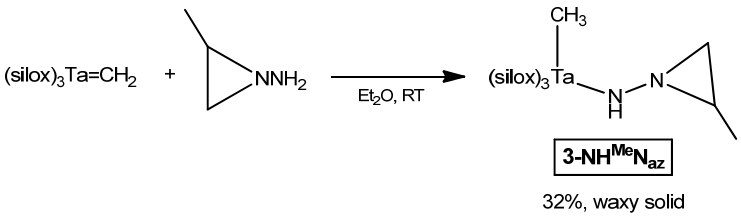

Eq. 2.10

The high solubility, thermal instability, and the presence of side products complicated isolation. The ^{1}H NMR spectrum of 3-NH^{Me}N$_{az}$ shows several aziridine resonances as

overlapping with the edge of the silox resonance, though the structure was confirmed by ^{1}H-^{13}C and ^{1}H-^{15}N 2D-techniques.

Thermolysis of **3-NH^{Me}N$_{az}$** for 10 h at 80 °C leads to complete consumption of the starting material and evolution of methane, although the ^{1}H NMR spectrum showed a considerable quantity of silanol and at least nine different silox resonances. Additional baseline resonances, representing at *most* 20% of the material, were observed that initially eluded analysis. The relevant region of the spectrum is presented in Figure 2.9.

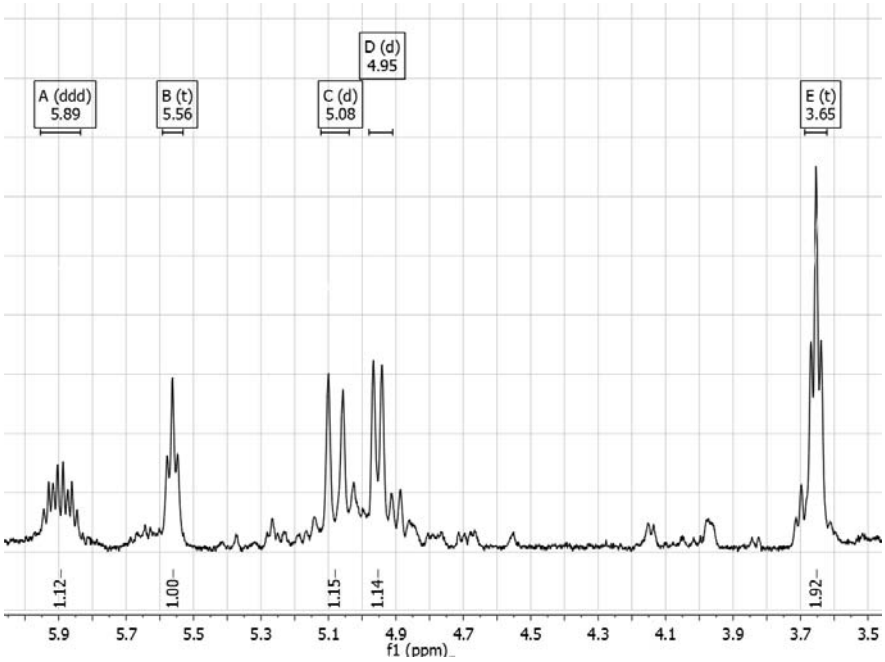

Figure 2.12. Downfield region of the 1H NMR spectrum of the thermolysis of **3-NH^{Me}N$_{az}$**. The boxes above each peak denote shifts and coupling schemes obtained from spin simulation.

If any **3=NN$_{az}$** had been produced in the thermolysis it was hoped that it would react with added **1** and eliminate propene to form **[1]$_2$N$_2$**. Both [(silox)$_3$Ta]$_2$C$_2$ and [(silox)$_3$Nb]$_2$C$_2$, which would share solubility properties with **[1]$_2$N$_2$**, are virtually insoluble in all common organic solvents and it was hoped that any small amount of

[1]$_2$N$_2$ produce would be easily isolable. After an excess of **1** was added to a C_6D_6 solution of **3-NH^{Me}N$_{az}$** and heated to 80 °C for a few minutes, yellow needles crystallized from solution. The crystalline material was too insoluble to obtain NMR spectra and the crystals were of insufficient size for structural analysis. Recrystallization from hot THF for 24 h produced crystals amenable to X-ray analysis. The molecular structure of the product is presented in Figure 2.10, selected parameters are presented in Table 2.1 and the crystallographic data are presented in Table 2.2.

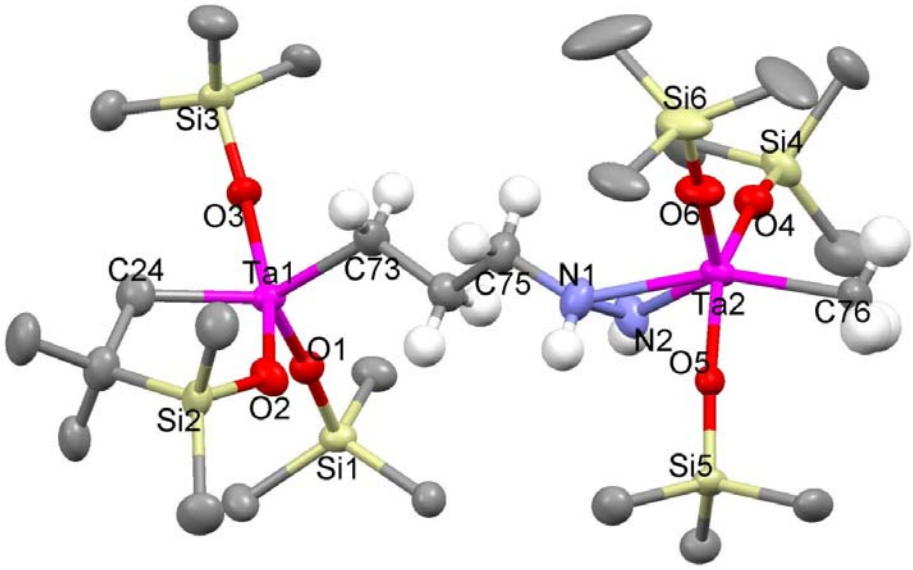

Figure 2.13. Molecular structure of **5**. Methyl groups of the silox ligands have been omitted for clarity.

Table 2.1. Selected bond angles and interatomic distances for **5**.

Selected Bond Distances (Å)		Selected Bond Angles (degrees)	
Ta1-C73	2.133(7)	O1-Ta1-O3	104.79(18)
Ta1-C24	2.217(7)	O1-Ta1-O2	100.35(18)
Ta2-N2	2.008(6)	O3-Ta1-O2	154.61(18)
Ta2-C76	2.213(7)	C73-Ta1-C24	124.6(3)
Ta2-N1	2.283(6)	O6-Ta2-O4	100.4(2)
Ta1-O1	1.861(4)	O6-Ta2-O4	105.30(19)
Ta1-O2	1.931 (4)	O6-Ta2-O5	105.30(19)
Ta1-O3	1.905(4)	O4-Ta2-O5	152.67(18)
Ta2-O4	1.915(4)	N2-Ta2-C76	132.6(3)
Ta2-O5	1.951(4)	C76-Ta2-N1	159.4(3)
Ta2-O6	1.876(5)		

Table 2.2. X-ray crystallographic data for **5**, **7-Cl_2**, **1=$CPPh_3$**,

Crystal Data			
Formula	$C_{76}H_{171}N_2O_6Si_6Ta_2$	$C_{48}H_{108}Cl_2N_2O_4Si_4Ta_2$	$C_{55}H_{96}O_3PSi_3Ta$
Formula Weight	1739.59	1322.52	1101.51
Crystal System	Triclinic	Monoclinic	Monoclinic
Space Group	P-1	P2(1)/c	P2(1)/n
Z	2	4	4
a, Å	12.7517(6)	14.6904(6)	11.8368(2)
b, Å	17.5127(9)	27.0349(10)	22.2055(4)
c, Å	23.2899(11)	17.4888(7)	22.1197(4)
α, deg	103.755(2)	90	90
β, deg	90.922(2)	113.637(2)	90.1200(10)
γ, deg	110.627(2)	90	90
Volume, $Å^3$	4698.7(4)	6363.0(4)	5813.97
D (calc.), g/cm^3	1.230	1.381	1.258
Absorption coeff., mm^{-1}	2.446	3.633	2.108
F(000)	1838	2712	2320
Crystal Size, mm	0.20 x 0.10 x 0.03	0.25 x 0.20 x 0.15	0.25 x 0.20 x 0.15
Data Collection and Refinement			
Temp, K	173(2)	173(2)	173(2)
Wavelength (λ), Å	0.71073	0.71073	0.71073
θ limits, deg	0.91 to 25.35	1.69 to 26.37	1.84 to 30.53
Index Ranges	$-15 \le h \le 13, -21 \le k \le 21, -28 \le l \le 28$	$-18 \le h \le 18, -33 \le k \le 28, -21 \le l \le 21$	$-16 \le h \le 16, -31 \le k \le 18, -31 \le l \le 31$
Reflections Collected	57689	58495	73173
Absorption Correction	Semi-empirical from equivalents	Semi-empirical from equivalents	Semi-empirical from equivalents
Max. and Min. Transmission	0.9414 to 0.6404	0.6118 and 0.4637	0.7517 to 0.6324
Refinement Method	Full-matrix least-squares on F^2	Full-matrix least-squares on F^2	Full-matrix least-squares on F^2
Data/Restraints/Params.	17150 / 1098 / 940	12659 / 1 / 531	17745 / 0 / 568
Goodness-of-Fit on F^2	1.058	1.014	1.028
Final R Indices [$I>2\sigma(I)$]	R1 = 0.0612, wR2 = 0.1415	R1 = 0.0566, wR2 = 0.1309	R1 = 0.0404, wR2 = 0.0739
R Indices (all data)	R1 = 0.0912, wR2 = 0.1534	R1 = 0.0980, wR2 = 0.1561	R1 = 0.0674, wR2 = 0.0824
Largest Diffraction Peak and Hole (e^- $Å^3$)	3.284 and -1.978	5.572 and -2.115	1.274 and -0.648

The structure of **5** betrays its origin from ring-opening of the **3-NH^{Me}N$_{az}$**, as shown in Figure 2.11, and also clarifies the source of the ^{1}H NMR shifts in Figure 2.8.

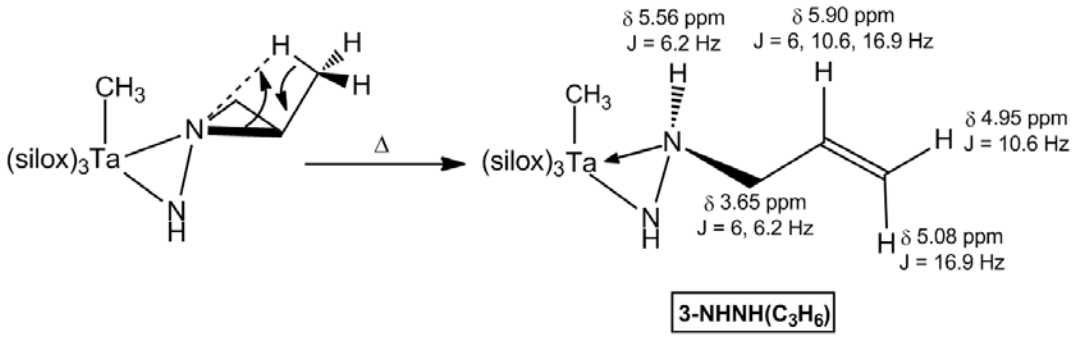

Figure 2.14. Proposed structure for the product of thermolysis of **3-NH^{Me}N$_{az}$**.

In the structure of **5**, Ta1 originates from the insertion of the olefin terminus of **3-NHNH(C_3H_6)** into HTa(κ-O,C-OSi^{t}Bu$_2$CMe$_2$CH$_2$)(silox)$_2$ arising from cyclometallation of **1**. Aziridines are known to be susceptible to ring opening in the presence of cationic catalysts,[16c] thus rationalizing formation of **3-NHNH(C_3H_6)**.

2.5. Attempts at Coupling 1=NH and 1=NLi.

The nitride anion of **1**, **1=NLi**, seemed like the most attractive synthon towards **[1]$_2$N$_2$** since numerous 2e$^-$ oxidation routes suggest themselves. The nitride anion can be prepared via deprotonation of the parent imide as in Eq. 2.11.

$$(silox)_3TaNH + {}^tBuCH_2Li \xrightarrow[-CMe_4]{THF} (silox)_3TaNLi \quad 78\% \qquad \textbf{Eq. 2.11}$$
(-78°C → RT)

The first series of reactions focused on treating **1=NLi** with metal halides with well-known reductive elimination chemistry. When **1=NLi** was treated with either (DME)NiCl$_2$, (PEt$_3$)$_2$PdCl$_2$, or (PPh$_3$)$_2$PtCl$_2$ at low temperature in THF and allowed to warm to room temperature the only observable product was the parent imide **1=NH**. In all cases there were observable color changes indicative of a reaction, so it was

concluded that generation of the (L)M(NTa(OSi^{t}Bu$_3$)$_3$)X species led only to Ta-M bond homolysis or outer-sphere ET from **1=NLi** to produce the nitride radical which subsequently abstracted an H-atom from the solvent to generate **1=NH**. Similarly, attempts to generate **1=NX** (X = Br, I) in cold hydrocarbon solutions produced mixtures of products including **1=NH**. Calculations[21] on (HO)$_3$TaNH and (HO)$_3$TaN· + H· allowed an estimate of the NH-bond strength of 112 kcal mol^{-1}, unsurprising given the large amount of s-character in the bond, and gave credence to the idea that the nitride radical was scavenging H· from solvent. Treatment of Cp_2TiCl_2 with **1=NLi** allowed isolation of Cp$_2$Ti(NTa(OSi^{t}Bu$_3$)$_3$)Cl as a brown solid. Thermolysis in the presence of excess **1=NLi** resulted in the formation of only **1=NH**, indicative of Ti-Ta bond homolysis. It seemed that the attack of the second nitride anion might be too slow for these systems, necessitating the higher temperatures more favorable for bond homolysis. As such, **1=NLi** was treated with half an equivalent of CBr_4 in the hope of eventually thermally extruding :CBr_2 and generating the NN bond, however only **1=NH** was identified in the complex product mixture. In an attempt to circumvent these issues, **1=NLi** was treated with $NOBF_4$ in the hope of generating **1=NNO** for subsequent deoxygenation and trapping with excess **1**. However, after the addition of $NOBF_4$ to **1=NLi** at low temperature, gas evolution was observed and the major product was (silox)$_3$TaO. A few attempts were made to couple the two parent imide fragments using Pd(PPh$_4$)$_4$ and ethylene as a hydrogen trap, however decomposition to Pd^0 and PPh_3 was observed with no change in the amount of **1=NH**. Attempts at preparing **1=NBr** from **1=NH** and NBS were similarly unsuccessful, most likely because of the strength of the NH bond in **1=NH**. These results are all summarized in Figure 2.12.

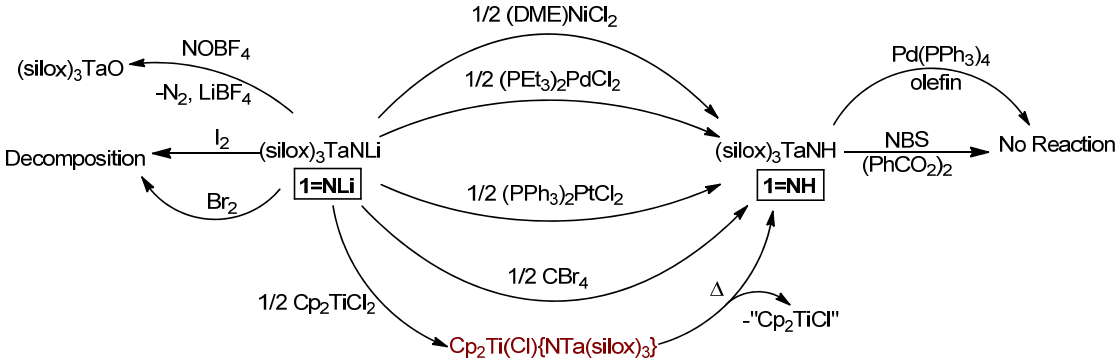

Figure 2.15. Various attempts at coupling **1=NH** and **1=NLi**.

2.6. Salt Metathesis

The least sophisticated route towards $\mathbf{[1]_2N_2}$ is salt metathesis of a precursor dinitrogen compound with Na(silox), in this case Schrock's $[(THF)_2TaCl_3]_2N_2$ (**6**).[13] Treatment of **6** with six equivalents of Na(silox) gave multiple products from which only $[(silox)_2TaCl]_2N_2$ ($\mathbf{7\text{-}Cl_2}$) was isolated in 20% yield as a highly soluble yellow solid. Treatment of **6** with four equivalents of Na(silox) in THF allowed isolation of $\mathbf{7\text{-}Cl_2}$ in decent yield according to Eq. 2.12.

$$[(THF)_2TaCl_3]_2N_2 + 4.05\ Na(silox) \xrightarrow[\substack{-78°C \rightarrow RT \\ 24h}]{Et_2O} [(silox)_2TaCl]_2N_2 \qquad \textbf{Eq. 2.12}$$

The ^{1}H NMR spectrum of $\mathbf{7\text{-}Cl_2}$ consists of a singlet at 1.26 ppm, in contrast to other $(silox)_2M$ dimers that exhibit two silox environments due to an energetically preferred *gauche*-arrangement of ligands that have relatively large barriers to M-M bond rotation.[23] Compound $\mathbf{7\text{-}Cl_2}$ was crystallized from slow evaporation of a 1:1 pentane:hexamethyldisiloxane mixture at –78 °C and a crystal amenable to X-ray analysis was selected. The molecular structure of $\mathbf{7\text{-}Cl_2}$ is presented in Figure 2.13,

selected parameters are presented in Table 2.3 and the crystallographic data are presented in Table 2.4.

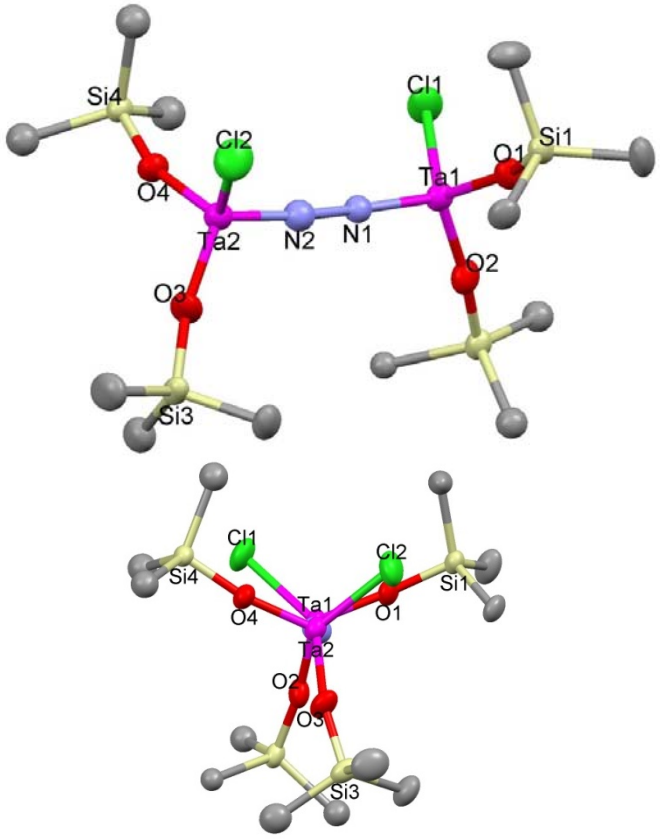

Figure 2.16. Side-on (top) and end-on (bottom) molecular views of **7-Cl$_2$**. Methyl groups have been removed for clarity.

Table 2.3. Selected bond angles and interatomic distances for **7-Cl$_2$**.

Selected Bond Distances (Å)		Selected Bond Angles (degrees)	
Ta1-O1	1.869(6)	O1-Ta1-O2	110.7(3)
Ta1-O2	1.871(7)	O2-Ta1-Cl1	108.5(3)
Ta1-Cl1	2.312(2)	O1-Ta1- Cl1	109.5(2)
Ta2-O3	1.868(7)	Cl1-Ta1-N1	107.5(3)
Ta2-O4	1.854(6)	O3-Ta2-O4	109.6(3)
Ta2-Cl2	2.307(3)	O4-Ta2-Cl2	109.5(2)
Ta1…Ta2	4.862(2)	O3-Ta2-Cl2	109.8(2)
		Cl2-Ta2-N2	107.9(3)
		Ta1-N1-N2	173.7(7)
		Ta2-N2-N1	172.3(7)
		d(Cl1-Ta1…Ta2-Cl2)	98.9(3)

The structure of **7-Cl$_2$** is plagued by two disordered silox groups and poorly-located nitrogen atoms that all needed isotropic refinement. As such the Ta=N and N-N distances are unreliable, however the overall Ta-Ta distance is well determined and can be used to estimate d(NN). Using the crystallographically-characterized[12a] (silox)$_3$Ta=NPh as a guide we can estimate the d(Ta=N) in **7-Cl$_2$** to be 1.77 Å, resulting in a d(NN) of 1.32. Since the actual d(Ta=N) in **7-Cl$_2$** is unknown this can only be taken to mean that the actual d(NN) is likely to be within the range for an N_2^{4-} ligand.

Attempts at installing additional silox groups via metathesis with Na(silox) or Tl(silox) required thermally forcing conditions and gave mixtures consistent with decomposition. The chlorides in **7-Cl$_2$** could, however, be exchanged with methyl groups using CH_3MgBr in ether according to Eq. 2.13.

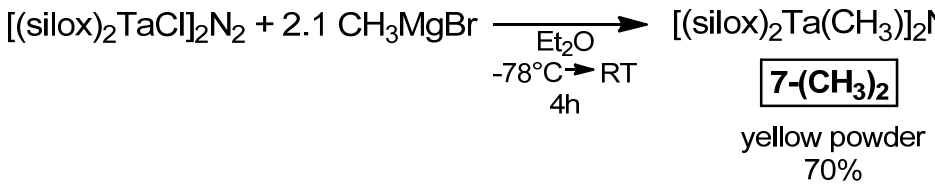

Eq. 2.13

The dimethyl compound **7-(CH$_3$)$_2$** was treated with two equivalents of silanol in C_6D_6 in the hope of generating **[1]$_2$N$_2$** via deprotonation, however only decomposition was observed.

2.7. Collateral Discoveries

During the course of the investigations of amine additions across the M=C bond in **1=CH$_2$**, copious quantities of **1=CH$_2$** were required. Producing it entailed addition of THF to a mixture of solid **1** and Ph_3PCH_2 via vacuum transfer at –78 °C and stirring for 4 h. Although **1=CH$_2$** was the only known product of the transylidation besides PPh_3, its production was always accompanied by a moderate amount of gas production. A second silox resonance, besides **1=CH$_2$**, was observed at

1.31 ppm in crude reaction mixtures, and it appeared to be correlated with a set of aromatic resonances distinct from the PPh_3 produced as a byproduct. Once crystalline **1=CH$_2$** had been separated, the PPh_3 was precipitated as $[PPh_3CH_3]I$ with excess MeI and the new compound could be isolated as colorless crystals from pentane. ^1H and $^{31}P\{^1H\}$ spectroscopies showed the material to contain both $(silox)_3Ta$ and PPh_3 moieties, but a long-duration ^{13}C NMR spectrum eventually revealed an extra carbon at 175.01 ppm with a J_{CP} of 53 Hz. The proposed structure and mechanism for its formation are presented in Figure. 2.11.

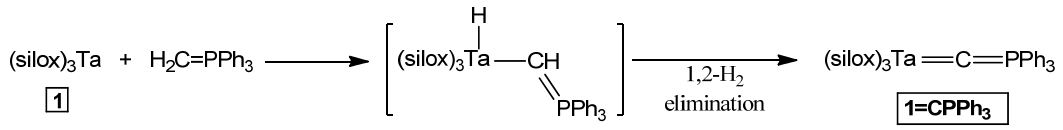

Figure 2.17. Proposed formation of 1=CPPh$_3$.

To confirm this hypothesis a colorless crystal was selected for X-ray analysis. Its structure is presented in Figure 2.14, selected parameters are presented in Table 2.5 and the crystallographic data are presented in Table 2.6.

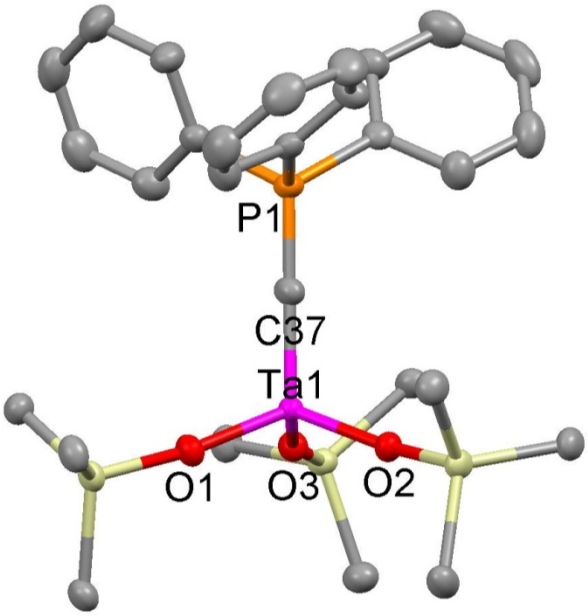

Figure 2.18. Molecular structure of 1=CPPh$_3$. Methyl groups and hydrogens have been omitted for clarity.

Table 2.4. Selected bond angles and interatomic distances for **1=CPPh$_3$**.

Selected Bond Distances (Å)		Selected Bond Angles (degrees)	
Ta1-C37	1.862(3)	Ta1-C37-P1	177.83(17)
C37-P1	1.667(2)	C37-Ta1-O1	109.24(9)
Ta1-O1	1.9122(16)	C37-Ta1-O2	108.66(9)
Ta1-O2	1.9072(15)	C37-Ta1-O3	108.27(9)
Ta1-O3	1.9139(16)		

As suggested in Figure 2.13, **1=CPPh$_3$** can be thought of as arising from oxidative addition of the CH-bond of the methylidene moiety followed by 1,2-elimination of H_2. This reaction happens simultaneously with the methylene transfer reaction to produce **1=CH$_2$**, but based on the product ratio of **1=CH$_2$**:**1=CPPh$_3$** synthesized at –78 °C (60:40, ^{1}H NMR), it is a somewhat slower process. Addition of THF to a mixture of solid **1** and Ph_3PCH_2 at *room temperature* resulted in a product ratio of 70:30, favoring **1=CH$_2$**. The structure of **1=CPPh$_3$** shows a very short Ta-C bond of 1.862(3) Å, consistent with the range expected for a triple bond,[24] and the P-C bond distance of 1.667(2) Å is consistent with either considerable double bond character or significant ionic character. These lengths are suggestive of a resonance structure of the type shown in Eq. 2.14.

$$(silox)_3Ta{=}C{=}PPh_3 \longleftrightarrow (silox)_3\overset{\ominus}{Ta}{\equiv}C{-}\overset{\oplus}{P}Ph_3 \qquad \textbf{Eq. 2.14}$$

Other compounds of Ta with this ligand have been produced,[25] though they were produced from Ta(V) starting materials. The only other published account of oxidative addition of Ph_3PCH_2 is to $Ru_3(CO)_{12}$ and proceeds by initial attack of the methylidene on CO and subsequent migration, oxidative addition and CO loss to produce $Ru_3(CO)_9(\mu^2\text{-}H)_2(\mu^3\text{-}CPPh_3)$.[26] The triple-bond character aroused the possibility that PPh_3 might be displaced or otherwise removed to reveal a nucleophilic carbide. It had already been determined that the compound was inert to CH_3I, and thus was unlikely

competent for PPh_3 dissociation, and it was also found to be inert to substitution with ammonia. However, treatment of a C_6D_6 solution of **1=CPPh$_3$** with excess CO led to the generation of the previously characterized[27] ketenylidene **1=CCO** as confirmed by ^{1}H NMR and IR spectroscopies.

The failure of **3-NHNH$_2$** to eliminate CH_4 rapidly enough to avoid dimerization processes suggested an alternative alkylhydrazide might be produced that would more rapidly eliminate RH. Other alkylidene complexes of **1** are known to exist in equilibrium with their olefin-adduct counterparts,[28] and it was thought that the addition of hydrazine might drive the reaction forward as alkylidene was converted to alkylhydrazide. An equilibrium mixture of (silox)$_3$Ta(η-C_2H_4) (**1-C$_2$H$_4$**), (CH_3CH_2)Ta(κ-O,C-OSi^{t}Bu$_2$CMe$_2$CH$_2$)(silox)$_2$ (**1-cymet-Et**), and (silox)$_3$Ta(η^1-$CHCH_3$) (**1=CHCH$_3$**) were treated with excess hydrazine in d_6-benzene at room temperature, resulting in complete consumption of **1=CHCH$_3$** and the appearance of a new product consistent with that illustrated in Figure 2.15.

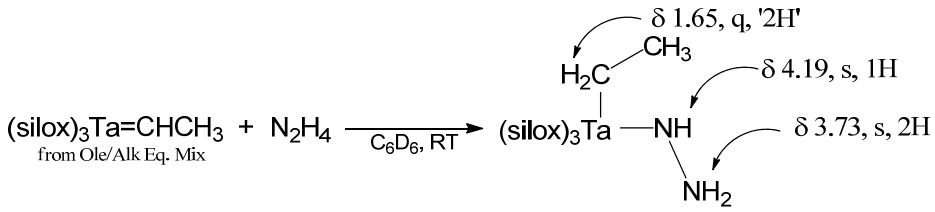

Figure 2.19. Synthesis and spectral data for putative (silox)$_3$Ta(Et)(NHNH$_2$)

The relative amounts of **1-C$_2$H$_4$** and **1-cymet-Et** appeared unchanged. Heating at 80 °C for 2 h resulted in complete consumption of the new compound and evolution of ethane (δ 0.80 ppm), however the reaction could not be driven forward to yield a clean product. The synthesis of pure **1=CHCH$_3$** was attempted by transylidation with Ph_3PCHCH_3, however the complex mixture of products containing several TaH resonances (δ 21.96-23.00 ppm) indicated side reactions due to CH-activation.

Diazoalkanes are the more common reagent for generation of alkylidenes,[29] and their reactivity with **1** and **2-PMe$_3$** had not previously been studied. Due to its stability and lack of β-hydrogens that might complicate alkylidene transfer, Ph_2CN_2 was chosen first to treat with **1** in C_6D_6 at room temperature. The color immediately changed from light blue to light yellow and gave a ^{1}H NMR spectrum consisting of a single silox resonance and five aromatic signals (10H), the latter consistent with two, distinct, rotationally-symmetric phenyl groups. The most reasonable explanation for this data was that **8** was the diphenyldiazomethane complex of **1** of the type shown in Figure 2.16.

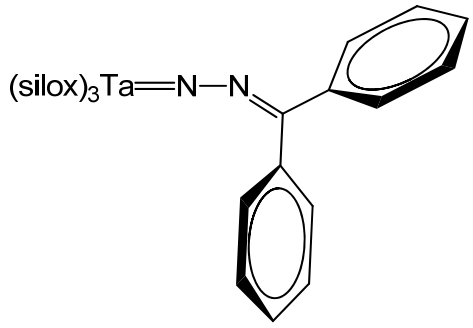

Figure 2.20. Proposed skeletal structure of **8** illustrating the bent C_{im}-N-N angle.

Such diazoalkane complexes are known to have a bent C-N-N angle,[30] such as in $Cp_2Nb(H)(NNCPh_2)$ (124.2°), and this would resolve the phenyl group inequivalence. It was hoped that this compound might at least generate the alkyl hydrazide and N_2 thermally in the presence of hydrazine. Treatment of this compound (**8**) with 1.2 eq hydrazine in C_6D_6 followed by thermolysis (50 °C) led to slow ($t_{½}$~48 h) decomposition of the starting material and production of significant (30%) silanol. The product expected from 1,2-NH addition and RH-elimination, diphenylmethane, was never observed.

Realizing the possibility that steric hindrance was preventing N_2 loss, **1** was treated with $(CH_3)_3SiCHN_2$ in C_6D_6 at room temperature producing a mixture of two

products. Each product, **9a** and **9b**, consisted of three singlets in an 81:9:1 ratio and were formed in a 1:1 ratio. Heating the mixture for 10 h at 100 °C resulted in quantitative conversion (>95%) of **9a** to **9b**. The structures of **9a** and **9b** were initially thought to be the diazoalkane and alkylidene complexes, respectively, but this later proved to be incorrect. Both compounds seemed immune to the presence of H_2 during thermolysis, and once **9b** formed it was very thermally robust – **9b** was indefinitely stable up to 180 °C.

For corroboration with the Nb system, treatment of **2-PMe$_3$** with Ph_2CN_2 in C_6D_6 at room temperature produced a new product (**10**) that had shifts very similar to **8**. Similarly, **2-PMe$_3$** was treated with $(CH_3)_3SiCHN_2$ in C_6D_6 at room temperature producing only a single product (**11**) that had ^{1}H NMR shifts comparable to **9b**. In **10** and **11** there was more information to be gleaned; the ^{93}Nb nucleus is highly sensitive to coordination environment and exhibits large differences in chemical shift (+1000 to -1000 ppm) and half-height peak width (from ~ 100Hz to ~20 kHz) between different species (see **Appendix – ^{93}Nb NMR**). The ^{93}Nb spectra of **10** and **11** had shifts wildly different from other alkylidenes, which usually appear between -100 to 100 ppm, and **11** possessed an exceptionally narrow peak width. In fact, **11** possessed a peak width narrower than $(silox)_3NbO$ (**2=O**), indicating a *highly* symmetric electric field around Nb during the timescale of the experiment. These spectral data are summarized in Table 2.6.

Table 2.5. Selected NMR data for compounds **8-11**, **2=O**, **2=CHCH$_3$**, **2-C$_2$H$_4$**.

	^{1}H NMR (ppm)						^{93}Nb NMR	
Compound	^{t}Bu	o-Ph	m-Ph	p-Ph	M=CH	Si(CH$_3$)$_3$	Shift (ppm)	$\nu_{½}$
8	1.25	7.71 7.49	7.22 7.11	7.12 7.04	–	–	–	–
10	1.26	7.66 7.47	7.21 7.08	7.12 7.03	–	–	-864.1	6 kHz
9a	1.28	–	–	–	7.11	0.33	–	–
9b	1.30	–	–	–	7.95	0.17	–	–
11	1.30	–	–	–	7.80	0.11	-965.07	276 Hz
2=O	1.28	–	–	–	–	–	-947.1	2 kHz
2=CH(CH$_3$)	1.28	–	–	–	8.45	–	-30	1.9 kHz
2-C$_2$H$_4$	1.21	–	–	–	–	–	370	2.6 kHz

The similarity of the ^{1}H NMR spectra between **8** and **10** is certainly suggestive that they are structurally similar. The very low ^{93}Nb shift for **10** puts it in the regime of compounds of Nb that are ionic in nature and supports the diazoalkane structure proposed in Figure 2.16. The similarity of ^{1}H NMR shifts between **9b** and **11** suggests that they too are alike structurally, and the corroboration of the ^{93}Nb NMR shifts of **10** and **11** indicates that both **9b** and **11** are also diazoalkane complexes. The presence of a *second* complex in the Ta reaction (**9a)** which thermally converts to **9b** suggests that it is simply an isomer of **9b** that is less thermodynamically stable. For complexes of asymmetric diazoalkanes (N_2CHR) one can imagine two structural isomers including the N-N-C bend, *cis* and *trans* with respect to the pseudo-imine linkage, and are presented in Figure 2.17.

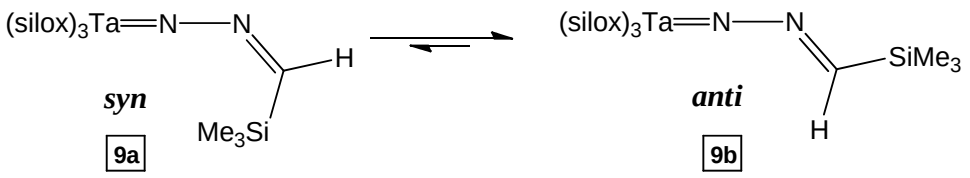

Figure 2.21. Proposed isomerism between *cis* and *trans* diazoalkane complexes of **1**.

Of the two possible stereoisomers, it would be expected for the *syn*-diazoalkane complex of Nb to have a broader peak width than the *anti* (as explained in the Appendix); as such that is how to best assign the structure of **11**. As for Ta, it is plausible there are two preferred modes of attack of **1** on $(CH_3)_3SiCHN_2$ leading to the two proposed structures. The manifestation of only one isomer of the corresponding Nb-diazoalkane complex may be due to a combination of lower barrier of interconversion for Nb, as compared to Ta, for analogous density of states arguments as laid out in Chapter 1.

Conclusion

The parent imide of $(silox)_3Ta$, **1=NH**, is sufficiently thermodynamically downhill that **1** apparently seeks to extract 'NH' whenever possible. This is analogous to the O-atom abstraction chemistry of **1**, wherein highly unusual species can be generated based on the high oxophilicity of **1**. Additionally, the very strong strength of the NH bond in **1=NH** meant that coupling attempts of **1=NLi** were dominated largely by electron transfer and H-atom abstraction processes to produce the parent imide. Attempts to avoid this through the use of high-valent species to generate Ta(V) compounds, designed to be attacked by **1** and generate $\mathbf{[1]_2N_2}$, were hampered by undesired side reactions. Attempting salt metathesis with a complex with the dinitrogen ligand preinstalled partially worked, stalling at the addition of four silox groups instead of the desired six. We observed the unprecedented *selective* loss of $^tBu_3SiOH$ from an unusual dimerization reaction to a tetraazabimetallacycle and a novel route to phosphaalkylidynes.

Experimental

General Considerations. All manipulations were carried out either using a nitrogen glovebox or high-vacuum and Schlenk techniques. All glassware was oven dried. Benzene-d_6 was refluxed over sodium metal, vacuum distilled and stored under nitrogen over activated 4Å molecular sieves. All solvents were distilled from sodium metal or sodium benzophenone-ketyl solutions. N-amino-2-methylaziridine,[16a] N-amino-2-phenylaziridine,[16b] CH_2PPh_3,[31] $(CH_3)CHPPh_3$,[31] $(silox)_3NbPMe_3$,[9b] $PhCHN_2$,[33] Ph_2CN_2,[34] $(silox)_3TaNH$,[5] $(silox)_3TaNLi$,[5] and $(silox)_3Ta$[32] were synthesized via literature procedures. $(silox)_3TaCH_2$ was initially synthesized by literature procedures;[17] an improved synthesis is detailed below. Hydrazine and 2-methylaziridine were purchased from Sigma-Aldrich and vacuum distilled immediately prior to use.

^1H and $^{13}C\{^1H\}$ NMR spectra were obtained on Varian 300 MHz (Mercury), 400 MHz (INOVA), 500 MHz (INOVA), and 600 MHz (INOVA) spectrometers. ^1H-^{15}N and ^1H-^{13}C 2D NMR spectra were obtained on Varian 500 MHz (INOVA), and 600 MHz (INOVA) spectrometers. $^{31}P\{^1H\}$ spectra were obtained on 400 MHz (INOVA) and 500 MHz (INOVA) spectrometers referenced to external H_3PO_4. For historical consistency, NMR shifts for silox-containing compounds are referenced to benzene-d_6 (^1H, δ 7.15 ppm; ^2H, δ 7.15 ppm; ^{13}C, δ 128.39 ppm). ^{93}Nb NMR spectra were obtained in C_6D_6 and referenced to external $NbCl_5$ in acetonitrile (0.00 ppm).

Synthesis. 1. $(silox)_3TaCH_2$. To a small bomb was added 2.01 g (2.4 mmol) $(silox)_3Ta$ and 690 mg PPh_3CH_2 and a magnetic stir bar. THF (40 mL) was added at room temperature and the bomb was sealed. After stirring for 1 h at room temperature the solution was degassed and transferred to a swivel-frit assembly in the glovebox. The solution was filtered, concentrated to 15 mL and cooled to –78 ºC to yield 1.43 g

(70%) of yellow crystals which were collected by filtration. This material had a 6% (by mass) impurity of PPh_3 and was deemed suitable for further reactivity.

2. $(silox)_3Ta(CH_3)(NHNH_2)$. A 10 mL round bottom flask was charged with 560 mg (0.665 mmol) $(silox)_3TaCH_2$ and 8 mL benzene and attached to a small swivel frit assembly. The apparatus was degassed on the vacuum line, backfilled with argon and 100 μL hydrazine (3.1 mmol, 4.7 eq) was added under argon purge. The solution was rigorously stirred for 45 min and then the solvent was removed *in vacuo*. The resultant off-white solid was triturated twice with 5 mL THF and then 5 mL pentane was added via vacuum transfer. The suspension was cold-filtered (–78 ºC) and the filter cake washed with 5 mL pentane and dried *in vacuo*. This material was dissolved in 20 mL benzene in the box and filtered through fresh celite twice, each time followed by a 20 mL benzene wash. The filtrates were combined and the solvent was removed *in vacuo* to yield 360 mg (49%) as a white powder. ^{1}H NMR (C_6D_6): δ 1.08, (s, CH_3, 3H), 1.26 (s, ^{t}Bu, 81H), 3.63 (s, NH_2, 2H), 4.11 (s, NH, 1H). ^{13}C NMR (C_6D_6): δ 23.78 ($C(CH_3)_3$), 30.43 ($C(CH_3)_3$), 33.79 ($TaCH_3$). ^{15}N NMR (C_6D_6, ^{1}H-^{15}N gHMBCAD): δ 64.80 (J_{NH}=78 Hz, NH_2), 148.47 (J_{NH}=78 Hz, NH). Anal. Calc'd for $C_{37}H_{87}N_2O_3Si_3Ta$: C, 50.89; H, 10.04; N, 3.21. Found C, 50.94; H, 10.28; N, 3.09.

3. **$[(CH_3)(silox)_2Ta](\mu\text{-}N_\alpha H\text{-}N_\beta)(\mu\text{-}N_\gamma HN_\delta H)[(CH_3)(silox)_2Ta]\bullet 2\,{}^tBu_3SiOH$.** A small bomb was charged with 95 mg $(silox)_3Ta(CH_3)(NHNH_2)$ (0.11 mmol) and 2 mL benzene was added. The bomb was heated to 75 °C for 24 h and subsequently evacuated of all volatiles. The resulting oil was dissolved in pentane, removed from the bomb and placed in a 4-dram vial where the solvent was removed *in vacuo* to yield 90 mg of a slightly-yellow liquid (0.052 mmol, 95%). ^{1}H NMR analysis indicated complete conversion. ^{1}H NMR (C_6D_6): δ 1.21(s, CH_3, 3H), 1.24 (s, ^{t}Bu, 27H), 1.26 (s, ^{t}Bu, 27H), 1.28 (s, ^{t}Bu, 27H), 1.30 (s, ^{t}Bu, 27H), 3.00 (s, $N_\gamma H$, 1H), 5.42 (s, $N_\alpha H$, 1H), 6.38 (s, $N_\delta H$,1H). ^{13}C NMR (C_6D_6): δ 24.01 ($C(CH_3)_3$), 24.10 ($C(CH_3)_3$), 24.15

($C(CH_3)_3$), 24.49 ($C(CH_3)_3$), 30.83 ($C(CH_3)_3$), 30.88 ($C(CH_3)_3$), 31.04 ($C(CH_3)_3$), 31.11 ($C(CH_3)_3$), 38.31 (CH_3). ^{15}N NMR (C_6D_6, ^{1}H-^{15}N gHMBCAD): δ 79.50 (J_{NH}=72 Hz, N_γH), 131.27 (J_{NH}=72 Hz, N_αH), 179.70 (J_{NH}=75 Hz, N_δH), 298.23 ($^2J_{NH}$=8 Hz, N_β) .

4. (silox)$_3$Ta(CH$_3$)(NHNCH$_2$CH(CH$_3$)). A 10 mL round-bottom flask was charged with 200 mg (silox)$_3$TaCH$_2$ (0.24 mmol) and attached to a 180° valve adapter. The assembly was evacuated and 2 mL of diethyl ether was added via vacuum transfer. To this solution was added 250 μL N-amino-2-methylaziridine (3 mmol) at room temperature under argon counter-flow. The solution discolored over a period of five minutes and the solvent and excess aziridine removed *in vacuo* and the resulting waxy solid was left under dynamic vacuum for 45 minutes. The solid was recrystallized from pentane (0.5 mL) at –40 °C allowing for slow evaporation and washed with 0.5 mL cold (–40 °C) pentane to yield 70 mg (0.077 mmol, 32%) of a thermally-sensitive waxy solid. ^{1}H NMR (C_6D_6): δ 1.06 (d, J = 6 Hz, CH_3, 3H), 1.24 (dqd, J = 6 Hz, 8 Hz, 1 Hz, C*H*(CH_3), 1H), 1.33 (s, ^{t}Bu, 81H), 1.44 (dd, J = 4, 8Hz, C*H*H, 1H), 1.54 (dd, J= 4 Hz,1 Hz, CH*H*, 1H), 5.69 (br. s, N*H*, 1H). ^{13}C NMR (C_6D_6): δ 24.16 ($C_{az}CH_3$), 24.62 ($C(CH_3)_3$), 30.92 ($C_{az}H_2C_{az}H$), 31.20 ($C_{az}H_2C_{az}H$), 31.36 ($C(CH_3)_3$), 43.10 (CH_3). ^{15}N NMR (C_6D_6, ^{1}H-^{15}N gHMBCAD): δ 81.99(N_{az}), 244.46 (J_{NH}=72 Hz, NH).

5. [(silox)$_3$MeTa](μ-η^2-N,N:η^1-CNHNHCH$_2$CH$_2$CH$_2$)[Ta(κ-O,C-OSi^{t}Bu$_2$CMe$_2$CH$_2$)(silox)$_2$]. To a re-sealable NMR tube was added 61 mg (silox)$_3$Ta(CH$_3$)(NHN(aziridine)) (0.067 mmol) and 0.7 mL C_6D_6. The tube was heated for 4 h at 80 °C until the starting material had disappeared. The resulting solution was removed from the tube and placed in a 1-dram vial and a solution of (silox)$_3$Ta (58 mg in 1 mL, 0.070 mmol) was added. From the resulting green solution yellow needles precipitated which were isolated by decanting the mother-liquor. The

needles were washed with pentane and dried *in vacuo* to yield 15 mg of effectively insoluble material. The needles were recrystallized from hot THF (80 °C) overnight and were amenable to X-ray crystallography.

5. $[(silox)_2TaCl]_2N_2$. To a 50 mL round bottom flask was added 1.0 g $[TaCl_3(THF)_2]_2N_2$ (1.12 mmol) and 1.09 g sodium silox (4.56 mmol, 4.06 eq.) and the flask was attached to a swivel-frit assembly. The apparatus was evacuated, the flask cooled to –78 ºC and 25 mL of THF was added via vacuum transfer. The flask was allowed to warm to room temperature and stirred 18h during which time the color changes from red-orange to yellow. The solvent was removed *in vacuo* and 10 mL of pentane was added via vacuum transfer. Filtering the suspension, concentrating the solution to 5 mL and cooling to –78 ºC afforded yellow microcrystals which were dried *in vacuo*. After collection of a second crop the total yield was 828 mg (56%). X-ray diffraction quality crystals were grown by slow evaporation of a 1:1 pentane:hexamethyldisiloxane solution at –78 ºC over a period of 4 h. ^{1}H NMR (C_6D_6): δ 1.26 (s, 108H). ^{13}C NMR (C_6D_6): δ 23.76 ($C(CH_3)_3$), 30.39 ($C(CH_3)_3$).

6. $[(silox)_2Ta(CH_3)]_2N_2$. A 25 mL round bottom flask charged with 100 mg (0.075 mmol) $[(silox)_2TaCl]_2N_2$ was attached to a small swivel-frit assembly. The apparatus was evacuated and 10 mL Et_2O was added at –78 ºC via vacuum transfer. After the solid dissolved 0.08 mL CH_3MgBr (2.0 M in Et_2O, 2.1 eq) was added via syringe under argon purge. As the solution was allowed to warm to room temperature a white precipitate appeared, which re-dissolved upon warming fully. After 30 minutes at room temperature a white precipitate again formed and the solution was filtered. The solution was filtered, concentrated to 2 mL and cooled to –78 ºC, affording a light-yellow powder that was collected by filtration and dried *in vacuo* (50 mg, 52%). ^{1}H NMR (C_6D_6): δ 1.24 (s, ^{t}Bu & CH_3, 112H). ^{13}C NMR (C_6D_6): δ 23.79 ($C(CH_3)_3$), 30.44 ($C(CH_3)_3$), 33.87 ($TaCH_3$).

7. $(silox)_3Ta{=}C{=}PPh_3$. A 50 mL round bottom flask was charged with 1.96 g (2.4 mmol) $(silox)_3Ta$ and 687 mg PPh_3CH_2 and a magnetic stir bar. The flask was affixed to a swivel-frit assembly and the apparatus was evacuated on the line. THF (40 mL) was condensed into the round bottom at –78ºC and the solution was allowed to slowly warm to room temperature overnight. The solution was degassed, filtered, concentrated to 15 mL and cold-filtered (–78ºC) to yield 1.15 g $(silox)_3TaCH_2$ (58%). The filtrate residue was dissolved in 5 mL pentane and cooled to –78ºC to yield 371 mg of an off-white powder identified as an equimolar mixture of PPh_3 and $(silox)_3TaCPPh_3$. This material was dissolved in 5 mL benzene and CH_3I (2 eq., relative to PPh_3) was added and stirred overnight. A white precipitate was separated by filtration and the solvent was removed *in vacuo* to yield 256 mg (10%, based on $(silox)_3Ta$) of $(silox)_3TaCPPh_3$ as a white powder. X-ray quality crystals were grown from cooling a saturated pentane solution to -40ºC. ^{1}H NMR (C_6D_6): δ 1.31 (s, ^{t}Bu, 81H), 7.11 (m, ^{p}CH, 9H), 7.78 (m, ^{o}CH, 6H). ^{13}C NMR (d_8-THF): δ 25.21 ($C(CH_3)_3$), 31.31 ($C(CH_3)_3$), 128.75 (^pCH), 131.15 (^mCH), 133.94 (^oCH), 136.37 (d, J_{CP} = 88 Hz, ^{ipso}CH), 175.01 (d, J_{CP} = 53 Hz, Ta=*C*=P). ^{31}P NMR (C_6D_6): δ –4.26.

NMR Tube Experiments

Hydrazine, N-amino-2-methylaziridine N-amino-2-phenylaziridine were freshly-distilled from KOH under argon prior to use and was added via gas-tight microliter syringe to NMR tubes under argon counterflow prior to sealing.

Single-Crystal X-ray Diffraction Studies. Upon isolation, the crystals were covered in polyisobutenes and placed under a 173K N_2 stream on the goniometer head of a Siemens P4 SMART CCD area detector (graphite-monochomated Mo Kα radiation, λ = 0.71073 Å). The structures were solved by direct methods (SHELXS). All non-

hydrogen atoms were refined anisotropically unless otherwise stated, and hydrogen atoms were treated as idealized contributions (Riding model).

1. [(silox)$_3$MeTa](μ-η^2-N,N:η^1-C-NHNHCH$_2$CH$_2$CH$_2$)[Ta(κ-O,C-OSi^{t}Bu$_2$CMe$_2$CH$_2$)(silox)$_2$] (5). A colorless plate measuring 0.03×0.10×0.20 mm^3 was obtained from hot THF solution. A total of 57,689 reflections were collected with 17,150 being symmetry independent (R_{int} = 0.0762), and 11,582 were greater than 2σ(I). A semiempirical absorption correction from equivalents was applied, and the refinement utilized $w^{-1} = s^2(F_o^2) + (0.0640p)^2 + 15.5864p$, where $p = (F_o^2 + 2F_c^2)/3$.

2. [(silox)$_2$TaCl]$_2$N$_2$ (7-Cl$_2$). A colorless block measuring 0.15×0.20×0.25 mm^3 was obtained from slow evaporation of a 1:1 pentane:hexamethyldisiloxane solution at –78 °C over a period of 4 h. A total of 58,495 reflections were collected with 12,659 being symmetry independent (R_{int} = 0.0686), and 8,578 were greater than 2σ(I). A semiempirical absorption correction from equivalents was applied, and the refinement utilized $w^{-1} = s^2(F_o^2) + (0.0605p)^2 + 73.4015p$, where $p = (F_o^2 + 2F_c^2)/3$. The ^{t}Bu-groups of two silox ligands were severely disordered and modeled isotropically. The two nitrogen atoms in between the Ta atoms were poorly resolved and also had to be refined isotropically.

3. (^{t}Bu$_3$SiO)$_3$Ta=CPh$_3$ (1=CPPh$_3$). A colorless block measuring 0.15×0.20×0.25 mm^3 was obtained from cooling a saturated pentane solution to –40 °C. A total of 73,173 reflections were collected with 17,745 being symmetry independent (R_{int} = 0.0254), and 3371 were greater than 2σ(I). A semiempirical absorption correction from equivalents was applied, and the refinement utilized $w^{-1} = s^2(F_o^2) + (0.0260p)^2 + 0.0173p$, where $p = (F_o^2 + 2F_c^2)/3$.

REFERENCES

1. (a) Barney, B. M.; Laryukhin, M.; Igarashi, R. Y.; Lee, H.; Dos Santos, P. C.; Yang, T.; Hoffman, B. M.; Dean, D. R.; Seefeldt, L. C. *Biochemistry* **2005,** *44,* 8030-8037. (b) Barney, B. M.; Lee, H.; Dos Santos, P. C.; Hoffman, B. M.; Dean, D. R.; Seedfeldt, L. C. *Dalton Trans.***2006,** 2277-2284.
2. (a) Schrock, R. R. *Acc. Chem. Res.* **2005,** *38,* 955-962 (b) Hazari, N. *Chem. Soc. Rev.*, **2010,** *39,* 4044-4056.
3. (a) Laplaza, C. E.; Cummins, C. C. *Science* **1995,** *268,* 861-863. (b) Laplaza, C. E.; Johnson, M. J. A.; Peters, J.; Odom, A. L.; Kim, E.; Cummins, C. C.; George, G. N.; Pickering, I. J. *J. Am. Chem. Soc.* **1996,** *118,* 8623-8638. (c) Pool, J. A.; Lobkovsky, E.; Chirik, P. J. *Nature* **2004,** *427,* 527-530. (d) Vidyaratne, I.; Scott, J.; Gambarotta, S.; Budzelaar, P. H. M. *Inorg. Chem.* **2007,** *46,* 7040-7049.
4. Turner, H. W.; Fellmann, J. D.; Rocklage, S. M.; Schrock, R. R. *J. Am. Chem. Soc.* **1980,** *102,* 7811-7812.
5. Hulley, E. B.; Bonanno, J. B.; Wolczanski, P. T.; Cundari, T. R.; Lobkovsky, E. B. *Inorg. Chem.* **2010,** *49,* 8524-8544.
6. Hirsekorn, K. F.; Hulley, E. B.; Wolczanski, P. T.; Cundari, T. R. *J. Am. Chem. Soc.* **2008,** *130,* 1183-1196.
7. *Tables of Interatomic Distances and Configurations in Molecules and Ions*; Chemical Society Special Publications; Sutton, L. E., Ed.; The Chemical Society: London, 1958; Vol. 11.
8. Eliezer, I.; Moualem, A. *Chem. Phys.* **1973,** *58,* 1147-1148.
9. (a) Veige, A. S.; Slaughter, L. M.; Wolczanski, P. T.; Matsunaga, N.; Decker, S. A.; Cundari, T. R. *J. Am. Chem. Soc.***2001,** *123,* 6419- 6420. (b) Veige, A. S.; Slaughter, L. M.; Lobkovsky, E. B.; Wolczanski, P. T.; Matsunaga, N.; Decker, S. A.; Cundari, T. R. *Inorg. Chem.* **2003,** *42,* 6204-6224.

10. Cui, Q.; Musaev, D. G.; Svensson, S. S.; Morokuma, K. *J. Am .Chem. Soc.* **1995,** *117,* 12366-12367.
11. Hirsekorn, K. F.; Veige, A. S.; Wolczanski, P. T. *J. Am. Chem. Soc.* **2006,** *128,* 2192-2193.
12. (a) Bonanno, J. B.; Wolczanski, P. T; Lobkovsky, E. B. *J. Am. Chem. Soc.* **1994,** *116,* 11159-11160. (b) Bonanno, J. B.; Henry, T. P.; Neithamer, D. R.; Wolczanski, P. T.; Lobkovsky, E. B. *J. Am. Chem. Soc.* **1996,** *118,* 5132-5133
13. Rocklage, S. M.; Schrock, R. R. *J. Am. Chem. Soc.* **1982,** *104,* 3077-3081
14. Chadaeyne, A. **2005**, unpublished results.
15. Covert, K. J.; Neithamer, D. R.; Zonnevylle, M. C.; LaPointe, R. E.; Schaller, C. P.; Wolczanski, P. T. *Inorg. Chem.* **1991,** *30,* 2494-2508.
16. (a) $^{Me}N_{az}NH_2$: Hillers, S.; Eremeev, A. V.; Lidaks, M.; Pestunovich, V. A.; Liepin, E.; Kalvins, I. *Khim. Geterotsikl. Soedin.* **1971,** *7,* 45-48. (b) $^{Ph}N_{az}NH_2$: Müller, R. K.; Joos, R.; Felix, D.; Schreiber, J.; Wintner, C.; Eschenmoser, A. *Org. Synth.* **1976**, *55*, 114-117. (c) Chandrasekhar, S.; Prakash, S. J.; Shyamsunder, T.; Ramachandar, T. *Synth. Commun.* **2004,** *34,* 3865-3873.
17. Bonanno, J. B. Ph.D. Thesis, Cornell University, Ithaca, NY, **1996**.
18. Graefe, A. F.; Meyer, R. E. "1,1'-Biaziridine compounds." US Patent 3070596. 25 Dec. 1962.
19. Koshino, H.; Uzawa, J. *Kagaku Seibutsu* **1995**, *33*, 252-258.
20. (a) Blum, L.; Williams, I. D.; Schrock, R. R. *J. Am. Chem. Soc.* **1984,** *106,* 8316-8317. (b) Sellmann, D.; Soglowek, W.; Knoch, F.; Moll, M. *Angew. Chem., Int. Ed. Engl.* **1989,** *28,* 1271-1272. (c) Fryzuk, M. D.; Love, J. B.; Rettig, S. J.; Young, V. G. *Science* **1997,** *275,* 1445-1447 (d) Bernskoetter, W. H.; Pool, J. A.; Lobkovsky, E.; Chirik, P. J. *J. Am. Chem. Soc.* **2005,** *127,* 7901-7911. (e)

Saouma, C. T.; Müller, P.; Peters, J. C. *J. Am. Chem. Soc.* **2009,** *131,* 10358-10359.

21. Calculations performed using the Gaussian03 software package (ref. 22) at the B3PW91 level using the CEP-31GP effective core potential basis set. Structures were optimized using the default convergence criteria prior to vibrational analysis.
22. Gaussian 03, Revision C.02, M. J. Frisch, G. W. Trucks, H. B. Schlegel, G. E. Scuseria, M. A. Robb, J. R. Cheeseman, J. A. Montgomery, Jr., T. Vreven, K. N. Kudin, J. C. Burant, J. M. Millam, S. S. Iyengar, J. Tomasi, V. Barone, B. Mennucci, M. Cossi, G. Scalmani, N. Rega, G. A. Petersson, H. Nakatsuji, M. Hada, M. Ehara, K. Toyota, R. Fukuda, J. Hasegawa, M. Ishida, T. Nakajima, Y. Honda, O. Kitao, H. Nakai, M. Klene, X. Li, J. E. Knox, H. P. Hratchian, J. B. Cross, V. Bakken, C. Adamo, J. Jaramillo, R. Gomperts, R. E. Stratmann, O. Yazyev, A. J. Austin, R. Cammi, C. Pomelli, J. W. Ochterski, P. Y. Ayala, K. Morokuma, G. A. Voth, P. Salvador, J. J. Dannenberg, V. G. Zakrzewski, S. Dapprich, A. D. Daniels, M. C. Strain, O. Farkas, D. K. Malick, A. D. Rabuck, K. Raghavachari, J. B. Foresman, J. V. Ortiz, Q. Cui, A. G. Baboul, S. Clifford, J. Cioslowski, B. B. Stefanov, G. Liu, A. Liashenko, P. Piskorz, I. Komaromi, R. L. Martin, D. J. Fox, T. Keith, M. A. Al-Laham, C. Y. Peng, A. Nanayakkara, M. Challacombe, P. M. W. Gill, B. Johnson, W. Chen, M. W. Wong, C. Gonzalez, and J. A. Pople, Gaussian, Inc., Wallingford CT, 2004.
23. Miller, R. L.; Lawler, K. A.; Bennett, J. L.; Wolczanski, P. T. *Inorg. Chem.* **1996,** *35,* 3242-3253.
24. (a) Churchill, M. R.; Youngs, W. J. *Inorg. Chem.* **1979,** *18,* 171-176. (b) Churchill, M. R.; Wasserman, H. J.; Turner, H. W.; Schrock, R. R. *J. Am. Chem. Soc.* **1982,** *104,* 1710-1716.

25. (a) Li, X.; Schopf, M.; Stephan, J.; Harms, K.; Sundermeyer, J. *Organometallics* **2002,** *21,* 2356-2358 (b) Li, X.; Wang, A.; Wang, L.; Sun, H.; Harms, K; Sundermeyer, J. *Organometallics* **2007,** *26,* 1411-1413.
26. Bohle, D. S.; Heineke, D.; Tiripicchio, A.; Tiripicchio Camellini, M.; Vahrenkamp, H.*Angew. Chem.* **1990,** *102,* 938-939.
27. Neithamer, D. R.; LaPointe, R. E.; Wheeler, R. A.; Richeson, D. S.; Van Duyne, G. D.; Wolczanski, P.T. *J. Am. Chem. Soc.* **1989,** *111,* 9056-9072.
28. Hirsekorn, K. F.; Veige, A. S.; Marshak, M. P.; Koldobskaya, Y.; Wolczanski, P. T.; Cundari, T. R.; Lobkovsky, E. B. *J. Am. Chem. Soc.* **2005,** *127,* 4809-4830.
29. (a) Herrmann, W. A. *Angew. Chem., Int. Ed. Engl.* **1974,** *13,* 599. (b) Herrmann, W. A.; Reiter, B.; Biersack, H. *J. Organomet. Chem.* **1975,** *97,* 245-251. (c) Schwab, P.; Grubbs, R. H.; Ziller, J. W. *J. Am. Chem. Soc.* **1996,** *118,* 100-110. (d) Klose, A.; Solari, E.; Floriani, C.; Re, N.; Chiesi-Villa, A.; Rizzoli, C. *Chem. Commun.* **1997,** 2297-2298. (e) Nomura, M.; Michon, C.; Berger, A.; Pfeffer, M.; de Cian, A.; Kyritsakas-Gruber, N. *J. Organomet. Chem.* **2006,** *691,* 846-858.
30. Nikonov, G. I.; Putala, M.; Zinin, A. I.; Kazennova, N. B.; Lemenovskii, D. A.; Batsanov, A. S.; Struchkov, Y. T. *J. Organomet. Chem.* **1993,** *452,* 87-90
31. (a) Koester, R.; Simic, D.; Grassberger, M. A. *Liebigs Annalen* **1970,** *739,*211-219. (b) Johnson, L. K.; Frey, M.; Ulibarri, T. A.; Virgil, S. C.; Grubbs, R. H.; Ziller, J. W. *J. Am. Chem. Soc.* **1993,** *115,* 8167-8177.
32. LaPointe, R. E.; Wolczanski, P. T.; Mitchell, J. F. *J. Am .Chem. Soc.* **1986,** *108,* 6382-6384.
33. Xavier, C. *Org. Synth.* **1986,** *64,* 207-216.
34. Javed, M. I.; Brewer, M. *Org. Synth.* **2008,** *85,* 189-195.

Chapter 3

Activation of White Phosphorus (P_4) with $(silox)_3Ta$ and $(silox)_3NbPMe_3$[‡]

Introduction

While attempts to prepare $[(silox)_3M]_2N_2$ were underway (M = Nb, Ta), it became desirable to determine if we could make the related phosphorus complexes $[(silox)_3M]_2P_2$. In stark contrast to elemental nitrogen, elemental phosphorus (as P_4) is readily activated by transition metal complexes and some reactive organic species. There are hundreds of early- and late-metal examples of P_4 activations, many of which result in conversion of P_4 into dozens of different catenated P_n products with varied coordination aptitudes. Several of the known structures are shown in Figure 3.1.[1]

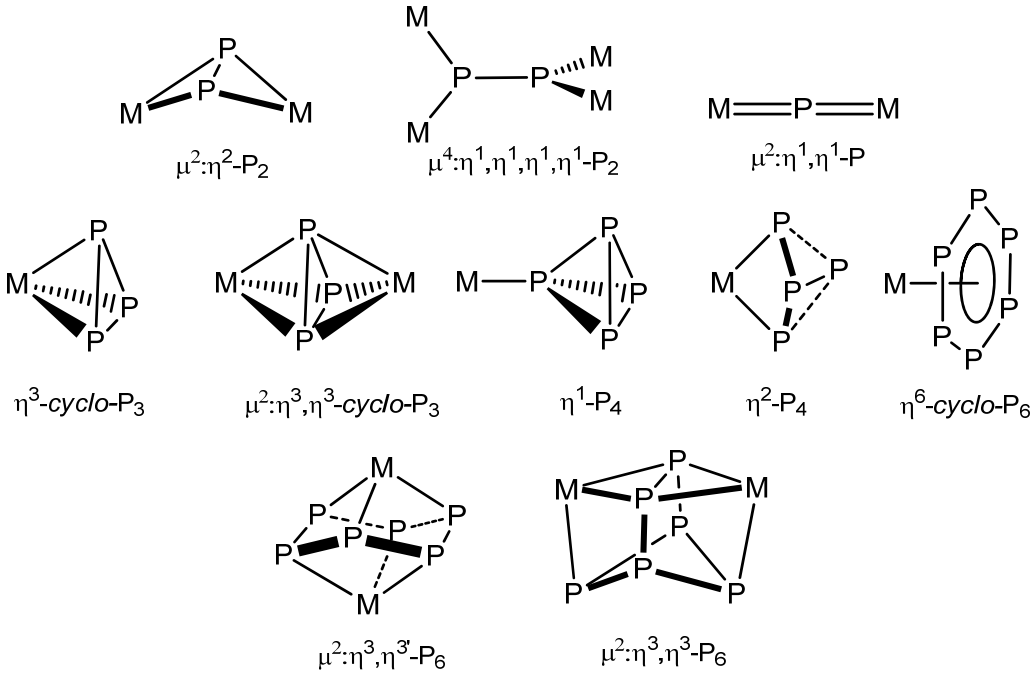

Figure 3.1. Some of the previously observed products from transition metal coordination and activation of P_4.

[‡] Reproduced with permission from: Hulley, E. B.; Wolczanski, P. T.; Lobkovsky, E. B. *Chem. Comm.* **2009,** 6412-6414

Both early- and late-metal compounds can provide any of these structures, but amongst the most common is the bridging μ^2:η^2,η^2-P_2 architecture. This can be viewed as originating via the reactions shown in Figure 3.2.

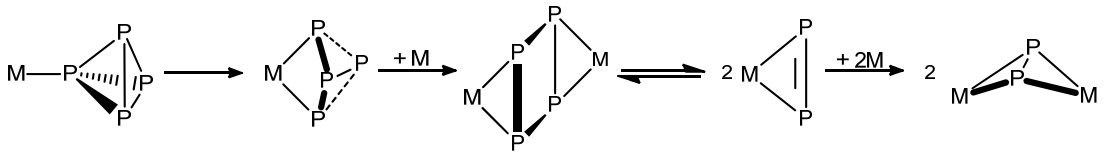

Figure 3.2. One of the possible mechanisms of synthesis of $M_2(\mu^2$:η^2,η^2-$P_2)$.

There are several possible ways to obtain the μ^2-P_2 fragment;[2] systems that involve less-reducing metal centers may go by different means due to the stability of the aromatic *cyclo*-P_4^{2-} ion. Within the $(silox)_3M$ system (M = Ta, **1**; M = Nb, **2**), however, we might expect reversible cleavage of the intermediate *cyclo*-P_4^{4-} complex to proceed to products. Other examples of this butterfly dimer include $[Cp^*Re(CO)_2]_2(\mu^2$:η^2,η^2-$P_2)$,[3] $[CpCr(CO)]_2(\mu^2$:η^2,η^2-$P_2)$,[4] $[CpMo(CO)]_2(\mu^2$:η^2,η^2-$P_2)$,[4] and $[Nb((NpN(Ar))_3]_2(\mu^2$:η^2,η^2-$P_2)$[5] ($Cp^* = \eta^5$-C_5Me_5, $Np = CH_2{}^tBu$).

The success of these systems led us to suspect that $[(silox)_3M]_2P_2$ might be easily prepared. The interest was both in the comparison to a dinitrogen complex (Chapter 2) and in the possibility that the severe steric bulk of the silox groups would prevent the side-on η^2,η^2-coordination mode in favor of the yet-unseen end-on coordination. There has been some development in the way of phosphorus chemistry within the $(silox)_3M$ system, both in the deliberate synthesis of phosphinidenes and in the P-C bond activation of $(silox)_3NbPMe_3$.[6] Bonnano[7] previously established the oxidative-addition/1,2-elimination reactivity of $(silox)_3Ta$ with primary amines and extended the work to phosphines and arsines. Addition of phenylphosphine to **1** yields the observed phosphide-hydride prior to 1,2-elimination of H_2 as shown in Equation 3.1.

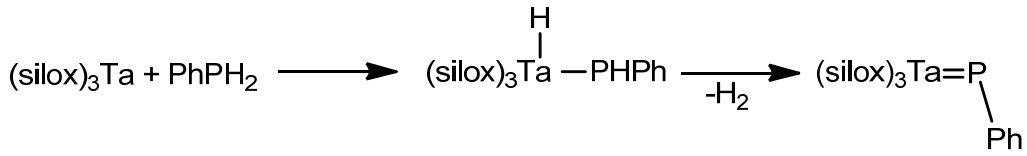

3.1

Using PH_3, the corresponding parent phosphinidene was prepared (**1=PH**), deprotonated to the phosphide anion (**1≡P$^-$**), and alkylated with TMSCl (to **1=PTMS**). Similar oxidative-addition/1,2-elimination chemistry was extended to Nb by Hirsekorn via $(silox)_3NbPMe_3$, and in a similar manner prepared **2=PH**, **2≡P$^-$**, and **2=PCH$_3$**.[6]

The crystal structure of **1=PPh** reveals interesting geometric consequences of its electronic structure. The bond angle of 110.2° differs from that for the corresponding phenylimide (172.4°) due to poor s-p mixing for P – the bonding from P to Ta and C_{ph} is essentially p-orbital based and the bond angles approach 90°.[8,9] The diphosphorus compounds $[(silox)_3M]_2P_2$ for Nb and Ta are likely to be best described as diphosphinidene complexes, analogous to the diimide character of $[(silox)_3M]_2N_2$, and as such would be expected to have similar structures. It's expected, therefore, that the diphosphinidene structures would have a zig-zag structure and M-P bond lengths in the range of a double bond.

Results and Discussion

$(silox)_3Ta$ (**1**) was treated with ¼ eq. of P_4 in toluene at –78 °C for 7 h, allowed to warm to room temperature slowly and stirred for 12 h. During the course of the reaction the solution darkened from pale blue to black and, eventually, yellow as an orange-brown solid precipitated from solution. This solid proved insoluble in all common organic solvents and defied NMR analysis. Single crystals were grown from a hot-THF suspension and X-ray analysis indicated the product was the desired $[(silox)_3Ta]_2(\mu^2{:}\eta^1,\eta^1\text{-}P_2)$ (**$[1]_2P_2$**), produced in 77% yield. The structure is provided in Figure 3.3, selected parameters are presented in Table 3.1 and the crystallographic data are presented in Table 3.3.

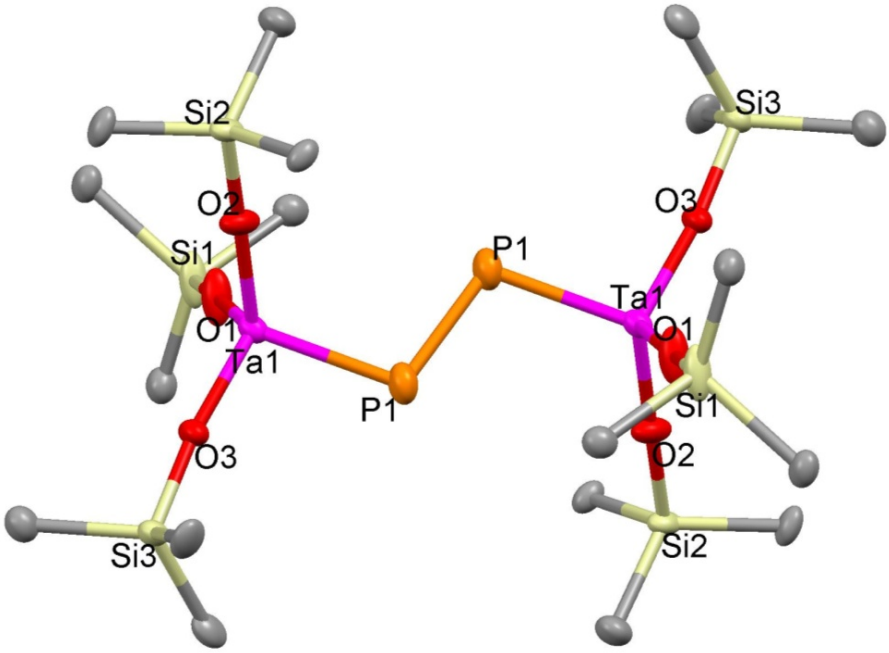

Figure 3.3. Molecular structure of **$[1]_2P_2$**. Methyl groups have been removed for clarity.

Table 3.1. Selected bond angles and interatomic distances for **[1]$_2$P$_2$**.

Selected Bond Distances (Å)		Selected Bond Angles (degrees)	
Ta1-O1	1.874(3)	O1-Ta1-P1	110.85(8)
Ta1-O2	1.872(2)	O2-Ta1-P1	111.85(9)
Ta1-O3	1.858(2)	O3-Ta1-P1	99.14(8)
Ta1-P1	2.3158(11)	Ta1-P1-P1'	105.67(6)
P1-P1'	2.1709(19)	O1-Ta1-O2	106.83(12)
O1-Si1	1.672(3)	O2-Ta1-O3	114.10(10)
O2-Si2	1.672(3)	O3-Ta1-O1	106.83(11)
O3-Si3	1.685(2)		

As is frequently observed, the structure of **[1]$_2$P$_2$** was plagued by significant disorder in the ^{t}Bu-groups on the silox ligands. The structure is symmetric with respect to inversion and thus the two halves of the molecule are identical. The Ta-P bond distance is 2.3158(11) Å, which compares very well with that in **1=PPh** (2.317(4) Å), and is consistent with a phosphinidene (Ta=P) assignment. The P-P distance of 2.1709(19) Å is also consistent with that expected for a P-P single bond, and is only slightly shorter than the P-P bonds in P_4 itself (2.21 Å).[10] There is a curious asymmetry in the silox core with respect to the phosphinidene linkage; the O1-Ta1-P1 and O2-Ta1-P1 bond angles are larger than O3-Ta1-P1 by an average of 12.2°. This tilting of the phosphinidene moiety away from O1 and O3 allows the phosphinidene moiety of the opposing Ta to sit within the gap between those two silox groups and *vice versa*. The longer Ta-O1 and Ta-O2 bond lengths relative to Ta-O3 can be explained as a mild *trans*-influence of the Ta=P bond. Though soluble enough at 80 °C to recrystallized over the course of a week, no signal attributable to **[1]$_2$P$_2$** was found in the ^{1}H, ^{13}C, ^{31}P{H} NMR spectra at 80 °C nor in ^{31}P CP-MAS NMR spectra. In C_6D_6, **[1]$_2$P$_2$** was found to be relatively thermally robust (120 °C), decaying slowly to silanol and other unidentified silox-containing products. The fate of the P_2-moiety was not determined due to lack of significant ^{31}P NMR signals.

The relatively easy success of Ta is in some contrast with the more complicated reactivity of P_4 with **2-PMe$_3$**. When conducted at room temperature, the

treatment of **2-PMe$_3$** with ¼ equivalent of P_4 in toluene yields 70% of a purple insoluble solid that could, as with **[1]$_2$P$_2$**, be recrystallized from hot THF solution. A crystal amenable to X-ray diffraction was selected and its structure is presented in Figure 3.4, selected parameters are presented in Table 3.2 and the crystallographic data are presented in Table 3.3.

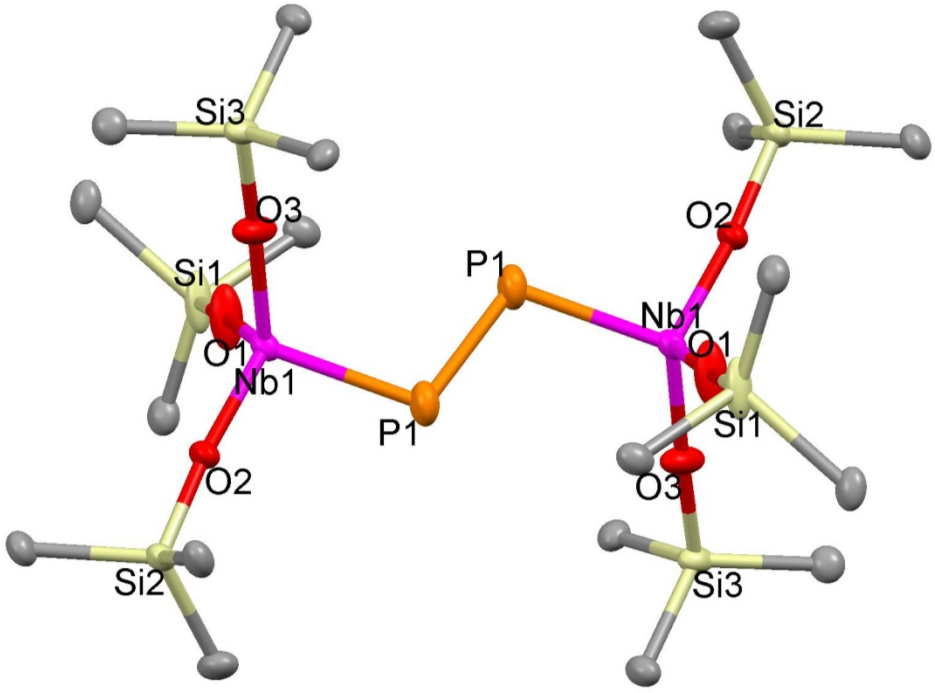

Figure 3.4. Molecular structure of **[2]$_2$P$_2$**. Methyl groups have been removed for clarity.

Table 3.2. Selected bond angles and interatomic distances for **[2]$_2$P$_2$**.

Selected Bond Distances (Å)		Selected Bond Angles (degrees)	
Nb1-O1	1.8876(17)	O1- Nb1-P1	109.72(6)
Nb1-O2	1.8652(13)	O2- Nb1-P1	98.72(5)
Nb1-O3	1.8815(15)	O3- Nb1-P1	111.07(6)
Nb1-P1	2.3250(7)	Nb1-P1-P1'	106.15(4)
P1-P1'	2.1430(13)	O1- Nb1-O2	114.70(8)
O1-Si1	1.6657(18)	O2- Nb1-O3	115.23(7)
O2-Si2	1.6774(14)	O3- Nb1-O1	107.18(8)
O3-Si3	1.6701(17)		

Table 3.3. X-ray crystallographic data for $[\mathbf{1}]_2\mathbf{P}_2$, $[\mathbf{2}]_2\mathbf{P}_2$, and $[(\mathbf{silox})_3\mathbf{Nb}(^c\mathbf{P}_3)]_2$.

Crystal Data			
Formula	$C_{72}H_{162}O_6P2Si_6Ta_2$	$C_{72}H_{162}Nb_2O_6P_2Si_6$	$C_{72}H_{162}Nb_2O_6P_6Si_6$
Formula Weight	1716.40	1540.32	1664.20
Crystal System	Triclinic	Triclinic	Monoclinic
Space Group	P-1	P-1	P-1
Z	1	1	4
a, Å	12.9611(7)	12.9765(6)	33.163(2)
b, Å	13.1197(7)	13.1430(6)	13.0037(9)
c, Å	16.0871(9)	16.0885(8)	22.9736(15)
α, deg	67.135(3)	67.128(2)	90
β, deg	68.391(3)	68.430(2)	103.448(3)
γ, deg	61.970(2)	61.974(2)	90
Volume, Å^3	2166.2(2)	2173.19(18)	9635.6(11)
D (calc.), g/cm^3	1.316	1.177	1.147
Absorption coeff., mm^{-1}	2.687	0.426	0.453
F(000)	902	838	3592
Crystal Size, mm	0.20 x 0.15 x 0.03	0.40 x 0.35 x 0.05	0.25 x 0.10 x 0.05
Data Collection and Refinement			
Temp, K	173(2)	173(2)	203(2)
Wavelength (λ), Å	0.71073	0.71073	0.71073
θ limits, deg	1.41 to 26.52	1.82 to 30.51	1.96 to 23.26
Index Ranges	$-16 \le h \le 16, -16 \le k \le 16, -20 \le l \le 20$	$-18 \le h \le 18, -18 \le k \le 18, -22 \le l \le 22$	$-36 \le h \le 36, -14 \le k \le 14, -25 \le l \le 25$
Reflections Collected	37459	59669	52990
Absorption Correction	Semi-empirical from equivalents	Semi-empirical from equivalents	Semi-empirical from equivalents
Max. and Min. Transmission	0.9359 and 0.6156	0.9790 and 0.8480	0.9777 and 0.8952
Refinement Method	Full-matrix least-squares on F^2	Full-matrix least-squares on F^2	Full-matrix least-squares on F^2
Data/Restraints/Params.	8957 / 1576 / 679	13250 / 894 / 694	6930 / 392 / 406
Goodness-of-Fit on F^2	1.018	1.017	1.092
Final R Indices [$I>2\sigma(I)$]	R1 = 0.0454, wR2 = 0.0896	R1 = 0.0452, wR2 = 0.1128	R1 = 0.1095, wR2 = 0.2526
R Indices (all data)	R1 = 0.0645, wR2 = 0.1054	R1 = 0.0642, wR2 = 0.1235	R1 = 0.1236, wR2 = 0.2584
Largest Diffraction Peak and Hole (e^- Å^3)	1.821 and -1.058	0.725 and -0.848	0.741 and -1.227

The structure confirmed the identity of the purple product as $[(silox)_3Nb]_2(\mu^2:\eta^1,\eta^1\text{-}P_2)$ (**[2]$_2$P$_2$**). As with the Ta congener **[2]$_2$P$_2$** was insoluble in all common solvents and no solution NMR spectral data could be obtained. CP-MAS ^{31}P experiments yielded a solid-state spectrum with a peak at -101 ppm, a resonance that is inconsistent with the expected shift based on DFT calculations[11] (438 ppm). The identity of the -101 ppm shift could not be determined. The structure of **[2]$_2$P$_2$** is almost identical to that of **[1]$_2$P$_2$**; indeed, the crystal structure data for both compounds are strikingly similar. The O-Nb-P bond angles reproduce the tilt of the phosphinidene linkage to one of the silox groups and the Nb-O distances opposite the Nb-P double-bond again show lengthening due to the *trans*-influence. The P-P distance in **[2]$_2$P$_2$** is 0.03Å shorter than the Ta congener, suggesting *slightly* stronger bonding interaction. Although the Nb-P bond distance is almost 0.01 Å longer than the Ta-P bond in **[1]$_2$P$_2$**, the two bond distances are effectively statistically equivalent (~3σ). The niobium diphosphorus dimer **[2]$_2$P$_2$** proved as thermally robust as the Ta congener, and it seemed inert to 1,3-cyclohexadiene (1,3-CHD) under thermolysis conditions. Cummins' previous studies on extrusion of P_2 from the diphosphaazide complex $(Np(Ar)N)_3Nb(P_2NMes)$ in neat 1,3-CHD showed it was potent for scavenging of P_2 via two Diels-Alder reactions to produce a $C_{12}H_{16}P_2$ organic tetracycle.[12] This same product was not observed in any thermolysis reactions of 1,3-CHD with **[1]$_2$P$_2$** or **[2]$_2$P$_2$**.

The curiosity of the Nb-system arose when the reaction was conducted the same way as for Ta. When **2-PMe$_3$** was treated with ¼ eq. P_4 in toluene and kept at –78 °C for 12 h, a small amount of **[2]$_2$P$_2$** was produced along with a different major product characterized by its red color and significant solubility. The red material was crystallized from cold (–40 °C) ether and a crystal was selected for analysis by X-ray

diffraction. The structure is provided in Figure 3.5, selected parameters are presented in Table 3.4 and the crystallographic data are presented in Table 3.3.

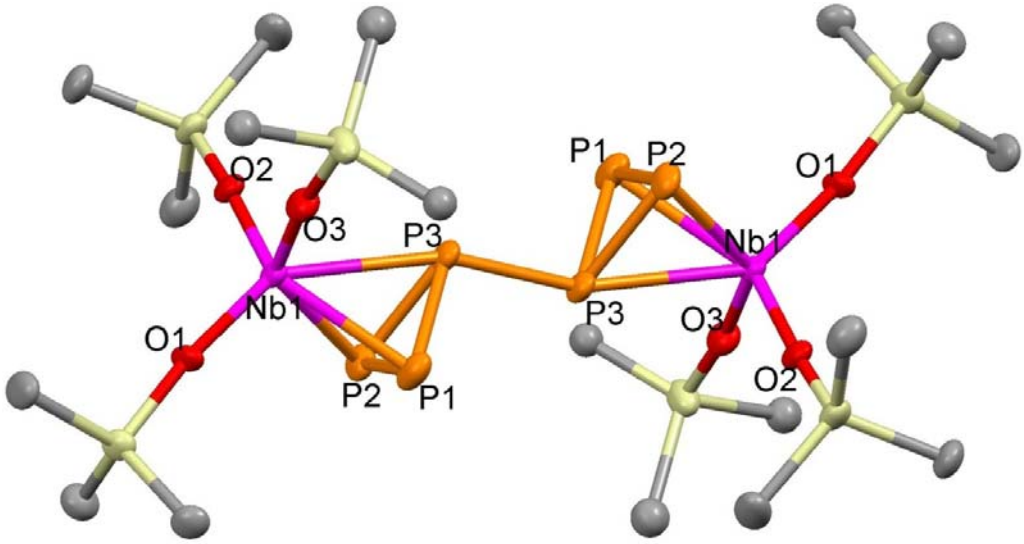

Figure 3.5. Molecular structure of **[2-^{c}P$_3$]$_2$**. Methyl groups have been removed for clarity.

Table 3.4. Selected bond angles and interatomic distances for **[2-^{c}P$_3$]$_2$**. P* refers to the P1/P2 centroid.

Selected Bond Distances (Å)		Selected Bond Angles (degrees)	
Nb1-O1	1.838(5)	O1- Nb1-P*	100.6(2)
Nb1-O2	1.917(6)	O2- Nb1-P*	115.6(2)
Nb1-O3	1.898(6)	O3- Nb1-P*	115.5(2)
Nb1-P1	2.550(2)	O1- Nb1-P3	142.66(19)
Nb1-P2	2.567(3)	O2- Nb1-P3	90.66(17)
Nb1-P3	2.773(2)	O3- Nb1-P3	91.94(18)
P3-P3'	2.214(4)	Nb1-P3-P3'	162.50(18)
P1-P2	2.167(4)	O1- Nb1-O2	110.8(2)
P2-P3	2.166(4)	O2- Nb1-O3	104.1(3)
P3-P1	2.167(4)	O3- Nb1-O1	110.7(3)

This soluble red product was identified by crystallography to be [(silox)$_3$Nb(η^2-^{c}P$_3$)]$_2$, a dimer of a Nb-*cyclo*-P$_3$ complex. Unfortunately, due to significant disorder in the silox groups, a disordered solvent molecule that had to be removed using the SQUEEZE algorithm, and problems caused by twinning, the structure is of rather poor overall quality. The core, however, of **[2-^{c}P$_3$]$_2$** is well resolved and shows a 2.214(4) Å

P-P bond connecting the two dimer halves, in very good agreement with the expected P-P single bond length (2.21 Å, *vide supra*). The P1-P2, P2-P3, and P3-P1 bond lengths in the *cyclo*-P_3 ring are slightly shorter (2.167(4) Å, on average), but still within single-bond length. There is a stronger interaction between Nb and P1 or P2 than with P3, and though the Nb-P3 distance is longer than the sum of covalent radii (2.773(2) Å vs. 2.58 Å),[13] it is only slightly longer than the Nb→P bond in [(silox)$_3$NbP(H)-Nb(silox)$_3$] (2.67 Å).[7] Thus each *cyclo*-P_3 subunit can be considered as a P_3^{2-} (triphosphirene) ligand on each Nb. The overall geometry about each Nb can be considered pseudo-tetrahedral with the fourth coordination site taken up by the η^2-P_2 interaction.

The ^{31}P NMR spectrum of **[2-^{c}P$_3$]$_2$** manifests as a slightly broad ($\nu_{½}$ = 30 Hz) singlet at –139.4 ppm, in contrast to the expected doublet and triplet signals implied by the two different P-environments in the solid-state structure. It was surmised that rapid interconversion of the phosphorus atoms was occurring at room temperature and a variable-temperature experiment was conducted. The spectra are shown in Figure 3.4.

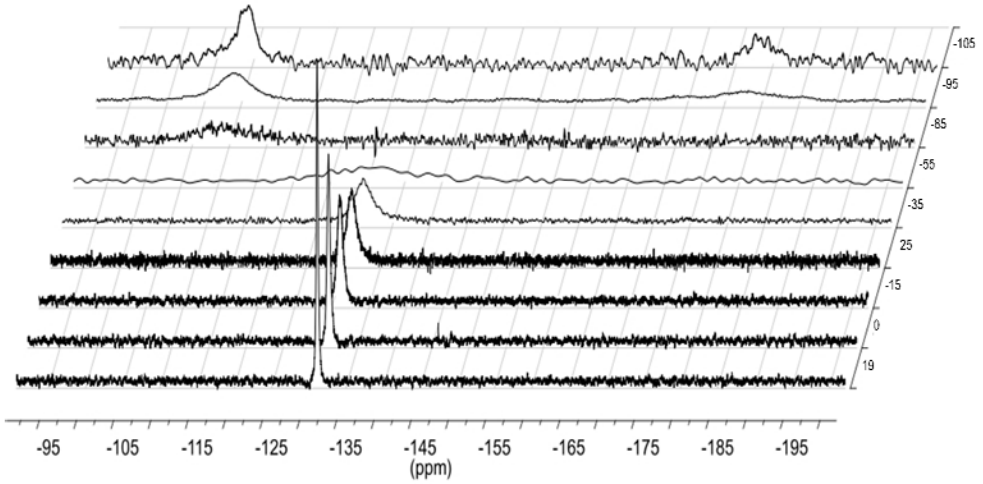

Figure 3.6. Variable temperature ^{31}P NMR spectra of **[2-^{c}P$_3$]$_2$**.

Decoalescence was observed around –55 °C and two individual signals were resolved at –105 °C at –129.6 ppm ($\nu_{1/2}$ = 560 Hz) and –197.8 ppm ($\nu_{1/2}$ = 730 Hz) that integrated ~2:1, respectively. The spectrum at each temperature was fit to a two-site exchange model to obtain a rate of interconversion and the activation parameters were extracted from an Eyring plot of the rate constants. These data and the fit parameters are shown in Figure 3.5.

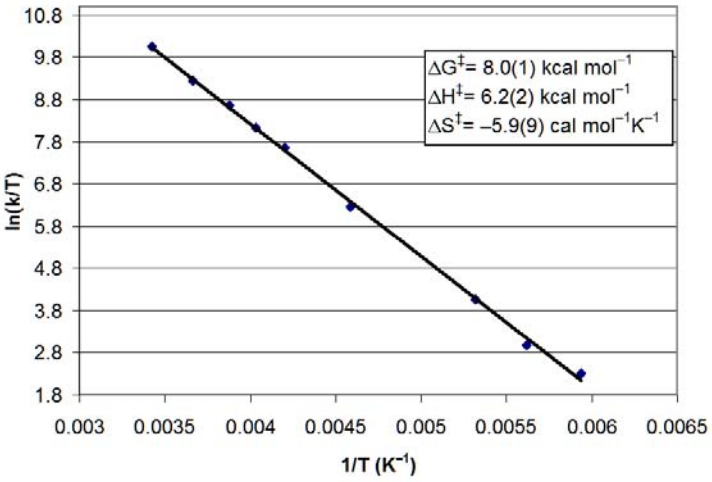

Figure 3.7. Eyring plot for the interconversion of phosphorus environments in **[2-^{c}P$_3$]$_2$**.

The mildly negative entropy of activation suggests a transition state that is more rigid than the ground state structure. One can imagine a 1,3-shift of the phosphorus of one *cyclo*-P_3 ring followed by bond reorganization.

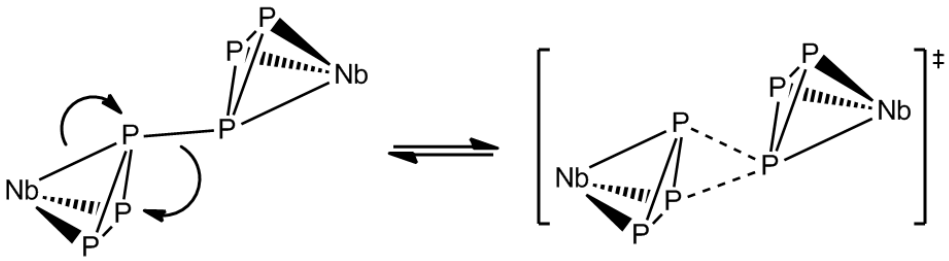

Figure 3.8. Possible transition state for the interconversion of phosphorus environments in **[2-^{c}P$_3$]$_2$**.

Some syntheses of **[2-^{c}P$_3$]$_2$** were accompanied by small amounts (0-14%) of a different compound that had NMR resonances indicative of a related structure, (silox)$_3$Nb(^{c}P$_3$H) (**2-^{c}P$_3$H**). The ^{1}H and ^{31}P{^{1}H} NMR data are presented in Figure 3.6.

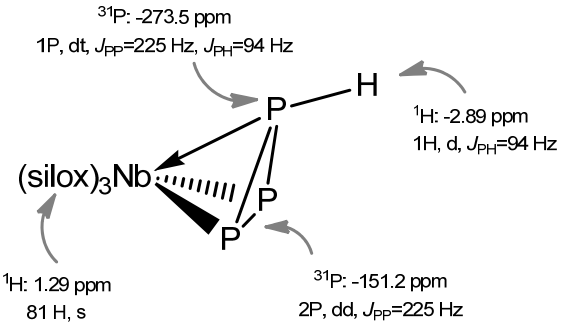

Figure 3.9. Spectral characterization of **2-^{c}P$_3$H**.

The coupling constants observed in **2-^{c}P$_3$H** can be expected to be about the same order as those expected for **[2-^{c}P$_3$]$_2$** based on the solid-state structure, however they were not observed in the low temperature spectra because of the rather large linewidths. Efforts to produce this compound deliberately from **[2-^{c}P$_3$]$_2$** and 1,3-cyclohexadiene or 1,4-cyclohexadiene either thermally or photochemically were unsuccessful.

The phosphorus architecture in **[2-^{c}P$_3$]$_2$** suggested the possibility of being able to synthesize an as-yet unseen allotrope of phosphorus, P_6. Such an allotrope has been the subject of several theoretical studies,[14] and previous work with the (silox)$_3$Nb system suggested it may be facile to remove the metal scaffold under the right conditions. Several attempts to remove (silox)$_3$Nb as (silox)$_3$NbO using N_2O, pyridine-N-oxide, and ethylene oxide resulted in either no reaction (N_2O, ethylene oxide) or the production of oxygenated phosphorus compounds (pyridine-N-oxide). Treatment of **[2-^{c}P$_3$]$_2$** with ethylene to produce (silox)$_3$Nb(C_2H_4) also showed no sign of demetallation at elevated temperatures (>120 °C). Treatment of **[2-^{c}P$_3$]$_2$** with 1,4-quinone in the hope of producing polymeric [(silox)$_3$Nb(1,4-benzenediolate)]$_n$

resulted in the immediate formation of an orange-yellow solid, however the ^{31}P NMR showed no evidence of soluble P-containing compounds and mass spectrometry of the solid failed to show the mass for P_6 or other phosphorus allotropes. The complex was not completely inert, for treatment of **[2-^{c}P$_3$]$_2$** with excess **2-PMe$_3$** resulted in the immediate formation of **[2]$_2$P$_2$**.

It was hoped that mild oxidation of the complex would induce P-P bond formation and facilitate P_6 elimination,[15] and as a first attempt **[2-^{c}P$_3$]$_2$** was treated with 1 eq. I_2 in pentane to produce a yellow-orange solid. The ^{1}H NMR spectrum indicated the solid was a mixture of **[2-^{c}P$_3$]$_2$**, (silox)$_3$NbI$_2$ (**2-I$_2$**, confirmed by independent synthesis), and a new product. The new compound had two broad ^{31}P NMR signals at -6.39 ppm (ν ½ ~ 650 Hz) and -11.91 ppm (ν ½ ~ 320 Hz) that integrated roughly 1:2, respectively. Since dynamic behavior was likely responsible for the breadth of the peaks, this new compound was studied in a VT-NMR experiment, and the spectra are shown in Figure 3.6. During the course of this experiment, the new product was observed to decay at elevated temperatures with concomitant increase in the amounts of **2-I$_2$** and **[2-^{c}P$_3$]$_2$**. This suggested the product was in fact (silox)$_3$Nb(^{c}P$_3$)(I) (**[2-(^{c}P$_3$)(I)]**).

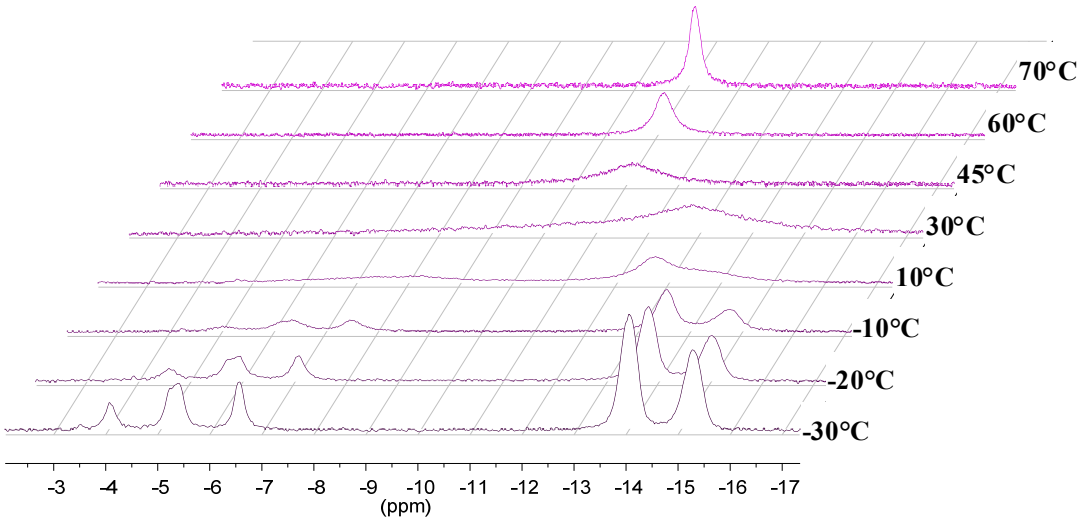

Figure 3.10. Variable temperature ^{31}P NMR spectra of **[2-(^{c}P$_3$)(I)]**.

These spectra were fit to a two-site exchange model to extract the interconversion rate constant, which were then fit to the Eyring equation to obtain activation parameters as, shown in Figure 3.7.

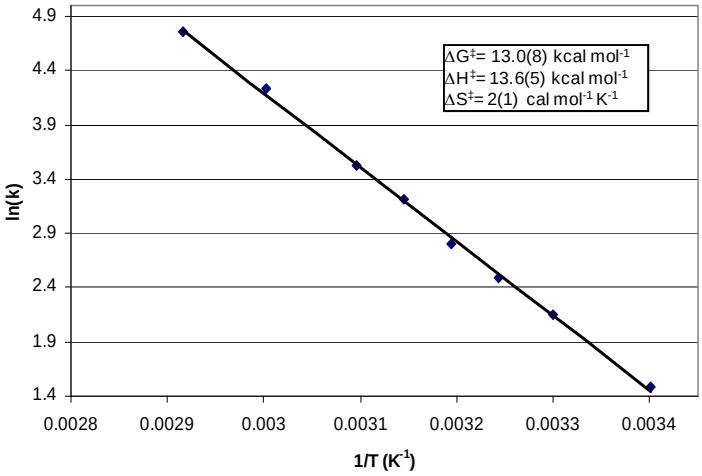

Figure 3.11. Eyring plot for the interconversion of phosphorus environments in **[2-(^{c}P$_3$)(I)]**.

The structure of **[2-(^{c}P$_3$)(I)]** was tentatively assigned as shown in Figure 3.8. The coupling constants for the two phosphorus environments are similar to **2-(^{c}P$_3$H)**, however the chemical shift is far removed from either **[2-(^{c}P$_3$)]$_2$** or **2-(^{c}P$_3$H)**.

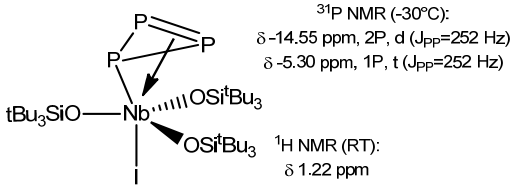

Figure 3.12. Proposed structure and spectral characterization of **[2-(^{c}P$_3$)(I)]**.

Conclusion

The activation of P_4 by **1** and **2-PMe$_3$** is remarkably facile and leads to the desired products under optimized conditions. The isolation of a novel catenation of P_6 is also interesting, and leads to questions about the mechanisms of these multistep activations that as yet remain unanswered.

Experimental

General Considerations. All manipulations were carried out either using a nitrogen glovebox or high-vacuum and Schlenk techniques. All glassware was oven dried. Benzene-d_6 was refluxed over sodium metal, vacuum distilled and stored under nitrogen over activated 4Å molecular sieves. All solvents were distilled from sodium metal or sodium benzophenone-ketyl solutions.

^1H, ^2H and $^{13}C\{^1H\}$ NMR spectra were obtained on Varian 300 MHz (Mercury), 400 MHz (INOVA), 500 MHz (INOVA), and 600 MHz (INOVA) spectrometers. For historical consistency, NMR shifts for silox-containing compounds are referenced to benzene-d_6 (^1H, δ 7.15 ppm; ^{13}C, δ 128.39 ppm). CP-MAS NMR experiments were conducted at room temperature on a Varian 400 MHz (Varian) spectrometer. $(silox)_3Ta$[16a] and $(silox)_3NbPMe_3$[16b] were synthesized according to literature procedures.

Synthesis. 1. $[(silox)_3Ta]_2P_2$ ($[1]_2P_2$). To a 50 mL round bottom flask was added 432 mg (0.52 mmol) $(silox)_3Ta$ and 16 mg (0.13 mmol) P_4 and the flask was attached to a small swivel-frit assembly. The assembly was evacuated on the vacuum line and 25 mL toluene was added via vacuum transfer at –78° C. The solution was warmed to room temperature and allowed to stir for 6 hours. The resulting brown-orange suspension was filtered and washed twice with 10 mL portions of pentane and the solid dried *in vacuo* to yield 332 mg (77%). This material was recrystallized in hot THF or hot benzene over the course of a week in a sealed NMR tube. Anal. calc'd for $C_{72}H_{162}O_6P_2Si_6Ta_2$: C, 50.38%; H, 9.51%. Found: C, 50.32 %; H, 9.77%.

2. $[(silox)_3Nb]_2P_2$ ($[2]_2P_2$). To a small vial containing 10 mL toluene was added 300 mg (0.37 mmol) $(silox)_3NbPMe_3$ in the glovebox. A solution of 10 mg P_4 (0.08 mmol) in 5 mL toluene was added dropwise to the vial at room temperature. After completion of addition the vial was capped and shielded from light and stirred

for 4 hours at RT. The resulting black suspension was filtered and washed with 20 mL pentane and the solid dried *in vacuo* to yield 200 mg (70%) of purple $[(silox)_3Nb]_2P_2$. This material was recrystallized in hot THF or hot benzene over the course of a week in a sealed NMR tube. Anal. calc'd for $C_{72}H_{162}O_6P_2Si_6Nb_2$: C, 56.14%; H, 10.60%. Found: C, 55.99 %; H, 11.00%.

3. $[(silox)_3Nb(^cP_3)]_2$ ($[2\text{-}(^cP_3)]_2$). To a 50 mL round bottom flask was added 1.40 g (1.72 mmol) $(silox)_3NbPMe_3$ and 165 mg (1.33 mmol) P_4 and the flask was attached to a small swivel-frit assembly. The assembly was evacuated on the vacuum line and 40 mL toluene was added via vacuum transfer at –78° C. The flask was stirred at –78° C for 7 hours and then warmed to –40° C and stirred for an additional 4 hours. The solution was allowed to warm to room temperature and then stirred for an additional 20 hours. Three-quarters of the solvent was removed *in vacuo* and the solution was filtered and washed ten times with 10 ml toluene. The toluene was stripped and 10 ml pentane was added via vacuum transfer. The solution was cooled to –78° C and cold-filtered to yield 832 mg (58%) upon drying. ^{1}H NMR (C_6D_6): δ 1.31 (s, 81H). ^{13}C NMR (C_6D_6): δ 24.64 ($C(CH_3)_3$), 31.55 ($C(CH_3)_3$). $^{31}P\{^1H\}$ NMR (C_6D_6): δ -139.40 (s, 6P). Anal. calc'd for $C_{72}H_{162}O_6P_6Si_6Nb_2$: C, 51.96%; H, 9.81%. Found: C, 51.97 %; H, 9.76%.

4. **$[(silox)_3Nb(^cP_3)]I$ ($[2\text{-}(^cP_3)(I)]$)**. A 100 mL round bottom flask was charged with **$[2(^cP_3)]_2$** (100 mg, 0.06 mmol) and affixed to a 180° needle valve. The flask was evacuated and pentane (50 mL) was added. A solution of I_2 (16 mg, 0.06 mmol) in pentane (12.5 mL) was added dropwise. There was a color change to red-orange as the solution was stirred for 30 min. The resulting suspension was stripped to yield a mixture of **$[2\text{-}(^cP_3)(I)]$**, **$[2(^cP_3)]_2$**, and $(silox)_3NbI_2$ as a red-orange powder. ^{1}H NMR (C_6D_6): δ 1.22 (s, 81H). $^{31}P\{^1H\}$ NMR (C_6D_6, 70°): δ –10.5 (s, 3P).

Single-Crystal X-ray Diffraction Studies. Upon isolation, the crystals were covered in polyisobutenes and placed under a 173K N_2 stream on the goniometer head of a Siemens P4 SMART CCD area detector (graphite-monochomated Mo Kα radiation, $\lambda = 0.71073$ Å). The structures were solved by direct methods (SHELXS). All non-hydrogen atoms were refined anisotropically unless otherwise stated, and hydrogen atoms were treated as idealized contributions (Riding model).

1. [(silox)$_3$Ta]$_2$P$_2$ ([1]$_2$P$_2$). An orange plate measuring 0.20 × 0.15 × 0.03 was obtained from hot THF solution. A total of 37,459 reflections were collected with 8,957 being symmetry independent ($R_{int} = 0.0924$), and 7,095 were greater than $2\sigma(I)$. A semiempirical absorption correction from equivalents was applied, and the refinement utilized $w^{-1} = s^2(F_o^2) + (0.0466p)^2 + 0.0000p$, where $p = (F_o^2 + 2F_c^2)/3$.

2. [(silox)$_3$Nb]$_2$P$_2$ ([2]$_2$P$_2$).A purple plate measuring 0.40 × 0.35 × 0.05 mm^3 was obtained from hot THF solution. A total of 59,669 reflections were collected with 13,250 being symmetry independent ($R_{int} = 0.0660$), and 10,194 were greater than $2\sigma(I)$. A semiempirical absorption correction from equivalents was applied, and the refinement utilized $w^{-1} = s^2(F_o^2) + (0.0689p)^2 + 0.0000p$, where $p = (F_o^2 + 2F_c^2)/3$.

3. [(silox)$_3$Nb(^{c}P$_3$)]$_2$ ([2(^{c}P$_3$)]$_2$). A colorless block measuring 0.20 × 0.15 × 0.03 mm^3 was obtained from cooling a saturated ether solution to –40 °C. A total of 52,990 reflections were collected with 8,957 being symmetry independent ($R_{int} = 0.0924$), and 5,871 were greater than $2\sigma(I)$. A semiempirical absorption correction from equivalents was applied, and the refinement utilized $w^{-1} = s^2(F_o^2) + (0.0000p)^2 + 550.0000p$, where $p = (F_o^2 + 2F_c^2)/3$.

REFERENCES

1. (a) Cossairt, B. M.; Piro, N. A.; Cummins, C. C. *Chem. Rev.* **2010,** *110,* 4164-4177. (b) Caporali, M.; Gonsalvi, L.; Rossin, A.; Peruzzini, M. *Chem. Rev.* **2010,** *110,* 4178-4235.
2. Stephens, F. H.; Johnson, M. A.; Cummins, C. C.; Kryatova, O. P.; Kryatova, S. V.; Rybak-Akimova, E. V.; McDonough, J. E.; Hoff, C. D. *J. Am Chem. Soc.* **2005,** *127,* 15191-15200.
3. Scherer, O. J.; Ehses, M.; Wolmershäuser, G. *J. Organomet. Chem.* **1997,** *531,* 217-221.
4. Scherer, O. J.; Sitzmann, H.; Wolmershäuser, G. *J. Organomet. Chem.* **1984,** *268,* C9–C12.
5. Goh, L. Y.; Chu, C. K.; Wong, R. C. S.; Hambley, T. W. *J. Chem. Soc., Dalton Trans.* **1989,** 1951–1956.
6. Figueroa, J. S.; Cummins, C. C. *J. Am. Chem. Soc.* **2003,** *125,* 4020-4021.
7. Hirsekorn, K. F.; Veige, A. S.; Wolczanski, P. T. *J. Am. Chem. Soc.* **2006,** *128,* 2192-2193.
8. Bonanno, J. B.; Wolczanski, P. T; Lobkovsky, E. B. *J. Am. Chem. Soc.* **1994,** *116,* 11159-11160.
9. (a) 13. Drago, R. S. *J. Phys. Chem.* **1958,** *62,* 353–357. (b) 14. Power, P. P. *Chem. Rev.* **1999,** *99,* 3463–3503.
10. Corbridge, D. E. C.; Lowe, E. J. *Nature* **1952**, *4328*, 629.
11. Cummins, C. C., private communication, 25 June 2008.
12. Piro, N. A.; Figueroa, J. S.; McKellar, J. T.; Cummins, C. C. *Science* **2006,** *313,* 1276-1279.
13. Bondi, A. *J. Phys. Chem.***1964,** *68,* 441-451.

14. (a) Nagese, S.; Ito, K. *Chem. Phys. Lett.* **1986,** *126,* 43-47. (b) Oles, A. M.; Fulde, P.; Boehm, M. C. *Chem. Phys.* **1987,** *117,* 385-403. (c) Janoschek, R. *Chem. Ber.* **1989**, *122,* 2121-2124. (d) Warren, D. S.; Gimarc, B. M. *J. Am. Chem. Soc.* **1992,** *114,* 5378-5385. (e) Haeser, M.; Schneider, U.; Alrichs, R. *J. Am. Chem. Soc.* **1992,** *114,* 9551-9559. (f) Kobayashi, K.; Miura, H.; Nagese, S. *J. Mol. Struc.-THEOCHEM.* **1994,** *117,* 69-77. (g) Haesar, M. *J. Am. Chem. Soc.* **1994,** *116,* 6925-6926. (h) Guo, L.; Wu, H.; Jin, Z. *J. Mol. Struc.-THEOCHEM.* **2004,** *677,* 59-66. (i) Hilberty, P. C.; Volatron, F. *Heteroatom Chem.***2007,** *18,* 129-134.

15. (a) Francis, M. D.; Hitchcock, P. B.; *Organometallics* **2003,** *22,* 2891-2896. (b) Fox, A.; Wright, R. J.; Rivard, E.; Power, P. P. *Angew. Chem. Int. Ed. Engl.***2005,** *44,* 7729-7733.

16. (a) LaPointe, R. E.; Wolczanski, P. T.; Mitchell, J. F. *J. Am .Chem. Soc.* **1986,** *108,* 6382-6384. (b) Veige, A. S.; Slaughter, L. M.; Lobkovsky, E. B.; Wolczanski, P. T.; Matsunaga, N.; Decker, S. A.; Cundari, T. R. *Inorg. Chem.* **2003,** *42,* 6204-6224.

Chapter 4

Synthesis and Reactivity of Destabilized 2-Aza-Allyl Anionic Ligands

Introduction

During the course of investigation of tripodal ligands designed around M-C bond formation, Frazier discovered a novel ligand fragmentation to yield the stable 1,3-dipyridyl-2-azapropenylide anion (smif) coordinated to Cr (Eq. 4.1).[1]

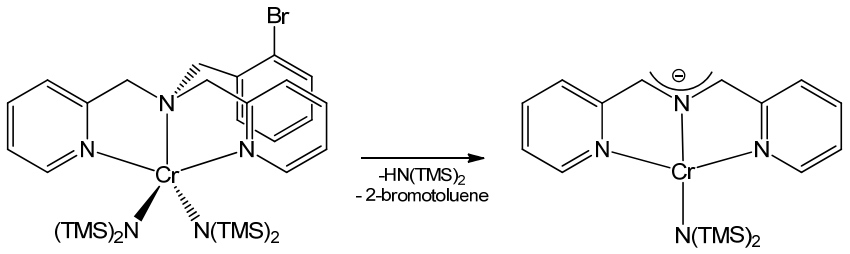

Eq. 4.1

The 2-aza-allyl anion, the defining feature of the smif ligand, is related to a class of reactive organic frameworks known as azomethine ylides. Constructs such as those shown in Figure 4.1 have been extensively explored within the context of 1,3-dipolar additions to various dipolarophiles.[2]

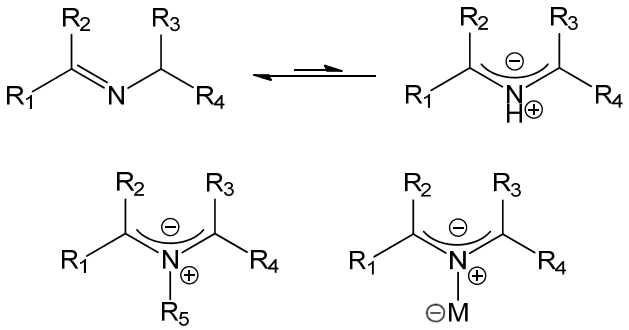

Figure 4.1. Imine/azomethine ylid equilibrium (top) and alkylated and metallated azomethine ylid analogs (bottom). Typically R_2 = H, R_4 = EWG.

Metallated 2-aza-allyl constructs have been implied by numerous metal-catalyzed cycloadditions,[3] but complexes employing this moiety had not been crystallographically characterized prior to the chromium species in Eq.1.

The protonated ligand, smifH, proved easy to synthesize via condensation of 2-aminomethylpyridine and pyridine-2-carboxaldehyde.[4] Using $M^{II}(amide)_2$ precursors (M=Fe, Cr) the octahedral $M(smif)_2$ compounds were prepared via deprotonation, and the Ti, V, Mn, Co, and Ni congeners through a variety of metathetical strategies.[5] $Cr(smif)_2$ and $Fe(smif)_2$ were the two first prepared, and their unusually intense electronic absorption spectra (25,000–45,000 M^{-1} cm^{-1}) and the diamagnetism of $Fe(smif)_2$ prompted the synthesis of the remaining first-row species. The fact that smif was a strong-field ligand for Fe was somewhat surprising given the large number of high-spin neutral octahedral Fe-complexes.[6] Interestingly, it was noticed that adding *ortho*-methyl groups affected the electronic structure of the resulting Fe-complex; systematically increasing the number of methyl groups from one in Fe(smif)(^{o}Me-smif) to four in Fe(^{o}Me_2-smif)$_2$ changed the ground state from S=0 to S=2.

The 2-aza-allyl moiety itself proved quite stable; several of the bis(smif) compounds were sublimable and $Fe(smif)_2$ appeared to be a thermodynamic sink in many reactions of (smif)Fe($N(TMS_2)$) and Fe($N(CH_2Py)_2)_2$. The anionic character of the backbone could be exploited, however, such as in the attack of $Fe(smif)_2$ on organic isocyanates shown in Figure 4.2. Such an attack is largely due to the anionic nature of the carbons in the 2-aza-allyl backbone, as Na(smif) accomplishes this same insertion of isocyanates.

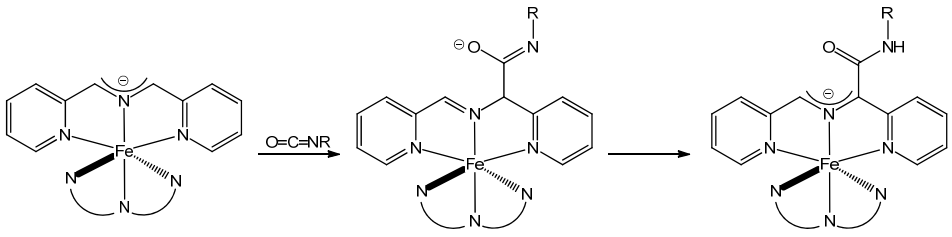

Figure 4.2. Attack of $Fe(smif)_2$ on an organic isocyanate.

The reactivity to polar substrates speaks to the ability of the backbone to behave as a closed-shell anion. Other reactions suggest the 2-aza-allyl moiety has modest diradical

character. The backbone of $Fe(smif)_2$ was found to be capable of [2+3] cycloaddition of non-polar p-tolylacetylene, changing the 2-aza-allyl anion into a dihydropyrrolide anion. Most interestingly, $(smif)Fe(N(TMS)_2)$ was shown to be monomeric in solution yet dimeric in the solid state (Eq. 4.2).

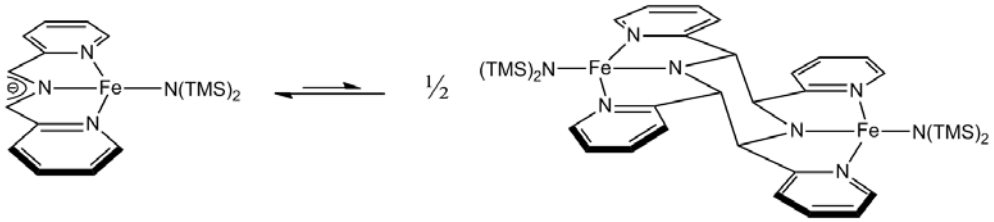

Eq. 4.2

This dual dipolar/biradical reactivity is a common feature of azomethine ylides,[2b] and electronic structure calculations have previously shown that both representations are involved in describing the ground state.[7] The fact that this dimerization is observable for $(smif)Fe(N(TMS)_2)$ and absent for $(smif)Cr(N(TMS)_2)$ pointed to metal-ligand interactions subtly affecting aza-allyl stability. While the studies of the smif-based compounds were ongoing, attempts were made to determine the generality of the 2-aza-allyl anion as a stable entity in a ligand.

Volpe[8] prepared a series of iron complexes based on the possibility of coupling the apparent stability of the 2-aza-allyl framework with metal-carbon bonds installed by orthometallation. Synthetic efforts were successful in producing organometallic iron(II) and iron(III) aza-allyl species wherein the ligand had a single pyridine ring. Attempts at making an analogous iron(III) complex with both pyridines of smif replaced with orthometallated phenyl-groups failed, presumably due to the reduction to iron(II) and generation of a reactive 2-aza-allyl radical. The structures of these species are shown in Figure 4.3.

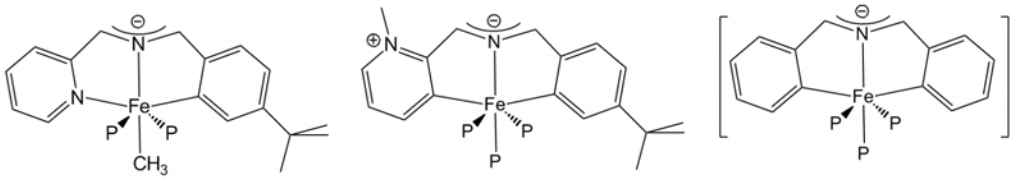

Figure 4.3. Prepared (left, center) and proposed (right) 2-aza-allyl-based ligands. (P = PMe_3)

Clearly, the electron-withdrawing effects of the pyridine ring were critical in stabilizing the anionic nature of the aza-allyl. It is within this context that a series of ligands was devised in an attempt to exploit the aza-allyl architecture. Initial efforts were devoted to macrocyclic ligands that incorporated multiple aza-allyl units, while later efforts were focused on open poly-dentate variants. The different ligand frameworks targeted are shown in Figure 4.4.

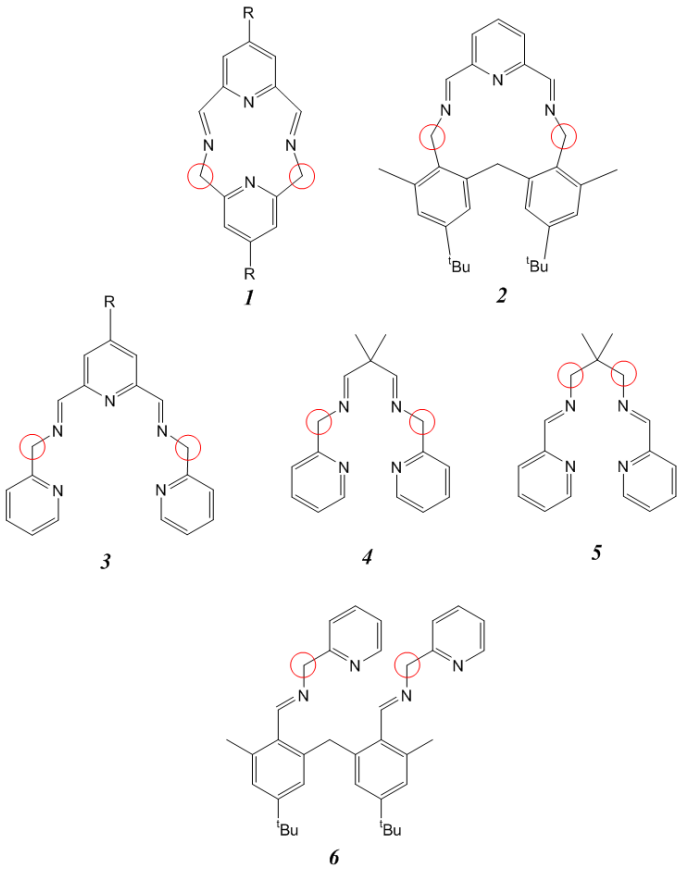

Figure 4.4. Ligand architectures targeted for study. Deprotonable positions are highlighted. R = H, ^{t}Bu.

Variant **1** was intended to act as the simplest macrocyclic analog of smif, whereas variants **3-5** were designed to explore the incorporation of the 2-aza-allyl anion in polydentate environments. Variants **5** and **6** were designed to take advantage of the structural rigidity of the 2-aza-allyl moiety, forcing an alkyl group with weak C-H bonds to be adjacent to a metal center. Some of these ligands, as discussed later, were found to be prone to irreversible C-C coupling reactions of the sort illustrated in Figure 4.5.

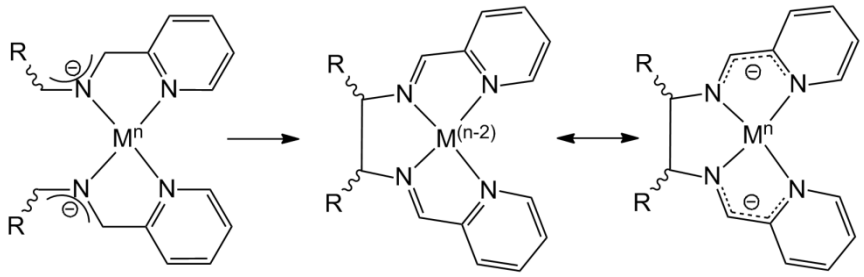

Figure 4.5. Coupling of 2-aza-allyl anions to yield iminopyridine ligands.

The coupling of the two anionic fragments yields a formally neutral imino-pyridine (ImPy) fragment and a reduced metal center. The ImPy fragments have been shown to be potent electron-acceptors, however, and their complexes frequently possess structural parameters indicative of mono- or bis-reduction when bound to sufficiently reducing metal centers.[9] The reduction of an ImPy unit results in population of a π*-orbital that has increased C-N single-bond character and increased C_{im}-C_{py} double-bond character. These structural changes have been correlated with the amount of reduction by Wieghardt *et al.*,[9c] as shown in Figure 4.6.

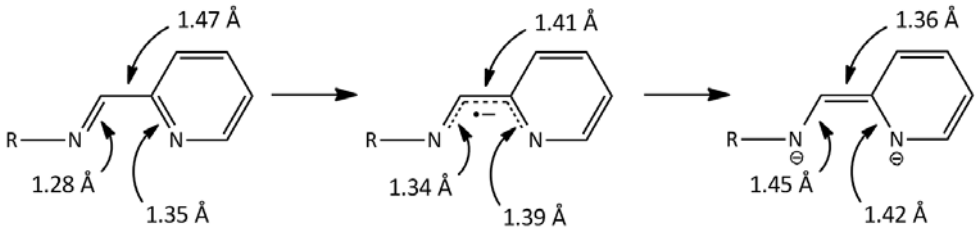

Figure 4.6. Characteristic bond-length changes upon reduction of ImPy moieties.

Many of the metal-ImPy complexes studied possess mono-reduced ImPy ligands; these organic radicals can have unusual interactions with each other and with paramagnetic metal centers and some discussion of the electronic structures of such compounds is necessary.

Broken Symmetry and the Electronic Structure of M(ImPy)$_n$ Complexes

Complexes such as that shown in Figure 4.5 are best described as containing ligand-centered radicals; part of the reason for this is illustrated in Figure 4.6.

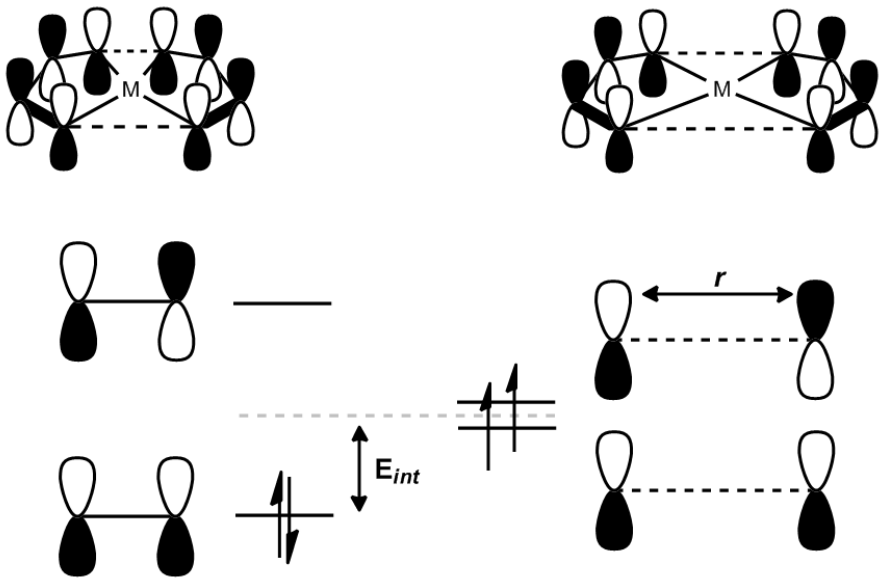

Figure 4.7. Near (left) and distant (right) interactions of two p-orbitals (bottom) and two ligand π*-orbitals (top).

A first approach to representing the electronic structure of two mono-reduced ligands is depicted in the left-hand portion of Figure 4.7; constructive and destructive interference would lead to pseudo-bonding and pseudo-antibonding MOs. The two electrons would thus be placed within the lower-lying MO and a closed-shell configuration would be expected. As the two component ligand orbitals are drawn apart (increasing *r*), however, the interaction energy E_{int} should approach zero and the two electrons should approach a triplet ground-state configuration. In the systems that

have been studied previously and those that will be addressed in this chapter, the spatial overlap of the component ligand orbitals is so low as to favor the latter description. As such, there is little covalency between the two π^* orbitals and the two electrons should approach an open-shell configuration.

There is an added complication in metal complexes of ligand-localized radicals; since there are filled and unfilled metal orbitals of appropriate symmetry to interact with the ligand radicals, predicting the ground state of weakly- to non-interacting systems cannot be confined to the MO treatment in Figure 4.7. First used to explain anomalous magnetic behavior in metal oxide materials, the modern usage of the Goodenough-Kanamori[10] approach states that the interaction of a filled orbital between two half-filled orbitals will result in the stabilization of a diamagnetic ground state.[11] This is shown pictorially in Figure 4.8.

Figure 4.8. Expected spin orientations in weakly-coupled biradicals in the absence (left) and presence (right) of a filled intermediate orbital. Note that this is a valence bond approach, not MO-based.

The nature of the antiferromagnetic interaction has been termed 'semi-covalent exchange', but can also be thought of as a form of spin polarization. This model is only useful in the case where the metal orbitals are all filled; more elaborate systems with partially-empty metal orbitals are too complicated to generalize and have a myriad of available electronic states.

The energetic proximity of the ground- and excited-states in such weakly-interacting systems leads to significant electron correlation problems. As such, no single electron configuration can properly represent the ground state wavefunction and

mixtures of electron configurations must be used. This is an age-old problem in computational chemistry, as even molecules as simple as H_2 cannot be properly described without including a small amount of excited-state electron configurations.[12] As a single-determinant computational technique, DFT will give misleading results when calculating pure singlet and triplet states of highly-correlated systems. Techniques that *do* properly treat electron correlation (such as Configuration Interaction and Coupled Cluster methods) are computationally expensive even for molecules that do not contain metal atoms. As such, a compromise technique known as Broken Symmetry has been developed by Noodleman *et al*. that allows approximations to the multi-configurational solution.[13] If we consider two weakly-interacting p-orbitals (as shown in Figure 4.9), we can represent the ground state using either the Two-Configuration Self-Consistent Field (TCSCF) approach or using the Broken-Symmetry (BS) formalism.

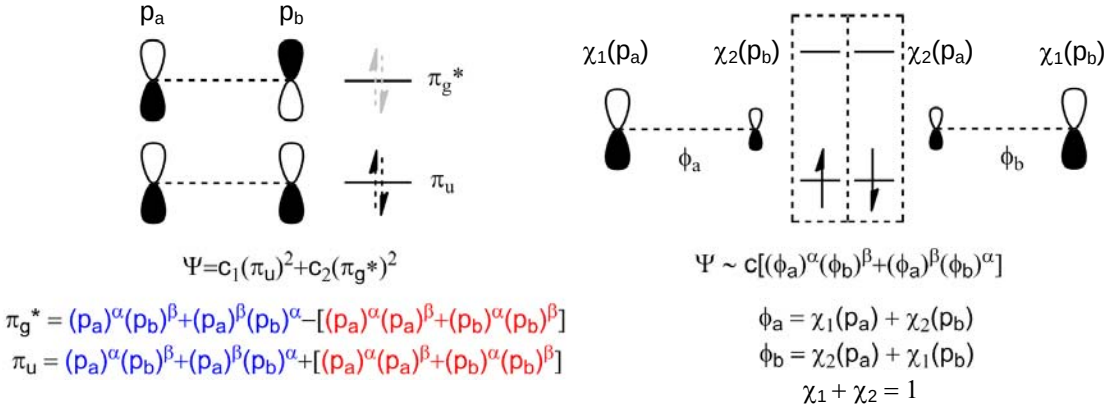

Figure 4.9. Orbital diagrams and corresponding wavefunction descriptions of the TCSCF (left) and BS (right) approaches to the electronic structure of two weakly-interacting p-orbitals. χ_1 and χ_2 are coefficients that modify the contributions from p_a and p_b for a given α or β B.S. solution.

The reason the pure $(\pi_u)^2$ description fails to represent the ground state properly is due to the ionic (shown in red) and covalent (shown in blue) contributions to such a

wavefunction. The ionic contributions represent the two electrons in the system being localized on one atom or the other; as the distance between the interacting atoms increases, this character becomes destabilizing as it requires energy to overcome the coulombic attraction. Allowing the $(\pi_g^*)^2$ configuration to mix with the ground state allows the subtraction of this ionic contribution. At the limit where the two atoms are infinitely separated, the two configurations have equal weight ($c_1 = c_2$). This is the essence of TCSCF, and it is inherently a multi-determinant technique.

In Broken Symmetry calculations this situation is rectified using a single determinant approach, by allowing the *spatial* components of the α and β electrons to differ. That is, it is the spatial symmetry of the wavefunction that is broken. As the interaction between the two orbitals is diminished, each electron is allowed to localize on one atom with its partner on the other. The actual output of a BS calculation is composed of only one spin configuration (e.g. $(\phi_a)^\alpha(\phi_b)^\beta$) and is thus not an eigenfunction of the spin operator $\hat{S}$, but the broken symmetry approach allows a single configuration to approximate the character of multi-configuration solutions. Pure closed-shell configurations can be represented as two spin-paired electrons at the same energy (with the same spatial wavefunction) because there is no energetic preference for one spin over another. In BS solutions, as with other open-shell calculations, the α and β electrons have different energy and spatial distributions. Most of these electrons are *nearly* spin-paired, in that each α has a β spatial partner at nearly the same energy, but the frontier orbitals are essentially single electron wavefunctions. This is represented in the right side of Figure 4.9 as a dashed box around the two functions that have the same spatial distribution. The high, unoccupied orbital represents the energy of an electron of opposite spin but similar spatial distribution of its lower energy (filled) counterpart.

A common practice in interpreting BS solutions involves perfoming a Corresponding Orbital Transformation (COT),[13c] which involves further mixing of the BS orbitals. In systems with significant spin polarization and multiple pairs of weakly-interacting electrons, the uncoupled electrons may not be the HOMOs of the system. Moreover, the spatial distributions of the BS orbitals are determined variationally and may lack any resemblance to canonical molecular orbitals. The COT procedure further mixes the BS solutions to maximize the number of α/β pairs with the same, or essentially the same, spatial distribution. After this procedure there are a number of α/β pairs that have quite different spatial distributions. The spatial overlap (S) is then calculated; familiar spin-paired (spatially identical) orbitals have an S = 1. The remaining orbitals will have an S considerably smaller than 1. These molecular orbitals, called magnetic orbitals, are more likely to resemble the shape of valence-bond type orbitals but their energies have lost all meaning. Using the BS approach on systems with significant electron correlation effects may result in having to choose between determining the energies of unfamiliar orbitals or familiar orbitals with meaningless energies.

Many of the resulting complexes synthesized in the following work have complicated electronic structure, some of which will be discussed. However, electron-correlation issues are extensive enough that many of these complexes are likely better treated with a more sophisticated approach than Broken Symmetry.

Results and Discussion

4.1. Ligand Architectures Incorporating 2,6-Disubstituted Pyridines

The initial ligand structures were based around the designs in Figure 4.10.

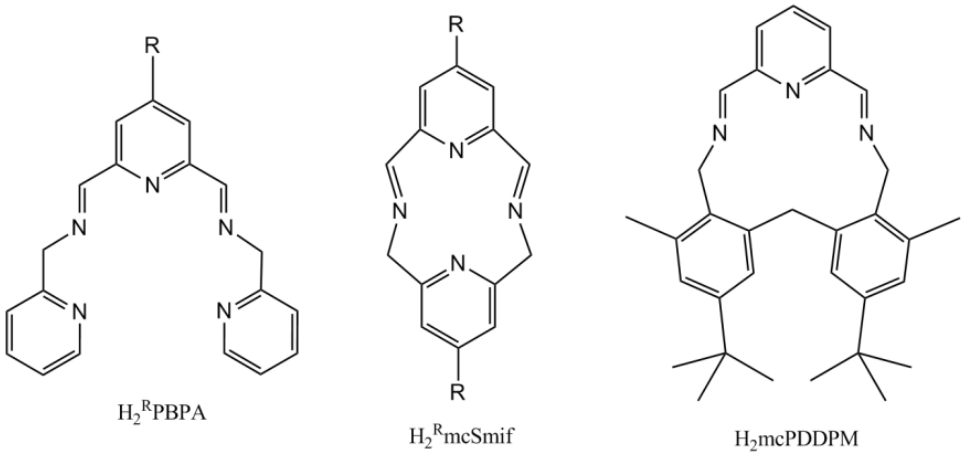

H_2^RPBPA $H_2^RmcSmif$ $H_2mcPDDPM$

Figure 4.10. Ligands incorporating the 2,6-disubstituted pyridine fragment. R = H, ^{t}Bu.

In the first two ligands in Figure 4.10, suspected (and later confirmed) solubility problems prompted the design of the ^{t}Bu variants. Both pyridine-2,6-diyl-bis(methanylylidene)bis(1-(4-R-pyridin-2-yl)methanamine) (H_2^RPBA, R= H, ^{t}Bu) and 2,11-diaza-[3.3](2,6)pyridinophane-1,7-diene ($H_2^RmcSmif$) were chosen based on what seemed like reasonable extensions of the smif coordination geometry. As discussed in the Introduction, it was also desirable to use the generation of the aza-allyl anion to encourage subsequent reactions. In the case of 2,10-diaza-(1,2),(2,1)-bis-(3-*tert*-butyl-5-methyl)benzo-(2,6)pyridinocyclodecaphane-1,11-diene (H_2mcPDDM) and an open-chain analog (discussed in Section 4.2), the diphenylmethane moiety within the ligand precursor was hoped to be amenable to CH-activation. These designs centered around 2,6-disubstituted pyridine fragments whose synthons had literature precedent for R = H (2,6-bis(aminomethyl)pyridine and 2,6-bis(carboxaldehyde)-pyridine), but had not been previously synthesized for R = ^{t}Bu. The aldehyde and amine fragments are both synthesized via the 2,6-di(methanol)pyridine intermediate,

which is commercially available for R = H. The synthesis of the ^{t}Bu-derivative is shown in Scheme 4.1.[14]

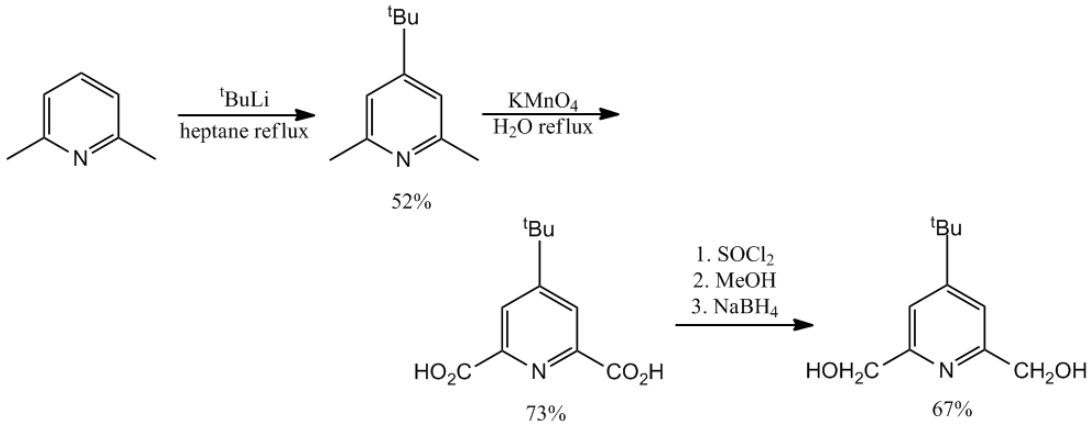

Scheme 4.1. Synthesis of (4-(tert-butyl)pyridine-2,6-diyl)dimethanol.

The product diol can be isolated in modest overall yield from 2,6-lutidine (25%), however each step can be conducted on a large scale (>10g) using low-cost reagents. Conversion of the diol to the dialdehyde proceeds relatively smoothly via Swern oxidation, shown in Eq. 4.3.

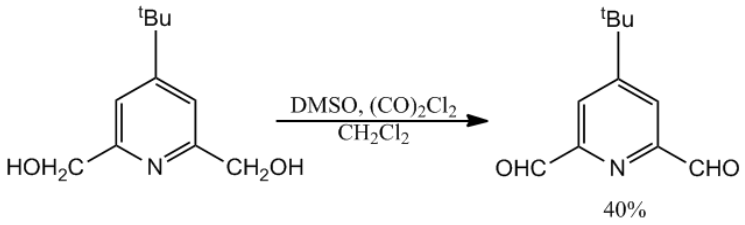

Eq. 4.3

The protonated form of the diamine used to condense with this dialdehyde in the synthesis of H_2^{tBu}mcSmif was prepared from the diol via the dibromide, as shown in Scheme 4.2.

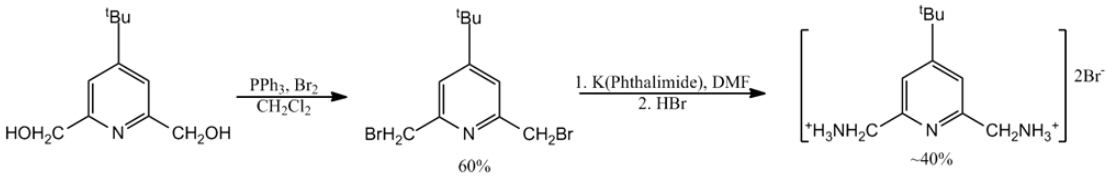

Scheme 4.2. Synthesis of (4-(tert-butyl)pyridine-2,6-diyl)dimethanaminium dibromide.

Aminomethylpyridine itself is known to decompose via scavenging CO_2 from the atmosphere,[14] and the bis(aminomethyl)pyridines prepared in this study seemed to be similarly air-sensitive. As such, the hydrobromide salts of the two derivatives (R = H, ^{t}Bu) were deprotonated via KH or KO^{t}Bu and isolated under air-free conditions immediately prior to condensation reactions.

The open-chain ligand $H_2{}^H$PBA was synthesized via condensation; the syntheses and ^{1}H NMR spectral characteristics are shown in Figure 4.11.

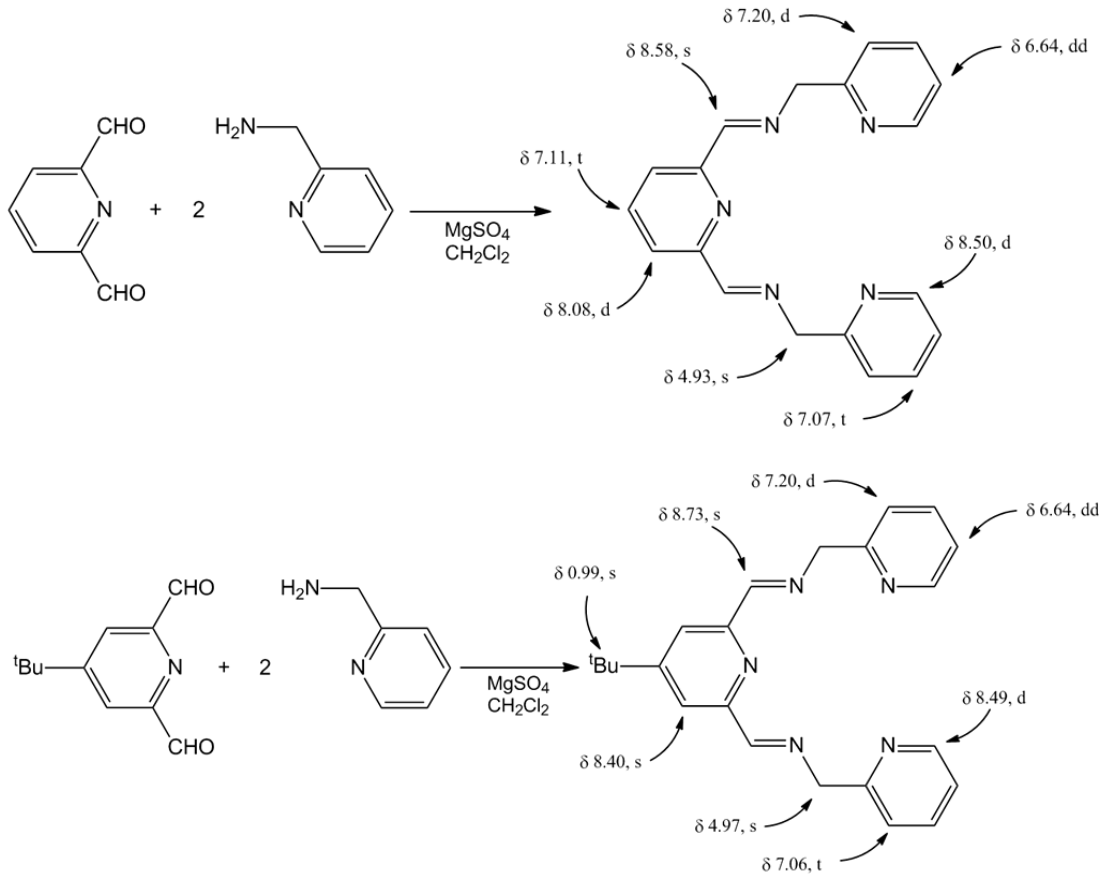

Figure 4.11. Synthesis of and spectral properties of $H_2{}^R$PBA, R= H, ^{t}Bu.

Attempts to metallate $H_2{}^H$PBA with $Fe(N(TMS)_2)_2(thf)$ or $Cr(N(TMS)_2)_2(thf)_2$ in C_6D_6 yielded only highly colored insoluble material. ^{1}H NMR spectra of these tubes were too broad to determine the fate of the reactants. It seems plausible that the planar

nature of the ligand would be responsible for the poor solubility properties. The most straightforward ligand modification involved *tert*-butyl substitution in the 4-position of the central pyridine. The modified ligand H_2^{tBu}PBA fared no better during metallation attempts, producing similarly dark-colored precipitates.

The preparation of H_2^{H}mcSmif appeared facile enough; macrocyclization reactions are favored over polymerization at high dilution, and NMR experiments revealed a single product could be obtained at 0.07 M. The synthesis and NMR spectral properties of the condensation product, consistent with those expected for H_2^{H}mcSmif, are shown in Figure 4.11.

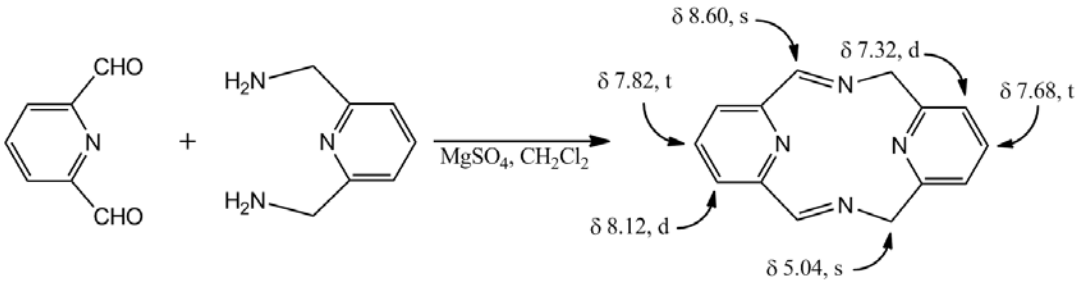

Figure 4.12. Synthesis of and spectral properties of putative H_2^{H}mcSmif.

This material proved to be of relatively low solubility in benzene. When treated with $Fe(N(TMS)_2)_2(thf)$ in C_6D_6 or d_8-THF, copious amounts of indigo solid were produced that defied NMR characterization, although HMDS was clearly visible. Working on the assumption that solubility of the nascent complex was the primary issue, the mono-*tert*-butyl-substituted variant was prepared as shown in Figure 4.12.

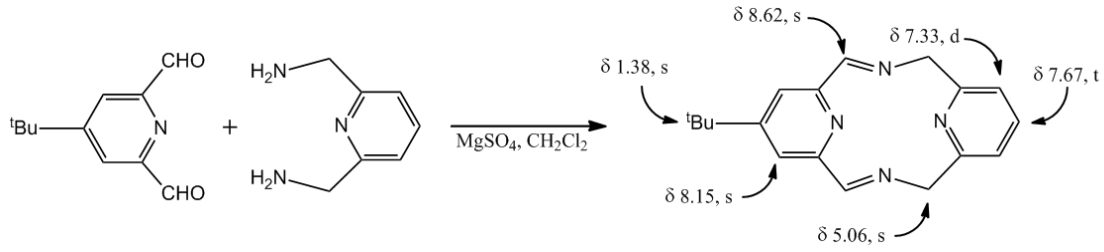

Figure 4.13. Synthesis of and spectral properties of putative H_2^{tBu}mcSmif.

Although the new variant was itself more soluble, it fared little better upon treatment with $Fe(N(TMS)_2)_2(thf)$. Evolution of HMDS was observed, signifying deprotonation, but there was no spectral indication of the desired complex and copious amounts of indigo solid formed. For unknown reasons, attempts to condense 4-^{t}Bu-2,6-bis(carboxaldehyde)pyridine with 4-^{t}Bu-2,6-bis(aminomethyl)pyridine failed to yield isolable products.

The synthesis of the other macrocyclic ligand, H_2mcPDDM, was more elaborate since the diphenylmethane-based diamine required independent synthesis. The substitution pattern on the phenyl rings was chosen on the basis of ease of synthesis.[15] The overall preparation is described in Scheme 4.3.

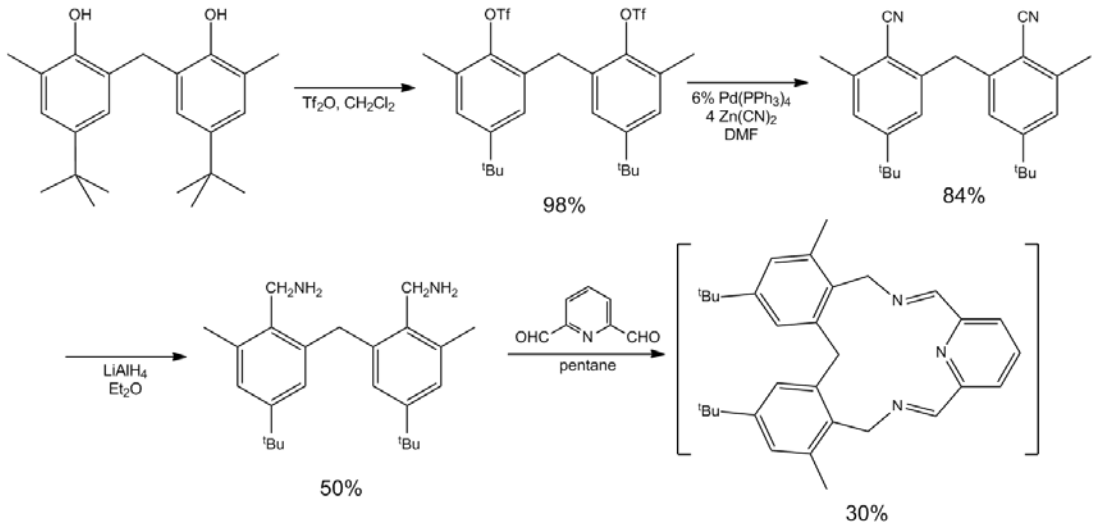

Scheme 4.3. Synthesis of H_2mcPDDM from 6,6'-methylenebis(4-(tert-butyl)-2-methylphenol).

The palladium-catalyzed cyanation of aryltriflates remains an active area,[16] and the synthesis from the diphenylmethane bis(triflate) above was optimized to yield 84% of the target nitrile. Reduction using $LiAlH_4$ was not as straightforward. The amine itself, a yellow oil, appears to be unstable in air with respect to cyclization and loss of ammonia. The diamine also defied purification from organic byproducts, and could

only be isolated in ~80% purity. Treatment of this yellow oil with 2,6-bis(carboxaldehyde)pyridine in pentane at 0.05 M resulted in precipitation of a white powder over the course of a week. This material has ^{1}H NMR spectral characteristics consistent with the expected C_{2v}-symmetric macrocycle. Treatment of this material with [Fe(2,4,6-trimethylphenyl)$_2$]$_2$[41] or (py)$_2$Fe(CH$_2$^{t}Bu)$_2$[56] in C_6D_6 over the course of 24 h appeared to produce the same yellow-green paramagnetic product. Resonances consistent with the same product were observed using Fe(N(TMS)$_2$)$_2$(thf), however the product mixture was significantly more complicated. Curiously, the number of resonances for this new complex was consistent with a non-deprotonated ligand environment. When treated with excess CO in C_6D_6, the solution changed color to red and ^{1}H NMR shifts consistent with diamagnetic and paramagnetic species were present. Solution IR data for this red material indicated two CO environments at 1958 cm^{-1} and 1896 cm^{-1}. This carbonylation was reversible, however, as solutions left open to a nitrogen atmosphere for days returned to their original yellow-green color. A single crystal was grown from slow evaporation of ethereal solutions and a structure was obtained. The structure is provided in Figure 4.13, selected parameters are presented in Table 4.1 and the crystallographic data are presented in Table 4.2.

Selected Bond Distances (Å)		Selected Bond Angles (degrees)	
Fe-N1	2.209(2)	N1-Fe-N2	73.06(8)
Fe-N2	2.057(2)	N2-Fe-N3	74.61(8)
Fe-N3	2.135(2)	N1-Fe-N3	147.22(8)
Fe-N4	2.215(2)	N4-Fe-N5	73.05(9)
Fe-N5	2.025(2)	N5-Fe-N6	74.44(8)
Fe-N6	2.143(2)	N4-Fe-N6	147.07(8)
C1-N1	1.296(3)	N1-Fe-N6	92.29(8)
C7-N3	1.311(4)	N3-Fe-N4	92.29(8)
C22-N4	1.286(3)	N2-Fe-N5	165.46(9)
C28-N6	1.320(4)		
C1-C2	1.432(4)		
C6-C7	1.423(4)		
C22-C23	1.435(4)		
C27-C28	1.419(4)		

Table 4.1. Selected bond angles and interatomic distances for (**^{PDI}MC**)**Fe**.

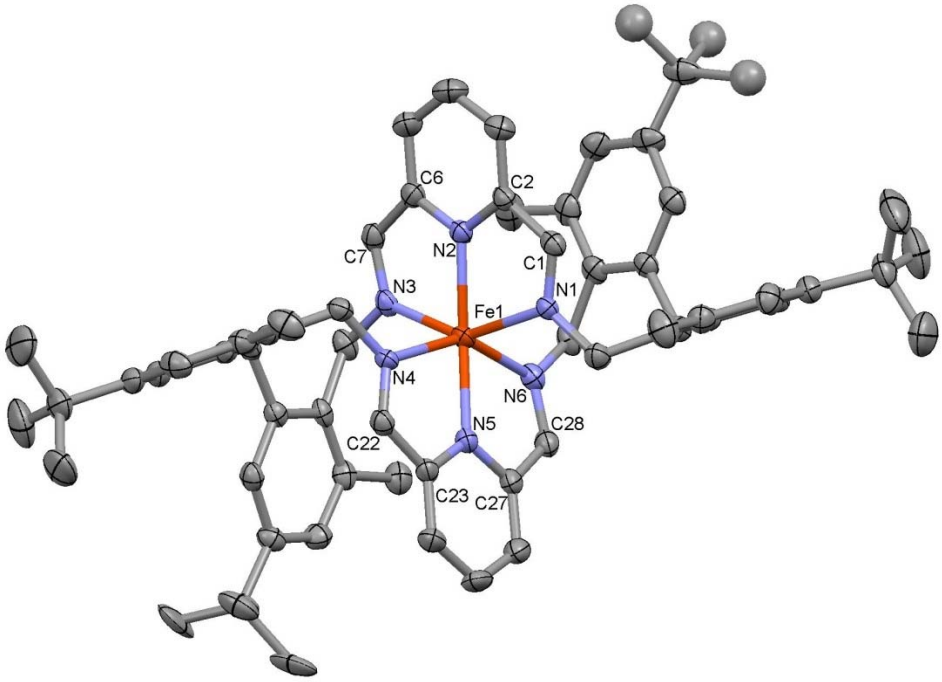

Figure 4.14. Molecular structure of **(**^{PDI}**MC)Fe**. Hydrogen atoms and a molecule of diethyl ether have been removed for clarity.

The structure of the complex, now termed **(**^{PDI}**MC)Fe**, made it clear that the initial condensation produced a macrocycle twice as large as intentioned. The structure of **(**^{PDI}**MC)Fe** is very similar to several of a series of pyridine-diimine complexes synthesized by Chirik *et al.*[17] The pyridine-diimine family of ligands is redox active and shows similar oxidation-state-dependent structural parameters, as shown below in Figure 4.14.

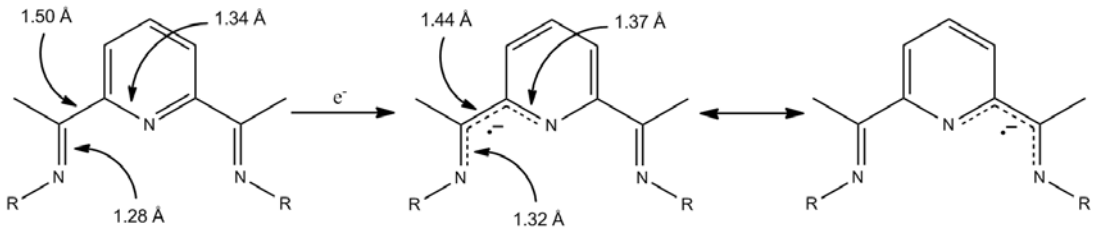

Figure 4.15. Structure and average bond lengths for the PDI ligand family and its anion. R = Aryl, Alkyl. (from Ref. 56)

When the R-group substituent of (^{R}PDI)$_2$Fe is isopropyl or cyclohexyl, the ligands are tridentate and pseudo-octahedral. The structural parameters of these two complexes were shown to be consistent with each PDI ligand containing a single electron with an overall Fe(II) oxidation state. Using the larger 2,6-disubstituted aryl substituents on the imine positions encourages dissociation of one of the ligand arms to yield a pseudo-tetrahedral geometry. The structure of **(^{PDI}MC)Fe** is nominally octahedral, with a slight distortion in the coordination environment around Fe, such that each PDI-fragment has a short and a long Fe-N_{im} bond length. There was a modest amount of disorder within two of the ^{t}Bu groups and they needed to be refined isotropically. The Fe-N bond lengths are consistent with a high-spin Fe center, and the magnetic moment of 2.0 μ_B as measured by Evans' method suggests antiferromagnetic coupling of the two unpaired electrons of the ligand with the four unpaired electrons of the iron. Although the magnetic moment is lower than expected, it is consistent with the previous observations of Chirik *et al.* who observed magnetic moments between 1.8-2.5 μ_B.[17]

4.2. Reactivity of ((ImCH$_2$Py)Ar)$_2$CH$_2$ with Cr(II) and Fe(II) Amides

The considerable difficulties present in synthesizing the desired macrocyclic frameworks encouraged us to focus on the remaining open-chain variants. Beginning with the open-chain variant of H_2mcPDDM, the synthesis was modified to avoid use of the unstable and impure diamine. Starting with the bis(arylnitrile)methane synthesized as before, the bis(aldehyde) was produced via DIBAL-H reduction, subsequent hydrolysis and condensation with two equivalents of 2-(aminomethyl)pyridine as shown in Scheme 4.4.

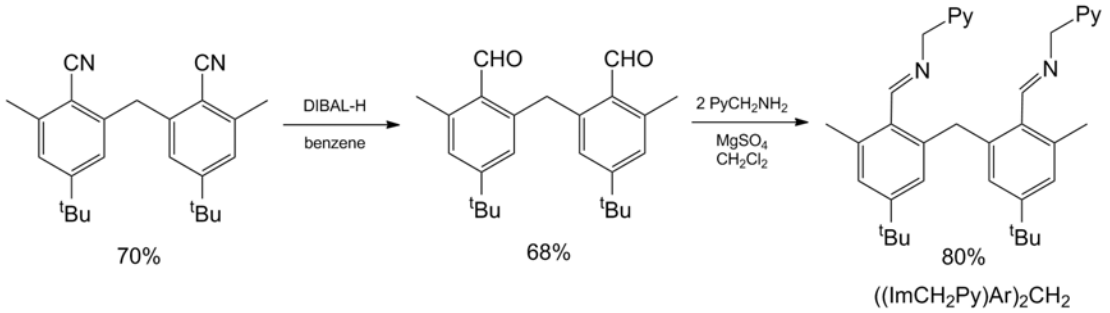

Scheme 4.4. Synthesis of $((ImCH_2Py)Ar)_2CH_2$.

Attempts to metallate this new ligand began with $Cr(N(TMS)_2)(thf)_2$. Treatment of this Cr(II) amide with one equivalent of the ligand in C_6D_6 resulted in a color change from lavender to deep red and the evolution of THF and HMDS in a 1:1 ratio. There were no observable paramagnetic products at any point in the reaction. After 1-2 days at room temperature significant amounts of dark crystals formed at the bottom of the NMR tube. A modest scale-up of this reaction in benzene allowed the isolation of a new complex as a dark red powder in 55% yield. This material was crystallized from THF at –40°C and a single crystal was selected for X-ray analysis. The structure is provided in Figures 4.16 and 4.17, selected parameters are presented in Table 4.3 and the crystallographic data are presented in Table 4.2.

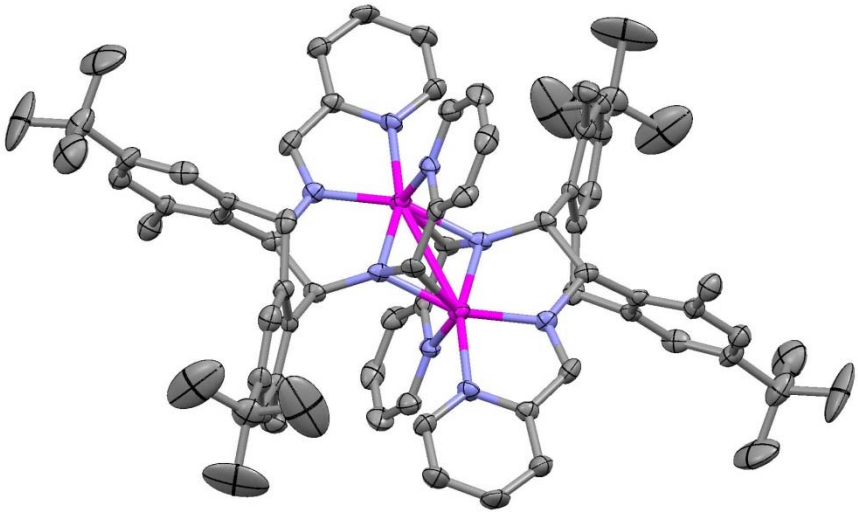

Figure 4.16. Molecular structure of **(12-Cr)$_2$**. Hydrogen atoms and two molecules of THF have been removed for clarity.

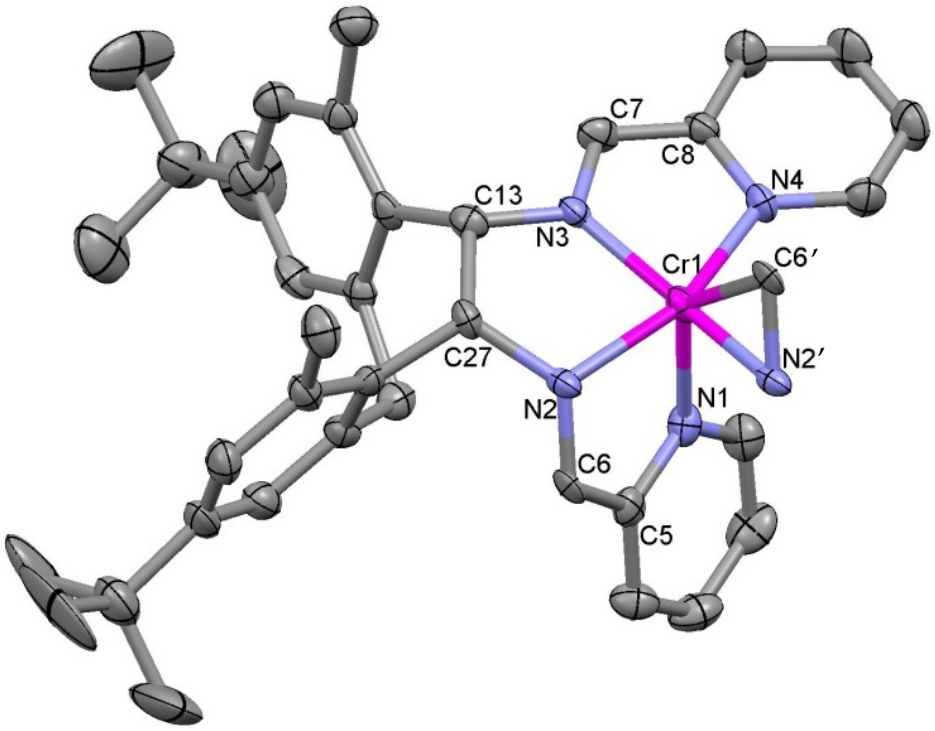

Figure 4.17. A rotated view of the coordination environment of **(12-Cr)$_2$**.

Table 4.2. Selected bond angles and interatomic distances for **(12-Cr)$_2$**.

Selected Bond Distances (Å)		Selected Bond Angles (degrees)	
Cr-Cr’	2.8977(12)	N1-Cr-N3	106.97(11)
N1-Cr	2.057(3)	N1-Cr-N2	82.48(11)
N2-Cr	2.012(3)	N1-Cr-N4	97.29(11)
N3-Cr	1.929(3)	N2-Cr-N4	159.74(12)
N4-Cr	2.017(3)	N1-Cr-N2’	91.72(11)
N2’-Cr	2.003(3)	N3-Cr-C6’	121.47(13)
C6’-Cr	2.090(4)	Cr-C6’-Cr’	70.79(11)
N1-C5	1.370(5)	Cr-N2’-Cr’	92.40(11)
C5-C6	1.442(5)	N2-Cr-C6’	100.14(12)
C6-N2	1.425(4)	N2-Cr-N2’	87.61(11)
N2-C27	1.511(4)		
C27-C13	1.572(5)		
C13-N3	1.482(4)		
N3-C7	1.341(5)		
C7-C8	1.395(5)		
C8-N4	1.383(5)		

Table 4.3. X-ray crystallographic data for **(^{PDI}MC)Fe** and **(12-Cr)$_2$**.

Crystal Data		
Formula	$C_{68}H_{88}FeN_6O$	$C_{90}H_{116}Cr_2N_8O_4$
Formula Weight	1061.29	1477.91
Crystal System	Triclinic	Triclinic
Space Group	P-1	P-1
Z	2	1
a, Å	10.3791(5)	9.9818(8)
b, Å	14.1947(6)	13.6414(11)
c, Å	22.0531(10)	15.5199(11)
α, deg	107.363(2)	81.202(4)
β, deg	97.088(2)	78.482(3)
γ, deg	96.290(2)	78.893(3)
Volume, Å^3	3040.3(2)	2017.5(3)
D (calc.), g/cm^3	1.159	1.216
Absorption coeff., mm^{-1}	0.295	0.325
F(000)	1144	792
Crystal Size, mm	0.20 x 0.15 x 0.05	0.20 x 0.15 x 0.10
Data Collection and Refinement		
Temp, K	173(2)	173(2)
Wavelength (λ), Å	0.71073	0.71073
θ limits, deg	1.96 to 23.31	1.53 to 21.97
Index Ranges	$-11 \le h \le 11$, $-15 \le k \le 15$, $-24 \le l \le 24$	$-18 \le h \le 18$, $-18 \le k \le 18$, $-22 \le l \le 22$
Reflections Collected	39612	19149
Absorption Correction	Semi-empirical from equivalents	Semi-empirical from equivalents
Max. and Min. Transmission	0.9854 and 0.9434	0.9682 and 0.9379
Refinement Method	Full-matrix least-squares on F^2	Full-matrix least-squares on F^2
Data/Restraints/Params.	8647 / 15 / 708	4899 / 30 / 488
Goodness-of-Fit on F^2	1.023	1.033
Final R Indices [$I>2\sigma(I)$]	R1 = 0.0568, wR2 = 0.1221	R1 = 0.0577, wR2 = 0.1247
R Indices (all data)	R1 = 0.0947, wR2 = 0.1373	R1 = 0.1055, wR2 = 0.1473
Largest Diffraction Peak and Hole (e^- Å^3)	0.530 and -0.351	0.398 and -0.315

The molecular structure of **(12-Cr)$_2$** is C_2-symmetric and best described as being composed of two trigonal-bipyramidal Cr centers bound by mutual η^1:η^2-imine interactions. The pseudoaxial atoms are N2 and N4, whereas N1, N3 and the η^2-imine are in pseudoequatorial positions. As is clear from the structure, the two imine carbons in the starting ligand have become reductively coupled and formal loss of two hydrogen atoms (Figure 4.18).

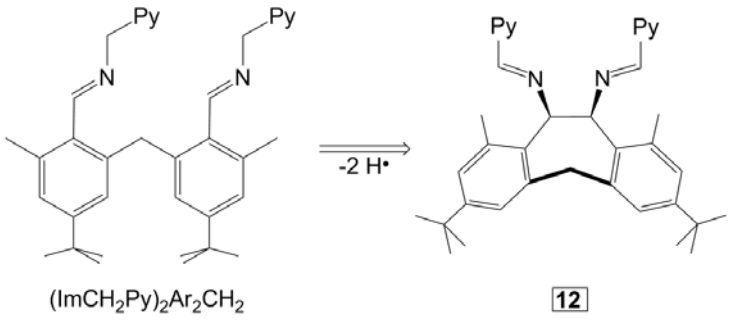

Figure 4.18. Illustration of the dehydrogenative coupling to form the ligand framework in **(12-Cr)$_2$**.

The bond length between N2 and C6 of the η^2-imine is exceptionally long (1.425(4) Å) and consistent with a single-bond formulation.[9c] The other bond length values within this imino-pyridine moiety (d(C5-N1) = 1.370(5) Å, d(C5-C6) = 1.442(5) Å) are in-between neutral and mono-reduced using the formalism described in Figure 4.6. These data are consistent with reduction being localized to the η^2-imine and suggests that a metallaziridine resonance structure is most reasonable. The second, non-shared imino-pyridine moiety has bond lengths consistent with mono-reduction. Based on these structural parameters, each Cr is best thought of as being in the +3 oxidation state. A solution magnetic moment of 3.8 μ_B is close to the 4.0 μ_B expected for two non-interacting *S*=1 centers. More elaborate magnetic measurements (SQUID) are needed to properly address the magnetism of this compound.

The reactivity of **(12-Cr)$_2$** was not extensively explored. Attempts to produce monomeric species via treatment with ethylene and CO did not produce isolable products, and diazoalkanes appeared to be unreactive. When treated with two equivalents of pyridine-N-oxide and heated for 24h (50 °C) only one equivalent of pyridine was produced, suggesting the formation of an oxo-bridged dimer that was unreactive to further oxidizing equivalents.

Treatment of $(ImCH_2Py)_2Ar_2CH_2$ with $Fe(N(TMS)_2)(thf)$ in C_6D_6 resulted in a color change from nearly colorless to green, followed by a darkening to red-brown over the course of two minutes. The ^{1}H NMR spectrum at this time showed the presence of THF and HMDS in a 1:1 ratio. Over the course of two days the ^{1}H NMR spectrum showed the presence of a diamagnetic material that was analyzed by multiple 2D NMR techniques. The observable NMR shifts and their assignments are shown in Figure 4.19.

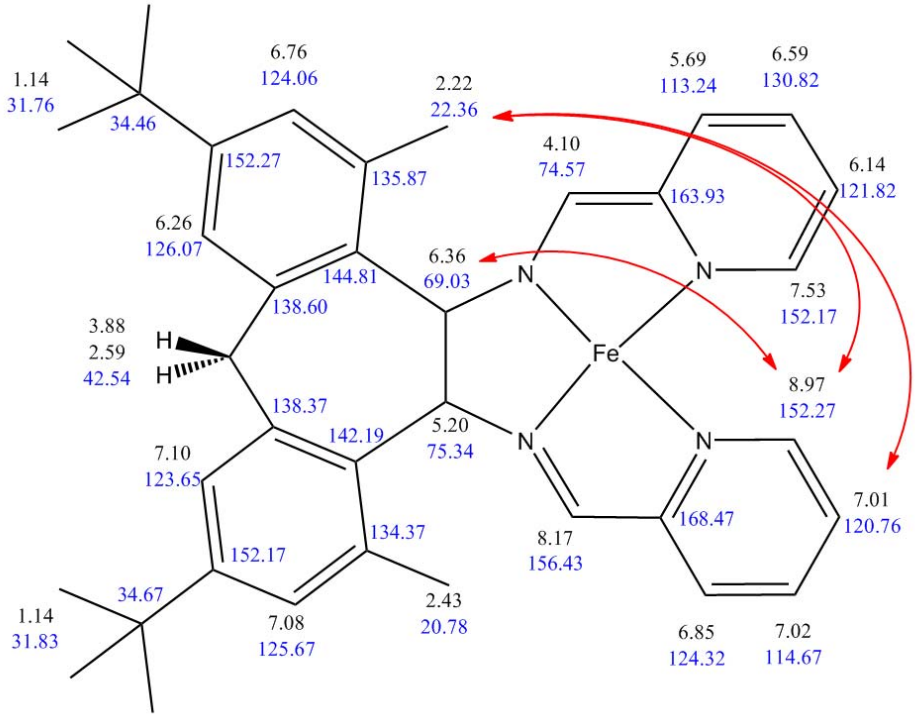

Figure 4.19. ^{1}H (black)/^{13}C (blue) NMR Spectral data for putative **(12-Fe)$_2$**. NOESY correlations are shown in red.

The $^{1}H/^{13}C$ HSQCAD experiment correlated the observable protons with their respective carbons, whereas the gCOSY experiment allowed correlation of adjacent protons. The crucial COSY interaction proved to be between the protons at 6.36 ppm and 5.20 ppm, indicating connectivity of the two benzylic carbons of the nascent dibenzocycloheptane ring and *cis* stereochemistry of the methine protons. Again, the deprotonation of $(ImCH_2Py)_2Ar_2CH_2$ ultimately led to coupling of the two imine carbons and reduction to a formally zero-valent metal. The chemical shifts of the two imino-pyridine moieties are in stark contrast; one possess 'normal' chemical shifts (i.e., in close agreement with non-complexed imino-pyridines), whereas the other has shifts significantly upfield. The chemical shifts for reduced imino-pyridine fragments in nominally diamagnetic complexes are normally outside the usual range for aromatic protons. The ligand reduction in **(12-Fe)$_2$** is distinct from that in **(12-Cr)$_2$**; the structural data for the dichromium species indicated localized reduction of the η^2-imine to a metallaziridine, whereas the reduction is delocalized into the pyridine ring in the diiron complex. Accordingly, Figure 4.20 is drawn to reflect a doubly-reduced imino-pyridine fragment.

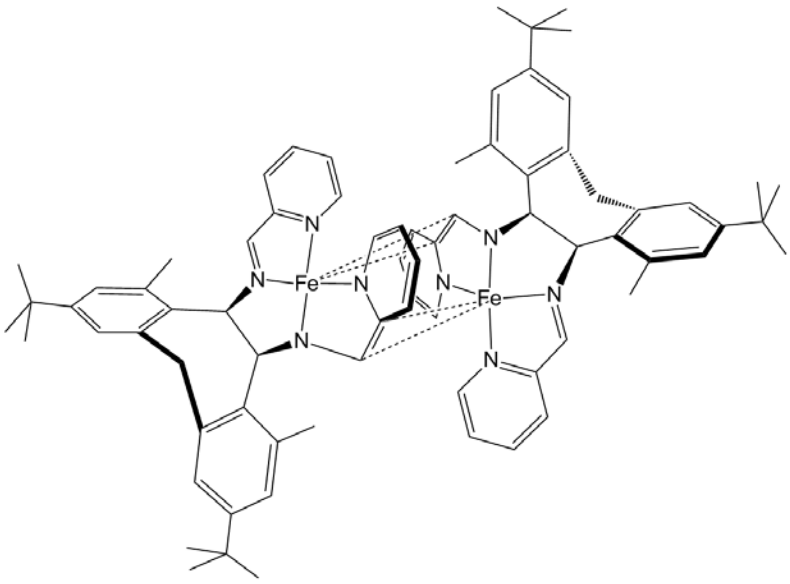

Figure 4.20. Proposed structure of **(12-Fe)$_2$**. The NOESY interactions are indicated.

The NOESY crosspeaks from the methyl and methine protons of the cycloheptane ring to the *ortho* and *meta* protons of the non-reduced pyridine ring are only feasible in a dimer similar to **(12-Cr)$_2$**. A schematic of this interaction is shown in Figure 4.18. Working on the assumption that the ligands do not contain unpaired electrons, the diamagnetism of **(12-Fe)$_2$** implies that the Fe atoms are either low spin or intermediate- to high-spin with some degree of Fe-Fe bonding. Crystals of **(12-Fe)$_2$** eluded isolation and thus the molecular structure could not be determined, so a computational analysis was not attempted.

The reductive coupling of the two imine carbons in both the Cr and Fe cases resulted in *cis*-stereochemistry with respect to the imino-pyridines on the cycloheptane ring. There are several possible mechanisms for this coupling, two of which are shown in Figure 4.21.

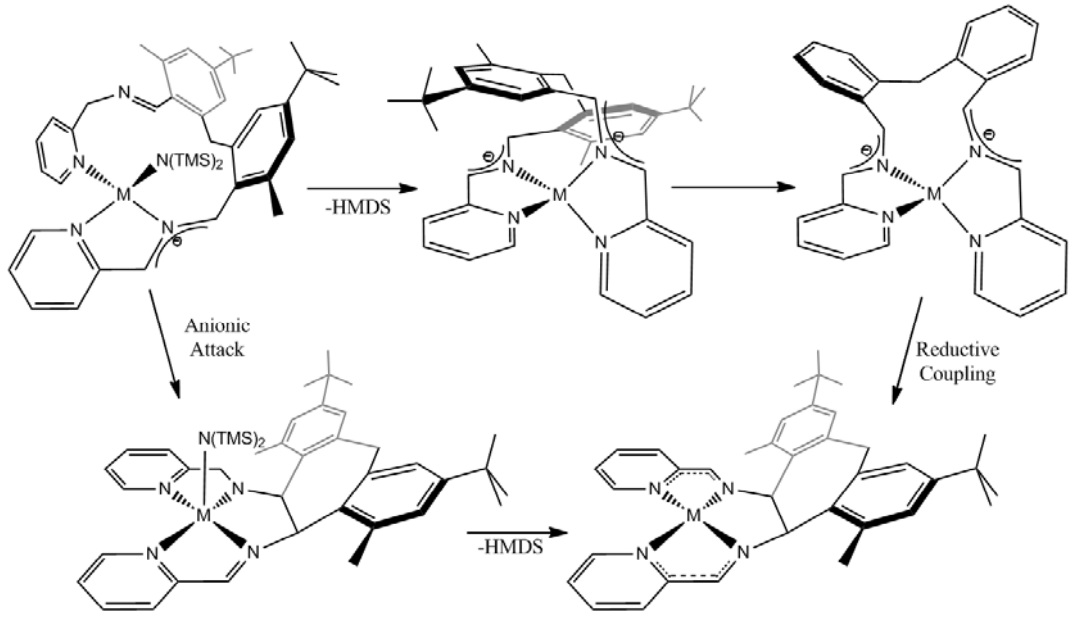

Figure 4.21. Two proposed mechanisms for the production of **(12-M)$_2$** (M = Cr, Fe).

Starting from a monodeprotonated complex, it seems reasonable to assume a *syn*-disposition about the 2-aza-allyl anion. Assuming coordination of the other half of the

ligand prior to coupling, the starting complex is shown as coordinating the remaining pyridine although it seems equally plausible the imine-arm may coordinate. Following the top of Figure 4.21, a second deprotonation to give a bis(*syn*-aza-allyl) complex could follow. The reductive coupling of two *syn* aza-allyl anions should result in *trans*-orientation in the nascent cycloheptane ring, so either one or both of the aza-allyl anions must isomerize to the *anti* isomer to yield a *cis* orientation. The reductive coupling would yield a pseudo-square-planar complex with reduced imino-pyridine ligands. Following the lower pathway in Figure 4.21, it may not be necessary to generate a second aza-allyl anion. The first anion might nucleophilically attack the remaining imine to generate a bis(amido) metal complex. A second deprotonation would yield a doubly-reduced imino-pyridine fragment. Electronic reorganization to two mono-reduced iminopyridines might then occur, and then dimerization to the observed product would follow.

Although a setback in terms of generating aza-allyl species, this was an intriguing result in the context of generating organic frameworks. Upon hydrolysis, this ring closure could represent a way of forming *cis* cyclic diamines. Alternatively, if this C-C coupling was found to be reversible, it could represent a way of storing energy in the form of chemical bonds and an opportunity to explore redox-mediated C-C bond formation.[36] As such, work was continued with the simpler 2,2-dimethylpropane-based ligands.

4.3. Synthesis and Metallation of $Me_2C(CH_2ImPy)_2$

The simpler of the two isomeric ligands designed to enforce a square-planar arrangement of aza-allyl moieties, $Me_2C(CH_2ImPy)_2$ (NpImPy) was prepared by a straightforward condensation of commercially-available pyridine-2-carboxaldehyde and 1,3-diamino-2,2-dimethylpropane as shown in Eq. 4.4.

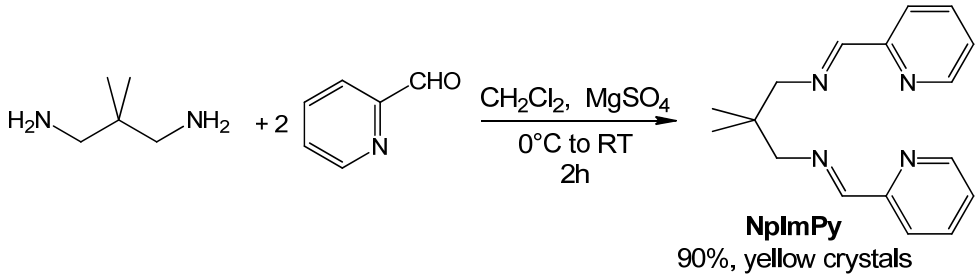

Eq. 4.4

Initial efforts started by attempting metallation with precursors that had been successful in smif and bis(iminoaryl)methane ligand installations.

Reactivity with $Cr(N(TMS)_2)_2(thf)_2$

Treatment of NpImPy with one equivalent of $Cr(N(TMS)_2)_2(thf)_2$ in C_6D_6 resulted in an immediate color change from light lavender to blue-purple. The ^1H NMR spectrum immediately after mixing was consistent with simple adduct formation – large paramagnetic peaks at 38 ppm ($\nu_{1/2}$ ~ 2000 Hz), 31 ppm ($\nu_{1/2}$ ~ 1300 Hz) and 0.2 ppm ($\nu_{1/2}$ ~ 200 Hz) and a small amount of free HMDS. There were no resonances consistent with free NpImPy nor free THF, suggesting a coordination complex of formulation $Cr(N(TMS)_2)_2(\kappa^2\text{-NpImPy})(THF)_n$, where *n* is 1 or 2 (Eq. 4.5). As the reaction was monitored by NMR spectroscopy at room temperature over the course of fifteen minutes, the broad resonance at 0.2 ppm began to decrease at the expense of a sharp singlet at 0.11 ppm that was consistent with HMDS. Over the course of 48 h the HMDS production appeared to have stalled, and the peak at 38 ppm had disappeared with little additional change in the spectrum. During this time the tube had changed from purple to intensely yellow. Gently heating the tube for 3.5 h at 45 °C had no observable effect, though further heating at 60 °C for 4 h resulted in total elimination of the broad peak at 0.2 ppm and production of a new resonance at 0.67 ppm ($\nu_{1/2}$ ~ 140 Hz). Further heating at 60 °C for 15.5 h resulted in the apparent shift of the 0.67 ppm resonance to 1.23 ppm ($\nu_{1/2}$ ~ 50 Hz) and the appearance of another resonance at 4.97 ppm ($\nu_{1/2}$ ~ 1200 Hz). There was little change in any other part of the spectrum,

yet the tube had changed color to green by this point. The addition of 1.3 eq. of PMe_3 resulted in a new resonance at –2.78 ppm, the apparent shift of the 1.23 ppm resonance to 1.41 ppm, and a related change of the 4.97 ppm resonance to 3.83 ppm (see Fig. 4.22).

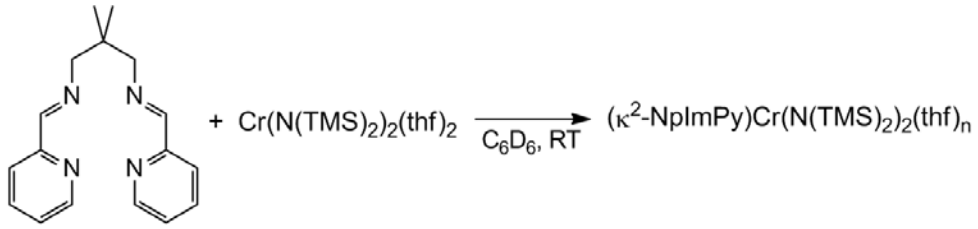

Eq. 4.5

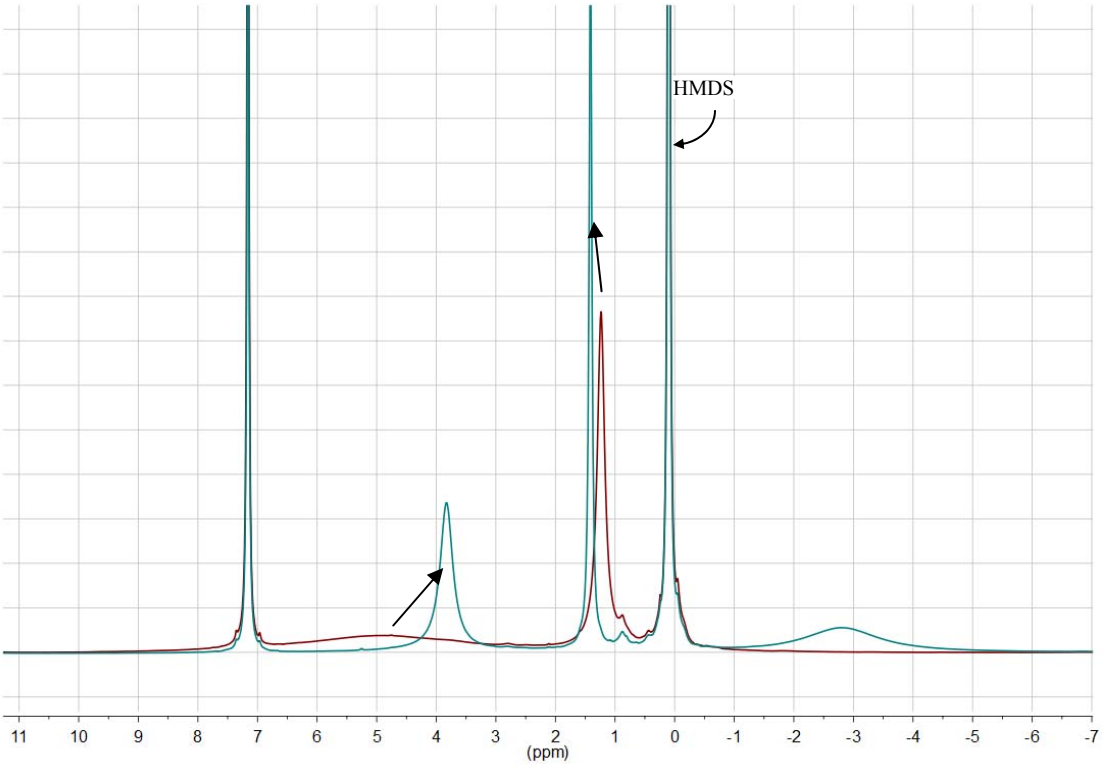

Figure 4.22. ^{1}H NMR Spectrum of the reaction between NpImPy and $Cr(N(TMS)_2)_2(thf)_2$ in C_6D_6 after 20h of heating at 60 °C before (maroon trace) and after (blue trace) the addition of 1.3 eq. PMe_3.

From the above considerations it seemed plausible that the initial purple color was due to a simple coordination complex that, over the course of several days (with gentle heating), slowly eliminated at most one equivalent of HMDS. Whatever the form of

the deprotonated ligand, the complex formed must still have either retained its THF ligands or been in exchange with free THF at sufficient rate to render it unobservable spectroscopically. As the tube was heated further, more shifts appeared that were eventually identified as consistent with THF, suggesting an isomerization and release of bound THF. During these processes the other observable paramagnetic resonances failed to change significantly in intensity and suggested the presence of a complex mixture.

Reactivity with $Fe(N(TMS)_2)_2(thf)$

Treatment of **NpImPy** with one equivalent of $Fe(N(TMS)_2)_2(thf)$ in C_6D_6 resulted in an immediate color change from very pale green to yellow-green. The ^1H NMR spectrum obtained immediately after mixing suggested simple adduct formation (cf. Eq. 4.5). Free THF was immediately visible ($\nu_{1/2}$ ~13 Hz), although it could not be integrated reliably to determine the relative amount. Over a period of 12 h, the tube darkened to forest green and a spectrum revealed some HMDS and the disappearance of free THF. Several new paramagnetic peaks had appeared between 50 ppm and 250 ppm that did not mutually integrate. Heating the tube for a period of 3.5 h at 45 °C and then 15.5 h at 60 °C had little observable effect on the spectrum though the solution had darkened to black. Little useful information could be gleaned from these data.

Further attempts at producing isolable deprotonated complexes with $ZnEt_2$ and LiHMDS in C_6D_6 produced magenta solutions that were both hopelessly complicated mixtures with broad, nearly featureless peaks between 9-6 ppm and 5-0 ppm.

Reactivity with $Ni(COD)_2$

Since deprotonation routes to aza-allyl complexes using NpImPy appeared to be elusive, a different approach was taken. In terms of successfully making a stable M(II) square-planar complex, nickel has the greatest precedent. Aside from alkyl and aryl complexes that would be prone to reductive elimination, there are few nickel

complexes with internal bases to use as starting materials. $Ni(COD)_2$ was chosen due to the potential for CH-oxidative-addition and H-transfer to the COD ligands. Treatment of $Ni(COD)_2$ with NpImPy in C_6D_6 immediately resulted in a color change from colorless to forest green. The ^1H NMR spectrum revealed a single compound whose spectrum was consistent with a single Ni-atom coordinated by one NpImPy ligand and two equivalents of free COD (Eq. 4.6).

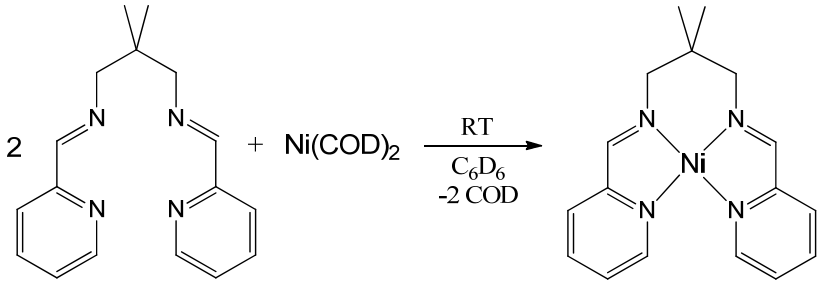

Eq. 4.6

The proton *ortho* to the pyridine nitrogen was shifted significantly downfield (9.29 ppm) relative to the free ligand (8.48 ppm) and the imine CH-proton was shifted significantly upfield (7.67 ppm) relative to the free ligand (8.59 ppm). Aside from those irregularities, the NMR spectrum indicated a new compound with seven resonances that must have mirror-symmetry.

As a formally d^{10} complex with 18 electrons, there should be no ligand-field stabilization energy and a tetrahedral geometry should be preferred. The ligand itself cannot support a tetrahedral metal atom in a mononuclear complex. It was therefore possible that the complex existed as an L_2Ni_2 dimer that could attain pseudo-tetrahedral geometry and contain sufficient symmetry or dynamic behavior to give only seven ^1H NMR resonances. The compound was crystallized from a saturated pentane solution at –40 °C and a crystal amenable to x-ray crystallographic study was selected. The structure is provided in Figure 4.23, selected parameters are presented in Table 4.4 and the crystallographic data are presented in Table 4.8. The structure of monomeric (NpImPy)Ni is distorted square-planar, with the ligating nitrogen atoms

displaced an average of 16.7° above (N1, N3) and below (N2, N4) the square plane. The average of the imine C-N bond lengths is 1.323(3) Å and the average of the C_{py}-C_{im} bond lengths is 1.411(3) Å; both are consistent with the molecule possessing two monoreduced imino-pyridine moieties. The Ni-N_{im} and Ni-N_{py} bond distances are consistent with a low-spin Ni(II) complex.[18]

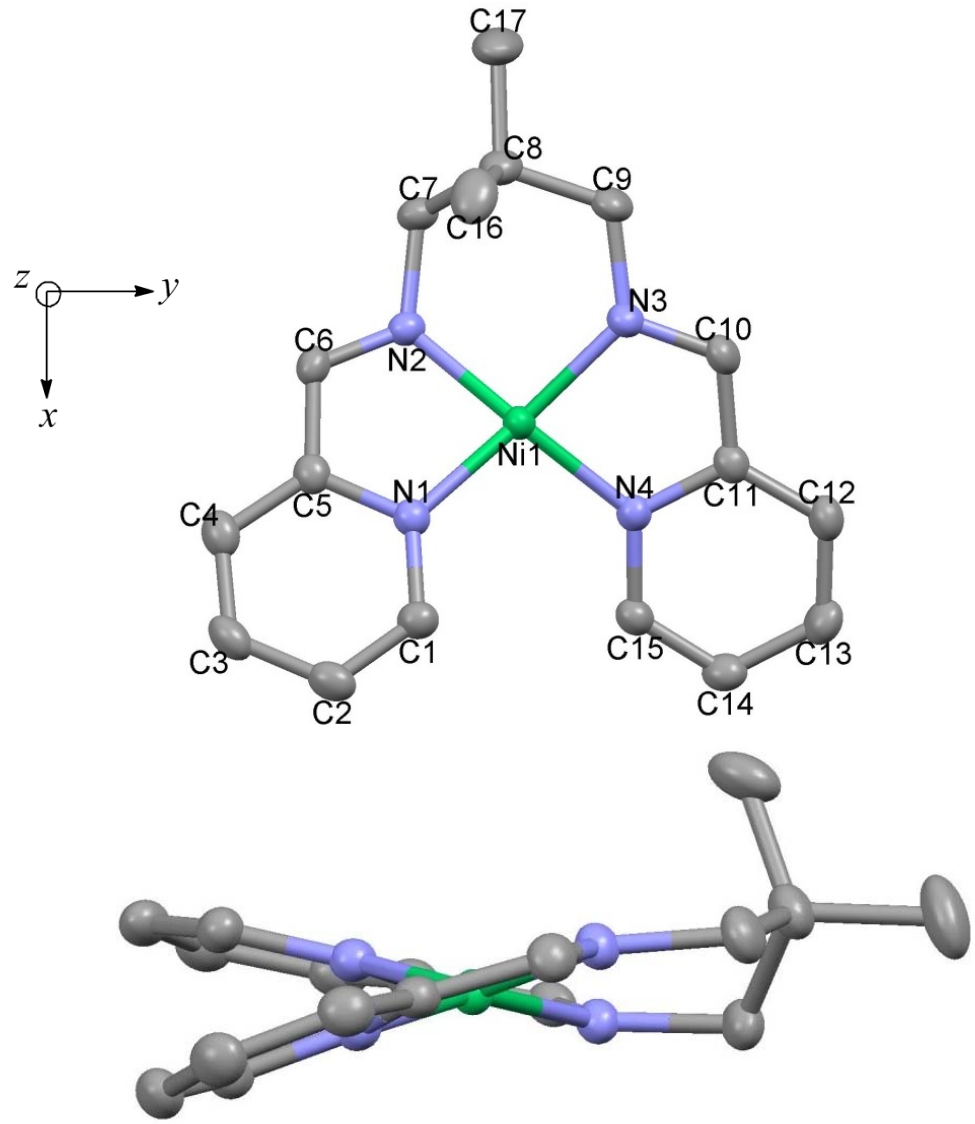

Figure 4.23. Solid-state structure of (NpImPy)Ni as viewed above the square plane (top) and from the side along the square plane (bottom). Hydrogen atoms have been removed for clarity.

Table 4.4. Selected bond angles and interatomic distances for **(NpImPy)Ni**. Distances in bold refer to computed values.

Selected Bond Distances (Å)			Selected Bond Angles (degrees)	
Ni-N1	1.9091(12)	**1.951**	N1-Ni-N2	79.68(5)
Ni-N2	1.8670(12)	**1.909**	N2-Ni-N3	94.67(5)
Ni-N3	1.8754(12)	**1.901**	N3-Ni-N4	79.68(5)
Ni-N4	1.9038(12)	**1.957**	N4-Ni-N1	104.55(5)
N1-C5	1.3780(18)	**1.389**	N1-Ni-N3	104.41(5)
C5-C6	1.411(2)	**1.410**	N2-Ni-N4	89.71(5)
C6-N2	1.3186(18)	**1.332**	N1-N2-N3-N4	33.59(10)
N3-C10	1.3269(19)	**1.328**	(dihedral)	
C10-C11	1.410(2)	**1.412**		
C11-N4	1.3827(18)	**1.390**		

Electronic Structure of (NpImPy)Ni

As one of the simplest bis(imino-pyridine) complexes synthesized, relatively high-level Broken Symmetry calculations on the untruncated molecule were performed with ease. The computed ligand field, structural parameters and frontier magnetic orbitals are presented in Figure 4.24.

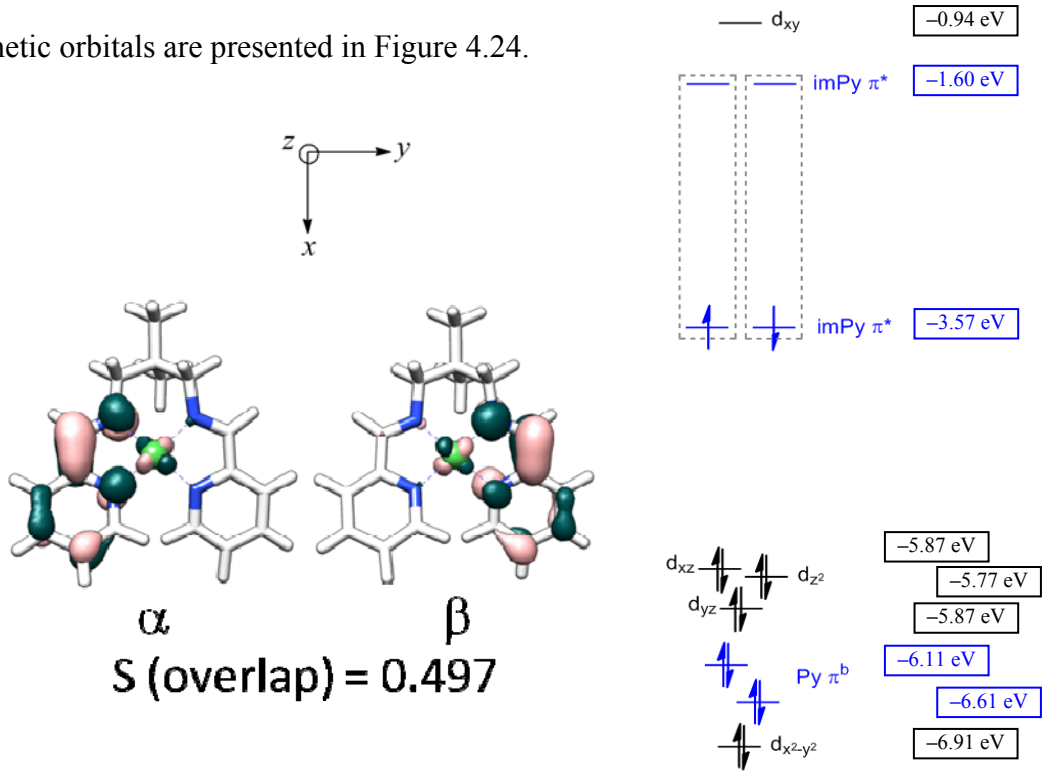

Figure 4.24. Calculated electronic structure of **(NpImPy)Ni**. The empty, high-lying orbitals in the dashed boxes represent energies of electrons of opposite spin in the same spatial distribution as their filled, low-lying parner.

The calculated structure of (NpImPy)Ni agrees relatively well with the X-ray data. Geometry optimizations using B3LYP, although superior at modeling the electronic structure of systems with Broken Symmetry solutions, are known to overestimate metal-ligand bond lengths.[19] The metal orbitals are split into the familiar pattern for square-planar d^8 species. The high-lying SOMOs are composed of two electrons, one localized in each imino-pyridine fragment, that are antiferromagnetically (AFM) coupled to each other. Since there is only one pair of weakly-coupled electrons in this system and there is very little spin density on Ni, the two BS SOMOs are nearly identical to the magnetic orbitals. The AFM coupling constant[20] determined by the Broken-Symmetry [1,1] calculation is –1499 cm^{-1}. This system represents an interesting contrast to Weighardt's analogous pseudotetrahedral Ni complex[9a] shown in Figure 4.25.

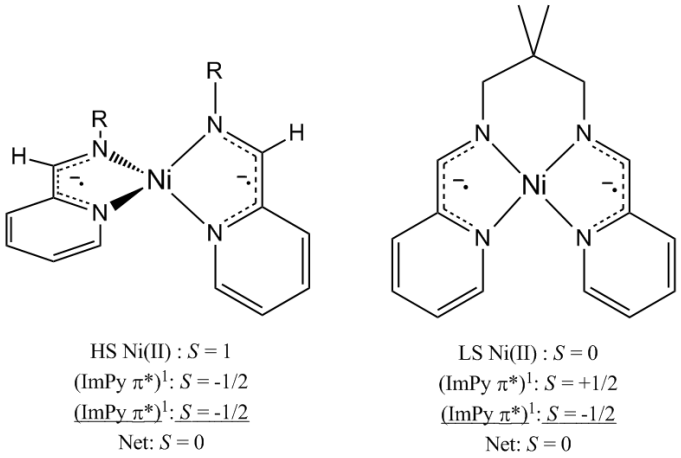

Figure 4.25. Comparison of **(NpImPy)Ni** with $(RImPy)_2Ni$. (R = 2,6-diisopropylphenyl)

The average Ni-N_{im} bond distance is 1.912 Å and the average Ni-N_{py} bond distance is 1.941 Å in the pseudotetrahedral complex. Both of these are considerably shorter in **(NpImPy)Ni**, consistent with the expected diminished σ*-character of a low spin complex.

In the hope of eventually generating an aza-allyl complex, the compound was treated with AgOTf in CH_3CN to yield an orange compound consistent with a monooxidized species (Eq. 4.7).

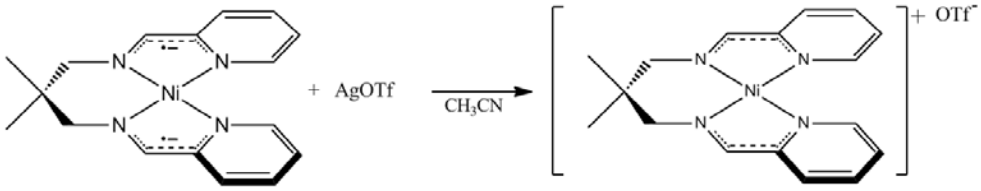

Eq. 4.7

The ^1H NMR spectrum of the cation in CD_3CN was consistent with a C_1-symmetric species and suggested the presence of coordinated solvent. Elemental analysis of crystalline material after trituration with THF was consistent with the unsolvated cation. The effective magnetic moment of 2.1 μ_B obtained by Evans' method (CD_3CN) is consistent with an $S = ½$ compound. Attempts to deprotonate the monocation with LiHMDS or Li(^{neo}pentyl) resulted merely in reduction to the starting material.

Cyclic voltammetric studies were performed in order to better understand the redox properties of **(NpImPy)Ni**. The voltammograms conducted in THF with a scan rate of 50 mV s^{-1} are presented in Figures 4.26 and 4.27.

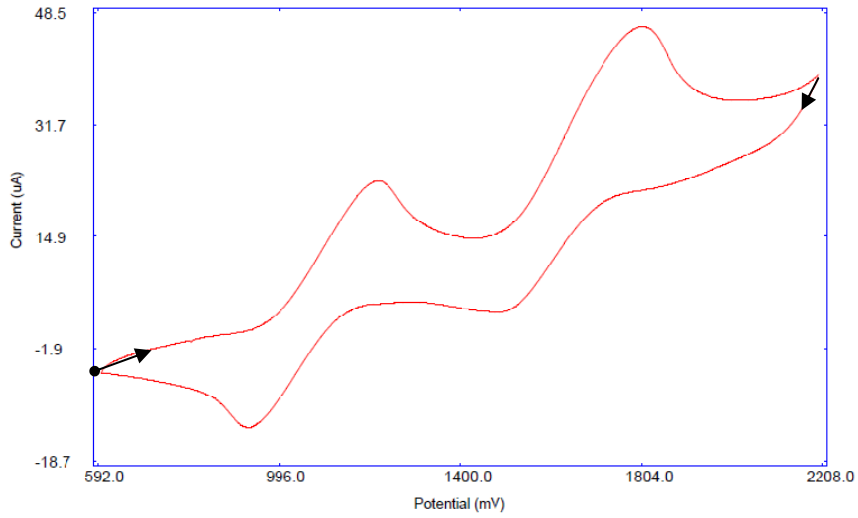

Figure 4.26. Reductive cyclic voltammogram of **(NpImPy)Ni** in THF at 50 mV s^{-1}. (Ref. Ag/Ag^+)

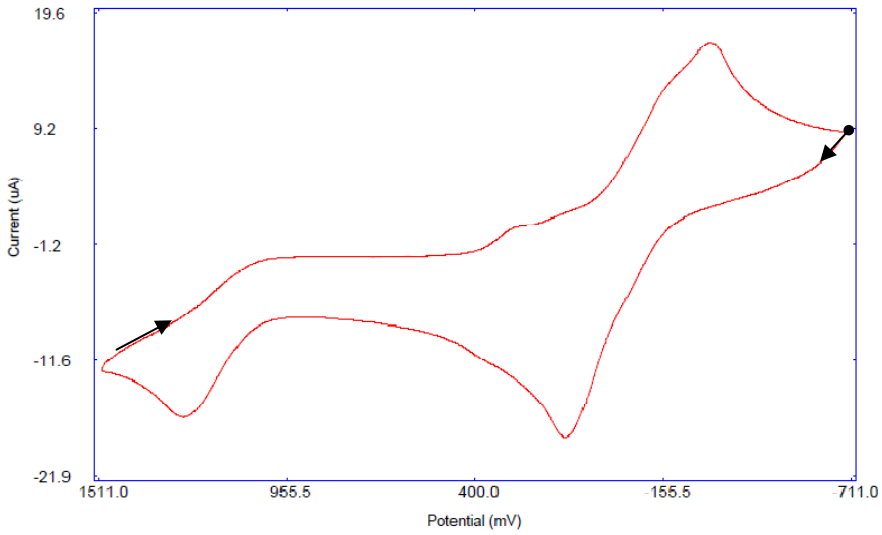

Figure 4.27. Oxidative cyclic voltammogram of **(NpImPy)Ni** in THF at 50 mV s^{-1}. (Ref. Ag/Ag^{+})

On the reductive scan there are two observable redox waves; a chemically reversible wave at –1.07 V (peak separation 291 mV) and a chemically irreversible redox wave at –1.65 V. The wave at –1.07 V is tentatively assigned as the $E^{+/0}$ redox event; the event at higher reducing potential would then be consistent with the $E^{0/-}$ couple. In the oxidative direction there is a redox wave centered around –0.08V that is tentatively assigned as the $E^{+/2+}$ couple.

4.4. Synthesis of $Me_2C(ImCH_2Py)_2$ and Reactivity with $Cr(N(TMS)_2)_2(thf)_2$

An isomer of **NpImPy**, **$Me_2C(ImCH_2Py)_2$** was synthesized by means of condensation of two equivalents of aminomethylpyridine with dimethylmalonaldehyde in ether as shown in Eq. 4.8.

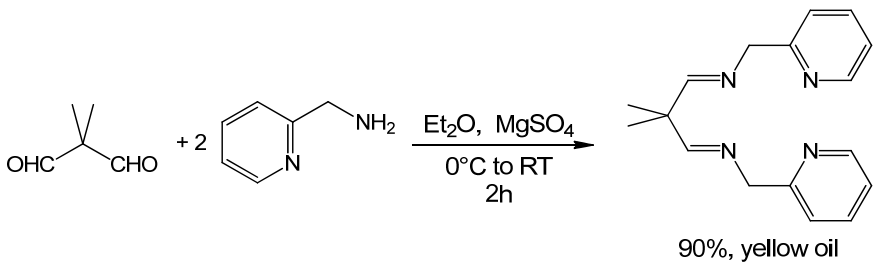

Eq. 4.8

In the first of a series of reactions attempting to install the ligand with an intact aza-allyl moiety, one equivalent of $Cr(N(SiMe_3)_2)_2(thf)_2$ was treated with **$Me_2C(ImCH_2Py)_2$** in d_6-benzene solution at room temperature. An immediate color change from lavender to red was observed, followed by a darkening to brown over the course of an hour. After 24h at room temperature red/brown crystalline blocks had formed in the bottom of the NMR tube, at which point the only significant signals in the ^1H NMR spectrum were identified as the expected HMDS and THF. The molar ratio of HMDS to THF (1:1) was consistent with complete consumption of the chromium starting material, assuming total dissociation of THF. A scaled-up reaction in C_6H_6 yielded 66% of a chromium complex as red/brown crystals amenable to X-ray crystallography, the structure of which is shown in Figure 4.28. Relevant distances and angles are presented in Table 4.5 and the crystallographic data are presented in Table 4.8. It was revealed that the eventual product of the reaction was a triply-CC-coupled dimer of the complex originally sought.

Table 4.5. Selected bond angles and interatomic distances for **14-Cr_2**. Distances and angles marked with an asterisk (*) represent averaged values from statistically equivalent parts of the molecule.

Selected Bond Distances (Å)		Selected Bond Angles (degrees)	
Cr-Cr'	2.5515(3)	N1-Cr-N2	79.68(7)*
Cr-N1	2.1065(17)*	N2-Cr-N3	94.67(7)*
Cr-N2	1.9323(17)*	N3-Cr-N4	79.68(7)*
Cr-N3	1.9454(17)*	N4-Cr-N1	104.55(7)*
Cr-N4	2.0362(17)*	N1-Cr-Cr'	104.41(3)
N2-C2	1.4442(24)*	N2-Cr-Cr'	89.71(3)
N3-C5	1.3393(25)*	N3-Cr-Cr'	84.94(3)
C5-C6	1.387(3)*	N4-Cr-Cr'	96.78(3)
C1-N1	1.347(3)*	N1'-Cr'-Cr	104.99(3)
C6-N4	1.3998(25)*	N2'-Cr'-Cr	90.96(3)
C2-C4'	1.5690(24)*	N3'-Cr'-Cr	86.46(3)
C3-C3'	1.5576(17)	N4'-Cr'-Cr	95.48(3)

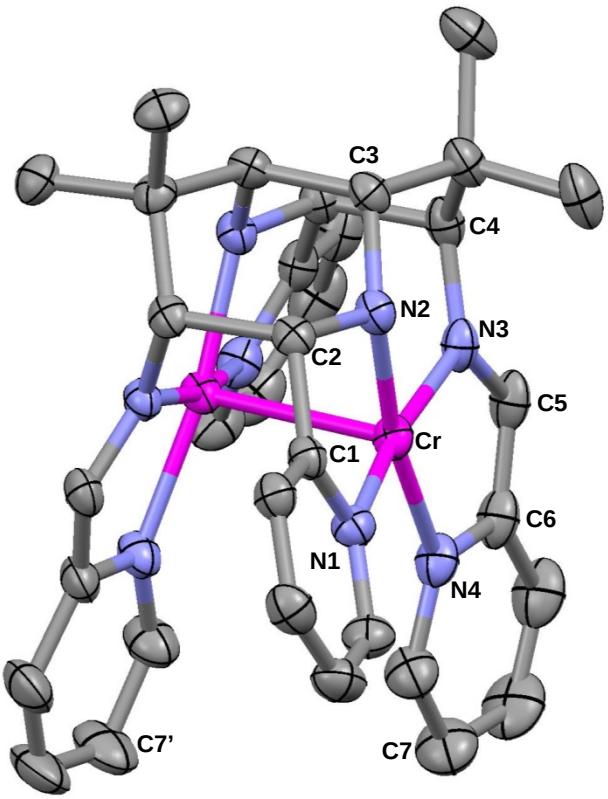

Figure 4.28. Molecular Structure of (**14-Cr$_2$**). Thermal ellipsoids are at 50% probability level and the occluded benzene molecules and hydrogen atoms have been omitted for clarity.

The molecule possesses slightly distorted C_2 symmetry with asymmetries likely imposed by packing forces. As a result, almost all of the metrical parameters of the dimer halves are statistically identical, with the periphery of the pyridine rings deviating (>3σ) the most from ideality.

The structure of **14-Cr$_2$** contains many subtle features that point to its unique electronic structure. Of critical importance to the interpretation of this and related compounds are the bond distances in the nascent imino-pyridine (ImPy) unit. The long imine C-N distance (1.3393(25) Å) and short C_{imine}-C_{py} distance (1.387(3) Å) are consistent with single-electron occupation of the ImPy π* orbital, as previously

discussed. Each chromium has such an interaction, as well as an anionic amide ligand (N2), giving a formal oxidation state of Cr^{+2}. Additionally the amido nitrogen (N2) is slightly pyramidalized ($\Sigma\{angles\} = 348.28°$), likely due to ligand constraints, suggesting incomplete N→Cr π-donation and a stronger Cr-Cr interaction. Electron counting would then give each chromium 13 e^-, suggesting a net quadruple bond was possible.Unfortunately the exact bond order is difficult to establish on structure alone, principally due to significant electron correlation problems and additional structural details discussed below.

The Cr-Cr distance of 2.5515(3) Å is on the long side of the quadruple bond range previously observed in paddlewheel Cr(II) dimers (2.18 Å – 2.61 Å).[21] Each chromium atom is constrained to a distorted square-planar ligand environment by the bite-angle of the two Py–C–C–N chelates (79-80°). Each Cr atom sits an average of 0.16 Å above the plane containing the four bound nitrogen atoms, with both metals drawn towards each other. The extensively-studied carboxylate-,[21,22] amidinate-,[23] and guanidinate-bridged[24] dimers are more rigorously square planar (displacements above the plane < 0.05A), primarily because the span of the bridge is closely matched to the distance for optimal δ-bond overlap. The steric demands of the two coupled **$Me_2C(ImCH_2Py)_2$** moieties are sufficiently different from many such Cr-dimers that they are unsuitable for comparison. Gambarotta and co-workers[25] reported the synthesis of a Cr-Cr dimer in 1989 that is similar in coordination environment to **14-Cr_2** utilizing the NacNac-derived macrocyclic ligand *tmtaa*, the structure of which is shown in Figure 4.29.

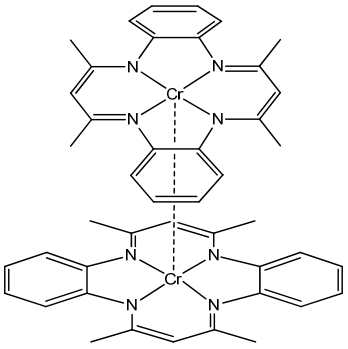

Figure 4.29. Skeletal drawing of $\{(tmtaa)Cr\}_2$ illustrating the 90° twist of the two complexes.

The alternating 2- and 3-carbon spacers between the ligating nitrogens is analogous to the coordination environment in **14-Cr$_2$**; concomitantly the average N-Cr-N bond angles (80.1(2)°, 92.9(2))° and average Cr-N bond lengths (1.999(8) Å) compare well with **14-Cr$_2$**. The Cr-Cr interaction in $\{(tmtaa)Cr\}_2$ is far more significant, as its Cr-Cr bond length of 2.096(1) Å is consistent with a quadruple bond. The authors caution against this classification, due to, "residual paramagnetism … that cannot be traced to chromic impurities," and preliminary HF-SCF calculations that suggest there is very little δ-overlap. Given the similarity in coordination environments, the stronger interaction in $\{(tmtaa)Cr\}_2$ is likely due to the vastly different structural features of **14-Cr$_2$**. In $\{(tmtaa)Cr\}_2$, the two Cr atoms can approach each other directly along a bond axis perpendicular to their square planes, but this is not the case for **14-Cr$_2$**, as shown below.

If we consider two square planar environments approaching one another, there are three important angles we can use to characterize the interactions between the metal centers. The δ-bond overlaps are the most sensitive to geometry, and for such interactions the first structural parameter to consider is the torsion angle. In dimers of

square planar systems the torsion angle between the square planes can be said to be between 0° (eclipsed) and 45° (staggered). In *distorted* square planar systems the loss of a 4-fold rotation axis of symmetry means that a 90° torsion angle is distinct from 0°. We can define a torsion angle (ω) in this system according to the diagram shown in Figure 4.30, where a C_2-symmetric molecule would have its torsion angle ω equal to its N1–M–M'–N4' dihedral angle.

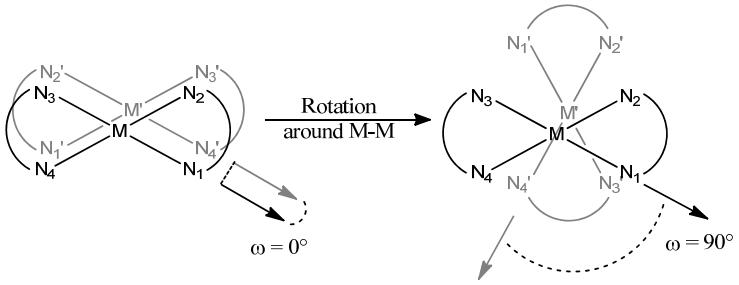

Figure 4.30. Definition of the torsion angle ω.

The average relative torsion angle (N_{py}–Cr–Cr'–N_{py}', Fig. 4.31) of the two pseudo-square planes of the two Cr atoms is 52.37(6)°. Using only the torsion angle as a guide, the overlap of the δ-bond components should 25.4% of the fully eclipsed value,[21] however additional structural features discussed below make this estimate an upper limit. This twist would be expected have no effect on the σ- or π-interactions since they are composed of approximately cylindrically-symmetric sets of orbitals, assuming this system was rigorously C_4-symmetric about the Cr–Cr axis. The distortion away from cylindrical symmetry should result in non-degenerate π-bonds, and additional distortions plus the interaction of the π*-orbitals of the imino-pyridine moiety complicates any qualitative bonding analysis (see **Electronic Structure of 14-Cr_2**).

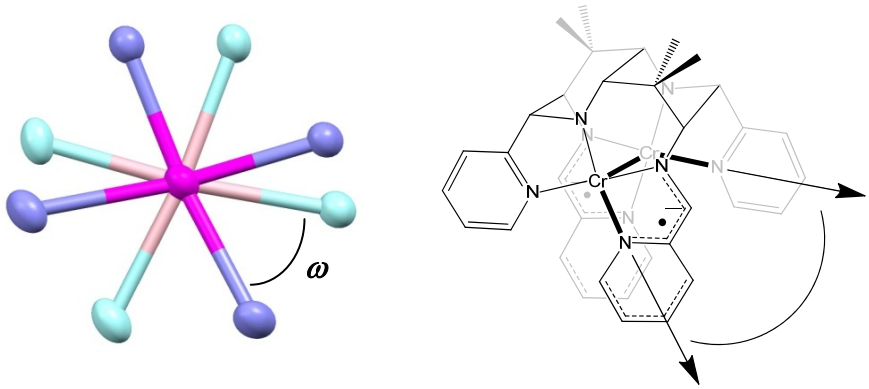

Figure 4.31. View along the Cr-Cr bond (left), with dark colors representing the front and light colors representing the back, and a skeletal drawing (right) indicating the relevant torsion angle

The second angle considered in this structure is the angle of approach of the two pseudo-square-planes (ϕ). The two extremes to consider are when the two planes are exactly face-to-face ($\phi = 0°$) and orthogonal ($\phi = 90°$). In **14-Cr$_2$,** the two square planes are inclined with respect to each other at an angle of 13.83(9)°, as shown in Figure 4.32.

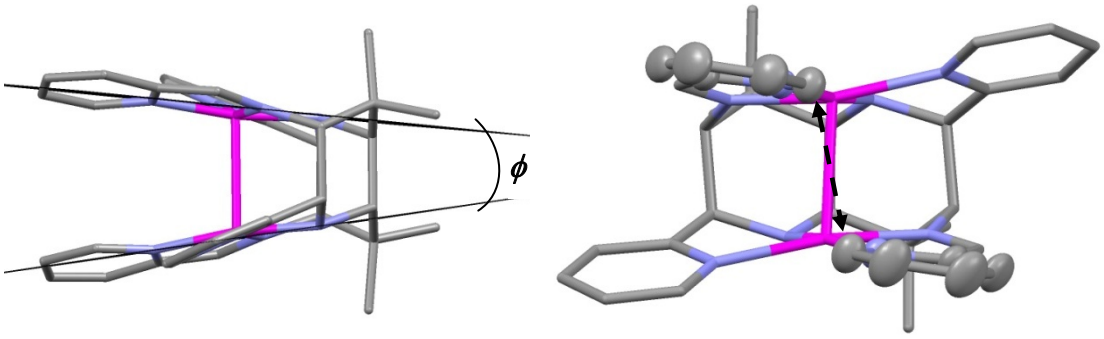

Figure 4.32. Views of **2-Cr$_2$** illustrating the approach angle ϕ (right) and the C7-C7' proximity (left).

As a consequence of this angle of approach, the N4–Cr–Cr' and N1–Cr–Cr' angles are 10-20° larger than the N2–Cr–Cr' or N3–Cr–Cr' angles. This inclination could simply be a result of the constraints of the *cis*-1,5-diazadecalin ligand framework. The twist engineered by the ligand backbone forces the ImPy π-system to face the π-system of

the pyridine directly bound to the diazadecalin framework. Such repulsion is offset only by the tethering of the backbone, resulting in the observed approach angle. However, the two pyridine rings of the ImPy units are in relatively close contact at the C7 and C7' positions (Figures 4.1, 4.5), and at 3.128(6) Å the contact is within the sum of their Van der Waals radii (3.40 Å).[26]

The third structural parameter to consider is the offset angle α of the two square planes. In this system it is the most subtle structural feature, but it is relevant in assessing the relative competition between the formation of a strong M-M bond at the expense of distorting the ligand backbone. Despite the large number of atoms in the decalin framework that might otherwise allow significant distortion, the three C-C bonds and *cis*-stereochemistry about the bridgehead make the backbone quite rigid. The definition of the offset angle of the two ligand planes is illustrated below in Figure 4.33.

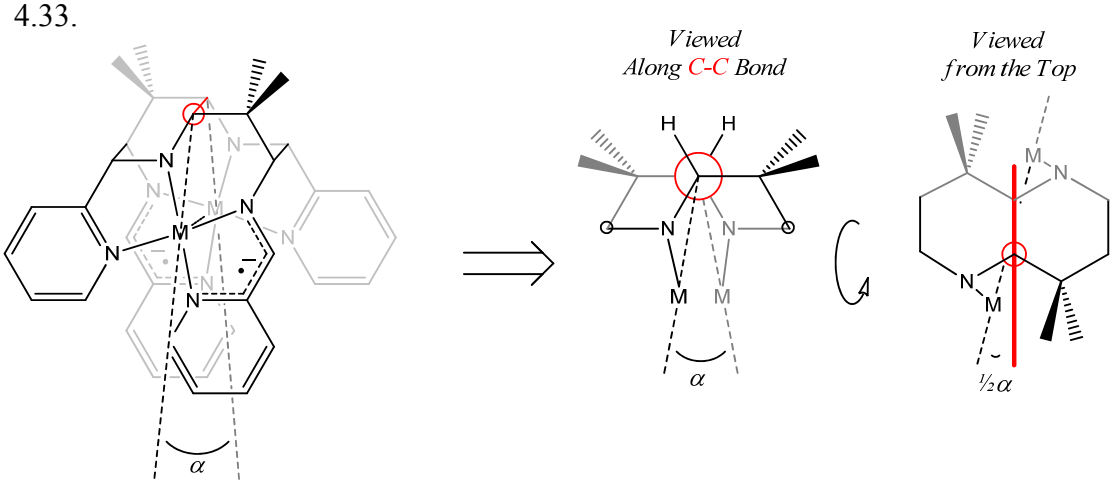

Figure 4.33. Skeletal drawings illustrating the square-plane offset angle α.

Due to the near-C_2-symmetry of **14-Cr$_2$**, an offset of 0°, signifying the greatest overlap of orbitals perpendicular to the ligand plane, would result in the M-M bond axis being coplanar with the bond axis of the bridgehead carbons of the *cis*-

diazadecalin backbone (Fig. 4.33, far right). The actual value of α in **14-Cr$_2$** is 1.9(1)°, signifying a strong tendency to ensure maximal M-M overlap. This measurement will be more relevant below when similar structures are considered.

The dimerization of **14-Cr$_2$** can be seen as arising from an asymmetric radical coupling of the ligand framework of the putative bis(aza-allyl) species (Scheme 4.5), but the actual mechanism of dimerization is likely more complex (*vide infra*).

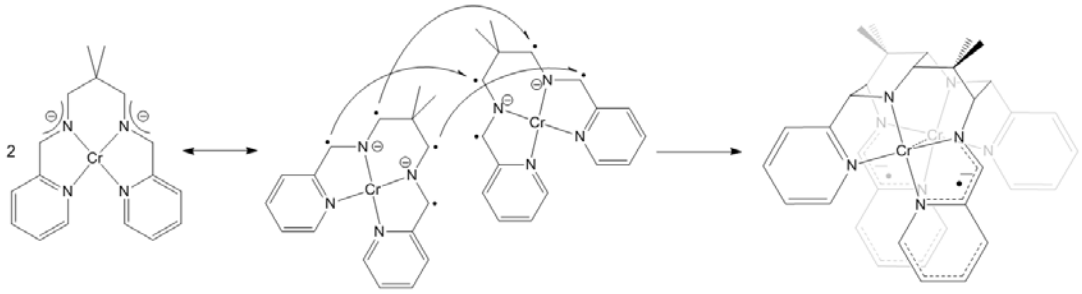

Scheme 4.5. Hypothetical dimerization of $(N_4)Cr$

One of the more notable features is the lack of axially-coordinating ligands. The axial positions are usually electrophilic enough to coordinate the solvents that have any solvating ability, thus growing crystals sufficient for X-ray analysis is likely to produce axially-ligated species. Solutions of **14-Cr$_2$** in non-polar solvents (diethyl ether, benzene, toluene) are brown-green whereas solutions in THF and DMF are the color of red ochre, suggesting that the complex is not immune from axial coordination. The use of $Cr(N(SiMe_3)_2)_2(thf)_2$ as a starting material ensured the presence of four equivalents of THF and four equivalents of $HN(TMS)_2$ per eventual dimer, so the lack of a coordinating ligand points to axial lability that seems unusual considering the electron-deficient nature of the complex. Moreover, there are few examples of Cr_2^{4+} dimers that have sufficient torsion to diminish δ-bond overlap to this extent.

The ultimate structure of the two coupled ligands, unfolded and protonated, is shown in Figure 4.34.

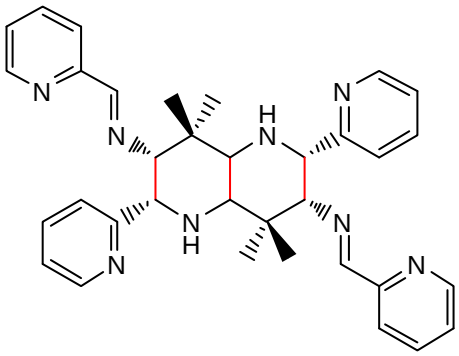

Figure 4.34. Skeletal schematic of the coupled neutral ligand. Bonds in red denote new CC-bonds between the precursor ligands.

The fusion of the two ligands forms a bicyclic ring structure whose core, *cis*-1,5-diazadecalin, is a relatively rare organic construct. There are no examples of the same core with quaternary carbons in the 4- and 8-positions of the bicycle, and the aforementioned parent compound itself has recently[27a] been targeted for use as a bidentate chiral ligand for asymmetric catalysis, as has the 5,7-bis(dimethyl)-derivative.[27b] While there are several similar structures in known biomolecules, very few have *cis*-stereochemistry at saturated bridgehead carbons. One such example is C-profluorocurine,[28] shown in Figure 4.35.

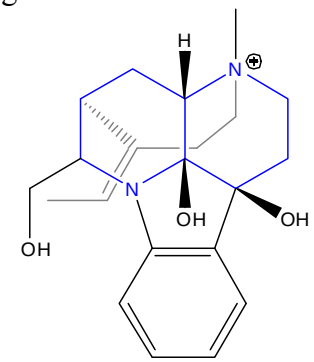

Figure 4.35. C-profluorocurine, an anti-inflammatory alkaloid, with its *cis*-1,5-diazadecalin core highlighted in blue.

The potential utility of such a coupling reaction and the unusual electronic structure of the dimer led us to explore the reaction of **$Me_2C(ImCH_2Py)_2$** with other metal precursors, the details of which are discussed in later sections.

Spectral Properties of 14-Cr_2

The dimer **14-Cr_2** was itself not seen spectroscopically in previous tube reactions, likely due to its low solubility and broadening from additional Cr-containing byproducts. The pure compound shows a clean ^{1}H NMR spectrum in d_8-toluene consistent with a diamagnetic ground state (shifts were in the 'diamagnetic region' of 12 ppm to –1 ppm). The peaks are significantly broader than one would expect ($\nu_{1/2} \geq$ 20 Hz) and the spectrum had an unusual temperature dependence (Figure 4.36). Analysis of the spectra obtained between –78 °C and 22 °C established a set of shifts and integrations consistent with the 18 protons in 14 distinct environments expected for **14-Cr_2**. As with other Cr_2^{2+} dimers,[22] the temperature-dependence of the chemical shifts can be modeled as the result of thermal population of a low-lying triplet state above a singlet ground state. In this model, the chemical shift of a proton (δ) at a given temperature (T) will be the sum of its shift in the singlet ground state (δ_{dia}) and a perturbation term related to the thermal population of that excited state, given by Eq. 4.9 below;

$$\delta = \delta_{dia} + \frac{2\left(\frac{\gamma_e}{\gamma_n}\right)\left(\frac{A}{kT}\right)}{3+e^{\frac{\Delta E_{ST}}{kT}}} \qquad \textbf{Eq. 4.9}$$

where γ_e and γ_n refer to the electron and proton gyromagnetic ratios, k is Boltzmann's constant (in appropriate units), A is the proton-electron hyperfine coupling constant (in MHz), ΔE_{ST} is the singlet-triplet energy gap (in cm^{-1}) and T is temperature (K).

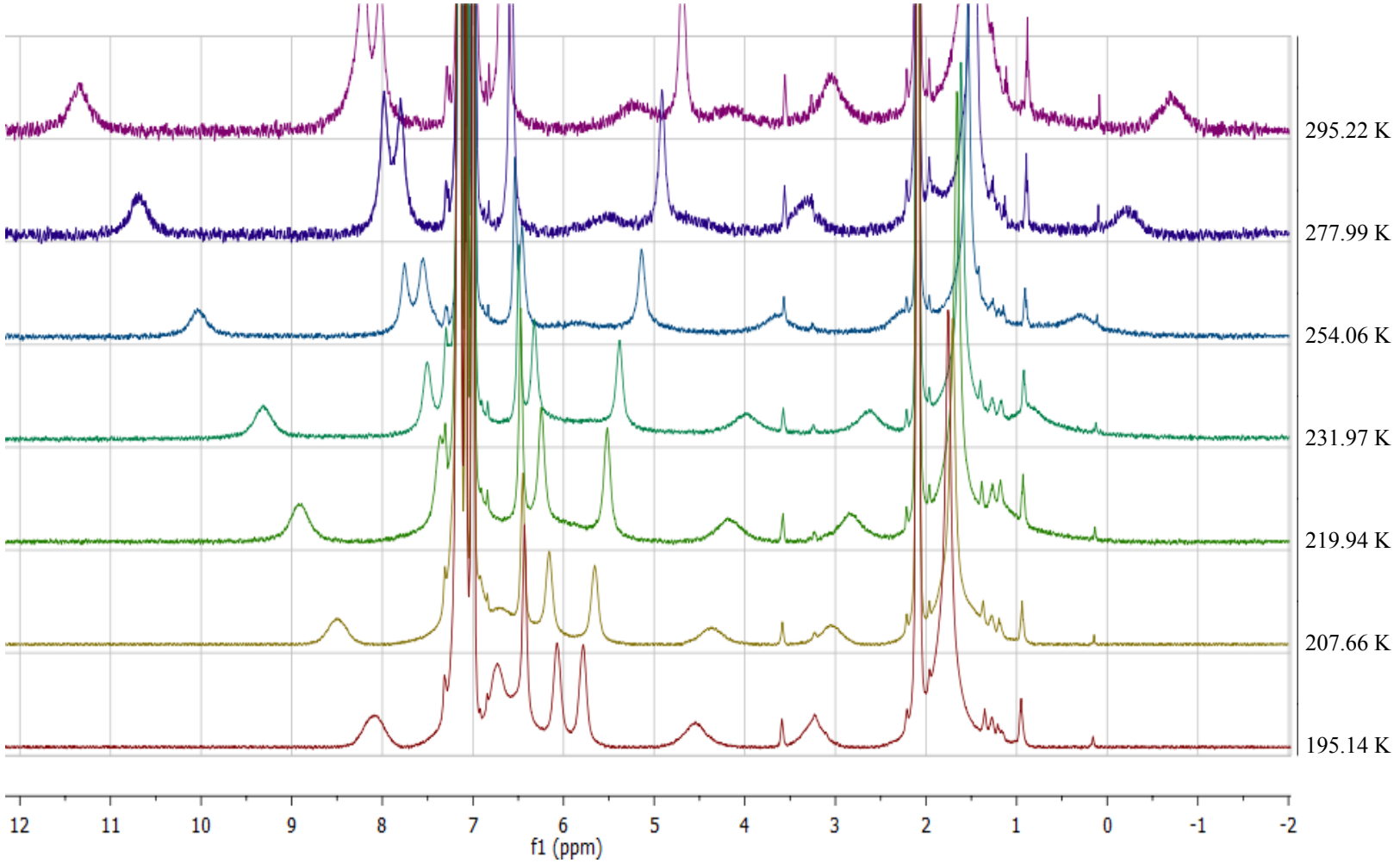

Figure 4.36. Variable-temperature ^{1}H NMR spectra of **2-Cr$_2$** in d_8-toluene.

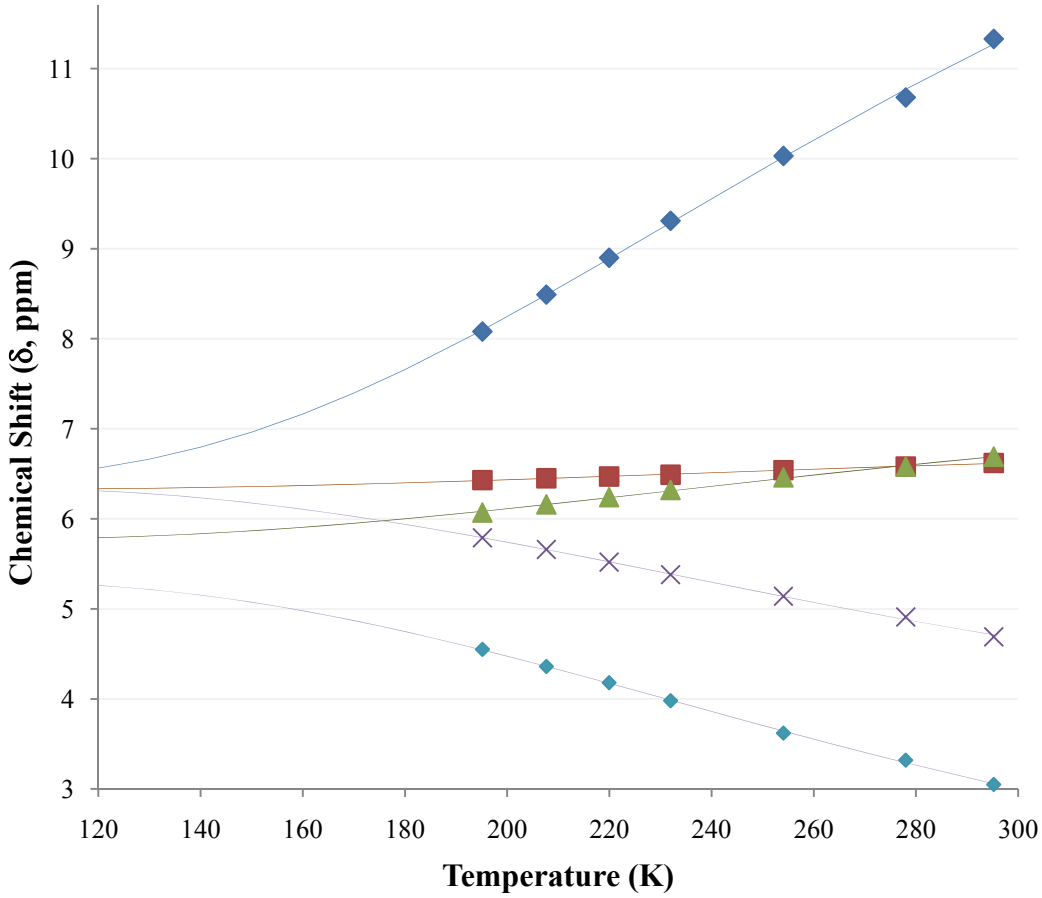

Figure 4.37. Experimental (points) and simulated (lines) chemical shifts for five of the observable protons of **14-Cr$_2$**.

Table 4.6. Parameters for least-squares regression fit to Eq. 4.2 for 1**4-Cr$_2$** NMR data. Numbers in parentheses represent 95% confidence limits (Univar).

Chemical Shift at RT (ppm)		11.33	6.62	6.69	4.69	3.05
Fit Parameters:	δ_{dia} (ppm)	6.41(26)	6.33(7)	5.76(8)	6.36(11)	5.33(13)
	A (MHz)	0.56(5)	0.033(1)	0.11(3)	-0.19(4)	-0.26(5)
	ΔE_{ST} (cm^{-1})	630(71)				

Using the above relation, the temperature dependencies of five ^{1}H signals of **14-Cr$_2$** were simultaneously fit to a nonlinear least-squares regression function. The data and corresponding fit are plotted in Figure 4.37 and the parameters of the fit are presented in Table 4.6. The simulated data fit the spectra well ($\Sigma[\chi^2] = 0.016$) and though it yields a significant uncertainty (11%) for the singlet-triplet gap ΔE_{ST}, this is not unreasonable given the lack of known diamagnetic chemical shifts (δ_{dia}). The fit shown in Fig. 4.36 is extrapolated to 120 K to illustrate that experimental determination of δ_{dia} laid well outside our instrumental capability. The calculated singlet-triplet gap (631(70) cm^{-1}) is consistent with others established for Cr_2^{4+} carboxylates,[22] but the structure of the triplet state is not as straightforward as in those systems due to significant ligand contribution to the M-M bonding orbitals.

Electronic Structure of 14-Cr$_2$

As briefly discussed above, chromium dimers containing the Cr_2^{4+} ion have previously been treated as containing multiple M-M bonding interactions. The classical treatment,[29] developed by Cotton *et al*., is shown in Figure 4.38.

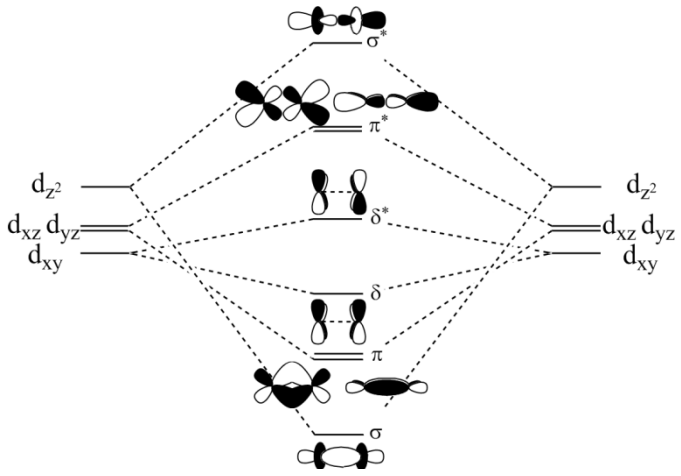

Figure 4.38. Molecular orbital diagram describing the bonding between two square planar metal centers. The high-lying d-interaction between the σ^* $d_{x^2-y^2}$ orbitals has been neglected.

The torsion angle in **14-Cr$_2$**, being close to 45°, should result in negligible δ-overlap and ensures that the bonding is dominated by σ- and π-interactions. The radical nature of the monoreduced imino-pyridine fragments immediately suggested a broken symmetry solution would resolve the apparent diamagnetism of the complex. A singlet was found that was composed of five uncoupled electron pairs. The two ligand-localized magnetic orbitals, plotted together, are shown in Figure 4.39.

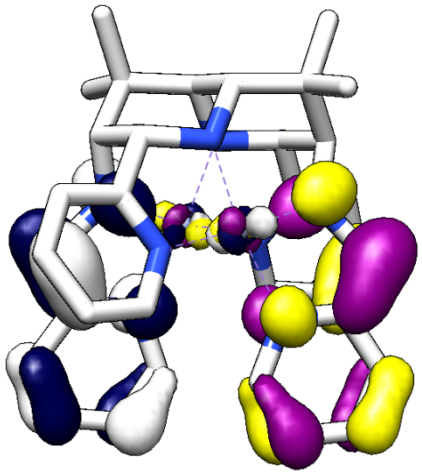

Figure 4.39. The ligand-localized α-spin (yellow/purple) and β-spin (white/blue) magnetic orbitals of 14-Cr$_2$. The lavender spheres represent the Cr atoms.

The two orbitals are antiferromagnetically coupled and represent single-electron occupation of each of the two imino-pyridine π^*-orbitals of the ligand. The low symmetry of this molecule ensures a significant amount of mixing of the atomic orbitals. The remaining magnetic orbital pairs are shown in Figure 4.38. Although there is a large amount of ligand involvement (particularly of the amido nitrogen), the spatial distribution of the broken symmetry molecular orbitals roughly correspond to the bonding orbitals represented in Figure 4.38. However, since the α- and β-spin functions are each localized separately, the broken symmetry solution corresponds with two high-spin Cr^{2+} centers that are AFM-coupled. As discussed previously, broken symmetry calculations attempt to incorporate multi-determinant character into

a single-determinant solution. The most reasonable conclusion to draw from these calculations is that they confirm that the molecule is probably poorly described by a single electron configuration, even one from a broken symmetry solution. This has, in fact, been established previously for the 'classically' quadruply-bound $Cr_2(HCO_2)_4$, where the $\sigma^2\pi^4\delta^2$ configuration was found to contribute less than 50% to the CASSCF solution.[30]

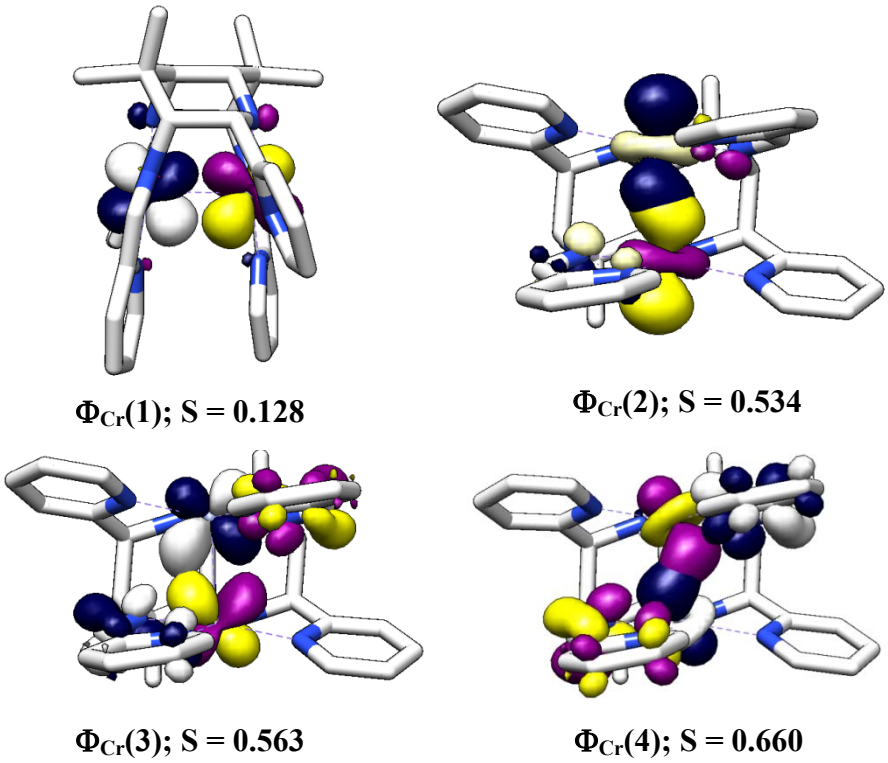

Figure 4.40. The remaining α (white/blue) and β (yellow/purple) magnetic orbitals of **14-Cr$_2$**. The orbital overlap (*S*) is indicated below each α/β pair.

Again, the magnetic orbitals represent unitary transformations of the canonical BS solutions that allow for identification of the orbital parentage of antiferromagnetically-coupled electron pairs. The orbitals plotted in Figures 4.39 and 4.40 represent the metal and ligand orbitals that constitute the weak bonds in the system. While orbitals $\Phi_{Cr}(1)$- $\Phi_{Cr}(3)$ have clear parentage (d_{xz}, d_{z^2}, and d_{yz} combinations, respectively), $\Phi_{Cr}(4)$ has multiple orbital parentages and cannot be clearly assigned.

4.5. Reactivity of $Me_2C(ImCH_2Py)_2$ with $Fe(N(TMS)_2)_2(thf)$

Treatment of the ligand precursor **$Me_2C(ImCH_2Py)_2$** at room temperature with one equivalent of $Fe(N(SiMe_3)_2)_2(thf)$ in benzene-d_6 solution resulted in a color change from nearly colorless to red. This red color darkens to brown over the course of a few hours, resulting in elimination of one equivalent of HMDS and the generation of a new paramagnetic species. The ^1H NMR spectrum, shown in Figure 4.41, is indicative of a complex with C_1 symmetry and one remaining $N(TMS)_2$ group with two inequivalent trimethylsilyl environments. Since the structure of the deprotonated ligand is unknown (vide infra, Fig. 4.42) it will be abbreviated "HN_4"

$$Me_2C(ImCH_2Py)_2 + Fe(N(TMS)_2)_2(THF)_2 \xrightarrow[-HMDS]{-THF} (HN_4)Fe(N(TMS)_2) \qquad \text{Eq. 4.10}$$

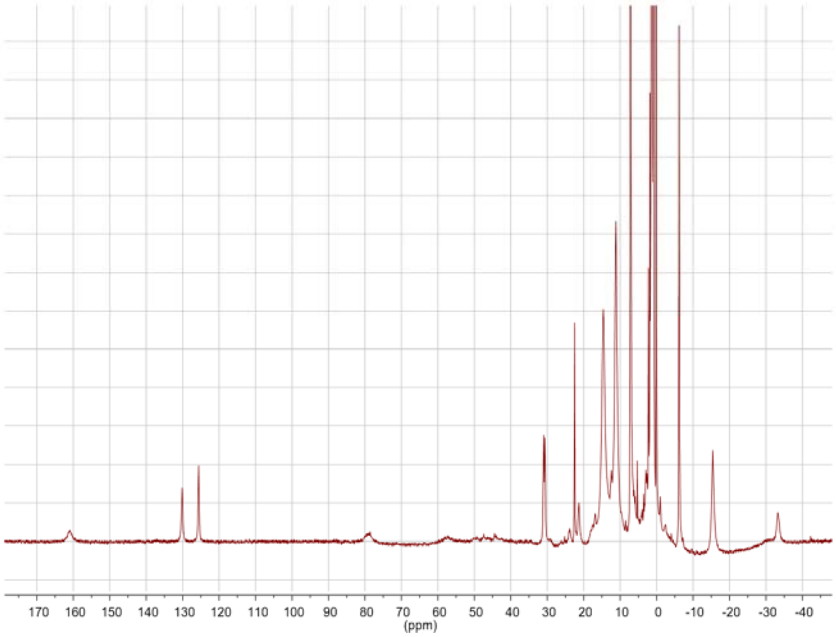

Figure 4.41. ^1H NMR spectrum of $(HN_4)Fe(N(TMS)_2)$.

The high solubility of this brown compound precluded its isolation as a crystalline solid. Samples of this material that had had solvent removed *in vacuo* had the consistency of a thick oil. Thermolysis (80 °C) of the compound produced a new

species, also with apparent C_1-symmetry, with concomitant evolution of another equivalent of HMDS. The rate of disappearance of $(HN_4)Fe(N(TMS)_2)$ is approximately first-order, however the rate constant ($\sim 6\times10^{-5}$ s^{-1}) varied significantly between different experiments. Attempts to scale-up the production of this second complex were hampered by the presence of starting material, and it was surmised that this second complex was in equilibrium with HMDS.

Although the paramagnetism of $(HN_4)Fe(N(TMS)_2)$ prevented spectroscopic determination of its structure, it seemed feasible that this complex had undergone some sort of CC-coupling. At this point any successful an tractable deprotonation of an aza-allyl precursor had resulted in coupling of the least-stabilized carbons. In the case of $(HN_4)Fe(N(TMS)_2)$, such a coupling may take a similar course as that for **$(12\text{-}Fe)_2$**. As shown in Figure 4.42, attack at the adjacent imine position by the unstabilized aza-allyl carbon and subsequent deprotonation would yield a bis(imino-pyridine) complex.

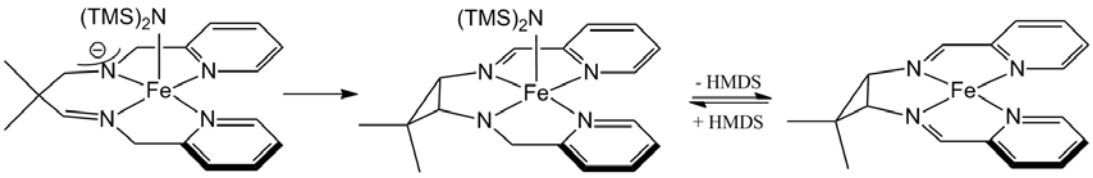

Figure 4.42. Possible structures of $(HN_4)Fe(N(TMS)_2)$ and its thermal degradation product.

It was thought that if this were operative, it may be possible to use an oxidant to intercept the bis(imino-pyridine) complex and develop a catalytic system to cyclize **$Me_2C(ImCH_2Py)_2$**. A hydrazine derivative could oxidatively add to the formally Fe^0 center to yield an iron imido species that could be competent for further deprotonation and coupling (Scheme 4.6).

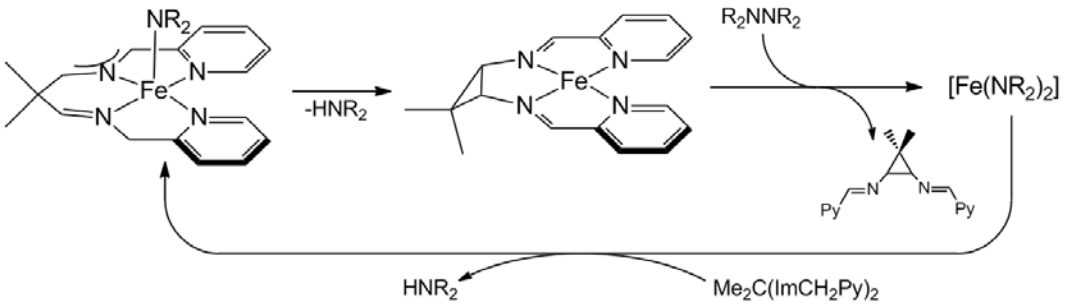

Scheme 4.6. Proposed catalytic cycle for oxidative cyclization of **$Me_2C(ImCH_2Py)_2$**.

To test this, **$Me_2C(ImCH_2Py)_2$** was treated with 10 mol % Fe(N(TMS)$_2$)(thf) and an equivalent of 1,2-diphenyl-1,2-dimethylhydrazine in C_6D_6. The full conversion to a new organic product took 2 d at room temperature, although the organohydrazine was unaffected. Perfoming the same reaction in the absence of the hydrazine led to the formation of the same product, identified as the pyrrolidine derivative shown in Eq. 4.10.

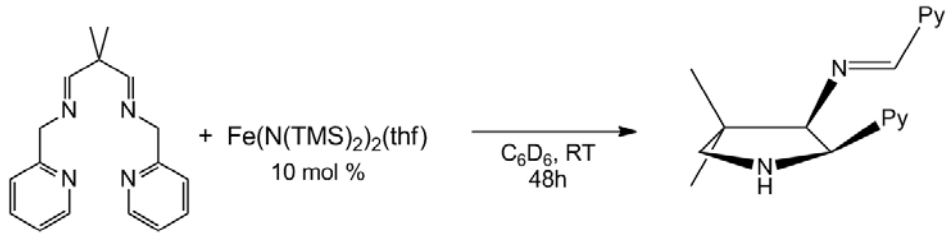

Eq. 4.10

This cyclization does not involve an oxidation change and can be thought of as a hydrocarbylation of one of the benzylic CH-bonds across the imine δ to that carbon. The diastereoselectivity is very high (>95%), as no resonances attributable to other isomers were detected. The *cis* orientation of the imino-pyridine and pyridine moieties on the pyrrolidine ring suggests that ring formation occurs while those nitrogens are bound to a single metal center, but exploration of this system revealed complicated mechanistic possibilities. When the catalyst loading was dropped to 5 mol % (0.005 M) with the substrate concentration held constant (0.10 M), only a trace amount of the

product was detected after four days (~40% starting diimine still present, Eq. 4.11). When the catalyst loading was kept at 5 mol % and its concentration held at 0.01 M (substrate concentration 0.20 M), about half of the substrate cyclized after five days (Eq. 4.10).

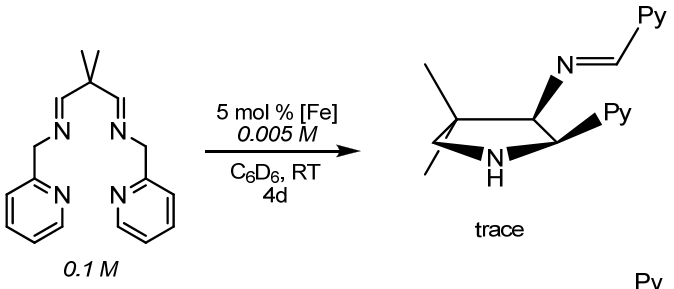

Eq. 4.9

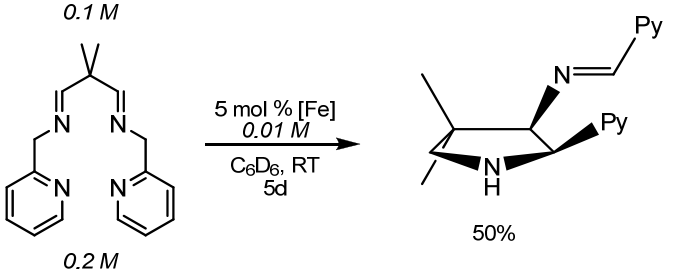

Eq. 4.10

Conducting the same reaction with tetradeuterated **$Me_2C(ImCD_2Py)_2$** resulted in the label distribution shown in Eq. 4.11.

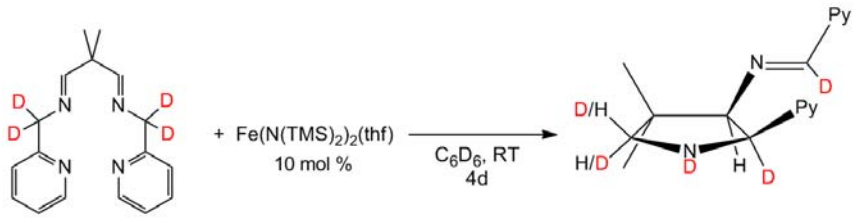

Eq. 4.11

The deuterium label was scrambled approximately 50:50 within the CH_2 α to the pyrrolidine nitrogen. This epimerization suggests a reversible β-hydride elimination step, however further studies suggested that more than one metal may be involved. In the catalytic reactions with $Me_2C(ImCH_2Py)_2$ a byproduct developed in sporadic amounts (5–10 mol%) that was identified as N-(2-methylpropylidene)-1-(pyridin-2-yl)methanamine (see Experimental). It was noted that the substrate ($Me_2C(ImCH_2Py)_2$) partially degrades to this material under ambient conditions.

Although $(HN_4)Fe(N(TMS)_2)$ (10 mol %) was competent for the cyclization, it took about twice as long to go to completion. To test if this cyclization was merely anionic in nature, LiHMDS was tested as a catalyst. Using 10 mol % LiHMDS in C_6D_6, isomerization of one of the imine arms occurred (Eq. 4.12).

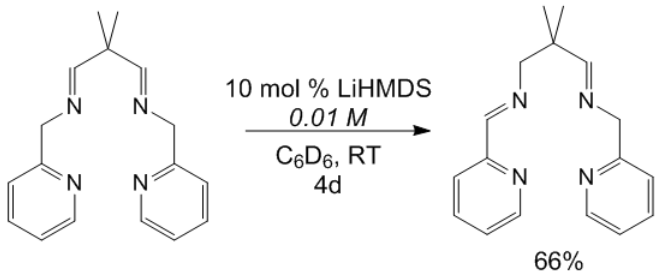

Eq. 4.12

After four days, 30% of the initial **$Me_2C(ImCH_2Py)_2$** remained and the generation of products appeared to stall. Using 20 mol % LiHMDS (Eq. 4.13) produced two major products after four days, one of which was identified as NpImPy.

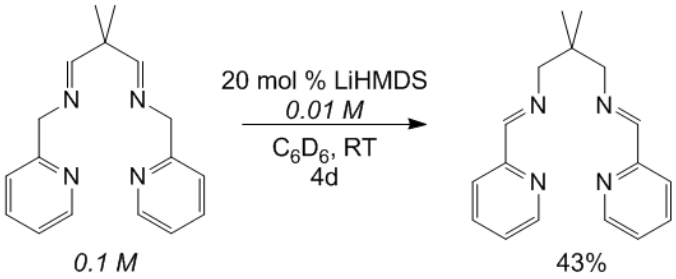

Eq. 4.13

The production of NpImPy was observed to pass through the same mono-isomerized product generated in Eq. 4.11. At no point during either of these LiHMDS experiments could the pyrrolidine product be conclusively identified. Using a cyclic variant of **$Me_2C(ImCH_2Py)_2$**, **1,1-^{c}Pent$(ImCH_2Py)_2$**, a related product to that shown in Eq. 4.9 was produced in ~90% ^{1}H NMR yield (15 mol% Fe, Eq. 4.14).

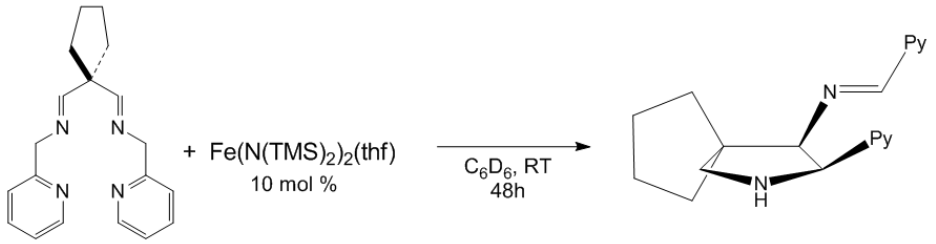

Eq. 4.14

Attempting the same cyclization with a cyclopropane backbone instead of a cyclopentane backbone (**1,1-^{c}Pr(ImCH$_2$Py)$_2$**, Eq. 4.15) led to the production of a complex mixture of products that lacked signals diagnostic of the pyrrolidine ring. Recent work suggests that constructs such as **1,1-^{c}Pr(ImCH$_2$Py)$_2$** are susceptible to facile cyclopropane ring-opening in basic conditions.[31]

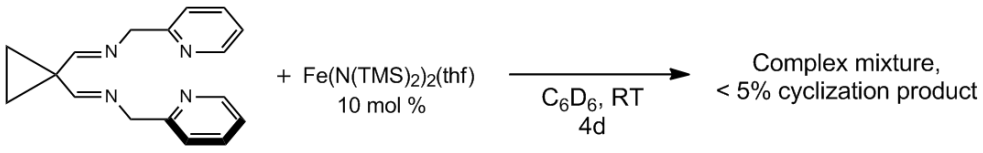

Eq. 4.15

4.6. Reactivity of Me$_2$C(ImCH$_2$Py)$_2$ with {Ni(NPh$_2$)$_2$}$_2$

Due to the more familiar 2-electron redox behavior of the metal, bis(amido) nickel compounds seemed more appropriate catalysts for the type of CC-coupling we sought (Fig. 4.39). Of the few well-characterized bis(amido)nickel compounds, {Ni(NPh$_2$)$_2$}$_2$ is one of the simplest and most readily-available. Catalytic amounts of {Ni(NPh$_2$)$_2$}$_2$ added to solutions of **Me$_2$C(ImCH$_2$Py)$_2$** and 1,2-dimethyl-1,2-diphenylhydrazine did not result in any observable catalytic conversion. When a stoichiometric amount of **Me$_2$C(ImCH$_2$Py)$_2$** was treated with ½ equivalent of {Ni(NPh$_2$)$_2$}$_2$ in C$_6$D$_6$, copious amounts of black solid precipitated out of solution. Assuming some sort of insoluble aggregate had formed, the tube was heated for 1 wk at 50 °C and two minor (<15%) products appeared in a 1:1 ratio according to Eq. 4.15.

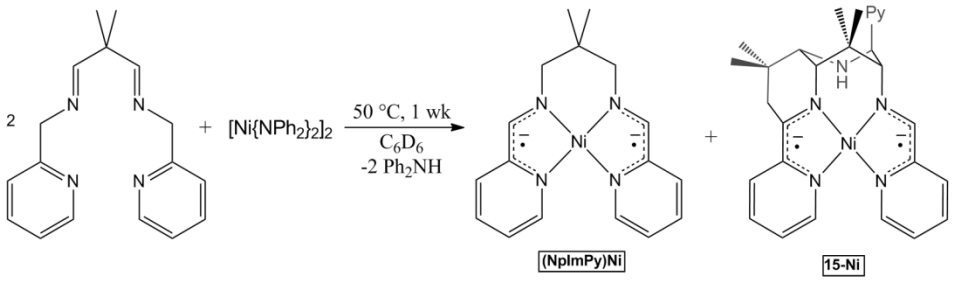

Eq. 4.15

The synthesis of **(NpImPy)Ni** can be rationalized as originating from epimerization to the more thermodynamically stable pair of imines under the basic reaction conditions, however the origin of **15-Ni** was puzzling. When **$Me_2C(ImCH_2Py)_2$** was treated with ½ $\{Ni(NPh_2)_2\}_2$ in THF, the deep blue color of the solvated nickel amide darkened to brown. After several hours at room temperature crystals started to precipitate from solution, and after ten days the black crystalline product was isolated in 55% yield. One of these crystals was amenable to X-ray analysis. The structure is provided in Figure 4.43, selected parameters are presented in Table 4.7 and the crystallographic data are presented in Table 4.8.

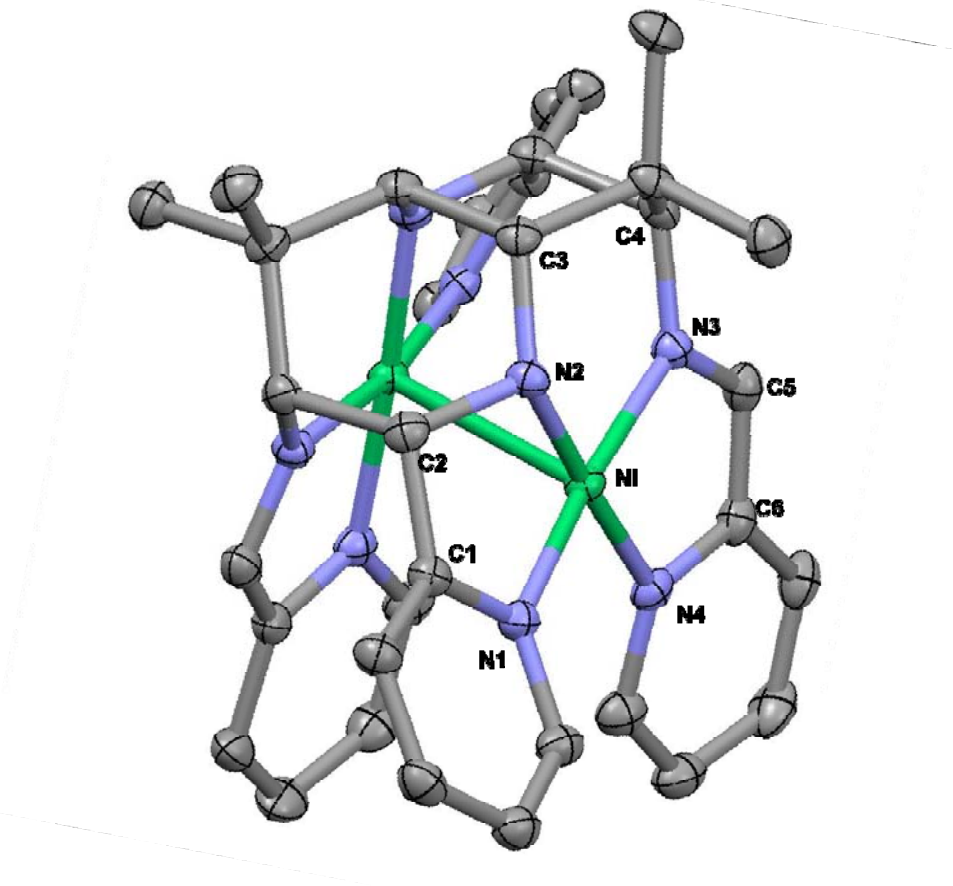

Figure 4.43. Molecular Structure of $(N_8)Ni_2$ (**$14\text{-}Ni_2$**). Thermal ellipsoids are at 50% probability level and hydrogen atoms have been omitted for clarity.

Table 4.7. Selected bond angles and interatomic distances for **14-Ni_2**.

Selected Bond Distances (Å)		Selected Bond Angles (degrees)	
Ni-Ni'	2.8164(6)	N1-Ni-N2	91.36(9)
Ni-N1	1.934(2)	N2-Ni-N3	95.3(1)
Ni-N2	1.880(2)	N3-Ni-N4	83.03(9)
Ni-N3	1.877(2)	N4-Ni-N1	99.90(9)
Ni-N4	1.934(2)	N1-Ni-Ni'	112.85(7)
N2-C2	1.444(3)	N2-Ni-Ni'	90.79(7)
N3-C5	1.332(3)	N3-Ni-Ni'	76.19(7)
C5-C6	1.395(4)	N4-Ni-Ni'	91.14(7)
C1-N1	1.354(3)		
C6-N4	1.391(4)		
C2-C4'	1.570(4)		
C3-C3'	1.547(6)		

Again we find that the ligand was successfully deprotonated in the desired positions, however the resulting complex was unstable with respect to CC-coupling. The structure of **14-Ni_2** shares many similar features as that of **14-Cr_2•2(C_6H_6)**. Some of the more subtle structural details will be discussed later (*vide infra*). The imino-pyridine bond lengths are consistent with monoreduction, and the presence of an amide leads to the conclusion of a formal oxidation state of Ni^{2+}. The Ni-Ni bond distance (2.8164(6) Å) is perplexing; although quite long (Σ(cov. rad.) = 2.4 Å), it is within the sum of the Van der Waals radii (3.3 Å) and indicative of some sort of bonding interaction. Each Ni center is best described as a distorted square planar complex. This should lead us to conclude that the orbital that would be used for σ-bonding, d_{z^2}, is doubly filled and should not have any net bonding stabilization. Such d^8-d^8 interactions are known for square-planar complexes of the late metals (e.g. Rh, Ir, Pt, Pd),[32] and have been explained within the context of Configuration Interaction. As shown in Figure 4.44, the mixing of excited states (of appropriate symmetry) into the ground state allows for a net stabilization. P-orbital mixing can minimize the

antibonding interaction of the two d_{z^2} orbitals at the expense of destabilizing unfilled p-p interactions.

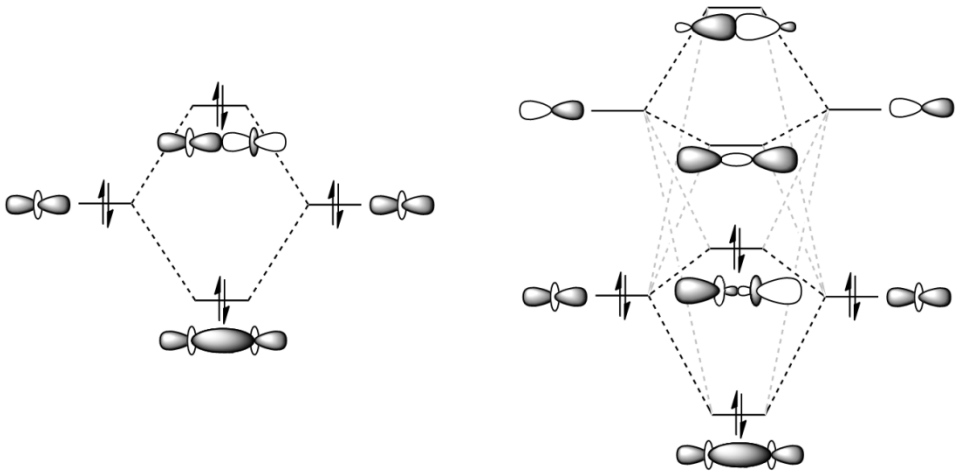

Figure 4.44. Molecular orbital diagrams for the d_{z^2}- d_{z^2} interaction in the absence (left) and presence (right) of configuration interaction contributions.

Previous computational studies concluded that such an interaction was inaccessible for Ni,[33] thus the apparent existence of such an interaction was of significant interest.

The reactivity of **14-Ni$_2$** was lightly investigated. Thermolysis of the dimer in C_6D_6 at 90 °C for 12 h produced **15-Ni** in 85% yield (by NMR). This suggests that the same dimer formed in relatively small quantities during the experiment from Eq. 4.14 and was degraded by thermolysis. The formal loss of Ni(PyCN)(H) from **14-Ni$_2$** to produce **15-Ni** could not be tracked to any specific product and likely formed an insoluble material. Attempts were made to isolate the neutral ligand **14-H$_2$** via sequestration of the nickel with dimethylglyoxime (Eq. 4.16).

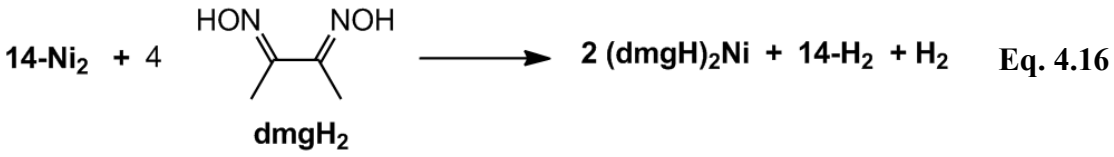

Eq. 4.16

Since each imino-pyridine is formally monoreduced, isolating the protonated and neutral ligand would require two oxidation events. The hope was for dimethylglyoxime, a potent sequestration agent for nickel, to act as a proton source toward the amide bases and an oxidant by formation of an equivalent of H_2. Although a small amount of combustible gas was produced (11% of expected) and the nickel was successfully sequestered as $(dmgH)_2Ni$ (confirmed by IR), the organic product was a mixture of the neutral ligand and ligands variants reduced at the imine positions (Figure 4.45). The products **14-H_2**, **16** and **17** were formed in a ratio of 1:1:0.4.

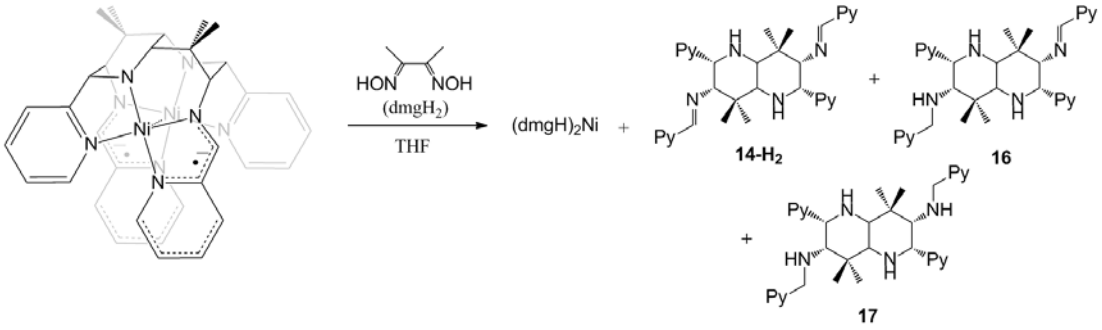

Figure 4.45. Product mixture from the reaction of **14-Ni_2** with dimethylglyoxime.

Since the dinickel compound could be made relatively easily, the dicobalt version was considered to be a reasonable target. The M-M interaction should be stronger, since a bond order of 1 is possible, and $Co(N(TMS)_2)_2(thf)$ is a readily-available starting material.

4.7. Reactivity of $Me_2C(ImCH_2Py)_2$ with $Co(N(TMS)_2)_2(thf)$

When **$Me_2C(ImCH_2Py)_2$** was treated with $Co(N(TMS)_2)_2(thf)$ in THF, the light green color of the cobalt amide darkened to blue-black. After several hours at room temperature crystals started to precipitate from solution, and after two days the blue-black crystalline product was washed with diethyl ether and isolated in 7% yield. One of these crystals was amenable to X-ray analysis. The structure is provided in

Figure 4.46, selected parameters are presented in Table 4.8 and the crystallographic data are presented in Table 4.7. The structure of **14-Co_2** is superficially very similar to **14-Ni_2**; they are both C_2-symmetric, crystallize in the same tetragonal space group ($I4_1cd$), and have virtually identical cell parameters. The imino-pyridine bond distances are again best modeled by mono-reduction, giving each cobalt an oxidation state of +2. The Co-Co bond length (2.9111(7) Å) is 0.04Å *longer* than the Ni-Ni bond length in **14-Ni_2**, and is considerably longer than expected for a Co-Co single bond (2.6-2.8 Å).[34]

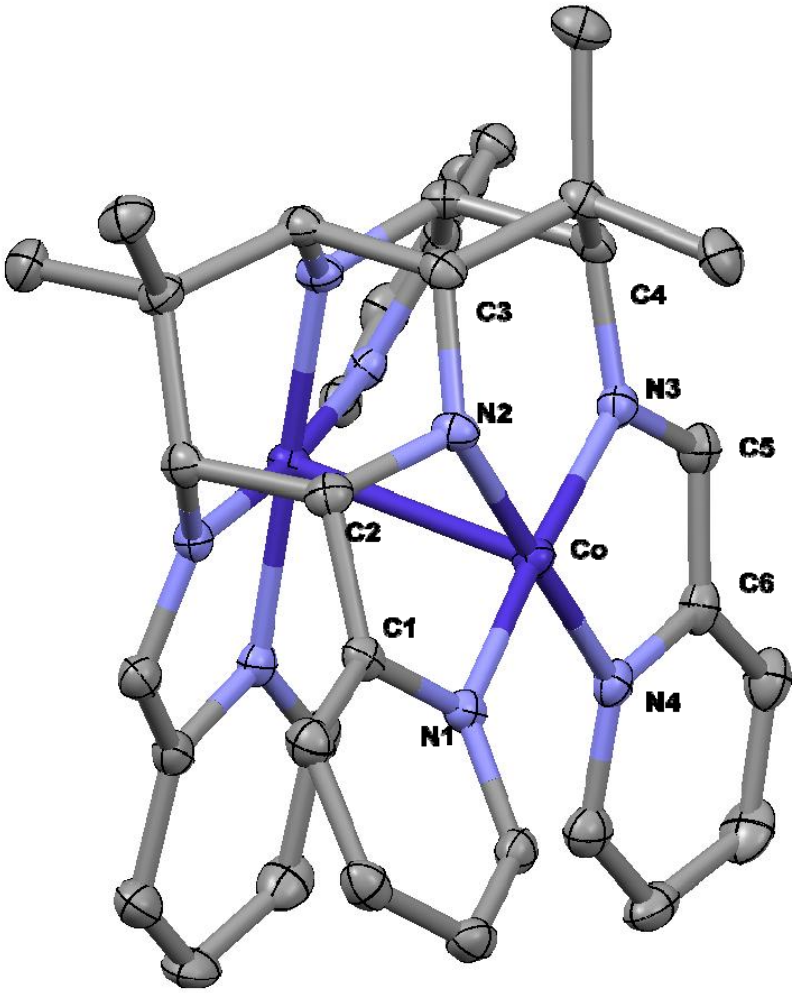

Figure 4.46. Molecular Structure of **14-Co_2**. Thermal ellipsoids are at 50% probability level and hydrogen atoms have been omitted for clarity.

Table 4.8. Selected bond angles and interatomic distances for **14-Co$_2$**.

Selected Bond Distances (Å)		Selected Bond Angles (degrees)	
Co-Co'	2.9111(7)	N1-Co-N2	81.65(8)
Co-N1	1.9536(17)	N2-Co-N3	95.83(8)
Co-N2	1.8382(19)	N3-Co-N4	82.35(7)
Co-N3	1.8693(18)	N4-Co-N1	100.28(7)
Co-N4	1.8965(18)	N1-Co-Co'	109.33(5)
N2-C2	1.440(3)	N2-Co-Co'	86.21(5)
N3-C5	1.316(3)	N3-Co-Co'	77.08(5)
C5-C6	1.408(3)	N4-Co-Co'	92.34(5)
C1-N1	1.394(3)		
C6-N4	1.394(3)		
C2-C4'	1.563(3)		
C3-C3'	1.572(5)		

Although the imino-pyridine fragments of **14-Cr$_2$**, **14-Co$_2$**, and **14-Ni$_2$** are best described as monoanions there are some minor differences. The imino-pyridine bond distances for **(NpImPy)Ni**, **14-Cr$_2$**, **14-Co$_2$**, and **14-Ni$_2$** are presented in Figure 4.47.

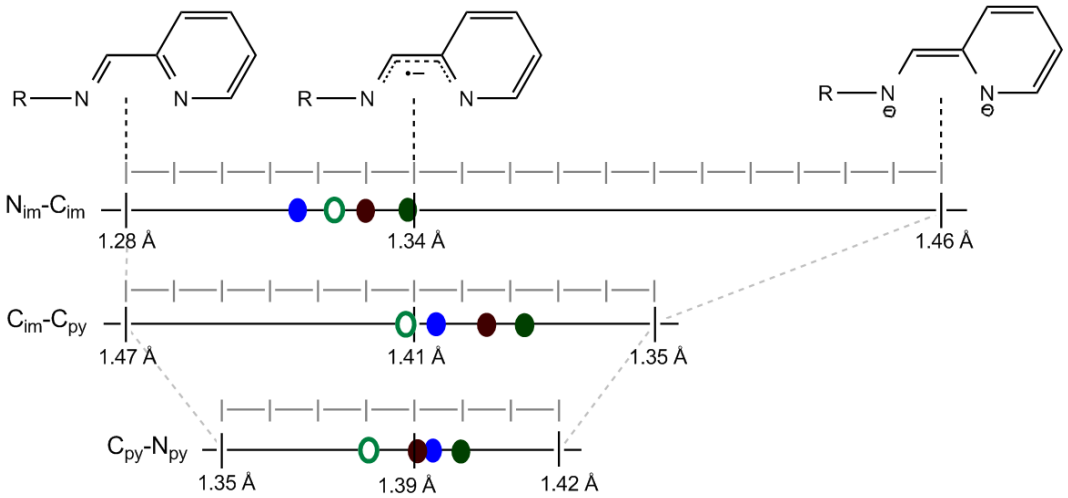

Figure 4.47. Comparison of the imino-pyridine bond distances for **(NpImPy)Ni** (hollow green ovals), **14-Cr$_2$** (solid green ovals), **14-Co$_2$** (blue ovals), and **14-Ni$_2$** (maroon ovals). The distance scales are centered on the monoreduced values.

Many of the imino-pyridine compounds analyzed by Weighardt *et al.*[9a] were based on N-aryl ligands, and the distances we expect for the current system will be somewhat different. There are a few related compounds with N-alkyl substituents and that allows adjustment of the scale,[9c] but the smaller ensemble hampers accurate classification of

oxidation state. The **(NpImPy)Ni** values are presented on the scale in Figure 4.43 to give some idea of what sort of perturbation to expect. The pyridine C-N bond lengths are the least sensitive to reduction and will not be discussed further. The N_{im}-C_{im} and C_{im}-C_{py} bond distances for the dinickel and dicobalt compounds are just within 3σ of each other and thus statistically indistinguishable, but the distances for the dichromium complex are clearly closer to the bis(reduced) end of the spectrum than those of the dicobalt complex.

The following discussion relies heavily on Figure 4.48, a structural comparison of the three dimers. The ligand framework of **14** is quite restricted with respect to the square-plane offset angle (α, see Fig. 4.34) and torsion angle (ω, see Fig. 4.31), since changes in these angles amount to distortions of the rigid cis-decalin core. The torsion angles ω for the dicobalt and dinickel compounds (59.66° and 58.60°, respectively) are appreciable larger than that of the dichromium compound (52.37°). The long Cr-Cr distance (2.5515(3) Å) suggests that δ-bonding interactions are minimal and that the diminished ω is primarily due to ligand torsions that maximize Cr-Cr σ- and π-interactions. The offset angle α can be seen as a measure of the tendency for the M-M bonding orbitals to interact with one another. Since the σ- and π-bonding orbitals of each metal atom are orthogonal to the plane of the four bound nitrogens, strong M-M interaction requires a low value for α. Within this context, the trend is as we expect; **14-Cr_2** has the lowest α, followed by **14-Co_2** and then **14-Ni_2**. The plane angles ϕ (see Fig. 4.33) vary non-intuitively across the series. The strong M-M interaction can be used to rationalize the fact that the dichromium complex has a smaller ϕ than the dicobalt (13.83° and 17.24°, respectively), but the smallest of the three is the dinickel congener (12.59°). The reason for this is uncertain, but may be related to the proximity of the *meta*-carbons of the imino-pyridine moieties (*vide infra*). In both the

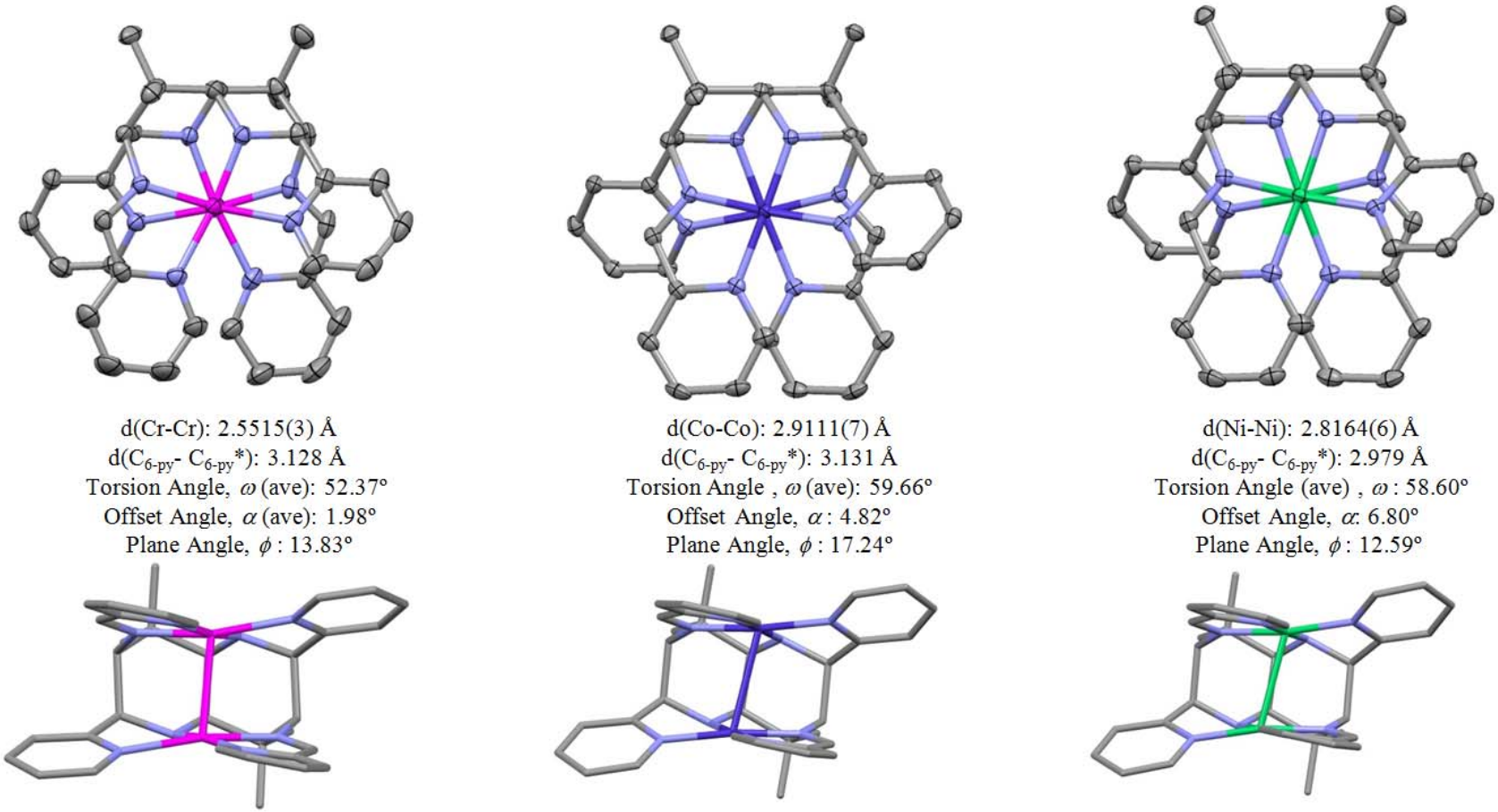

Figure 4.48. Structural comparison of **14-Cr$_2$**, **14-Co$_2$**, and **14-Ni$_2$**. The angles ω, α, and ϕ are defined in Section 4.4.

Table 4.9. Structural comparison of **(NpImPy)Ni**, **14-Cr_2•2(C_6H_6)**, **14-Co_2**, **14-Ni_2**, and **16-$TiCl_2$•½(C_6H_6)**

Crystal Data					
Formula	$C_{17}H_{20}N_4Ni$	$C_{46}H_{48}Cr_2N_8$	$C_{34}H_{36}Co_2N_8$	$C_{34}H_{36}Ni_2N_8$	$C_{20}H_{23}Cl_2N_4Ti$
Formula Weight	339.08	816.92	674.57	674.13	438.22
Crystal System	Monoclinic	Triclinic	Tetragonal	Tetragonal	Monoclinic
Space Group	P2(1)/c	P-1	I4(1)cd	I4(1)cd	P2(1)/n
Z	4	2	8	8	4
a, Å	14.9461(4)	10.3554(5)	15.506(2)	15.4762(9)	10.0514(4)
b, Å	7.3243(2)	12.1250(6)	15.506(2)	15.4762(9)	15.4640(6)
c, Å	15.6793(4)	18.9776(9)	23.508(4)	23.6634(14)	13.5561(4)
α, deg	90	93.287(2)	90	90	90
β, deg	112.463(2)	95.883(2)	90	90	94.3730(10)
γ, deg	90	110.272(2)	90	90	90
Volume, $Å^3$	1586.18(7)	2212.41(19)	5652.5(16)	5667.7(6)	2100.96(13)
D (calc.), g/cm^3	1.420	1.226	1.585	1.580	1.385
Absorption coeff., mm^{-1}	1.225	0.531	1.216	1.371	0.674
F(000)	712	856	2800	2816	908
Crystal Size, mm	0.20 x 0.10 x 0.03	0.40 x 0.30 x 0.10	0.20 x 0.20 x 0.15	0.40 x 0.25 x 0.10	0.35 x 0.10 x 0.05
Data Collection and Refinement					
Temp, K	173(2)	173(2)	173(2)	173(2)	173(2)
Wavelength (λ), Å	0.71073	0.71073	0.71073	0.71073	0.71073
θ limits, deg	2.63 to 28.42	2.01 to 28.74	3.06 to 28.27	2.54 to 31.20	2.00 to 30.51
Index Ranges	$-20 \le h \le 20$, $-9 \le k \le 9$, $-18 \le l \le 20$	$-13 \le h \le 13$, $-16 \le k \le 16$, $-22 \le l \le 25$	$-19 \le h \le 14$, $-20 \le k \le 18$, $-30 \le l \le 31$	$-14 \le h \le 20$, $-22 \le k \le 13$, $-34 \le l \le 31$	$-14 \le h \le 13$, $-22 \le k \le 22$, $-19 \le l \le 13$
Reflections Collected	14568	34998	12651	16541	24059
Absorption Correction	Semi-empirical from equivalents	Semi-empirical from equivalents	Semi-empirical from equivalents	Semi-empirical from equivalents	Semi-empirical from equivalents
Max. and Min. Transmission	0.9413 and 0.6401	0.9488 and .8156	0.8387 and 0.7930	0.8751 and 0.6101	0.9671 and 0.7984
Refinement Method	Full-matrix least-squares on F^2	Full-matrix least-squares on F^2	Full-matrix least-squares on F^2	Full-matrix least-squares on F^2	Full-matrix least-squares on F^2
Data/Restraints/Params.	3949 / 0 / 257	11136 / 0 / 509	3483 / 1 / 249	4538 / 1 / 201	6409 / 0 / 336
Goodness-of-Fit on F^2	1.044	1.104	1.002	0.998	1.010
Final R Indices [$I>2\sigma(I)$]	R1 = 0.0320, wR2 = 0.0876	R1 = 0.0381, wR2 = 0.1088	R1 = 0.0282, wR2 = 0.0617	R1 = 0.0385, wR2 = 0.0846	R1 = 0.0318, wR2 = 0.0732
R Indices (all data)	R1 = 0.0422, wR2 = 0.0939	R1 = 0.0521, wR2 = 0.1168	R1 = 0.0328, wR2 = 0.0638	R1 = 0.0559, wR2 = 0.0924	R1 = 0.0483, wR2 = 0.0810
Largest Diffraction Peak and Hole (e^- $Å^3$)	0.489 and -0.364	0.369 and -0.353	0.272 and -0.419	0.489 and -0.456	0.385 and -0.269

dichromium and dicobalt compounds these carbons are 3.13 Å apart, but they are 0.15 Å closer in the dinickel compound.

There are two major questions with these three compounds. What is the nature of the M-M interaction in **14-Ni$_2$**, and why is the Co-Co bond distance *longer* than the Ni-Ni distance? Calculations carried out on **14-Ni$_2$** suggested a possible origin of the 'forbidden' d^8-d^8 interaction. Using the Broken Symmetry formalism, **14-Ni$_2$** was found to be best described as an open-shell singlet with a single pair of antiferro-magnetically-coupled electrons (BS[1,1]). These two electrons are localized in the imino-pyridine π*-orbitals in a manner reminiscent of **(NpImPy)Ni** and represent the highest-lying orbitals in the system. The molecular orbital diagram for the ligand field is presented in Figure 4.49. Since the dinickel system is effectively electronically saturated **14-Ni$_2$** does not suffer from spin polarization effects and the BS[1,1] HOMOs are essentially identical to the magnetic orbitals. In the case of the **14-M$_2$** family, although spatial distributions of the α- and β-spin electrons are not identical, they are often similar and are plotted together (referred to as $\Phi_M(1^{\alpha\beta})$). In the cases where they are not similar, they are related by rotation about the C_2-axis and only one orbital has been plotted for clarity (referred to as $\Phi_M(1^{\alpha})$ or $\Phi_M(1^{\beta})$).

The spatial distribution of the bonding and antibonding combination of d_{z^2} orbitals reveals a plausible answer to the nature of this d^8-d^8 interaction. In the previous treatment (Figure 4.44), the antibonding character of the d_{z^2}–d_{z^2} combination was minimized by mixing in contributions from a higher-energy p-orbital. This model is based on the assumption that the two square-planar metal centers are approaching each other face-to face, but it has already been established that this is not the case for **14-Ni$_2$**. The output from electronic structure calculations indicated that the distortion to C_2-symmetry allows for the mixing of π-type orbitals into the ideally σ-type orbitals. The enlarged d_{z^2}–d_{z^2} orbital interactions are presented in Figure 4.50.

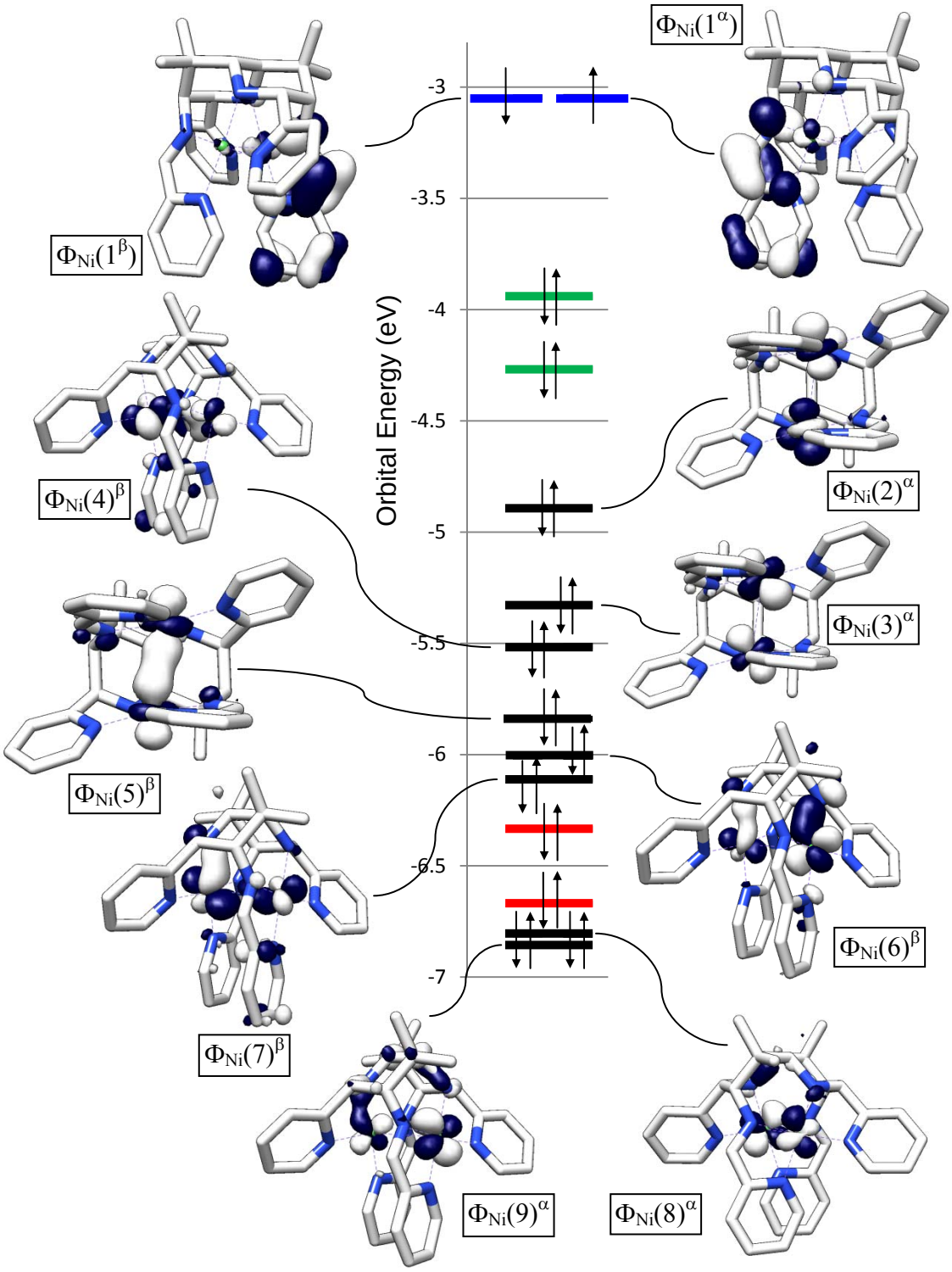

Figure 4.49. Calculated electronic structure of **14-Ni$_2$** using the Broken Symmetry BS[1,1] formalism. Black energy levels are metal based (>80% M character), green are N_{amide}-based, and red are Py π^b-orbitals.

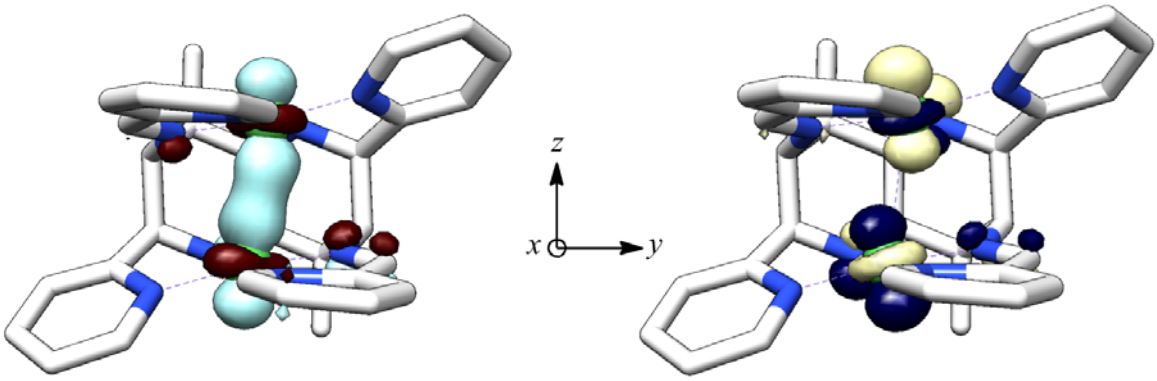

Figure 4.50. Computed molecular orbitals for the d_{z^2}- d_{z^2} bonding (left, $\Phi_{Ni}(5)$) and antibonding (right, $\Phi_{Ni}(2)$) interactions in **14-Ni$_2$**. The axes are indicated.

The orbitals that define the σ^b combination are essentially pure d_{z^2} orbitals, whereas the σ^* combination contains 22% d_{yz}-character. This mixing allows the the σ^* orbital to minimize antibonding interactions by rotating the two d_{z^2} orbitals out of mutual alignment. This interaction is shown schematically in Figure 4.51.

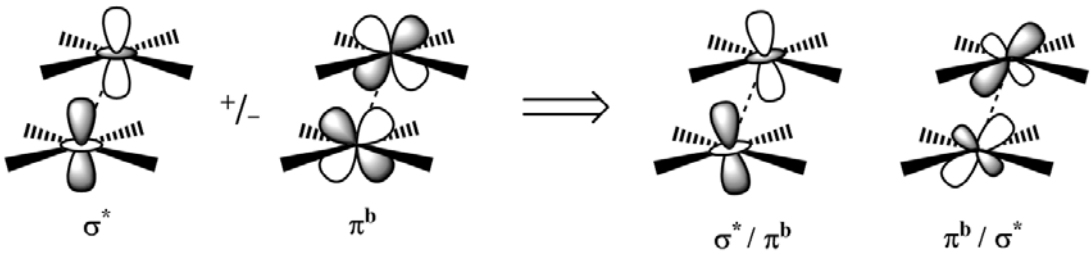

Figure 4.51. Illustration of the orbital mixing that allows minimization of σ^*-character.

The electronic structure of **14-Co$_2$** is not so straightforward. Recall that the imino-pyridine distances were consistent with monoreduction, giving a formal oxidation state of 2+ per cobalt. Assuming the M-M bonding scheme in Fig. 4.41 is accurate, depopulation of the d_{z^2}-d_{z^2} σ^* orbital is expected (relative to **14-Ni$_2$**). As shown in Figure 4.52, not only is this orbital is still filled, but the imino-pyridine π^* HOMO contains substantial metal-character (16%).

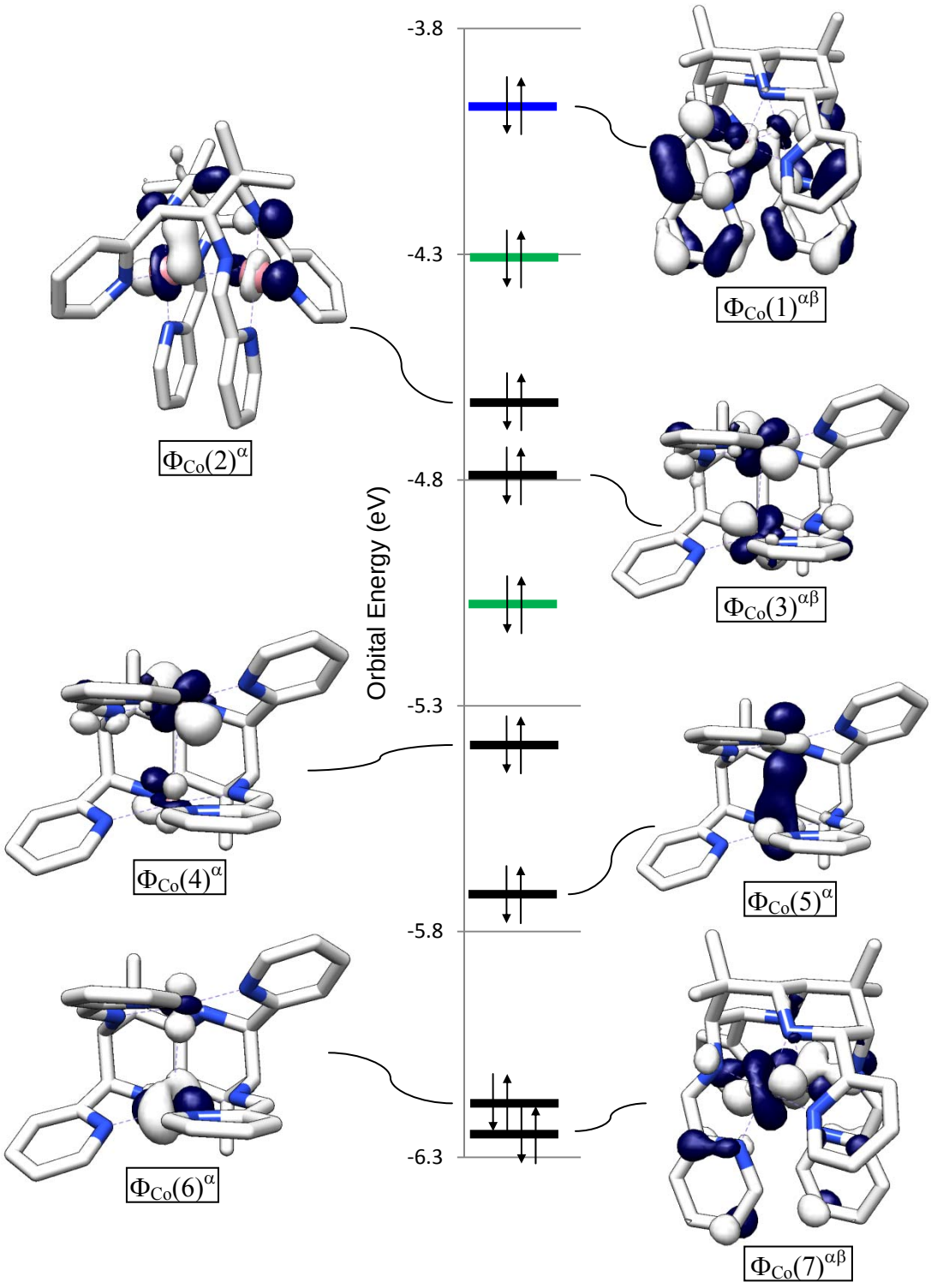

Figure 4.52. Calculated electronic structure of **14-Co_2** using the Broken Symmetry BS[2,2] formalism. The plotted orbitals are the geometry-basis wavefunctionsand the spins are indicated. Black levels are metal-based, green levels are N_{amide}-based, and the blue level is the imino-pyridine π^* orbital combination.

The corresponding magnetic orbitals for the **14-Co$_2$** system, which give an indication of spin localization, are presented in Figure 4.53.

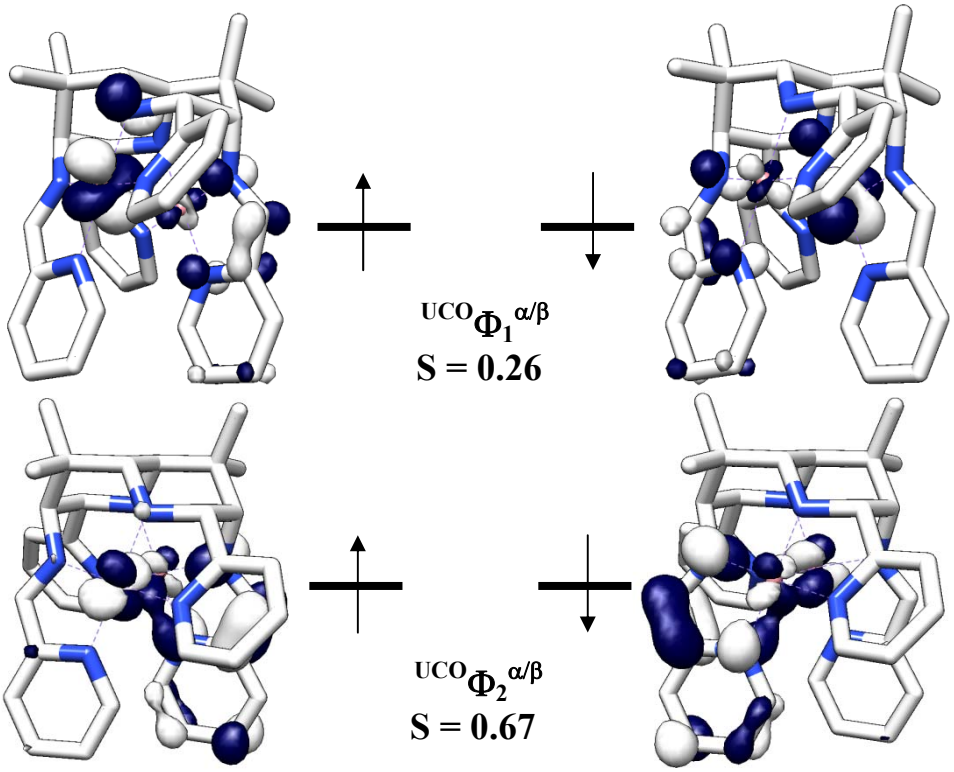

Figure 4.53. Magnetic orbitals of **14-Co$_2$** from BS[2,2] calculation.

Although it could be said that the $^{UCO}\Phi_1^{\alpha/\beta}$ orbitals contain more metal character than the $^{UCO}\Phi_2^{\alpha/\beta}$ orbitals, there is little ligand- or metal-localization. Because of this covalency, it is possible to rationalize an essentially Co(I) center despite the crystallographic data indicating monoreduction of the imino-pyridine moiety. Due to the statistical uncertainty in the imino-pyridine bond lengths, the **14-Co$_2$** and **14-Ni$_2$** distances are indistinguishable and any comparison is suspect. However, the **14-Co$_2$** distances are distinct from those for **14-Cr$_2$** and indicate that the imino-pyridines in **14-Co$_2$** are *somewhat* less reduced. The calculated Mayer bond order between the two Co atoms is 0.1221, only slightly larger than the 0.1018 calculated for the Ni-Ni bond in **14-Ni$_2$** (c.f. 0.4095 for **14-Cr$_2$**). The computational results suggest that **14-Co$_2$** is at

least partly described as a Co(I)-Co(I) dimer. In this way the problem may not be that the Co-Co bond is too long, but instead it is the Ni-Ni bond that is too *short*. One possibility is that the Ni-Ni distance has less to do with the metal interaction and more to do with and imino-pyridine π-interaction. In **14-Ni$_2$**, the *ortho*-carbons of the two imino-pyridine fragments are only 2.979 Å apart and well-within the sum of their van der Waals radii (3.4 Å).[26] The greater radical-anion character in the imino-pyridine π^*-orbitals for **14-Ni$_2$** indicated by the computational results could result in a significant AFM-type interaction. This interaction may, in turn, be stabilized by a compression that artificially brings the two Ni atoms closer. Such a π^* interaction has been observed in the $ZrX_2(disq)_2$ (X = Cl, Br, I; disq = *N*,*N*'-bis(*neo*-pentyl)-*ortho*-diimino-semiquinonate) family of complexes prepared by Heyduk *et al*.[35] A more comprehensive computational analysis is necessary to properly address these issues.

It was desirable to extend this family of compounds to the remaining members of the first row. Extending the bimetallic complexes of **14** to metals besides Cr, Co and Ni required precursor complexes containing metals in their +2 oxidation state with an internal base. It has already been shown (Section 4.5) that $Fe(N(TMS)_2)(thf)$ is not competent for the same C-C coupling reaction to produce **14**, and reactions conducted with $\{Fe(NPh_2)_2\}_2$, $Mn(N(TMS)_2)_2$, and $Zn(N(TMS)_2)_2$ failed to produce isolable products upon treatment with **Me$_2$C(ImCH$_2$Py)$_2$**. As best as can be determined, there is a lack of well-studied M(II) bis(amides) for metals earlier than Cr. The simple coordination complexes $(TMEDA)_2TiCl_2$ and $(TMEDA)_2VCl_2$ can be readily prepared, and it was hoped that the TMEDA may be a strong-enough Lewis-base to deprotonate **Me$_2$C(ImCH$_2$Py)$_2$** with concomitant loss of (TMEDA)•HCl.

4.8. Reactivity of $Me_2C(ImCH_2Py)_2$ with $(TMEDA)_2TiCl_2$

Treatment of a benzene solution of $(TMEDA)_2TiCl_2$ with a benzene solution of **$Me_2C(ImCH_2Py)_2$** resulted in the deposition of a crystalline red precipitate over the course of 24 h. ^1H NMR analysis of the red crystals indicated a C_s-symmetric molecule consistent with reductive coupling of the two imine fragments to a cyclopropane ring. The structure was confirmed by X-ray crystallography and is provided in Figure 4.54, selected parameters are presented in Table 4.9 and the crystallographic data are presented in Table 4.8.

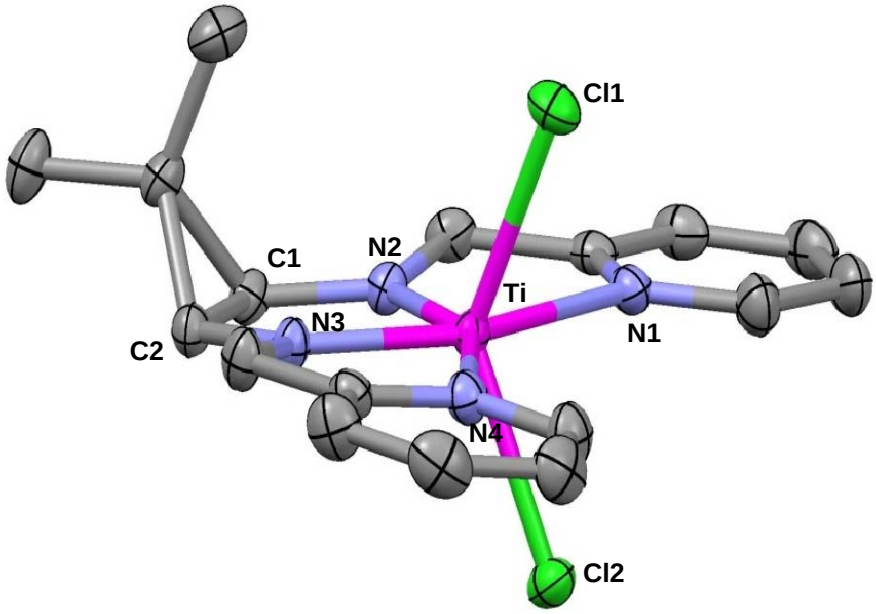

Figure 4.54. Molecular structure of **$^cPr(ImCH_2Py)_2TiCl_2 \bullet ½C_6H_6$**.

Table 4.10. Selected bond angles and interatomic distances for **$(^{cPr}Im_2Py_2)TiCl_2$**.

Selected Bond Distances (Å)		Selected Bond Angles (degrees)	
Ti-N1	2.2586(12)	N1-Ti-N2	73.83(4)
Ti-N2	1.9356(11)	N2-Ti-N3	77.96(5)
Ti-N3	1.9346(12)	N3-Ti-N4	74.03(5)
Ti-N4	2.2553(11)	N4-Ti-N1	134.21(4)
Ti-Cl1	2.3690(4)	Cl1-Ti-Cl2	133.931(17)
Ti-Cl2	2.3672(5)		
C1-C2	1.4916(19)		

The formation of **^{c}Pr(ImCH$_2$Py)$_2$TiCl$_2$** can be thought of as arising from a McMurry-type coupling of the two imines to yield a bis(amido)cyclopropane ring (Eq. 4.15). There are a few similar examples of reductive coupling of imines to cyclopropane rings,[36] although the C-C bonds formed in those cases are longer (1.517-1.639 Å).

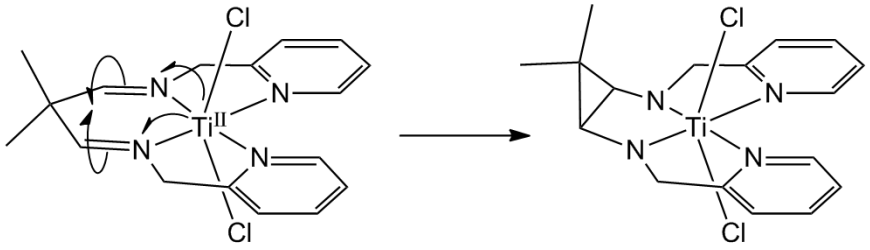

Eq. 4.15

In an attempt to use this compound to generate the desired intermediate **(N$_4$)Ti** (as in Figure 4.42), **^{c}Pr(ImCH$_2$Py)$_2$TiCl$_2$** was treated with LiHMDS in C_6D_6 at room temperature. There was an immediate color change from yellow-red to deep purple, and after several hours at room temperature a new species was observed consistent with monodeprotonation and substitution of the remaining chloride. The proposed transformation is shown in Scheme 4.6.

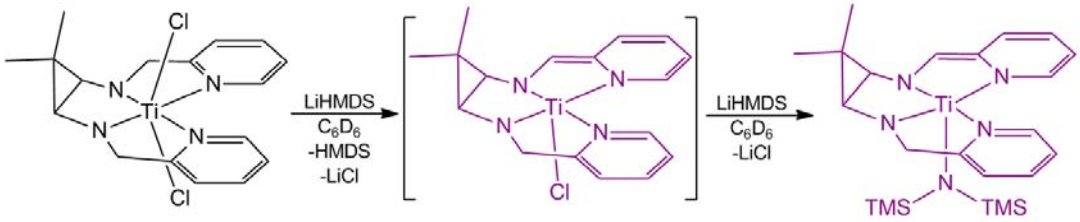

Scheme 4.7. Reactivity of **^{c}Pr(ImCH$_2$Py)$_2$TiCl$_2$** with LiHMDS.

The ^{1}H NMR spectrum contains resonances attributable to the desymmetrized **(^{cPr}HN$_4$)Ti(N(TMS)$_2$)** shown in Scheme 4.6. The two distinct TMS environments at 0.74 ppm and –0.02 ppm indicate hindered rotation about the Ti-N bond, possibly due to one of the TMS groups being localized in the pocket between the pyridine rings. Thermolysis of this compound at 100 °C for 3 days produced a mixture of unidentifiable products. When **^{c}Pr(ImCH$_2$Py)$_2$TiCl$_2$**was treated with NpLi in C_6D_6

for two days a new compound was identified consistent with **^{c}Pr(ImCH$_2$Py)$_2$Ti(Np)$_2$** (Eq. 4.16).

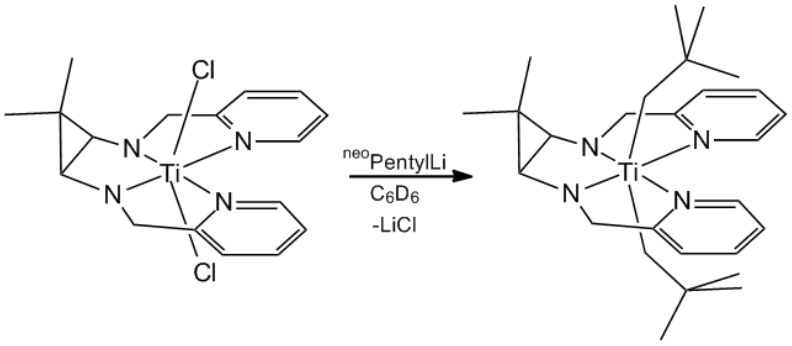

Eq. 4.16

Scale-up and isolation of this bis(alkyl) were hampered by formation of a purple solid that is as-yet unidentified. Attempts to reduce the dichloride with NaK and Na/Hg produced intractable mixtures of darkly-colored products.

Attempts to were made to elicit similar reactivity from (TMEDA)$_2$VCl$_2$. Although the vanadium precursor was reactive with **Me$_2$C(ImCH$_2$Py)$_2$**, the fate of the reactants could not be determined.

Conclusion

The ligand frameworks explored all involved multiple 2-aza-allyl fragments; it appears that 2-aza-allyl anion is stable enough to form, but unstable with respect to reductive C-C coupling or attack of a nearby imine. This could be the origin of the failure of the H$_2^{R}$PBA and H$_2^{R}$mcSmif ligand families; the relative lack of steric protection for the 2-aza-allyl moieties may have resulted in oligomerization via C-C coupling of the types discussed above. In many of the systems shown above it seems that reduced imino-pyridine moieties are thermodynamic sinks, suggesting an interesting route towards such complexes. The synthesis of **^{c}Pr(ImCH$_2$Py)$_2$TiCl$_2$** establishes the stability of the coordinated cyclopropane diamide construct and lends credence to the proposed structure of **(HN$_4$)Fe(N(TMS)$_2$)** (Fig 4.42).

Experimental

General Considerations. All manipulations were carried out either using a nitrogen glovebox or high-vacuum and Schlenk techniques unless otherwise stated. All glassware was oven dried. Benzene-d_6 and toluene-d_8 were refluxed over sodium metal, vacuum distilled and stored under nitrogen over activated 4Å molecular sieves. Acetonitrile-d_3 was dried over refluxing CaH_2, vacuum distilled and stored over CaH_2. Tetrahydrofuran-d_8 was refluxed over sodium, vacuum distilled and stored over sodium benzophenone-ketyl. All solvents were distilled from CaH_2, $LiAlH_4$, sodium metal or sodium benzophenone-ketyl solutions. Li(^{neo}Pentyl),[37] $FeBr_2(thf)_2$,[38] $Fe(N(TMS)_2)_2(thf)$,[39] $Cr(N(TMS)_2)_2(thf)_2$,[5b] $\{Fe(NPh_2)_2\}_2$,[40] $\{Fe(2,4,6\text{-trimethylphenyl})_2\}_2$,[41] $\{Ni(NPh_2)_2\}_2$,[42] $Mn(N(TMS)_2)_2$,[43] $Zn(N(TMS)_2)_2$,[44] $(TMEDA)_2TiCl_2$,[45] $(TMEDA)_2VCl_2$,[46] *tert*-butyl lutidene,[47] *tert*-butyl-2,6-pyridinedicarboxylic acid,[48] 2,6-pyridine dicarboxaldehyde,[49] 2,6-pyridine dimethylammonium dihydrobromide,[50] 1,1-cyclopentanedicarboxaldehyde,[51] and 6,6'-methylenebis(4-(*tert*-butyl)-2-methylphenol)[15] were prepared according to literature procedures. All other reagents were purchased from various suppliers and used as received.

^1H and $^{13}C\{^1H\}$ NMR spectra were obtained on Varian 300 MHz (Mercury), 400 MHz (INOVA), 500 MHz (INOVA), and 600 MHz (INOVA) spectrometers. ^1H and ^{13}C NMR shifts are referenced to benzene-d_6 (^1H, δ 7.16 ppm; ^{13}C, δ 128.39 ppm), toluene-d_8 (^1H, δ 2.09 ppm; ^{13}C, δ 20.40 ppm), acetonitrile-d_3 (^1H, δ 1.94 ppm; ^{13}C, δ 118.26 ppm), tetrahydrofuran-d_8 (^1H, δ 3.58 ppm; ^{13}C, δ 67.57 ppm), dichloromethane-d_2 (^1H, δ 5.32 ppm; ^{13}C, δ 53.84 ppm), deuterium oxide (^1H, δ 4.79 ppm; ^{13}C, *C*H_3CN spike, δ 1.79 ppm) .^{19}F spectra were obtained on Varian 400 MHz (INOVA) and referenced to $CFCl_3$ (δ = 0 ppm). Elemental analyses were performed by Robertson Microlit Laboratories in Madison, NJ. High-resolution mass spectra

were obtained on a JEOL GCMate II Mass Spectrometer using the EI+ mode (70 eV) operating at 3000 resolving power. Samples were introduced through a heated direct-insertion probe and PFK was used as an internal reference. Cyclic voltammogramic studies were performed on a BASi-EC Epsilon electrochemical workstation operating on the BASi Epsilon-EC software (version 2.00.71._USB). Voltammograms were recorded in THF solution at ~1 mM concentration using $[^{n}Bu_4N]PF_6$ (0.1 M) as an electrolyte with a 3 mm glassy-carbon working electrode, Pt-wire counter electrode, and Ag/Ag^+ reference electrode. The cyclic voltammetry experiments were referenced to the ferrocene$^{0/+}$ redox couple at +0.683 V.

Synthesis. 1. Dimethyl 4-(tert-butyl)pyridine-2,6-dicarboxylate. To a 100 mL round bottom flask was added 4-(tert-butyl)pyridine-2,6-dicarboxylic acid 11.01 g (49 mmol) and a reflux condenser was affixed. Thionyl chloride was added (50 mL, 0.69 mol), an oil bubbler was connected via Tygon tubing and the apparatus was set to reflux. After five hours evolution of SO_2 ceased and, upon cooling to room temperature, was stripped of volatiles *in vacuo*. Methanol (50 mL) was added in portions and the solution was refluxed for 3 h. The resultant solution was cooled to –78°C and the white crystalline precipitate was isolated via filtration in two crops. Drying the combined solids on the high-vacuum line yielded 10.7 g (43 mmol, 86%). ^{1}H NMR ($CDCl_3$): δ1.34 (s, C(C*H*$_3$)$_3$, 9H), 4.02 (s, OC*H*$_3$, 6H), 8.31 (s, C$_{py}$*H*, 2H).

2. (4-(tert-butyl)pyridine-2,6-diyl)dimethanol. Dimethyl 4-(tert-butyl)pyridine-2,6-dicarboxylate (10.7 g, 43 mmol) and $NaBH_4$ (6.77 g, 0.179 mol, 4.2 eq) were added to a 250 mL round bottom flask. Absolute ethanol (100 mL) was added, a reflux condenser was affixed and the system was purged with argon. The suspension was refluxed for 2 h under argon during which time there was significant gas evolution and a color change from light yellow to pink. Upon cooling to room temperature water (50 mL) and saturated Na_2CO_3 solution were added (25 mL) to the

flask and the resulting suspension was refluxed for an hour. After cooling two phases formed and the upper layer was separated and dried over $MgSO_4$. Removal of solvent *in vacuo* yielded 6.40 g (33 mmol, 78%) of a white powder. ^{1}H NMR ($CDCl_3$): δ 1.30 (s, C(CH_3)$_3$,9H), 3.56 (broad s, O*H*, 2H), 4.74 (s, CH_2, 4H), 7.17 (s, ^{m}C$_{py}$*H*, 2H). ^{13}C NMR ($CDCl_3$): δ 30.53 (C(*C*H$_3$)$_3$), 35.03 (*C*(CH$_3$)$_3$), 64.30 (*C*H$_2$OH), 116.83 (^{m}*C*$_{py}$H), 158.47 (^{o}*C*$_{py}$), 162.51 (^{p}*C*$_{py}$).

3. 4-(tert-butyl)pyridine-2,6-dicarbaldehyde. A 50 mL round bottom flask was charged with oxalyl chloride (0.44 g, 3.5 mmol) and CH_2Cl_2 (22 mL). The solution was cooled to –78 °C and a solution of DMSO (3.2 mL, 4.0 mmol) in CH_2Cl_2 (5 mL) was added dropwise. The resulting solution was stirred for 10 minutes at –78 °C. A solution of (4-(tert-butyl)pyridine-2,6-diyl)dimethanol (1.0 g, 5.2 mmol) in DMSO (3 mL) and CH_2Cl_2 (5 mL) was added dropwise. After stirring for 30 minutes triethylamine (7.2 mL, 52 mmol) was added and the suspension was stirred for 2 h while allowing to warm to room temperature. The reaction was quenched with water (35 mL) and the aqueous layer was extracted with CH_2Cl_2 (3 x 25 mL). The organic layers were combined and dried over $MgSO_4$. The solution was filtered and the solvent removed *in vacuo* yielding a brown solid. The product was purified by sublimation (70 °C), yielding 400 mg (2.1 mmol, 40%) off an off-white solid. ^{1}H NMR ($CDCl_3$): δ 1.39 (s, C(CH_3)$_3$, 9H), 8.18 (s, C$_{py}$*H*, 2H), 10.17 (s, C*H*O, 2H). ^{13}C NMR ($CDCl_3$): δ 30.46 (C(*C*H$_3$)$_3$), 35.56 (*C*(CH$_3$)$_3$), 122.56 (^{m}*C*$_{py}$H), 153.19 (^{o}*C*$_{py}$), 163.51 (^{p}*C*$_{py}$), 192.90 (*C*HO).

4. 2,6-bis(bromomethyl)-4-(tert-butyl)pyridine. Triphenylphosphine (8.14 g, 31 mmol) and CH_2Cl_2 (100 mL) were added to a 250 mL three-neck round bottom flask with an attached dropping funnel. The apparatus was purged with argon and cooled to 0 °C. Bromine (4.98 g, 31.1 mmol) and CH_2Cl_2 (10 mL) were added to the dropping funnel and the resulting solution was added over the course of five minutes.

After stirring for fifteen minutes (4-(tert-butyl)pyridine-2,6-diyl)dimethanol (3.0 g, 15.5 mmol) was added in one portion under argon counterflow. The suspension was stirred for 4 h and allowed to warm to room temperature. Removal of the solvent *in vacuo* results in a brown solid composed of triphenylphosphine oxide and 2,6-bis(bromomethyl)-4-(tert-butyl)pyridinium bromide. The ^{1}H NMR spectrum of the hydrobromide salt is as follows: 1.37 ppm, s, 9H; 5.08 ppm, s, 4H; 7.98 ppm, s, 2H; 12.50 ppm, broad s., 1H. The hydrobromide salt was dissolved in chloroform (100 mL) and stirred with 50 mL saturated Na_2CO_3 until evolution of CO_2 ceased. The chloroform was removed *in vacuo* and the resulting solid was suspended in 150 mL benzene. The suspension was heated to reflux and filtered hot to separate the triphenylphosphine oxide from the product. After ten repetitions, 2.96 g (9.3 mmol 60%) of light pink dibromide was isolated. ^{1}H NMR (C_6D_6): δ 1.22 (s, C(C*H*$_3$)$_3$, 9H), 4.43 (s, C*H*$_2$, 4H), 7.24 (s, C$_{py}$*H*, 2H). ^{13}C NMR ($CDCl_3$): δ 30.57 (C(*C*H$_3$)$_3$), 34.48 (*C*H$_2$Br), 35.01 (*C*(CH$_3$)$_3$), 120.13 (^{m}*C*$_{py}$H), 157.52 (^{o}*C*$_{py}$), 162.48 (^{p}*C*$_{py}$).

5. (4-(tert-butyl)pyridine-2,6-diyl)dimethanaminium dibromide. A 25 mL round bottom flask was charged with 2,6-bis(bromomethyl)-4-(tert-butyl)pyridine (2.61g, 8.2 mmol), potassium phthalimide (3.08 g, 16.6 mmol, 2.03 eq.) and 20 mL DMF under argon purge. The resulting solution was refluxed for 5 h and, upon cooling, was stripped of volatiles *in vacuo*. The residual material was treated with 100 mL water and the resulting suspension was filtered to yield an off-white solid. This solid, the bis(phthalimide), was treated with 40% HBr and refluxed for 3 h and the resulting suspension was filtered and washed with water to remove phthalimide. The aqueous solution was concentrated by half and cooled to -10 °C. The dihydrobromide salt was isolated by filtration and drying *in vacuo* to yield 1.50 g (4.2 mmol, 52%) as a white powder. ^{1}H NMR (D_2O): δ 1.11 (s, C(C*H*$_3$)$_3$, 9H), 4.18 (s, C*H*$_2$, 4H), 7.34 (s,

$C_{py}H$, 2H). ^{13}C NMR (D_2O): δ 29.99 ($C(CH_3)_3$), 34.95 ($CH_2NH_3^+$), 43.14 ($C(CH_3)_3$), 119.76 ($^mC_{py}H$), 151.56 ($^oC_{py}$), 164.15 ($^pC_{py}$).

6. [3.3](2,6)pyridinophane-1,7-diene (H_2^HmcSmif). A 100 mL round bottom flask was charged with 2,6-pyridine dimethylammonium dihydrobromide (1.27 g, 4.2 mmol) and sodium hydride (210 mg, 8.8 mmol, 2.1 eq). THF (40 mL) was added to the flask and a reflux condenser was affixed. After 5 h the solution was cooled, filtered, and the solvent was removed *in vacuo* to yield 379 mg (2.8 mmol, 65%) of the neutral diamine as a yellow crystalline solid. The diamine was added to a 100 mL round bottom flask with 20 mL CH_2Cl_2. 2,6-Pyridine dicarboxaldehyde (379 mg, 2.8 mmol, 1 eq.) in CH_2Cl_2 (20 mL) was added dropwise and the solution was stirred for 12 h, during which time a white precipitate formed. The precipitate was isolated by filtration and dried *in vacuo* to yield 350 mg (1.3 mmol, 46%). ^1H NMR ($CDCl_3$): δ 5.04 (s, CH_2, 4H), 7.32 (d, J = 7.5 Hz, $^mC_{py}H$, 2H), 7.68 (t, J = 7.5 Hz, $^pC_{py}H$, 1H), 7.82 (t, J = 8 Hz, $^mC_{py}H$, 1H), 8.12 (d, J = 8 Hz, $^pC_{py}H$, 2 H), 8.60 (s, ^{im}CH, 2H).

7. H_2^{tBu}mcSmif. A 250 mL Erlemmeyer flask was charged with 174 mg t-butyl 2,6-pyridine dicarboxaldehyde (0.91 mmol) and 25 mL CH_2Cl_2. A solution of 125 mg pyridine-2,6-diyldimethanamine (0.91 mmol) in 25 mL CH_2Cl_2 was added dropwise and the solution was stirred for 12 h. The volatiles were removed *in vacuo*, the residue was triturated with pentane and dried to yield 209 mg (0.67 mmol, 74%) of a flaky, yellow solid. ^1H NMR ($CDCl_3$): δ 1.38 (s, $C(CH_3)_3$, 9H), 5.06 (s, CH_2, 4H), 7.33 (d, J = 7.4 Hz, $^mC_{py}H$, 2H), 7.67 (t, J = 7.4 Hz, $^pC_{py}H$,1H), 8.33 (s, $^pC_{py}H$, 2H), 8.62 (s, ^{im}CH, 2H).

8. Bis(2-triflato-5-(tert-butyl)-3-methylphenyl)methane. To a 100 mL round bottom flask was added 6,6'-methylenebis(4-(tert-butyl)-2-methylphenol) (1.69 g, 5.0 mmol) and pyridine (1.6 mL, 25 mmol, 5 eq.). Upon cooling to 0 °C, a solution of trifluoromethanesulfonic anhydride (2.2 mL, 13.1 mmol, 2.6 eq.) in CH_2Cl_2 (50 mL)

was added dropwise over the course of 8 minutes under an argon atmosphere. The resulting solution was stirred for 30 minutes and allowed to warm to room temperature, stirring for an additional hour. The reaction mixture was quenched with 40 mL of 1.5M HCl and the layers were separated. The aqueous layer was washed 3x with 30 mL CH_2Cl_2 and the combined organic layers were dried over $MgSO_4$. The solvent was removed *in vacuo* and pentane (10 mL) was added to the resulting suspension. A white solid was removed via filtration and all volatiles removed *in vacuo* yielding 2.83 g (4.7 mmol, 94%) of the product as a yellow oil. ^{1}H NMR ($CDCl_3$): δ 1.21 (s, C(C*H*$_3$)$_3$, 18H), 2.41 (C*H*$_3$), 4.19 (C*H*$_2$), 6.88 (s, $^{6\text{-Ar}}$C*H*, 2H), 7.17 (s, $^{4\text{-Ar}}$C*H*, 2H). ^{19}F NMR ($CDCl_3$): –73.91(s, C*F*$_3$, 6F). ^{13}C NMR ($CDCl_3$): δ 17.69 (*C*H$_3$), 31.22 (C(*C*H$_3$)$_3$), 31.67 (*C*H$_2$), 34.62 (*C*(CH$_3$)$_3$), 118.75 (q, J = 320 Hz, *C*F$_3$), 126.98 ($^{4\text{-Ar}}$*C*H), 127.89 ($^{2\text{-Ar}}$*C*H), 131.13 ($^{3\text{-Ar}}$*C*), 132.08 ($^{1\text{-Ar}}$*C*), 144.23 ($^{5\text{-Ar}}$*C*), 151.32 ($^{2\text{-Ar}}$*C*).

9. Bis(2-cyano-5-(tert-butyl)-3-methylphenyl)methane. A 100 mL round bottom flask was charged with bis(2-triflato-5-(tert-butyl)-3-methylphenyl)methane (15.55 g, 25.7 mmol), zinc cyanide (7.20 g, 63.9 mmol, 2.5 eq), and $Pd(PPh_3)_4$ (1.7 g, 1.5 mmol, 6 mol %). DMF (15 mL) was added under argon purge and the system was set to reflux for 16h. Upon cooling the solid residue was crushed and suspended in 200 mL H_2O. This suspension was extracted 3x with 100 mL $CHCl_3$ and the combined organic layers were stripped of volatiles *in vacuo*. The solid was dissolved in CH_2Cl_2 and filtered through a pad of Celite. The solvent was removed *in vacuo* to yield an off-white solid which was washed with 50 mL cold (–78 °C) pentane. Drying the resulting white powder yielded 7.72 g (21.5 mmol, 84%) of the bis(nitrile). ^{1}H NMR ($CDCl_3$): δ 1.27 (s, C(C*H*$_3$)$_3$, 18H), 2.54 (s, C*H*$_3$, 6H), 4.37 (s, C*H*$_2$, 2H), 7.34 (s, $^{6\text{-Ar}}$C*H*, 2H), 7.36 (s, $^{4\text{-Ar}}$C*H*, 2H).

10. Bis(2-aminomethyl-5-(tert-butyl)-3-methylphenyl)methane ($(ImCH_2Py)_2Ar_2CH_2$). A 50 mL round bottom flask was charged with bis(2-cyano-5-(tert-butyl)-3-methylphenyl)-methane (3.54 g, 9.9 mmol) and 25 mL Et_2O was added via vacuum-transfer. The solution was cooled to 0 °C and lithium aluminum hydride (1.50 g, 39.6 mmol) was added in small portions. There was significant heat and gas evolution. After stirring for 1 h at room temperature the reaction was slowly hydrolyzed with water (0.3 mL) and 6 M NaOH (0.3 mL) and stirred for an additional 2 h. Additional water (2 mL) was added with copious stirring and then $MgSO_4$ (1 g) was added. After filtration through a pad of Celite and removal of solvent *in vacuo* a yellow oil was obtained (3.0 g, 84%). ^{1}H NMR (C_6D_6): δ 1.25 (s, C(C*H*$_3$)$_3$, 18H), 2.30 (s, C*H*$_3$, 6H), 3.75 (s, C*H*$_2$, 4H), 4.29 (s, Ar$_2$C*H*$_2$, 2H), 7.06 (s, $^{6\text{-Ar}}$C*H*, 2H), 7.13 (s, $^{4\text{-Ar}}$C*H*, 2H).

11. 2,10-diaza-(1,2),(2,1),(1,2),(2,1)-tetrakis-(3-tert-butyl-5-methyl)benzo-(2,6)pyridinocycloeikosiphane-1,11,12,21-diene (MC). A 100 ml round bottom flask was charged with 701 mg (1.91 mmol) bis(2-aminomethyl-5-(tert-butyl)-3-methylphenyl)methane and 25 mL benzene. A solution of 2,6-pyridine dicarboxaldehyde in benzene (25 mL) was added dropwise and the solution was stirred for a week at room temperature. A white precipitate formed which was isolated by filtration and washed with pentane to yield the product in 31 % yield (276 mg, 0.296 mmol). ^{1}H NMR ($CDCl_3$): δ 1.21 (s, C(C*H*$_3$)$_3$, 36H), 2.24 (s, C*H*$_3$, 12H), 4.26 (s, Ar$_2$C*H*$_2$, 4H), 4.81 (s, C*H*$_2$, 8H), 6.85 (s, $^{6\text{-Ar}}$C*H*, 4H), 7.06 (s, $^{4\text{-Ar}}$C*H*, 4H), 7.27 (t, J = 8 Hz, ^{p}C$_{py}$*H*, 2H), 7.61 (d, J = 8 Hz, ^{m}C$_{py}$*H*, 4H), 8.04 (s, ^{im}C*H*, 4H). ^{13}C NMR ($CDCl_3$): δ 19.94 (*C*H$_3$), 31.37 (C(*C*H$_3$)$_3$), 34.48 (Ar$_2$*C*H$_2$), 37.20 (*C*(CH$_3$)$_3$), 57.39 (N*C*H$_2$Py), 121.35 ($^{2\text{-Ar}}$*C*H), 125.00 (^{m}*C*$_{py}$), 137.52 ($^{5\text{-Ar}}$*C*H), 139.90 ($^{1\text{-Ar}}$*C*), 136.38 (^{p}*C*$_{py}$), 150.73 ($^{3\text{-Ar}}$*C*), 153.84 (^{o}*C*$_{py}$), 160.18 (^{im}*C*).

12. (2,10-Diaza-(1,2),(2,1),(1,2),(2,1)-tetrakis-(3-tert-butyl-5-methyl)benzo-(2,6)pyridinocycloeikosiphane-1,11,12,21-diene) iron dibromide (MC-$FeBr_2$). $FeBr_2(THF)_2$ (256 mg, 0.71 mmol) and MC (330 mg, 0.35 mmol) were added to a 25 mL round bottom flask and the flask was attached to a small swivel-frit assembly. The apparatus was evacuated, cooled to –78 °C, and THF (13 mL) was added via vacuum-transfer. The flask was stirred for 3.5 h and allowed to warm to room temperature, during which time a dark blue precipitate formed. The suspension was filtered and the blue solid was dried *in vacuo* to yield 330 mg (0.28 mmol, 81%). ^{1}H NMR (CD_2Cl_2): δ –143.46 (s, $\nu_{½}$ = 200 Hz, 1H), –3.42 (s, $\nu_{½}$ = 100 Hz, 1H), 0.73 (s, $\nu_{½}$ = 7 Hz, 9H), 1.28 (s, $\nu_{½}$ = 40 Hz, 2H), 6.63 (s, $\nu_{½}$ = 90 Hz, 6H), 8.59 (s, $\nu_{½}$ = 20 Hz, 2H), 9.45 (s, $\nu_{½}$ = 20 Hz, 2H), 11.87 (s, $\nu_{½}$ = 180 Hz, 2H), 33.59 (s, $\nu_{½}$ = 370 Hz, 2H), 50.26 (s, $\nu_{½}$ = 400 Hz, 2H), 80.17 (s, $\nu_{½}$ = 70 Hz, 2H).

13. (2,10-Diaza-(1,2),(2,1),(1,2),(2,1)-tetrakis-(3-tert-butyl-5-methyl)benzo-(2,6)pyridinocycloeikosiphane-1,11,12,21-diene) iron (MC-Fe). A 10 mL round bottom flask was charged with MC-$FeBr_2$ (50 mg, 0.043 mmol), 0.94% Na/Hg amalgam (371 mg, 0.15 mmol, 3.8 eq.), and THF (5 mL). The flask was affixed to a 180° needle-valve adapter and degassed on the high-vacuum line. After stirring at room temperature for 7 h the blue suspension had become a yellow-brown solution. The solvent was removed *in vacuo* and transferred to the glovebox. Benzene was added to the flask, the suspension was filtered, and the benzene was allowed to evaporate to yield 25 mg (0.025 mmol, 58%) of a brown solid. ^{1}H NMR (C_6D_6): δ –126.37 (s, $\nu_{½}$ =3440 Hz, 4H), –11.07 (s, $\nu_{½}$ = 960 Hz, C(CH_3)$_3$, 36H), –1.95 (s, $\nu_{½}$ = 220 Hz, 4H), 6.02 (s, $\nu_{½}$ = 320 Hz, 4H), 8.49 (s, $\nu_{½}$ = 260 Hz, CH_3, 12H), 74.95 (s, $\nu_{½}$ = 1300 Hz, 8H), 76.71 (s, $\nu_{½}$ = 2400 Hz, 2H), 79.08 (s, $\nu_{½}$ = 1200 Hz, 8H), 116.90 (s, $\nu_{½}$ = 2000 Hz, 8H), 172.57 (s, $\nu_{½}$ = 2160 Hz, 4H). μ_{eff} (Evans' method, C_6D_6, RT) = 2.0 μ_B.

14. 6,6'-Methylenebis(4-(tert-butyl)-2-methylbenzaldehyde). To a 50 mL round bottom flask was added bis(2-cyano-5-(tert-butyl)-3-methylphenyl)-methane (1.20 g, 3.3 mmol) and 25 mL benzene was added via vacuum-transfer. A solution of DIBAL-H in hexanes (10 mL, 10 mmol, 3 eq) was added dropwise at 0 °C and the solution was stirred for 2 d. Aqueous HCl (10 mL, 1M) was added dropwise during which there was gas evolution and a color change from yellow to pink and then back to yellow. The organic layer was concentrated by half and 4 mL concentrated HCl was added. The mixture was stirred rapidly and refluxed for 2 h. Upon cooling the organic layer was separated, dried over Na_2SO_4, and the solvent removed *in vacuo* yielding 0.643 g (1.6 mmol, 54%). ^{1}H NMR (C_6D_6): δ 1.09 (s, C(C*H*$_3$)$_3$, 18H), 2.40 (s, C*H*$_3$, 6H), 4.79 (s, Ar$_2$C*H*$_2$, 2H), 6.94 (s, $^{6\text{-Ar}}$C*H*, 2H), 6.95 (s, $^{4\text{-Ar}}$C*H*, 2H), 10.47 (s, ArC*H*O, 2H). ^{13}C NMR (C_6D_6): δ 21.20 (*C*H$_3$), 31.22 (C(*C*H$_3$)$_3$), 35.19 (*C*(CH$_3$)$_3$), 37.37 (*C*H$_2$), 127.12 ($^{5\text{-Ar}}$*C*H), 127.65 ($^{3\text{-Ar}}$*C*H), 130.97 ($^{1\text{-Ar}}$*C*), 141.87 ($^{6\text{-Ar}}$*C*), 143.79 ($^{2\text{-Ar}}$*C*), 156.47 ($^{4\text{-Ar}}$*C*), 192.56 (*C*HO).

15. ((Methylenebis(4-(tert-butyl)-2-methyl-6,1-phenylene))bis(methanylylidene))bis(1-(pyridin-2-yl)methanamine) ((ImCH$_2$Py)Ar)$_2$CH$_2$). Bis(2-carboxaldehyde-5-(tert-butyl)-3-methylphenyl)methane (0.600 g, 1.6 mmol) was added to a 20 mL scintillation vial with 2 mL CH_2Cl_2 and a solution of aminomethylpyridine (0.540 g, 5 mmol, 3 eq.) was added dropwise. Solid $MgSO_4$ (0.300 g, 2.5 mmol) was added in one portion and the suspension was stirred for 12 h. The suspension was filtered and the filter cake was washed with CH_2Cl_2. The solvent was removed *in vacuo* and the solid was crushed and suspended in cold (–40 °C) pentane. The supernatant was decanted and the residue dried to yield 0.740 g (1.4 mmol, 77 %) as a white solid. ^{1}H NMR (C_6D_6): δ 1.19 (s, C(C*H*$_3$)$_3$, 18H), 2.48 (s, C*H*$_3$, 6H), 4.73 (s, Ar$_2$C*H*$_2$, 2H), 4.94 (s, C*H*$_2$, 4H), 6.62 (dd, J = 4.7, 7.5 Hz, $^{5\text{-py}}$C*H*,

2H), 7.10 (s, $^{6\text{-Ar}}$C*H*, 2H), 7.10 (t, J = 7.5 Hz, $^{4\text{-py}}$C*H*, 2H), 7.12 (s, $^{4\text{-Ar}}$C*H*, 2H), 7.20 (d, J = 7.5 Hz, $^{3\text{-py}}$C*H*, 2H), 8.48 (d, J = 4.7 Hz, $^{6\text{-py}}$C*H*, 2H), 8.71 (s, $^{\text{im}}$C*H*, 2H).

16. Bis[3,7-di-tert-butyl-1,9-dimethyl-N10,N11-bis(pyridin-2-ylmethylene)-10,11-dihydro-5H-dibenzo[a,d][7]annulene-10,11-diamine] dichromium (12-Cr$_2$). A small bomb was charged with a solution of $(ImCH_2Py)Ar)_2CH_2$ (0.245 g, 0.45 mmol) in 5 mL C_6H_6 and a solution of $Cr(N(TMS)_2)_2(thf)_2$ (0.233 g, 0.45 mmol) in 5 mL C_6H_6 was added dropwise. The color changed from light lavender to purple, then brown/green, and finally red over the course of a few minutes. The bomb was sealed and stirred in a 50 °C oil bath for 1 h. The solvent was removed *in vacuo* and the residue was triturated with pentane to yield a red-brown powder (178 mg, 0.30 mmol, 67%). μ_{eff} (Evans' method, C_6D_6, RT) = 3.8 μ_B.

17. 2,2-Dimethyl-N^1,N^3-bis(pyridin-2-ylmethylene)propane-1,3-diamine (NpImPy). To a 20 mL scintillation vial was added 2-pyridinecarboxaldehyde (4.2 g, 39 mmol) in 2 mL Et_2O and $MgSO_4$(1 g, 8.3 mmol, 0.2 eq.). A solution of 2,2-dimethyl-1,3-diaminopropane in Et_2O (2 mL) was added dropwise at room temperature. The solution was allowed to stir for 2 h at room temperature at which point the $MgSO_4$ was removed by filtration. The yellow filtrate was stripped by rotary evaporation and the resultant yellow oil was evacuated on the high-vacuum line. After 2 h the oil had solidified and was isolated as yellow crystals in 95% yield (5.22 g, 18.6 mmol). The ^{1}H NMR spectrum matched the literature data.[54]

18. (NpImPy)Ni. A 25 mL round bottom flask was charged with NpImPy (0.400 g, 1.43 mmol), $Ni(COD)_2$ (0.390 g, 1.41 mmol) and 10 mL toluene, resulting in an immediate color change from colorless to deep green. The flask was affixed to a small swivel-frit assembly and degassed on the high-vacuum line. The solution was filtered and the volatiles removed *in vacuo*. The residual solid was triturated with

pentane (10 mL) and washed with cold pentane (–78 °C). The dark green/black product was isolated as a powder (0.390 g, 1.15 mmol, 81%). ^{1}H NMR (C_6D_6): δ 1.06 (s, CH_3, 6H), 3.05 (s, CH_2, 4H), 6.71 (dd, J = 6, 7 Hz, $^{5\text{-Py}}$CH, 2H), 6.85 (d, J = 8 Hz, $^{3\text{-Py}}$CH, 2H), 6.95 (dd, J = 6.5, 8 Hz, $^{4\text{-Py}}$CH, 2H), 7.67 (s, $^{\text{im}}$CH, 2H), 9.29 (d, J = 6 Hz, $^{6\text{-Py}}$CH, 2H). ^{13}C NMR (C_6D_6): 24.34 (*C*H_3), 41.09 (*C*$(CH_3)_2$), 71.62 (*C*H_2), 117.52 ($^{5}C_{\text{py}}$), 124.13 ($^{3}C_{\text{py}}$), 124.65 ($^{4}C_{\text{py}}$), 138.69 (C_{im}), 147.21 ($^{2}C_{\text{py}}$), 147.65 ($^{6}C_{\text{py}}$). Anal. calc'd for $C_{17}H_{20}N_4Ni$: C, 60.22%; H, 5.95%; N, 16.52%. Found: C, 59.97%; H, 6.04%; N, 16.14%.

19. [(NpImPy)Ni]OTf. A 25 mL round bottom flask was charged with (NpImPy)Ni (0.250 g, 0.74 mmol) and AgOTf (0.190 g, 0.74 mmol) and attached to a small swivel-frit assembly. The apparatus was evacuated on the high-vacuum line, cooled to –78 °C, and acetonitrile (10 mL) was transferred in via vacuum-transfer. The solution was thawed and allowed to stir at room temperature for 1 h, during which time the solution changed from dark green to red-orange. The precipitated silver metal was removed by filtration and the acetonitrile was removed *in vacuo*. The red-orange residue was triturated 10x with 10 mL portions of THF. The residue was then taken up in 5 mL THF and cooled to –78 °C, filtered, and dried *in vacuo* to yield 0.252 g (0.48 mmol, 65%) of red-orange crystalline solid. ^{1}H NMR (CD_3CN): δ –1.18 (s, 1H), 2.95 (s, CH_3, 3H), 3.79 (s, 1H), 4.64 (s, CH_3, 3H), 7.25 (s, 1H), 7.63 (s, 1H), 8.09 (s, 1H), 14.51 (m, 2H), 15.10 (s, 1H), 43.91 (s, 1H), 48.97 (m, 2H), 50.36 (m, 2H), 51.61 (m, 2H), 54.49 (s, 1H). Anal. Calc'd for $C_{18}H_{20}F_3N_4NiO_3S$: C, 44.29%; H, 4.13%; N, 11.68%. Found (first run): C, 44.13%; H, 4.27%; N, 11.04%. Found (second run): C, 44.20%; H, 4.07%; N, 11.07%.

20. Dimethylmalonaldehyde. A 500 mL three-necked round bottom flask was charged with oxalyl chloride (14.8 mL, 175 mmol) and CH_2Cl_2 (100 mL). The solution was cooled to –78 °C and a solution of DMSO (25 mL, 352 mmol) CH_2Cl_2

(50 mL) was added dropwise over the course of an hour with mechanical stirring while monitoring the solution temperature. The resulting solution was stirred for 1.5 h and a solution of neopentyl glycol (8.0 g, 77 mmol) in DMSO (5 mL) and CH_2Cl_2 (100 mL) was added dropwise over the course of 1.5 h. After stirring for an additional 1.5 h, diisopropylethylamine (60 mL, 344 mmol) was added dropwise over the course of a half hour and allowed to warm to room temperature. The reaction was quenched with saturated NH_4Cl (150 mL) and the aqueous layer was extracted with CH_2Cl_2 (150 mL). The organic layers were combined and washed with 2M HCl (2 x 100 mL) and dried over Na_2SO_4. The solution was filtered and the solvent was mostly removed via rotary evaporation. Diethyl ether was added (100 mL) and the solvent was again mostly removed via rotary evaporation, being careful to avoid totally stripping the material (polymerization occurs). The addition of 5 mL diethyl ether produces ~10 mL of a solution of approximately 5 M (~65% yield). ^{1}H NMR (C_6D_6): δ 0.70 (s, CH_3, 6H), 9.04 (s, C*H*O, 2H). ^{13}C NMR (C_6D_6): δ 17.07 (C(*C*H_3)$_2$), 58.86 (*C*(CH_3)$_2$), 200.22 (*C*HO).

21. (2,2-Dimethylpropane-1,3-diylidene)bis(1-(pyridin-2-yl)methanamine) (Me$_2$C(ImCH$_2$Py)$_2$). A solution of dimethylmalonaldehyde (1.96 g, 10 mmol) was added to a 20 mL scintillation vial with $MgSO_4$ (1.0 g, 8.3 mmol). The vial was sealed with a polyethylene cap and cooled to 0 °C. A solution of aminomethylpyridine (2.15 g, 20 mmol) in diethylether (5 mL) was added dropwise via syringe through the polyethylene cap. After stirring for 2 h while allowing to warm to room temperature, the solvent was removed by rotary evaporation and 5 mL diethyl ether was added. The suspension was filtered through a pad of Celite and the solvent was removed from the filtrate by rotary evaporation. The resulting orange oil was evacuated on the high-vacuum line for 1 h yielding 2.53 g (9.0 mmol, 90%) of light- and temperature-sensitive **Me$_2$C(ImCH$_2$Py)$_2$**. ^{1}H NMR (C_6D_6): δ 1.23 (s, C*H*$_3$, 6H), 4.77 (s, C*H*$_2$, 4H),

6.62 (dd, J = 5, 7 Hz, $^{5}C_{py}H$, 2H), 7.11 (dd, J = 7,8 Hz, $^{4}C_{py}H$, 2H), 7.31 (d, J = 8 Hz, $^{3}C_{py}H$, 2H), 7.62 (s, ^{im}CH, 2H), 8.48 (d, J = 5 Hz, $^{6}C_{py}H$, 2H).

22. Dichromium (4,4,8,8-tetramethyl-2,6-di(pyridin-2-yl)-3,7-bis((E)-(pyridin-2-ylmethylene)amino)octahydro-1,5-naphthyridine-1,5-diide)•2 C_6H_6 (14-Cr_2). A 20 mL scintillation vial was charged with 0.855 g $Cr(N(TMS)_2)_2(thf)_2$ (1.66 mmol) and 15 mL C_6H_6. A solution of **$Me_2C(ImCH_2Py)_2$** (0.484 g, 1.72 mmol, 1.04 eq.) in C_6H_6 (15 mL) was added dropwise while swirling, during which time the solution darkened from lavender to red. The vial was capped and left unstirred for 2 d and large red-brown crystals formed in the bottom of the vial. The supernatant was decanted and the crystals were washed with benzene and pentane. After removal of volatiles *in vacuo*, 0.325 g (0.40 mmol, 48%) of crystalline **14-Cr_2** was isolated. ^{1}H NMR (d_8-toluene, 32 °C): δ –0.92 (s, 1H), 1.26 (s, 1H), 1.40 (s, 3H), 1.46 (s, 3H), 2.91 (s, 1H), 3.98 (s, 1H), 4.61 (s, 1H), 5.08 (s, 1H), 6.64 (s, 1H), 6.73 (s, 1H), 8.11 (s, 1H), 8.29 (s, 1H), 8.44 (s, 1H), 11.59 (s, 1H). Anal. Calc'd for $C_{46}H_{48}N_8Cr_2$: C, 67.63%; H, 5.92%; N, 13.72%. Found: C, 67.74%; H, 6.10%; N, 12.99%.

23. Dinickel (4,4,8,8-tetramethyl-2,6-di(pyridin-2-yl)-3,7-bis((E)-(pyridin-2-ylmethylene)amino)octahydro-1,5-naphthyridine-1,5-diide) (14-Ni_2). A 15 mL scintillation vial was charged with 0.700 g $\{Ni(NPh_2)_2\}_2$ (0.886 mmol) and 1 mL THF. A solution of **$Me_2C(ImCH_2Py)_2$** (0.500 g, 1.78 mmol, 1.0 eq) in THF (5 mL) was added dropwise while swirling the vial, during which time the solution darkened from blue to brown. The vial was capped and left unstirred for 2 weeks and black-brown crystalline solid formed in the bottom of the vial. The supernatant was decanted and the crystals were washed with diethylether. After removal of volatiles *in vacuo*, 0.330 g (0.49 mmol, 55%) of crystalline 14-Ni_2 was isolated. ^{1}H NMR (C_6D_6): δ 1.22 (s, $\nu_{1/2}$ = 20 Hz, 1H), 1.37 (s, $\nu_{1/2}$ = 12 Hz, 1H), 1.49 (s, $\nu_{1/2}$ = 8 Hz, 3H), 1.58 (s, $\nu_{1/2}$ = 11 Hz, 1H), 2.12 (s, $\nu_{1/2}$ = 6 Hz, 3H), 3.02 (s, $\nu_{1/2}$ = 26 Hz, 1H), 4.14 (s, $\nu_{1/2}$ = 14 Hz, 1H),

5.28 (s, $\nu_{1/2}$ = 14 Hz, 1H), 5.60 (s, $\nu_{1/2}$ = 35 Hz, 1H), 5.66 (s, $\nu_{1/2}$ = 16 Hz, 1H), 6.03 (s, $\nu_{1/2}$ = 20 Hz, 1H), 6.38 (m, 2H), 7.35 (s, $\nu_{1/2}$ = 20 Hz, 1H). Anal. Calc'd for $C_{34}H_{36}N_8Ni_2$: C, 60.58%; H, 5.38%; N, 16.62%. Found: C, 60.84%; H, 5.61%; N, 14.11%.

24. Dicobalt (4,4,8,8-tetramethyl-2,6-di(pyridin-2-yl)-3,7-bis((E)-(pyridin-2-ylmethylene)amino)octahydro-1,5-naphthyridine-1,5-diide) (14-Co_2). A 15 mL scintillation vial was charged with 0.684 g $Co(N(TMS)_2)_2(thf)$ (0.901 mmol) and 1 mL THF. A solution of **$Me_2C(ImCH_2Py)_2$** (0.253 g, 0.902 mmol, 1.0 eq) in THF (5 mL) was added dropwise while swirling the vial, during which time the solution darkened from blue to brown. The vial was capped and left unstirred for 2 weeks and blue-black crystalline solid formed in the bottom of the vial. The supernatant was decanted and the crystals were washed with diethylether. After drying *in vacuo*, 0.022 g (0.033 mmol, 7%) of crystalline **14-Co_2** was isolated. ^{1}H NMR (d_8-THF): δ 0.84 (s, ^{9}C*H* 1H), 2.17 (s, CH_3, 6H), 3.85 (s, ^{10}C*H*, 1H), 4.05 (s, ^{7}C*H*, 1H), 4.11 (s, ^{2}C*H*, 1H), 4.13 (s, ^{6}C*H*,1H), 4.84 (s, ^{4}C*H*, 1H), 7.14 (s, ^{11}C*H*, 1H), 7.50 (s, ^{14}C*H*, 1H), 7.60 (s, ^{13}C*H*, 1H), 8.93 (s, ^{3}C*H*, 1H) 10.04 (s, ^{1}C*H*, 1H), 13.60 (s, ^{15}C*H*, 1H). ^{13}C NMR (d_8-THF): δ 27.18 (*C*H_3), 28.33 (*C*H_3), 43.11(^{8}*C*$(CH_3)_2$), 73.01 (^{10}*C*H), 79.82 (^{7}*C*H), 94.25 (^{9}*C*H), 114.70 (^{3}*C*H), 118.21 (^{12}*C*H), 122.53 (^{14}*C*H), 128.76 (^{4}*C*H), 129.90 (^{2}*C*H), 133.10 (^{13}*C*H), 138.63 (^{1}*C*H), 140.05 (^{5}*C*), 155.09 (^{15}*C*H), 167.20 (^{11}*C*). See below for the numbering scheme.

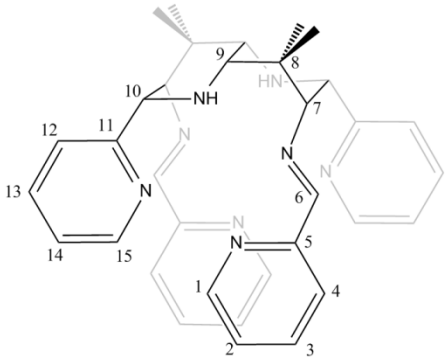

25. Dichlorotitanium (3,3-dimethyl-1,2-bis((pyridin-2-ylmethyl)amino)-cyclopropane-1,2-diide) •2 C_6H_6 ($^{cPr}Im_2Py_2$-$TiCl_2$). A 50 mL round bottom flask was charged with 0.967 g $(TMEDA)_2TiCl_2$ (2.75 mmol) and 40 mL C_6H_6. A solution of **$Me_2C(ImCH_2Py)_2$** (0.780 g, 2.78 mmol) in C_6H_6 (2 mL) was added dropwise at room temperature. The flask was attached to a medium swivel-frit assembly and degassed on the high-vacuum line. After stirring for 24 h about half of the solvent was removed *in vacuo* and the suspension was filtered. After stripping the solvent and drying *in vacuo* 1.044 g (2.38 mmol, 87%) of a light-red solid were isolated. ^{1}H NMR (C_6D_6): δ 1.07 (s, CH_3, 3H), 1.59 (s, CH_3, 3H), 3.13 (s, ^{cPr}CH_2, 2H), 4.61 (d, J = 21 Hz, C*H*H, 2H), 4.78 (d, J = 21 Hz, CH*H*, 2H), 6.51 (d, J = 8 Hz, ^{3}CH_{py}, 2H), 6.65 (dd, J = 6, 7 Hz, ^{5}CH_{py}, 2H), 6.89 (dd, J = 7, 8 Hz, ^{4}CH_{py}, 2H), 8.86 (d, J = 6 Hz, ^{6}CH_{py}, 2H). ^{13}C NMR (C_6D_6): δ 13.95 (*C*H_3), 25.56 (^{cPr}*C*H), 46.06 ($(CH_3)_2$*C*), 66.09 (^{cPr}*C*H), 68.97 (*C*H_2), 119.97 ($^3C_{py}$), 121.35 ($^5C_{py}$), 136.46 ($^4C_{py}$), 149.18 ($^6C_{py}$), 162.57 (^{im}*C*).

26. d_4-(2,2-Dimethylpropane-1,3-diylidene)bis(1-(pyridin-2-yl)-methanamine) ($Me_2C(ImCD_2Py)_2$). A solution of dimethylmalonaldehyde (0.210 g, 0.10 mmol) was added to a 20 mL scintillation vial with $MgSO_4$ (1.0 g, 8.3 mmol). The vial was sealed with a polyethylene cap and cooled to 0 °C. A solution of d_2-aminomethylpyridine (240 mg, 2.2 mmol) in dichloromethane (1 mL) was added dropwise via syringe through the poly-ethylene cap. After stirring for 2 h while allowing to warm to room temperature, the solvent was removed by rotary evaporation and 2 mL diethyl ether was added. The suspension was filtered through a pad of Celite and the solvent was removed from the filtrate by rotary evaporation. The resulting orange oil was dried on the high-vacuum line for 1 h yielding 0.246 g (0.87 mmol, 84%) of light- and temperature-sensitive **d_4-$Me_2C(ImCD_2Py)_2$**. ^{1}H NMR (C_6D_6): δ 1.24 (s, CH_3, 6H), 6.62 (dd, J = 5, 7 Hz, ^{5}C$_{py}$*H*, 2H), 7.10 (dd, J = 7,8 Hz, ^{4}C$_{py}$*H*, 2H), 7.31 (d, J = 8 Hz, ^{3}C$_{py}$*H*, 2H), 7.62 (s, ^{im}C*H*, 2H), 8.48 (d, J = 5 Hz, ^{6}C$_{py}$*H*, 2H).

27. Quench of 14-Ni_2. A 5 mL round bottom flask was charged with **14-Ni_2** (50 mg, 0.074 mmol) and dimethylglyoxime (35 mg, 0.30 mmol, 4.1 eq.) and affixed to a 180° needle valve adaptor. Diethyl ether (2 mL) was added via vacuum transfer and the suspension was stirred 16 h, during which time a color change from dark red to black was observed. The solvent was removed *in vacuo* and the gas content was passed through a dry-ice/acetone trap and two LN_2 traps and collected in the Toepler pump (<2 torr, non-combustible). Tetrahydrofuran (2 mL) was added to the flask via vacuum transfer and the resulting suspension was stirred for 2 d at room temperature, during which time the black precipitate turned bright red. The solvent was removed *in vacuo* and the gas content was passed through a dry-ice/acetone trap and two LN_2 traps and collected in the Toepler pump (8 torr, 11% of expected, combustible). Benzene-d_6 was added to the residue and the ^{1}H NMR spectrum was consistent with the presence of three major products; **14-H_2**, **16**, and **17**. The putative spectral features that were assigned to **14-H_2**, **16**, and **17** are as follows; **14-H_2**: δ 3.07 (d, J = 14 Hz, ^{7}C*H*, 2H), 3.91 (s, ^{9}C*H*, 2H), 4.62 (d, J = 14 Hz, ^{10}C*H*, 2H), 8.16 (d, J = 7.5 Hz, ^{1}C*H*, 2H), 8.30 (s, ^{6}C*H*, 2H), 11.53 (s, NH, 2H). **16**: δ 4.46 (d, J = 14 Hz, ^{10}C*H*, 1H), 4.67 (d, J = 9 Hz, ^{10}C*H*', 1H). **17**: δ 2.75 (d, J = 9 Hz, ^{7}C*H*, 2H), 3.70 (s, ^{9}C*H*, 2H), 4.43 (d, J = 9 Hz, ^{10}C*H*, 2H). The ratio of the products **14-H_2**, **16**, and **17** as determined by ^{1}H NMR was 1:1:0.4, respectively. High-resolution mass spectra contained molecular ions consistent with [**14-H_2**]$^+$ (calculated 558.3220, found 558.3246), [**16**]$^+$ (calculated 560.3376, found 560.3362), and [**17**]$^+$ (calculated 562.3532, found 562.3461). The ratio of the molecular ions for **14-H_2**, **16**, and **17** was roughly 1:1:0.4, respectively. The IR spectrum of the insoluble red solid was consistent with $(dmgH)_2Ni$.

NMR Tube Reactions. **28. $Fe(N(TMS)_2)_2(thf)$ + $(ImCH_2Py)_2Ar_2CH_2$: Production of bis[3,7-di-tert-butyl-1,9-dimethyl-N10,N11-bis(pyridin-2-ylmethylene)-10,11-dihydro-5H-dibenzo[a,d][7]annulene-10,11-diamine] diiron**

(12-Fe$_2$). $(ImCH_2Py)_2Ar_2CH_2$ (10 mg, 0.02 mmol) in C_6D_6 (0.3 mL) was added to a solution of Fe(N(TMS)2)2(thf) (8 mg, 0.02 mmol) in C_6D_6 (0.3 mL) in an NMR tube and sealed. The solution turned green upon thawing and turned red within five minutes, at which time HMDS and THF were visible in the ^{1}H NMR spectrum (~1:1 ratio, respectively), amongst several paramagnetic resonances. After 8 d at room temperature there had been nearly complete (>80%) conversion to a new diamagnetic product (all peaks have $\nu_{1/2} \geq 10$ Hz) . Spectral characteristics were determined by gCOSY, ^{13}C NMR, ROESY, and HSQCAD spectroscopies. ^{1}H (C_6D_6): δ 1.14 (s, $^{30}CH_3$ & $^{32}CH_3$, 18 H), 2.22, (s, $^{33}CH_3$, 3H), 2.43 (s, $^{28}CH_3$, 3H), 2.59 (d, J = 12 Hz, ^{14}CHH, 1H), 3.88 (d, J = 12 Hz, ^{14}CHH, 1H), 4.10 (s, ^{22}CH, 1H), 5.20 (s, ^{7}CH, 1H), 5.69 (s, ^{24}CH, 1H), 6.14 (s, ^{26}CH, 1H), 6.26 (s, ^{16}CH, 1H), 6.36 (s, ^{21}CH, 1H), 6.59 (s, ^{25}CH, 1H), 6.76 (s, ^{18}CH, 1H), 7.53 (s, ^{27}CH, 1H), 8.17 (s, ^{6}CH, 1H), 8.97 (s, ^{1}CH, 1H). ^{13}C (C_6D_6): δ 20.78 ($^{28}CH_3$), 22.36 ($^{33}CH_3$), 31.76 ($^{32}CH_3$), 31.83 ($^{30}CH_3$), 34.46 ($^{31}C(CH_3)_3$), 34.67 ($^{29}C(CH_3)_3$), 42.54 ($^{14}CH_2$), 69.03 (^{21}CH), 74.57 (^{22}CH), 75.34 (^{7}CH), 113.24 (^{24}CH), 114.67 (^{3}CH), 120.76 (^{2}CH), 121.82 (^{27}CH), 123.65 (^{12}CH), 124.06 (^{18}CH), 124.32 (^{4}CH), 125.67 (^{10}CH), 130.82 (^{25}CH), 134.37 (^{9}C), 135.87 (^{19}C), 138.37 (^{13}C), 138.60 (^{15}C), 142.19 (^{8}C), 144.81 (^{20}C), 149.25 (^{11}C), 150.31 (^{17}C), 152.17 (^{27}CH), 152.27 (^{1}CH), 156.43 (^{6}CH). See below for the numbering scheme.

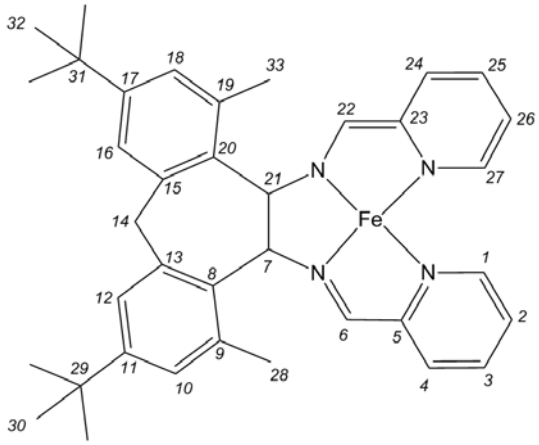

29. **Catalytic cyclization of $Me_2C(ImCH_2Py)_2$: (4,4-dimethyl-2-(pyridin-2-yl)-N-(pyridin-2-ylmethylene)pyrrolidin-3-amine).** An NMR tube was charged with **$Me_2C(ImCH_2Py)_2$** (21 mg, 0.075 mmol) and C_6D_6 (0.3 mL). A solution of $Fe(N(TMS)_2)_2(thf)$ (0.008 mmol) in C_6D_6 (0.3 mL) was added and the solution immediately turned red. After 37.5 h there was complete conversion to the title pyrrolidine product (TON = 11; TOF = 0.29 h^{-1}). ^1H (C_6D_6): δ 0.89 (s, *syn*-CH_3, 3H), 1.00 (s, *anti*-CH_3, 3H), 2.85 (dd, J = 7.6 Hz, 9.5 Hz, *syn*-$^2CH_2$, 1H), 3.08 (ddd, J = 7.6 Hz, 8 Hz, 9 Hz, ^1NH, 1H), 3.44 (dd, J = 7.6 Hz, 9.5 Hz, *anti*-$^2CH_2$, 1H), 3.58 (d, J = 5.5 Hz, ^4CH, 1H), 4.89 (dd, J = 5.5 Hz, 9 Hz, ^5CH, 1H), 6.42 (dd, J = 4.5 Hz, 7.5 Hz, Py_1-$^{5\text{-py}}CH$, 1H), 6.50 (dd, J = 4.5 Hz, 7.5 Hz, Py_2-$^{4\text{-py}}CH$, 1H), 6.92 (t, J = 7.5 Hz, Py_2-$^{5\text{-py}}CH$, 1H), 6.98 (t, J = 7.5 Hz, Py_1-$^{4\text{-py}}CH$, 1H), 7.21 (d, J = 7.5 Hz, Py_1-$^{3\text{-py}}CH$, 1H), 7.69 (dd, J = 7.5 Hz, Py_2-$^{3\text{-py}}CH$, 1H), 8.27 (s, ^{im}CH, 1H), 8.37 (d, J = 4.5 Hz, Py_1-$^{6\text{-py}}CH$, 1H), 8.39 (d, J = 4.5 Hz, Py_2-$^{6\text{-py}}CH$, 1H). See below for the numbering scheme.

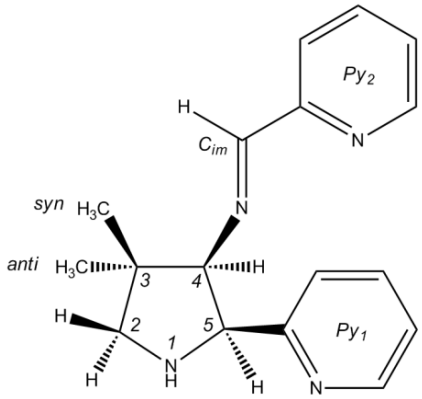

In the catalytic runs a minor byproduct was created that was consistent with N-(2-methylpropylidene)-1-(pyridin-2-yl)methanamine and confirmed by independent synthesis.[57] ^1H (C_6D_6): δ 0.96 (d, J = 7 Hz, CH_3, 6H), 2.27 (d of sep., J = 4 Hz, 7 Hz, Me_2CH, 1H) , 4.77 (s, CH_2, 2H), 6.64 (dd, J = 4.5 Hz, 8 Hz, Py_1-$^{5\text{-py}}CH$, 1H), 7.13 (t, J = 8 Hz, Py_1-$^{4\text{-py}}CH$, 1H), 7.37 (d, J = 8 Hz, Py_1-$^{3\text{-py}}CH$, 1H), 7.41 (d, J = 4 Hz, ^{im}CH, 1H), 8.49 (d, J = 4.5 Hz, Py_1-$^{6\text{-py}}CH$, 1H).

30. Catalytic cyclization of 1,1-^{c}Pent(ImCH$_2$Py)$_2$: (3-(pyridin-2-yl)-N-(pyridin-2-ylmethylene)-2-azaspiro[4.4]nonan-4-amine). An NMR tube was charged with **1,1-^{c}Pent (ImCH$_2$Py)$_2$** (21 mg, 0.068 mmol) and C_6D_6 (0.3 mL). A solution of Fe(N(TMS)$_2$)$_2$(thf) (0.007 mmol) in C_6D_6 (0.3 mL) was added and the solution immediately turned red. After 56 h there was complete conversion to the title pyrrolidine product (TON = 9.7; TOF = 0.17 h^{-1}). Spectral characteristics were determined by gCOSY, ^{13}C NMR, ROESY, and HSQCAD spectroscopies. ^{1}H (C_6D_6): δ 1.34 (m, ^{6}C*H*H, 1H), 1.35 (m, ^{8}C*H*H, 1H), 1.41 (m, ^{7}C*H*H, 1H), 1.46 (m, ^{9}C*H*H, 1H), 1.50 (m, ^{6}CH*H*, 1H), 1.52 (m, ^{8}CH*H*, 1H), 1.52 (m, ^{7}CH*H*, 1H), 1.56 (m, ^{9}CH*H*, 1H), 2.95 (d, J = 9.8 Hz, *syn*-^{2}C*H*$_2$, 1H), 3.59 (d, J = 9.8 Hz, *anti*-^{2}C*H*$_2$, 1H), 3.69 (d, J = 5 Hz, ^{4}C*H*, 1H), 4.86 (d, J = 5 Hz, ^{5}C*H*, 1H), 6.43 (dd, J = 4.5 Hz, 7.5 Hz, Py$_1$-$^{5\text{-py}}$C*H*, 1H), 6.51 (dd, J = 4.5 Hz, 7.5 Hz, Py$_2$-$^{4\text{-py}}$C*H*, 1H), 6.93 (t, J = 7.5 Hz, Py$_2$-$^{5\text{-py}}$C*H*, 1H), 7.01 (t, J = 7.5 Hz, Py$_1$-$^{4\text{-py}}$C*H*, 1H), 7.32 (d, J = 7.5 Hz, Py$_1$-$^{3\text{-py}}$C*H*, 1H), 7.76 (dd, J = 7.5 Hz, Py$_2$-$^{3\text{-py}}$C*H*, 1H), 8.35 (d, J = 4.5 Hz, Py$_1$-$^{6\text{-py}}$C*H*, 1H), 8.38 (d, J = 4.5 Hz, Py$_2$-$^{6\text{-py}}$C*H*, 1H). ^{13}C (C_6D_6): δ 25.32 (^{7}*C*), 25.32 (^{8}*C*), 57.54 (^{3}*C*(CH$_2$)$_4$), 58.97 (^{2}CH$_2$), 69.64 (^{5}*C*H), 83.38 (^{4}*C*H), 121.01 (Py$_1$-$^{6\text{-py}}$*C*H), 121.46 (Py$_2$-$^{3\text{-py}}$*C*H), 123.04 (Py$_1$-$^{3\text{-py}}$*C*H), 124.56 (Py$_2$-$^{4\text{-py}}$*C*H), 135.48 (Py$_1$-$^{4\text{-py}}$*C*H), 136.11 (Py$_2$-$^{5\text{-py}}$*C*H), 148.95 (Py$_1$-$^{6\text{-py}}$*C*H), 149.75 (Py$_2$-$^{6\text{-py}}$*C*H), 155.77 (Py$_1$-$^{2\text{-py}}$*C*) , 161.70 (^{im}*C*), 162.28 (Py$_2$-$^{2\text{-py}}$*C*). See below for the numbering scheme.

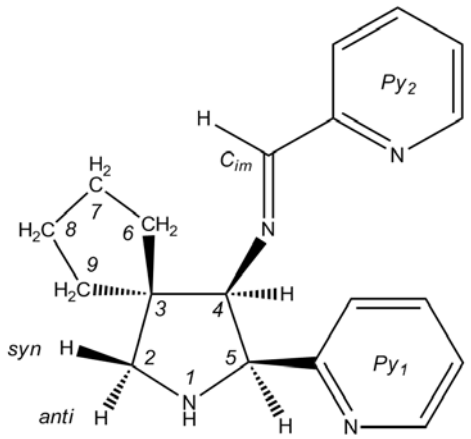

31. Thermolysis of 14-Ni$_2$: Synthesis of [(4a,8a)-4,4,8,8-tetramethyl-2,6-di(pyridin-2-yl)-N-(pyridin-2-ylmethylene)-1,2,3,4,4a,7,8,8a-octahydro-1,5-naphthyridin-3-amine] Nickel (15-Ni). An NMR tube was charged with **14-Ni$_2$** (10 mg, 0.015 mmol) and C_6D_6. The tube was heated at 50 °C for 10 h and then 90 °C for 12 h, during which time **15-Ni** was cleanly produced (>90%). Spectral characteristics were determined by gCOSY, 13C NMR, ROESY, and HSQCAD spectroscopies. ^{1}H (C_6D_6): δ 0.81 (s, ^{10}C*H*$_3$, 3H), 1.00 (s, ^{3}C*H*H, 3H), 1.09 (s, ^{9}C*H*$_3$, 3H), 1.39 (s, ^{11}C*H*$_3$, 3H), 1.49 (s, ^{12}C*H*$_3$, 3H), 1.90 (s, ^{8a}C*H*, 1H), 2.35 (s, ^{3}C*H*$_2$, 1H), 2.44 (s, ^{5}N*H*, 1H), 3.30 (s, ^{4a}C*H*, 1H), 4.41 (s, ^{7}C*H*, 1H), 4.76 (s, ^{6}C*H*, 1H), 6.45 (s, Py$_1$-$^{5\text{-py}}$C*H*, 1H), 6.63 (s, Py$_2$-$^{3\text{-py}}$C*H*, 1H), 6.72 (s, Py$_3$-$^{5\text{-py}}$C*H*, 1H), 6.77 (s, Py$_1$-$^{4\text{-py}}$C*H*, 1H), 6.78 (s, Py$_2$-$^{5\text{-py}}$C*H*, 1H), 6.87 (s, Py$_2$-$^{4\text{-py}}$C*H*, 1H), 7.04 (s, Py$_3$-$^{3\text{-py}}$C*H*, 1H), 7.06 (s, Py$_2$-$^{4\text{-py}}$C*H*, 1H), 7.29 (s, Py$_1$-$^{3\text{-py}}$C*H*, 1H), 8.47 (s, Py$_1$-$^{6\text{-py}}$C*H*, 1H), 9.17 (s, Py$_2$-$^{6\text{-py}}$C*H*, 1H), 9.36 (s, Py$_3$-$^{6\text{-py}}$C*H*, 1H). ^{13}C (C_6D_6): δ 24.74 (^{9}*C*H$_3$), 25.17 (^{10}*C*H$_3$), 26.30 (^{12}*C*H$_3$), 26.45 (^{11}*C*H$_3$), 34.80 (^{3}*C*H$_2$), 40.80 (^{8}*C*(CH$_3$)$_2$), 41.40 (^{4}*C*(CH$_3$)$_2$), 59.90 (^{4a}*C*H), 60.71 (^{6}*C*H), 65.01 (^{8a}*C*H), 73.40 (^{7}*C*H), 117.31 (Py$_2$-$^{5\text{-py}}$*C*H), 117.52 (Py$_3$-$^{5\text{-py}}$*C*H),121.35 (Py$_1$-$^{5\text{-py}}$*C*H), 121.61 (Py$_2$-$^{3\text{-py}}$*C*H), 123.15 (Py$_2$-$^{3\text{-py}}$*C*H), 123.98 (Py$_2$-$^{4\text{-py}}$*C*H), 124.36 (Py$_3$-$^{3\text{-py}}$*C*H), 124.67 (Py$_3$-$^{4\text{-py}}$*C*H), 136.15 (Py$_1$-$^{4\text{-py}}$*C*H), 140.98 (^{13}*C*H), 146.09 (Py$_2$-$^{2\text{-py}}$*C*), 146.34 (Py$_3$-$^{2\text{-py}}$*C*), 148.17 (Py$_1$-$^{6\text{-py}}$*C*H), 150.83 (^{2}*C*), 162.81 (Py$_1$-$^{2\text{-py}}$*C*H).

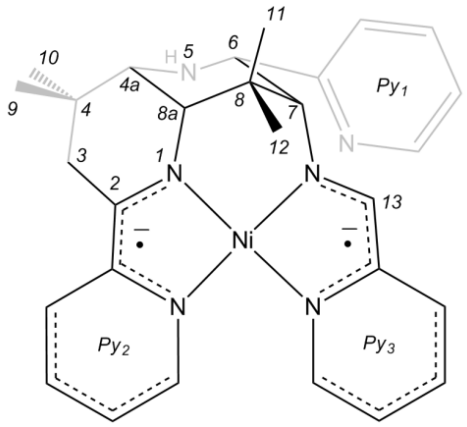

32. Bis(neopentyl) titanium (3,3-dimethyl-1,2-bis((pyridin-2-ylmethyl)amino)-cyclopropane-1,2-diide) (^{cPr}Im$_2$Py$_2$-TiNp$_2$). An NMR tube was charged with ^{cPr}**Im$_2$Py$_2$-TiCl$_2$** (30 mg, 0.068 mmol), NpLi (11 mg, 0.14 mmol, 2.1 eq.) and C_6D_6 (0.5 mL). After 2 d at room temperature a new product was observed that was consistent with the bis(neopentyl) complex. ^{1}H (C_6D_6): δ 0.69 (s, C*H*$_3$, 9H), 0.74 (s, C*H*$_2$, 2H), 0.78 (s, C*H*$_2$, 2H), 0.86 (s, C*H*$_3$, 9H), 1.27 (s, C*H*$_3$, 3H), 1.57 (s, C*H*$_3$, 3H), 3.00 (s, ^{cPr}C*H*, 2H), 4.76 (d, J = 21 Hz, CH*H*, 2H), 5.12 (d, J = 21 Hz, C*H*H, 2H), 6.75 (dd, J = 5.5, 7.5 Hz, ^{5}C*H*$_{py}$,), 6.77 (d, J = 7.5 Hz, ^{3}C*H*$_{py}$, 2H), 7.00 (t, J = 7.5 Hz, ^{4}C*H*$_{py}$, 2H), 8.63 (d, J = 5.5 Hz, ^{6}C*H*$_{py}$, 2H).

33. Catalytic cyclization of d$_4$-Me$_2$C(ImCD$_2$Py)$_2$: d$_4$-(4,4-dimethyl-2-(pyridin-2-yl)-N-(pyridin-2-ylmethylene)pyrrolidin-3-amine). An NMR tube was charged with **Me$_2$C(ImCH$_2$Py)$_2$** (21 mg, 0.075 mmol) and C_6D_6 (0.3 mL). A solution of Fe(N(TMS)$_2$)$_2$(thf) (0.008 mmol) in C_6D_6 (0.3 mL) was added and the solution immediately turned red. After 168 h there was 88% conversion to the title pyrrolidine product (TON = 9.7; TOF = 0.058 h^{-1}). There was 12% starting material remaining. There was some solid left in the tube that was not observed in the protio case. ^{1}H (C_6D_6): δ 0.89 (s, *syn*-CH$_3$, 3H), 1.01 (s, *anti*-CH$_3$, 3H), 2.84 (s, *syn*-^{2}C*H*D, 0.4 H), 3.43 (s, *anti*-^{2}CD*H*, 0.4 H), 3.58 (s, ^{4}C*H*, 1H), 6.43 (dd, J = 4.5 Hz, 7.5 Hz, Py$_1$-$^{5\text{-py}}$C*H*, 1H), 6.52 (dd, J = 4.5 Hz, 7.5 Hz, Py$_2$-$^{4\text{-py}}$C*H*, 1H), 6.93 (t, J = 7.5 Hz, Py$_2$-$^{5\text{-py}}$C*H*, 1H), 6.99 (t, J = 7.5 Hz, Py$_1$-$^{4\text{-py}}$C*H*, 1H), 7.22 (d, J = 7.5 Hz, Py$_1$-$^{3\text{-py}}$C*H*, 1H), 7.70 (dd, J = 7.5 Hz, Py$_2$-$^{3\text{-py}}$C*H*, 1H), 8.35 (d, J = 4.5 Hz, Py$_1$-$^{6\text{-py}}$C*H*, 1H), 8.37 (d, J = 4.5 Hz, Py$_2$-$^{6\text{-py}}$C*H*, 1H).

Single-Crystal X-ray Diffraction Studies. Upon isolation, the crystals were covered in polyisobutenes and placed under a 173K N_2 stream on the goniometer head of a Siemens P4 SMART CCD area detector (graphite-monochomated Mo Kα

radiation, $\lambda = 0.71073$ Å). The structures were solved by direct methods (SHELXS). All non-hydrogen atoms were refined anisotropically unless otherwise stated, and hydrogen atoms were treated as idealized contributions (Riding model).

1. MC(Fe)•Et_2O. A brown block measuring 0.20 × 0.15 × 0.05 was obtained from slow evaporation of an ethereal solution. A total of 39,612 reflections were collected with 8,647 being symmetry independent ($R_{int} = 0.0713$), and 5,920 were greater than $2\sigma(I)$. A semiempirical absorption correction from equivalents was applied, and the refinement utilized $w^{-1} = s^2(F_o^2) + (0.0601p)^2 + 1.5923p$, where $p = (F_o^2 + 2F_c^2)/3$.

2. 12-Cr_2. A black block measuring 0.20 × 0.15 × 0.10 was obtained from slow evaporation of THF. A total of 19,149 reflections were collected with 4,899 being symmetry independent ($R_{int} = 0.0922$), and 3,092 were greater than $2\sigma(I)$. A semiempirical absorption correction from equivalents was applied, and the refinement utilized $w^{-1} = s^2(F_o^2) + (0.0620p)^2 + 0.7318p$, where $p = (F_o^2 + 2F_c^2)/3$.

3. (NpImPy)Ni. A black parallelepiped measuring 0.40 × 0.15 × 0.05 was obtained from a cold diethyl ether solution. A total of 15,568 reflections were collected with 3,949 being symmetry independent ($R_{int} = 0.0404$), and 3,204 were greater than $2\sigma(I)$. A semiempirical absorption correction from equivalents was applied, and the refinement utilized $w^{-1} = s^2(F_o^2) + (0.0555p)^2 + 0.0436p$, where $p = (F_o^2 + 2F_c^2)/3$.

4. 14-Cr_2. A black plate measuring 0.40 × 0.30 × 0.10 was obtained from benzene. A total of 34,998 reflections were collected with 11,136 being symmetry independent ($R_{int} = 0.0336$), and 8,601 were greater than $2\sigma(I)$. A semiempirical absorption correction from equivalents was applied, and the refinement utilized $w^{-1} = s^2(F_o^2) + (0.0600p)^2 + 0.2306p$, where $p = (F_o^2 + 2F_c^2)/3$.

5. 14-Co_2. A black plate measuring 0.40 × 0.25 × 0.10 was obtained from THF solution. A total of 16,541 reflections were collected with 4,538 being symmetry independent (R_{int} = 0.0568), and 3,541 were greater than 2σ(I). A semiempirical absorption correction from equivalents was applied, and the refinement utilized w^{-1} = $s^2(F_o^2) + (0.0388p)^2 + 0.0000p$, where $p = (F_o^2 + 2F_c^2)/3$.

6. 14-Ni_2. A black block measuring 0.20 × 0.20 × 0.15 was obtained from THF solution. A total of 12,651 reflections were collected with 3,483 being symmetry independent (R_{int} = 0.0353), and 3,196 were greater than 2σ(I). A semiempirical absorption correction from equivalents was applied, and the refinement utilized w^{-1} = $s^2(F_o^2) + (0.0325p)^2 + 0.0000p$, where $p = (F_o^2 + 2F_c^2)/3$.

7. $^{cPr}Im_2Py_2$-$TiCl_2$. A red plate measuring 0.35 × 0.15 × 0.05 was obtained from benzene solution. A total of 24,059 reflections were collected with 6,409 being symmetry independent (R_{int} = 0.0294), and 5,015 were greater than 2σ(I). A semiempirical absorption correction from equivalents was applied, and the refinement utilized $w^{-1} = s^2(F_o^2) + (0.0369p)^2 + 0.6272p$, where $p = (F_o^2 + 2F_c^2)/3$.

Computational Details. Calculations performed using the Orca[52] software package. The hybrid functional B3LYP was used with the GTO basis sets published by the Ahlrichs group.[53] The triple-ζ basis set def2-TZVP(-f) was used for the metal and nitrogen while the remaining atoms were treated with the double-ζ split-valence basis set def2-SV(P). The RIJCOSX approximation[54] was used to speed up calculations using an auxiliary basis set that matched the orbital basis. The SCF-calculations were converged tightly; the energy change tolerance was 10^{-7} E_h and the tolerance in the DIIS error was 10^{-6} E_h. The geometry of (NpImPy)Ni was optimized using standard convergence criteria (ΔE < $5x10^{-6}$ E_h; RMS grad. < $1x10^{-4}$; max grad. < $3x10^{-4}$; RMS displacement < $2x10^{-3}$; max. displacement < $2x10^{-3}$ b). The

compounds **14-Cr_2**, **14-Co_2**, and **14-Ni_2** were calculated as single points at the crystallographically-determined geometry. The electronic structure of **14-Co_2** was initialized as a singlet [1,1] calculation but underwent spontaneous symmetry breaking to the [2,2] solution.

REFERENCES

1. Frazier, B. A.; Wolczanski, P. T.; Lobkovsky, E. B. *Inorg. Chem.* **2009,** *48,* 11576-11585.
2. (a) Grigg, R.; Armstrong, W. P. *Tetrahedron* **1988,** *44,* 1523-1534. (b) Freeman, F.; Govindarajoo, G. *Rev. Heteroatom Chem.* **1995,** *13,* 123-147.
3. (a) Nakao, Y.; Sakurai, K.; Nakahara, A. *Bull. Chem. Soc. Jpn.* **1967,** *40,* 1536-1538. (b) Grigg, R.; Devlin, J. *J. Chem. Soc., Chem. Commun.* **1986,** 631-632. (c) Grigg, R.; Gunaratne, Q. N.; Sridharan, V. *Tetrahedron* **1987,** *43,*5887-5888. (d) Grigg, R.; Montgomery, J.; Somasunderam, A. *Tetrahedron* **1992**, *47,* 10431-10442.
4. Incarvito, C.; Lam, M.; Rhatigan, B.; Rheingold, A.; Qin, C. J.; Gavrilova, A. L.; Bosnich, B. *J. Chem. Soc., Dalton Trans.* **2001,** *23,* 3478-3488.
5. (a) Frazier, B. A.; Wolczanski, P. T.; Lobkovsky, E. B.; Cundari, T. R. *J. Am. Chem. Soc.* **2009,** *131,* 3428-3429. (b)Frazier, B. A. Ph.D. Thesis, Cornell University, Ithaca, NY, **2010**.
6. Cotton, F. A.; Wilkinson, G. *Advanced Inorganic Chemistry*; Wiley-Interscience, New York, 1980.
7. Kahn, S. D.; Hehre, W. J.; Pople, J. A. *J. Am. Chem. Soc.* **1987,** *109,* 1871-1873.
8. Volpe, E. C.; Wolczanski, P. T.; Lobkovsky, E. B. *Organometallics* **2010,** *29,* 364-377.
9. (a) Lu, C. C.; Bill, E.; Weyhermüller, T.; Bothe, E.; Wieghardt, K. *J. Am. Chem. Soc.* **2008,** *130,* 3181-3197. (b) Trifonov, A. A.; Fedorova, E. A.; Borovkov, I. A.; Fukin, G. K.; Baranov, E. V.; Larionova, J.; Druzhkov, N. O. *Organometallics*, **2007,** *26,* 2488-2491. (c) Mondal, A.; Weyhermüller, T.; Wieghardt, K. *Chem. Commun.* **2009,** 6098-6100.

10. (a) Goodenough, J. B. *Phys. Chem. Solids* **1958,** *6,* 287-97 (b) Kanamori, J. *Phys. Chem. Solids* **1959,** *10,* 87-88.
11. Girerd, J.- J.; Journaux, Y. "Molecular Magnetism in Bioinorganic Chemistry," in: *Physical Methods in Bioinorganic Chemistry: Spectroscopy and Magnetism*, Que, L. Ed; University Science Books, Sausalito, CA, 2000.
12. Szabo, A.; Ostlund, N. S. "Modern Quantum Chemistry," Dover Publications, NY, 1996.
13. (a) Noodleman, L.; Norman, J. G. *J. Chem. Phys.* **1979,** *70,* 4903-4906. (b) Noodleman, L. *J. Chem. Phys.* **1980,** *74,* 5737-5743. (c) Neese, F. *J. Phys. Chem. Solids* **2004,** *65,*781-785.
14. Peterson, S. L.; Stucka, S. M.; Dinsmore, C. J. *Org. Lett.***2010,** *12,* 1340-1343.
15. Aoki, M.; Nakashima, K.; Kawabata, H.; Tsutui, S.; Shinkai, S. *J. Chem. Soc., Perkin Trans. 2* **1993,** *3,* 347-354.
16. (a) Zhu, S.- F.; Yang, Y.; Wang, L.- X.; Liu, B.; Zhou, Q.- L. *Org. Lett.* **2005,** *7,* 2333-2335. (b) Yamashita, M.; Yamamoto, Y.; Akiba, K.; Hashizume, D.; Iwasaki, F.; Takagi, N.; Nagase, S. *J. Am. Chem. Soc.* **2005,** *127,* 4354-4371. (c) Srivastava, R. R.; Zych, A. J.; Jenkins, D. M.; Wang, H.- J.; Chen, Z.-J.; Fairfax, D. J. *Syntetic Comm.* **2007,** *37,* 431-438.
17. Wile, B. M.; Trovitch, R. J.; Bart, S. C.; Tondreau, A. M.; Lobkovsky, E. B.; Milsmann, C.; Bill, E.; Wieghardt, K.; Chirik, P. J. *Inorg. Chem.* **2009,** *48,* 4190-4200.
18. Hussain, M. S. *J. Chem. Soc. Dalton. Trans.* **1982,** *12,* 2545-2547.
19. L. Que Jr., R. Y. N. Ho, *Chem. Rev.* **1996**, *96*, 2607-2624.
20. (a) Yamaguchi, K.; Takahara, Y.; Fueno, T. in: *Applied Quantum Chemistry*. Smith, V. H., Ed., Reidel, Dordrecht, 1986, pp 155. (b) Soda, T.; Kitagawa, Y.;

Onishi, T.; Takano, Y.; Shigeta, Y.; Nagao, H.; Yoshioka, Y.; Yamaguchi, K. *Chem. Phys. Lett.* **2000,** *319,* 223-230.

21. Cotton, F. A.; Walton, R. A. *Multiple Bonds between Metal Atoms*, 2nd ed.; Oxford University Press: Oxford, UK, 1993, Chapter 4.
22. Cotton, F. A.; Chen, H.; Daniels, L. M.; Feng, X. *J. Am. Chem. Soc.* **1992,** *114,* 8980-8983.
23. Bino, A.; Cotton, F. A.; Kaim, W. *Inorg. Chem.* **1979,** *18,* 3566-3568.
24. Cotton, F. A.; Timmons, D. J. *Polyhedron* **1997,** *17,* 179-184.
25. Edema, J. J. H.; Gambarotta, S.; Van der Sluis, P.; Smeets, W. J. J.; Spek, A. L. *Inorg. Chem.* **1989,** *28,* 3782-3784.
26. Bondi, A. *J. Phys. Chem.***1964,** *68,* 441-451.
27. (a) Li, X.; Schenkel, L. B.; Kozlowski, M. C. *Org. Lett.* **2000,** *2,* 875-878. (b) Xu, Z.; Kozlowski, M. C. *J. Org. Chem.***2002**, *67,* 3072-3078
28. Penelle, J.; Tits, M.; Christen, P.; Molgo, J.; Brandt, V.; Frederich, M.; Angenot, L. *Phytochemistry* **2000,** *53,* 1057-1066.
29. Cotton, F. A. *Inorg. Chem.* **1965,** *4,* 334-336.
30. (a) Andersson, K., Jr.; Bauschlicher, C. W.; Persson, B. J.; Roos, B. O. *Chem. Phys. Lett.* **1996,** *257,* 238-248.
31. Liang, F.; Lin, S.; Wei, Y. *J. Am .Chem. Soc.* **2011,** *in press.* doi: 10.1021/ja110870f
32. (a) Novoa, J. J.; Aullon, G.; Alemany, P.; Alvarez, S. *J. Am. Chem. Soc.* **1995,** *117,* 7169-7171. (b) Coleman, A. W.; Eadie, D. T.; Stobart, S. R.; Zaworotko, M. J.; Atwood, J. L. *J. Am. Chem. Soc.* **1982,** *104,* 922-923. (c) Roundhill, D.M.; Gray, H. B.; Che, C.-M. *Acc. Chem. Res.* **1989,** *22,* 55-61. (d) Bercaw, J.; Durrell, A.; Gray, H.; Green,J.; Hazari, N.; Labinger, J.; Winkler, J. *Inorg. Chem.* **2010,** *49,* 1801-1810.

33. Xia, B.-H.; Che, C.-M.; Phillips, D. L.; Leung, K.-H.; Cheung, K.-K. *Inorg. Chem.* **2002,** *41,* 3866-3875.

34. Kenny, J. P; King, B. R.; Schaefer, H. F., III. *Inorg. Chem.***2001,** *40,* 900-911.

35. Ketterer, N. A.; Fan, H.; Blackmore, K. J.; Yang, X.; Ziller, J. W.; Baik, M.-H.; Heyduk, A. F. *J. Am. Chem. Soc.* **2008,** *130,* 4364-4374.

36. (a) Jubb, J.; Floriani, C.; Chiesi-Villa, A.; Rizzoli, C. *J. Am. Chem. Soc.* **1992,** *114,* 6571-6573. (b) De Angelis, S.; Solari, E.; Floriani, C.; Chiesi-Villa, A.; Rizzoli, C. *J. Am .Chem. Soc.* **1994,** *116,* 5702-5713. (c) Piarulli, U.; Solari, E.; Floriani, C.; Chiesi-Villa, A; Rizzoli, C. *J. Am. Chem. Soc.* **1996,** *118,* 3634-3642. (d) Crescenzi, R.; Solari, E.; Floriani, C.; Chiesi-Villa, A.; Rizzoli, C. *Inorg. Chem.* **1998,** *37,* 6044-6051. (e) Crescenzi, R.; Solari, E.; Floriani, C.; Chiesi-Villa, A.; Rizzoli, C. *J. Am. Chem. Soc.* **1999,** *121,* 1695-1706. (f) Bachmann, J.; Nocera, D. G. *J. Am. Chem. Soc.* **2004,** *126,* 2829-2837. (g) Bachmann, J.; Nocera, D. G. *J. Am. Chem. Soc.* **2005,** *127,* 4730-4743. (h) Bachmann, J.; Hodgkiss, J. M.; Young, E. R.; Nocera, D. G. *Inorg. Chem.* **2007,** *46,* 607-609. (i) Bachmann, J.; Teets, T. S.; Nocera, D. G. *Dalton Trans.* **2008,** *34,* 4549-4551. (j) Bhattacharya, D.; Maji, S.; Pal, K.; Sarkar, S. *Inorg. Chem.* **2009,** *48,* 6362-6370

37. Kyushin, S.; Ikarugi, M.; Takatsuna, K.; Goto, M.; Matsumoto, H. *J. Organomet. Chem.***1996,** *510,* 121-133

38. Ittel, S. D.; English, A. D.; Tolman, C. A.; Jesson, J. P. *Inorg. Chim. Acta.* **1979**, *33*, 101-106.

39. (a) Olmstead, M. M.; Power, P. P.; Shoner, S. C. *Inorg. Chem.* **1991**, *30*, 2547-2551. (b) Andersen, R. A.; Faegri, K.; Green, J. C.; Haaland, A.; Lappert, M. F.; Leung, W. P.; Rypdal, K. *Inorg. Chem.* **1988**, *27*, 1782-1786.

40. Olmstead, M. M.; Power, P. P.; Shoner, S. C. *Inorg. Chem.* **1991,** *30,* 2547-2551.

41. Klose, A.; Solari, E.; Floriani, C.; Chiesi-Villa, A.; Rizzoli, C.; Re, N. *J. Am. Chem. Soc.* **1994,** *116,* 9123-35.

42. Hope, H.; Olmstead, M.; Murray, B. D.; Power, P. P. *J. Am. Chem. Soc.* **1985,** *107,* 712-13.

43. Buerger, H.; Wannagat, U. *Monatsh. Chemie.* **1964,** *95,* 1099-1102.

44. Rivillo, D.; Gulyas, H.; Benet-Buchholz, J.; Escudero-Adan, E. C.; Freixa, Z.; van Leeuwen, P. W. N. M *Angew. Chem. Intl. Ed.* **2007,** *46,* 7247-7250.

45. Edema, J. J. H.; Duchateau, R.; Gambarotta, S.; Hynes, R.; Gabe, E. *Inorg. Chem.* **1991,** *30,* 154-6.

46. Edema, J. J. H.; Stauthamer, W.; Van Bolhuis, F.; Gambarotta, S.; Smeets, W. J. J.; Spek, A. L. *Inorg. Chem.* **1990,** *29,* 1302-6.

47. Agami, C.; Platzer, N.; Sevestre, H. *Bull. Soc. Chim. Fr.* **1987,** *2,* 358-60.

48. Zhang, J.; Khaskin, E.; Anderson, N. P.; Zavalij, P. Y.; Vedernikov, A. N. *Chem. Commun.*, **2008,** *31,* 3625-3627.

49. Hicks, R. G.; Koivisto, B. D.; Lemaire, M. T. *Org. Lett.* **2004,** *6,* 887-1890.

50. Zepik, H. H.; Benner, S. A. *J. Org. Chem.* **1999,** *64,* 8080-8083.

51. Domin, D.; Benito-Garagorri, D.; Mereiter, K.; Froehlich, J.; Kirchner, K. *Organometallics* **2005,** *24,* 3957-3965.

52. Neese, F. Orca - an ab initio, DFT and Semiempirical Electronic Structure Package, Version 2.7, Revision 0; Institut für Physikalische und Theoretische Chemie, Universität Bonn: Bonn, Germany, August 2009.

53. (a) Schäfer, A.; Horn, H.; Ahlrichs, R. *J. Chem. Phys.* **1992,** *97,* 2571. (b) Schäfer, A.; Huber, C.; Ahlrichs, R. *J. Chem. Phys.* **1994,** *100,* 5829. (c)

Weigend, F.; Ahlrichs, R. *Phys. Chem. Chem. Phys.* **2005,** *7,* 3297. (d) Neese, F.; Wennmohs,F.; Hansen, A.; Becker, U. *Chem. Phys.* **2009,** *356,* 98.

54. Oshima, S.; Hirayama, N.; Kubono, K.; Kousen, H.; Honjo, T. *Anal. Sci.* **2002**, *18,* 1351-1355.

55. Fernandez, I.; Trovitch, R. J.; Lobkovsky, E.; Chirik, P. J. *Organometallics* **2008,** *27,* 109-118.

56. Bart, S. C.; Chlopek, K.; Bill, E.; Bouwkamp, M. W.; Lobkovsky, E.; Neese, F.; Wieghardt, K.; Chirik, P. J. *J. Am .Chem. Soc.***2006,** *128,* 13901-13912.

57. Peter, H.; Reinehr, D. *Helv. Chim. Acta* **1978,** *61,* 1115-1117.

APPENDIX

^{93}Nb NMR in Solution

Despite the ubiquitous usage of heteronuclei (^{13}C, ^{19}F, ^{31}P, ^{15}N) in NMR spectroscopic studies, observation of quadrupolar nuclei (I > ½) in solution has been relatively underutilized as an analytical tool in synthetic inorganic chemistry. Direct observation of quadrupolar metals has enjoyed some attention in solid-state[1] and biological applications,[2] but rapid relaxation and broad linewidths have limited the number of spectroscopic studies on soluble complexes. In recent years there have been several studies that involved ^{93}Nb NMR,[3] but there are relatively few *comprehensive* studies on a series of compounds.[4] During the investigations of Hirsekorn into the P-C bond cleavage chemistry of $(silox)_3NbPMe_3$,[5] it was noted that the ^{93}Nb NMR spectrum of $[(silox)_3NbP]Li$ manifested as a clean doublet at 463 ppm (J_{NbP} = 550 Hz, THF-d_8). This work was extended to include 16 other compounds that were readily available for study, and these results are presented in Table A.1. The chemical shifts are also presented in Figure A.1 as a chemical shift scale.

The ability to detect a ^{93}Nb signal is dependent on the linewidth of the signal, which is based on the T_1 and T_2 relaxation times. Since quadrupolar relaxation is usually the most efficient pathway for relaxation, the linewidth $\nu_{½}$ for the resonance of a quadrupolar nucleus is related to the T_1 relaxation as determined by Eq. A.1,[6]

$$\frac{1}{\nu_{1/2}} \propto \frac{1}{T_1} = \frac{3}{40}\frac{2I+3}{I^2(2I-1)}\left(1+\frac{\eta^2}{3}\right)\left(\frac{e^2qQ}{\hbar}\right)\tau_c \qquad \textbf{Eq. A.1}$$

where η is the asymmetry parameter, Q is the nuclear quadrupole moment, τ_c is the rotational correlation time, and the other terms have their usual meanings. These terms will be treated later in the discussion of signal linewidths.

Table A.1. ^{93}Nb Data for a series of available niobium complexes. ([Nb] = $(silox)_3Nb$)

Entry	Compound	Shift (ppm)	$\nu_{½}$ (Hz)	$^{1}J_{Nb-X}$ (T)
1	[Nb]=NN=CHTMS	-965.1	276	
2	[Nb]=O	-947.1	2000	
3	[Nb]=NN=CPh_2	-864.1	6000	
4	[Nb]Cl_2	-755.3	20000	
5	[Nb]=^{13}C=^{13}C =O	-652.8	1380	630 Hz (366 K)
6	[Nb]=$CHCH_3$	-27.62	1800	
7	[Nb]=CH_2	11.1	2600	
8	[Nb]=CH-CH=CH-CH_3 (trans?)	33.3	2500	
9	[Nb]=CH-CH=CH-CH_3CH_2Ph (trans?)	41	6000	
10	[Nb]=CH-CH=CH-CH_3 (cis?)	73.9	2700	
11	[Nb]=CH-CH=CH-CH_3CH_2Ph (cis?)	76.5	5000	
12	[Nb](C_2H_4)	296.3	2600	
13	[Nb](k^2-$CH_2(CH)_2CH_2$)	311.6	19000	
14	[Nb](α,α-d_2-VyCyPr) (diastereomer mix)	361.5	21000	
15	[Nb]=PH	528.3	13000	
16	[Nb]=P^- (THF-d^8)	463	1100	550 Hz (298 K)
17	[Nb]=PMe	660	12000	

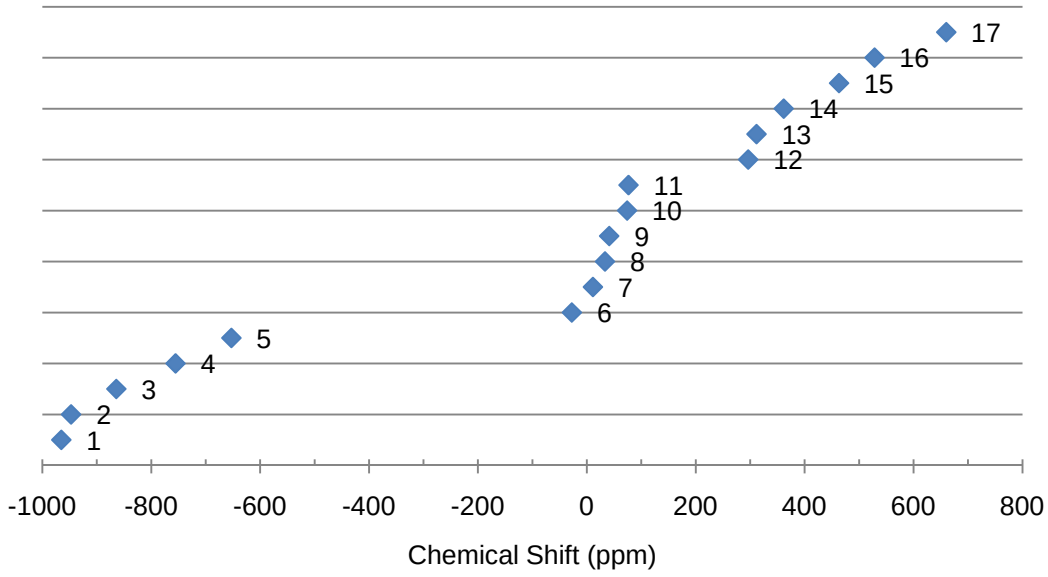

Figure A.1. Plot of ^{93}Nb chemical shifts for the complexes listed in Table A.1.

Chemical Shift Trends

Despite the disadvantages of quadrupolar nuclei, ^{93}Nb NMR has some advantages that make its use worthwhile. The nucleus itself is 100% abundant and its sensitivity is about half that of ^{1}H.[7] The broadness of the peaks in is offset by the wide chemical shift disparity (–1500 to 700).[4b] In general, the chemical shifts for ^{93}Nb species studied seem to increase with decreasing electronegativity. The first four of the series (cmpds. 1-4) are clearly Nb(V) species with considerable ionic character. There are six alkylidene species studied that fell between –30 and +80 ppm, and are quite distinct from the three olefin adducts studied (296 to 362 ppm). The diastereomeric 1-phenyl-2-vinylcyclopropane adducts (entry 14 in Table A.1) overlap. Although the peak could be modeled as two peaks at 323 ppm ($\nu_{½}$ = 16 kHz) and 377 ppm ($\nu_{½}$ = 20 kHz) that integrate 1:2.1 (close to the known diastereomer ratio of 1:1.8), this is only one of several models that fit the curve. The phosphinidene derivatives (entries 15-17) are the most downfield.

Peak Broadness

There are three primary issues that affect the broadness of the peaks within the context of Eq. A.1. The first is based on the asymmetry parameter, η, which is related to the electric field gradient (EFG) tensor elements V_{xx}, V_{yy}, and V_{zz} (Eq. A.2):

$$\eta = \frac{V_{xx} - V_{yy}}{V_{zz}} \qquad \textbf{Eq. A.2.}$$

From Eq. A.1 it can be seen that decreased symmetry in the EFG results in faster relaxation times and broader linewidths. Perfectly tetrahedral or octahedral symmetry would reduce η to zero and the linewidth would then be determined by other factors. The differences between P and O help rationalize the breadth of the two phosphinidenes (12-13 kHz) in comparison with the other pseudo-tetrahedral compounds (< 6 kHz). Other contributions to the linewidth are related to dynamic

processes. The linewidth of the ^{93}Nb signal is highly sensitive to hindered rotation about the Nb-X bond for two reasons. As in other NMR spectroscopies, dynamic processes that occur at rates on the order of the NMR experiment will broaden lines due to the large number of environments sampled by the nucleus under observation. With quadrupolar nuclei, the loss of symmetry incurs an additional penalty due to EFG asymmetry. The remaining contribution to line broadness reside in the rotational correlation time (τ_c); molecules that rotate slowly on the NMR timescale have a lower apparent EFG symmetry. The $(silox)_3Nb$ moiety is large and usually in the slow rotation limit, and linewidths are greatly assisted by elevated temperatures and concomitantly faster tumbling rates and sharper linewidths. This is most obvious with entry 5 in Table A.1, where the Nb-^{13}C coupling constant was visible only at 93 °C (Figure A.2.).

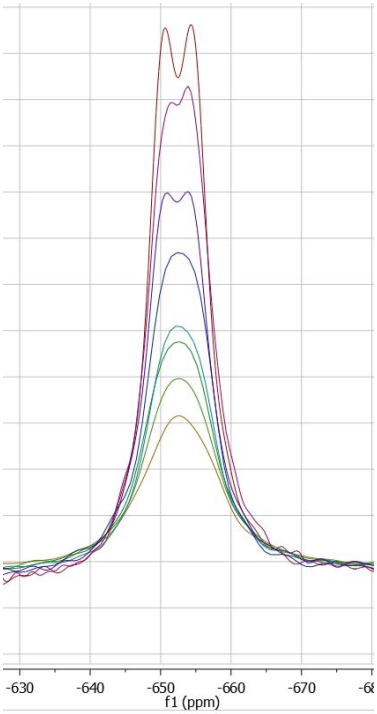

Figure A.2. Variable-temperature ^{93}Nb NMR spectra for $(silox)_3Nb^{13}C^{13}CO$ from 23 °C to 93 °C. The relative intensities are arbitrary.

Experimental

All manipulations were carried out either using a nitrogen glovebox or high-vacuum and Schlenk techniques. All glassware was oven dried. Benzene-d_6 was refluxed over sodium metal, vacuum distilled and stored under nitrogen over activated 4Å molecular sieves. Tetrahydrofuran-d_8 was refluxed over sodium metal, vacuum distilled and stored over sodium beenzophenone ketyl.

^{93}Nb NMR spectra were obtained on a Varian 500 MHz (INOVA) spectrometer operating at 122.32 MHz and externally referenced to saturated $NbCl_5$ in acetonitrile (0.00 ppm). In a typical procedure, a ^{31}P NMR experiment was loaded into the console software (VNMRJ 1.1B), the observe nucleus was changed to ^{93}Nb and the probe was tuned. Since the resonant frequency for ^{93}Nb is very close to that for ^{13}C, the probe settings (e.g. capacitor sticks, etc.) for ^{13}C NMR experiments should be a sufficient starting point from which to tune to ^{93}Nb. Shimming and locking on deuterated solvent are usually unnecessary since the ^{93}Nb signals are so broad (>200 Hz). Acquisition times ranged from 1 – 5 ms with no recycle delay and 20,000 – 100,000 transients were required to obtain satisfactory signal-to-noise (~ 100 sec total experiment time).

REFERENCES

1. (a) Jerschow, A. *Prog. Nuc. Mag. Res. Spec.* **2005,** *46,* 63-78. (b) Wimperis, S. *Mod. Mag. Res.* **2006,** *3,* 1487-1494.
2. (a) Aramini, J. M.; Vogel, H. J. *Biochem. Cell Bio.* **1998,** *76,* 210-222. (b) Wu, G. *Biochem. Cell Bio.* **1998,** *76,* 429-442.
3. (a) Calderazzo, F.; Felten, C.; Pampaloni, G.; Rehder, D. *J. Chem. Soc. Dalton Trans.* **1992,** 2003-2007. (b) Amini, M. M.; Mirzaee, M.; Yaganeh, F.; Khavasi, Hamid R.; Mirzaei, P.; Ng, S. W. *Trans. Metal Chem.* **2008,** *33,* 79-83. (c) Jura, M.; Levason, W.; Ratnani, R.; Reid, G.; Webster, M. *Dalton Trans.* **2010,** *39,* 883-891. (d) Bühl, M.; Wrackmeyer, B. *Magn. Reson. Chem.* **2010,** *48,* S61–S68.
4. (a) Kidd, R. G.; Spinney, H. G. *Inorg. Chem.* **1973,** *12,* 1967-1971. (b) Lee, G. R.; Crayston, J. A. *J. Chem. Soc. Dalton Trans.* **1991,** 3073-3076.
5. (a) Hirsekorn, K. F.; Veige, A. S.; Wolczanski, P. T. *J. Am. Chem. Soc.* **2006,** *128,* 2192-2193. (b) Hirsekorn, K. F. Ph.D. Thesis, Cornell University, Ithaca, NY, **2005**.
6. Butler, L. "The NMR Parameters for Oxygen-17," in *^{17}O NMR Spectroscopy in organic chemistry.* Boykin, D. W., ed. CRC Press: Boca Raton, FL, 1991.
7. Lu, Y.- J.; Lalancette, R.; Beer, R. H. *Inorg. Chem.* **1996,** *35,* 2524-2529.